

Project phase 1, WP1

# Review of the public KNMI induced earthquake catalogue from the Groningen gas field

June 2018

---



## Contents

|          |  |           |
|----------|--|-----------|
| <b>1</b> | <b>Introduction</b>                                      | <b>9</b>  |
| <b>2</b> | <b>Review of metadata</b>                                | <b>10</b> |
| 2.1      | Development of the station network . . . . .             | 10        |
| 2.1.1    | Context and overview . . . . .                           | 10        |
| 2.1.2    | Boreholes . . . . .                                      | 13        |
| 2.1.3    | Surface accelerometers . . . . .                         | 14        |
| 2.1.4    | Instrumentation by other institutes . . . . .            | 15        |
| 2.1.5    | Conclusions . . . . .                                    | 16        |
| <b>3</b> | <b>Review of existing data</b>                           | <b>19</b> |
| 3.1      | Induced seismicity catalogue . . . . .                   | 19        |
| 3.2      | Data completeness . . . . .                              | 23        |
| 3.2.1    | G-network . . . . .                                      | 23        |
| 3.2.2    | B-network . . . . .                                      | 26        |
| 3.2.3    | Old borehole network . . . . .                           | 27        |
| 3.3      | Data homogeneity . . . . .                               | 31        |
| 3.3.1    | Changes in station location . . . . .                    | 31        |
| 3.3.2    | Homogeneity of spatial coverage . . . . .                | 32        |
| 3.3.3    | Homogeneity of catalogue precision . . . . .             | 33        |
| 3.3.4    | Homogeneity of magnitude computation . . . . .           | 36        |
| 3.3.5    | Homogeneity of event detection . . . . .                 | 37        |
| 3.4      | Magnitude of completeness . . . . .                      | 39        |
| 3.4.1    | Context and overview . . . . .                           | 39        |
| 3.4.2    | Observations and analysis of previous work . . . . .     | 39        |
| 3.4.3    | Analysis by NORSAR . . . . .                             | 40        |
| 3.4.4    | Comparison to state-of-the-art and conclusions . . . . . | 42        |
| <b>4</b> | <b>Review of data processing</b>                         | <b>45</b> |
| 4.1      | Event detection . . . . .                                | 45        |
| 4.1.1    | Definitions . . . . .                                    | 45        |
| 4.1.2    | Detectability as conducted by KNMI . . . . .             | 45        |
| 4.1.3    | Detection on real data . . . . .                         | 46        |
| 4.1.4    | Other detection algorithms . . . . .                     | 54        |
| 4.1.5    | Conclusions . . . . .                                    | 55        |
| 4.2      | Event location and uncertainty . . . . .                 | 57        |
| 4.2.1    | Overview . . . . .                                       | 57        |

|                   |   |            |
|-------------------|---|------------|
| 4.2.2             | Description of analysed data . . . . .  | 58         |
| 4.2.3             | Current procedures by KNMI . . . . .  | 58         |
| 4.2.4             | Velocity model . . . . .  | 62         |
| 4.2.5             | Arrival-time data . . . . .   | 62         |
| 4.2.6             | Station contributions . . . . .   | 67         |
| 4.2.7             | Station distribution . . . . .  | 69         |
| 4.2.8             | Station residuals . . . . .   | 79         |
| 4.2.9             | Pick consistency . . . . .  | 82         |
| 4.2.10            | Comparison to state-of-the-art . . . . .  | 92         |
| 4.2.11            | Conclusions . . . . .   | 94         |
| 4.3               | Magnitude computation . . . . .   | 97         |
| 4.3.1             | Context and overview . . . . .  | 97         |
| 4.3.2             | Magnitude types . . . . .   | 97         |
| 4.3.3             | Magnitude scaling relations . . . . .   | 101        |
| 4.3.4             | Comparison to state-of-the-art and conclusions . . . . .                            | 103        |
| 4.4               | Stress drop computation . . . . .   | 107        |
| 4.4.1             | Context and overview . . . . .  | 107        |
| 4.4.2             | Observations and analysis of previous work . . . . .                                | 107        |
| 4.4.3             | Comparison to state-of-the-art and conclusions . . . . .                            | 109        |
| <b>5</b>          | <b>Review of advanced data analyses</b>   | <b>113</b> |
| 5.1               | Event relocation . . . . .  | 113        |
| 5.2               | Cross-correlation of waveforms . . . . .  | 116        |
| 5.2.1             | Overview . . . . .  | 116        |
| 5.2.2             | Cross-correlation for event detection . . . . .                                     | 116        |
| 5.2.3             | Cross-correlation for event clustering . . . . .                                    | 117        |
| 5.2.4             | Cross-correlation for sensor orientation . . . . .                                  | 118        |
| 5.2.5             | Cross-correlation for wave velocities determination . . . . .                       | 119        |
| 5.3               | Focal mechanism computation using P- and S-wave amplitudes and polarities . . . . . | 121        |
| 5.3.1             | Context and overview . . . . .  | 121        |
| 5.3.2             | Double couple mechanisms computed by KNMI . . . . .                                 | 123        |
| 5.3.3             | Comparison to state-of-the-art and conclusions . . . . .                            | 125        |
| 5.4               | Full waveform inversion for event location and source mechanism . . . . .           | 127        |
| 5.4.1             | Context and overview . . . . .  | 127        |
| 5.4.2             | Source mechanisms computed by Shell . . . . .                                       | 127        |
| 5.4.3             | Source mechanisms computed by KNMI . . . . .  | 130        |
| 5.4.4             | Comparison to state-of-the-art and conclusions . . . . .                            | 134        |
| <b>Appendix A</b> | <b>Station network</b>  | <b>139</b> |

|   |            |
|---|------------|
| A.1 List of stations (2018) . . . . .   | 139        |
| A.2 List of "missing" stations . . . . .  | 141        |
| A.3 Instruments and orientation . . . . .   | 143        |
| A.4 Data transmission . . . . .   | 144        |
| <b>Appendix B Reviewed papers on the Groningen gas field consulted during project</b> | <b>146</b> |
| <b>Appendix C KNMI reports on the Groningen gas field consulted during project</b>    | <b>152</b> |
| <b>Appendix D NAM reports on the Groningen gas field consulted during project</b>     | <b>153</b> |
| <b>Appendix E Other documents on the Groningen gas field consulted during project</b> | <b>154</b> |

## Executive summary

This report covers Work Package 1 (WP1) of the NORSAR project to review the public KNMI induced seismicity catalogue from the Groningen gas field. This report is an evaluation of the published reports, data, and procedures that are involved in generating the induced seismicity catalogue. The purpose is to identify areas that can be improved, either by revisiting existing data, or modifying current procedures for future improvements. The results include an independent assessment, recommendations and comparisons to state-of-the-art methodologies. In the following paragraphs we summarise our main findings.

**Development of the station network:** Since the first induced seismic event was felt near Assen in 1986, the instrumentation in and around the Groningen field has developed substantially. Understanding this development and its consequences for monitoring induced seismicity is all the more important, since the network has implications on the data analysis overall.

**Data completeness:** Data completeness refers to the availability of data in a certain period of interest. KNMI provides easily accessible metadata for qualitative evaluation of the completeness since 2015. The G- and B-networks show good completeness with only few stations having longer periods of data gaps. For multi-level stations, mostly all sensor levels of the given station show gaps; only on a few occasions there were failures of single sensors. This indicates problems with data transmission. Typically, the majority of data gaps were fixed promptly within two days, which is very good, given the complexity and size of the network.

**Data homogeneity:** The design of the G-network provides a very homogeneous coverage of the Groningen area. The additional stations of the B-network and the old borehole network provide a denser coverage in some areas. Since KNMI's latest processing scheme requires at least six triggered stations, the network provides a homogeneous coverage that is exceptional in comparison with other regional networks.

**Event detection:** KNMI have used standard detection methods and made them evolve together with the upgrades in the station network. Until 2010, the stations operated in triggered mode and event detection was performed on the boreholes only. Continuous data are sent to the KNMI data centre since 2010. SeisComp3 started to be tested at that time and has been fully implemented in June 2015.

**Event location and uncertainty:** The event location methodology used by KNMI has consistently used an iteratively linearised inversion throughout the catalogue period. Pick consistency for the

bulletin data was judged to be good overall, with only two significant outliers corresponding to valid travel-time residuals. However, the data within the bulletin shows inconsistencies in terms of how these residuals are recorded. The use of S-waves for locating earthquakes changes with the introduction of the G-network in 2014. From this time, the use of S-waves is phased out, with the event location relying solely on the P-wave arrival-times.

No location uncertainties are provided in the publicly available catalogue or in the bulletin data. An indication of location uncertainty can be gained from rms residual values, providing a goodness of fit for each event. We understand that location uncertainties have been computed, but they are stored internally at KNMI.

Throughout the catalogue, the event depth is fixed to 3 km. Establishing the correct depth of the Groningen induced seismicity has important consequences in terms of understanding the seismic hazard, and the improvement of event depth resolvability should be a priority. In addition, the availability of a 3D velocity model for Groningen offers the potential to improve event location accuracy.

Analysis of the Groningen induced seismicity bulletin has shown that in addition to the permanent stations, many temporary stations were used for event location. The locations of these stations and their waveform data are not publicly available, making the analysis of event quality limited where they were used.

NORSAR recommends that event depth should be estimated whenever possible and that location uncertainties should be determined, with all relevant parameteric data stored in the publicly available bulletin. The 3D velocity model should be employed to this end.

**Event relocation:** Recent work has involved trying to improve both the lateral locations of the Groningen seismicity and resolving the depth of the events. The EDT method, which KNMI has investigated, shows good potential for use with the expanded network, and has recently taken advantage of the 3D velocity model generated by NAM. However, the methodology relies on many station pairs making it incompatible with events occurring before the network expansion. The published work also limits itself to the P-wave data, which - although of higher quality - again provides limitations in terms of the resolvability of event locations.

NORSAR recommends continued research into alternative earthquake location and relocation methodologies including direct search methods, and potentially implementing the EDT method for routine processing. While not recommended for standard processing, we do see value in investigating relocation methodologies such as the double-difference method, to better link the seismicity to structural features and to act as an independent assessment of the induced seismicity catalogue, in terms of event precision.

**Magnitude computation:** For all induced events in the Groningen region, the determination of the local magnitude  $M_L$  at KNMI is part of the standard processing and the basis for the Groningen seismic hazard and risk models. Mainly for larger events also moment magnitudes  $M_W$  have been determined from a spectral analysis. Scaling relations between  $M_L$  and  $M_W$  have been developed for the whole range of Groningen seismicity, which is in agreement with recent theoretical and empirical publications on scaling relations elsewhere. NORSAR recommend to determine a piecewise continuous function. This would require a sufficient amount of data and it may therefore be worth trying to further expand the catalogue of moment magnitude estimates with newer data since the network was upgraded.

**Magnitude of completeness:** KNMI and NAM applied the maximum curvature method MAXC to estimate the magnitude of completeness  $M_C$ , which is a valid choice. The analysis performed by KNMI using synthetic data to estimate  $M_C$  and at the same time optimising the fit of a Gutenberg-Richter relation to the data might be the best choice for the Groningen seismicity analysis. Common to all studies is a significant decrease in  $M_C$  from 1.2 to 0.5 (observed from 2003 to 2016), despite the large uncertainties. This is consistent with network upgrades. However, the used 200 events per analysed time period might be too few events, and we recommend to increase the sample size to at least 300 events for a more stable analysis. Additionally, we recommend a moving time window approach to estimate temporal  $M_C$  rather than analysing defined time periods.

**Stress drop computation:** Different studies, all applying the same model-dependent spectral method, conclude that stress drop estimates of the Groningen induced seismicity can be considered low in comparison to average tectonic earthquakes. Overall, only few events have been analysed and the uncertainties of individual stress drop estimates are too large to derive a statistically significant trend. The two most common sources of epistemic uncertainty and bias in stress drop estimates are a limited bandwidth of the analysed data and the well known trade-off between source corner frequency and travel-path attenuation. In light of this, NORSAR recommends to analyse the sensitivity of the obtained stress drop results with respect to underlying assumptions such as frequency-independent  $Q$ , and to attempt a verification of the obtained stress drop estimates with an independent method. However, owed to the comparatively small size of the catalogue at Groningen, the options for independent spectral analysis methods are limited and need to be carefully evaluated with respect to sample size, coverage, and reliability.

**Cross-correlation of waveforms:** KNMI uses waveform cross-correlation techniques for multiple purposes, such as (1) the detection of low SNR events, (2) the clustering of events for their subsequent relocation, (3) the orientation of the sensors of the G-network and (4) the determination of the P- and S-wave velocities. Unfortunately, due to highly variable waveforms, the use of methods requiring

clustering of events (e.g. for event relocation) is limited.

**Focal mechanism computation using P- and S-wave amplitudes and polarities:** Due to the sparseness of the network before the installation of the G-network, the inversion for focal mechanisms of earthquakes is only feasible in particular cases. We advise against any attempt to retrieve further focal mechanisms for past events that occurred before the installation of sufficient G-network stations. Due to the complexity of the wavefield, we advise against the use of first motion P- and S-polarities or amplitudes. Instead, we recommend employing full waveform analysis methods.

**Full waveform inversion for event location and source mechanism:** NORSAR recommends to use full waveform methods for full moment tensor inversion on a larger population of earthquakes in the Groningen region. The Grond algorithm, which is currently applied and further tested by KNMI, including its probabilistic methods, is setting the state-of-the-art. Further, a 3D Green's function database should be developed independently from Shell's, to compare 1D with 3D source mechanism solutions.

Overall, taking into account that the KNMI induced seismicity catalogue covers the complete time period of seismicity occurring within the Groningen field, in which both the instrumentation of the field as well as methodologies for data processing changed considerably, we consider the catalogue as extensive and of high quality. Over the years, huge progress has been made; certainly in instrumentation of the field, which is by now probably the best monitored gas field globally, but not least in data accessibility via KNMI's online data portal, the standardisation of their processing methodology and their continuous effort in research for further improvements.



## 1 Introduction

The report is subdivided into three chapters, summarising the reviews of metadata (chapter 2), the existing data (chapter 3), data processing (chapter 4) and advanced data analysis (chapter 4.4).

The review of metadata consists of the review of the development of the station network and availability of associated metadata (section 2.1). It is complemented by an appendix containing detailed information on stations, instruments and orientation as well as data transmission (appendix A).

In the chapter on the review of existing data, we collected the reports on tasks directly related to the induced seismicity catalogue and tasks that required actual data processing by NORSAR. After a description of data resources employed during the review (section 3.1), we analyse data completeness (section 3.2), data homogeneity (section 3.3) and the magnitude of completeness (section 3.4).

The chapter reviewing the data processing contains tasks that required accessing the induced seismicity bulletin in addition (for an explanation of the terms “catalogue” and “bulletin” as employed by us, see section 3.1). The chapter comprises the topics of event detection (section 4.1), event location and associated uncertainties (section 4.2), the calculation of magnitudes and the relationship between magnitude scales (section 4.3) as well as the computation of stress drop (section 4.4).

The final chapter deals with advanced data analyses. However, in the framework of this project, it is not possible to retrace any of such advanced computations in detail, instead, available literature and reports have been summarised and compared to the state-of-the-art. This chapter comprises a review on event relocation (section 5.1), methods employing cross-correlation of waveforms (section 5.2), computation of focal mechanisms using using P- and S-wave amplitudes and polarities (section 5.3) as well as full waveform inversion for event location and source mechanism (section 5.4).

In addition, we collected the references to documents related to the Groningen field that we consulted during the course of the project in the appendix: reviewed papers in appendix B, KNMI reports in appendix C, NAM reports in appendix D and miscellaneous reports by other organisations, presentations and conference abstracts in appendix E. Note that this list cannot represent a complete list of publications related to the Groningen field, but we hope it may be useful for others engaged in this topic. Further, references that are cited within the text are collected at the end of each section separately.

One additional source of information that we used in this review are reports provided through the ACISM project (“Assessing the Capabilities of Induced Seismicity Monitoring for CO<sub>2</sub>-storage”). The ACISM project was a three-year project (2015-2017) conducted by NORSAR and financially supported by the Norwegian CLIMIT Fond through the Gassnova company. Project partners were KNMI and NAM, and the project had associated collaboration with GFZ Potsdam (Germany), Deschutes Signal Processing LLC (USA), University of Oslo (Norway), and Princeton University (USA).

## 2 Review of metadata

### 2.1 Development of the station network

#### 2.1.1 Context and overview

In the Netherlands, natural seismicity is mainly concentrated in the Southern part of the country (in the Limburg province between Belgium and Germany) where active faults are well-known. Thus, the very first seismometers were installed in this part of the Netherlands at the beginning of the 20<sup>th</sup> century (Dost and Haak, 2007).

On the contrary, the Northern part of the country was considered aseismic. This is where the gas fields are located, among which one of the largest in the world: Groningen. The field was discovered in 1959 and the production started in 1963. During more than 20 years, no (or no significant) seismic activity was recorded in the area. However, in December 1986, the Assen earthquake ( $M_L=2.8$ ) occurred, followed one year later by another event ( $M_L=2.5$ ) located only a few kilometres South of Assen (events 1 and 2 in the figure 2.3). Although these events could not be related with certainty to the gas field exploitation, it was decided to instrument the area to monitor its seismicity. The figure 2.2 shows a rough time-line of the seismic instrumentation in the Netherlands as well as some of the decisive events which motivated the installation of new sensors over the years.

After the first two significant events of 1986 ( $M_L=2.8$ ) and 1987 ( $M_L=2.5$ ), the Ministry of Economic Affairs asked KNMI to start monitoring the region. This was conveyed by the installation of a small-scale surface seismic network around Assen in 1988, composed of 6 short-period and vertical-component sensors. This network was operational until 1994 (Dost, 2016). In-between, the occurrence of a third significant earthquake in 1989 ( $M_L=2.7$ ) increased the need for even more monitoring capacities in the Groningen area (and more generally in North Netherlands). Since then, the seismic instrumentation has been greatly improved, keeping in mind two main goals: (1) a better characterisation of the seismicity (detection, location, source mechanism...) and (2) the seismic hazard mitigation.

Two types of instruments were installed in order to provide different and complementary information:

- **Borehole** seismometers present the advantage of improving the monitoring capacities, by both increasing the signal-to-noise ratio (SNR) of the signals (hence lowering the detectability of the seismic events) and allowing to get better constraints on the location depth. Their configuration has evolved over time (number of sensors, spacing between sensors, depth of sensors...; figure 2.2).
- **Surface accelerometers**, on the other hand, present the advantage of being able to record earthquake strong motions where seismometers may be saturated. Moreover, the data can be used to assess and compute the seismic hazard via Ground Motion Models (GMM) as well as to

study the impact on the structures and evaluate the damages. Finally, they are also useful to study the wave propagation at close epicentral distances.

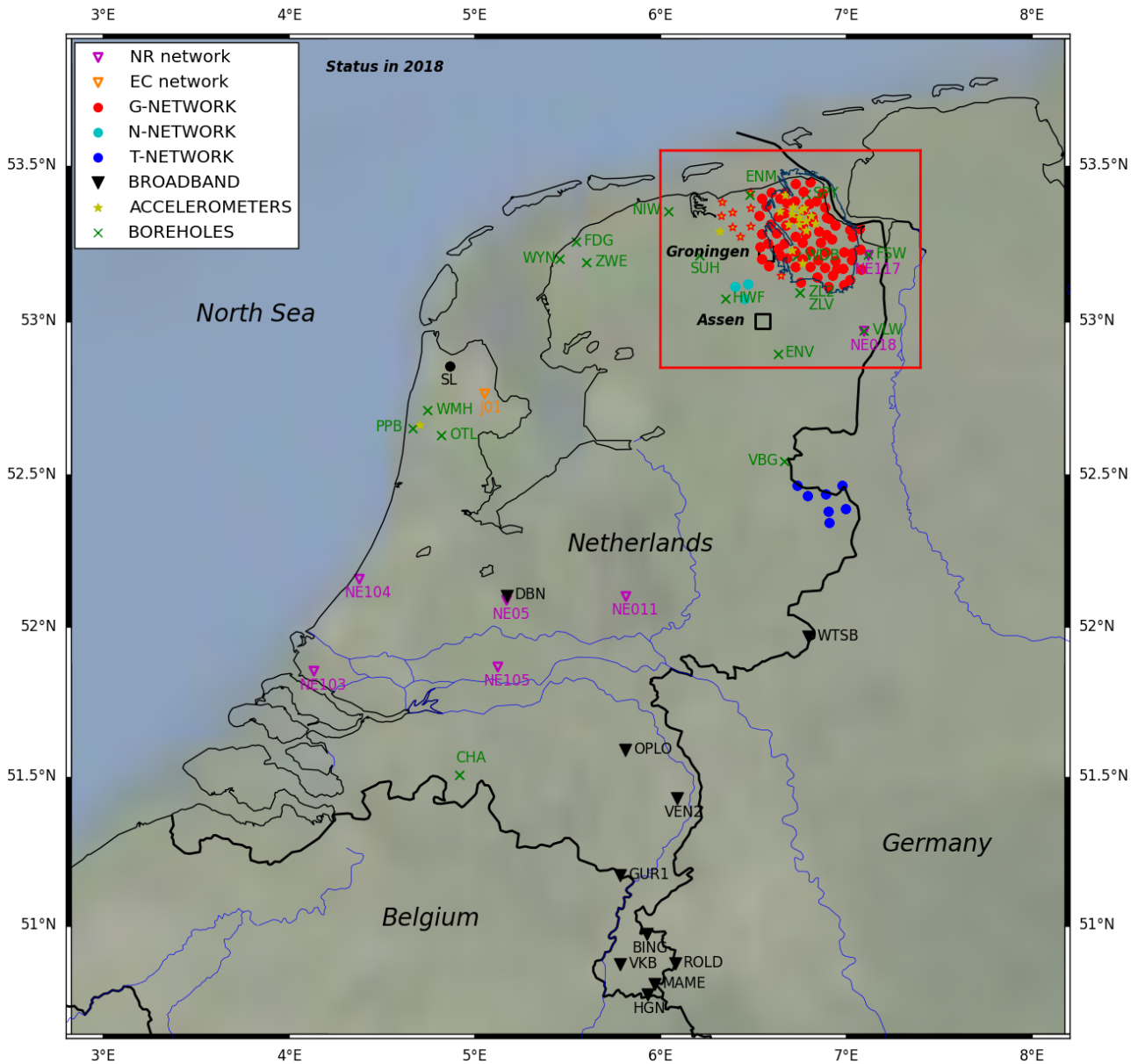


**Fig. 2.1:** Seismic instruments operated by KNMI across the Netherlands in 2018. The red square surrounds the area of interest around Groningen (see figure 2.3). Symbol code: reversed triangle=broadband; star=accelerometer; cross=borehole string; circle=borehole string and accelerometer at the surface.

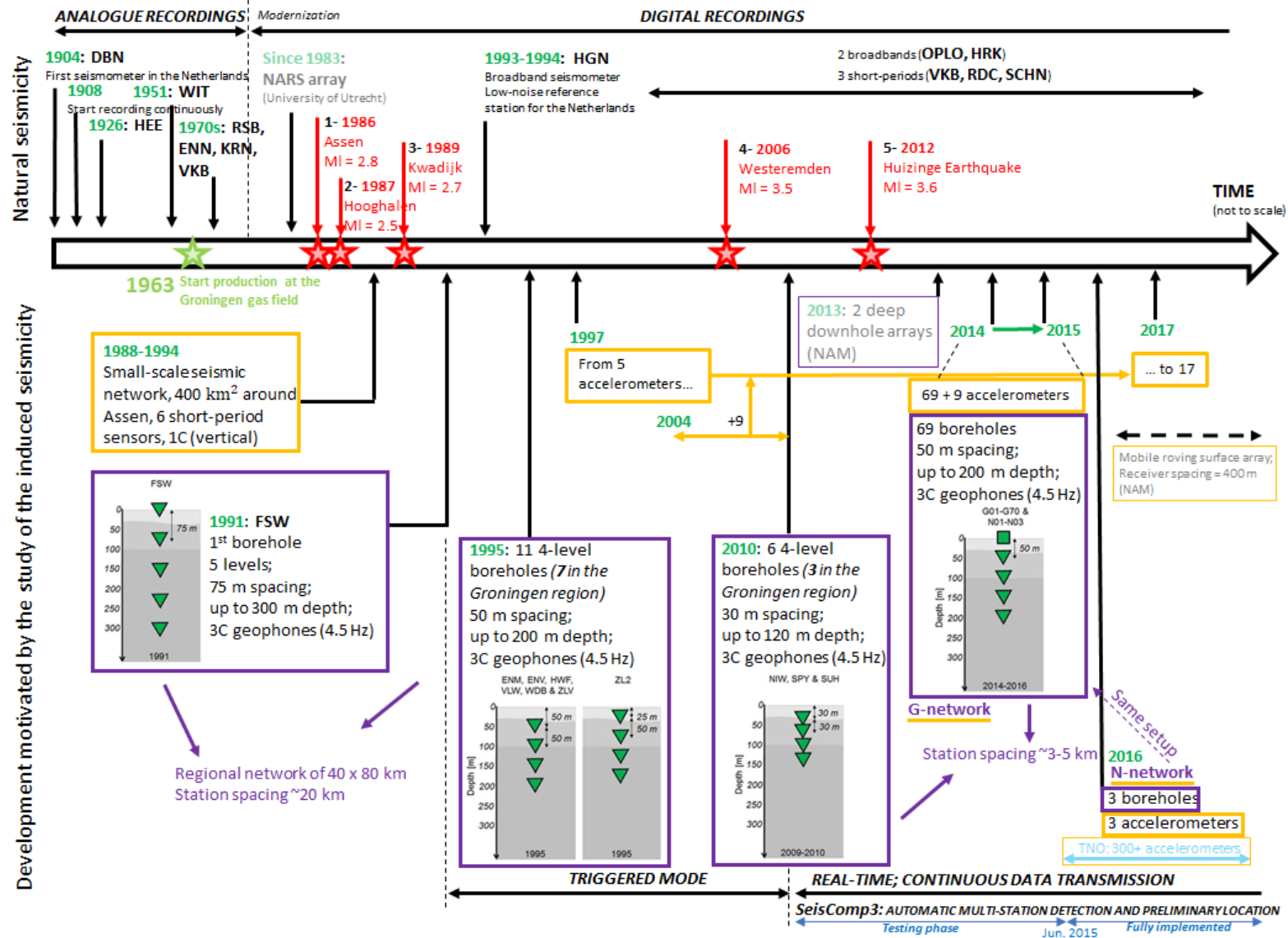


**Fig. 2.2:** Time-line of the development of the seismic instrumentation across the Netherlands. A particular focus on the development related to induced seismicity is given in the lower part. Some important dates are also indicated.

In the following two paragraphs, we briefly introduce the network development, both for boreholes and accelerometers, in the Groningen area. A complete list of stations is provided in table 10 in the appendix A.1. Some additional specifications on the orientation of sensors, instrument response and data transmission are also briefly discussed in the appendices A.3 and A.4. Please note that, following what we found in various documents produced by KNMI, the instrumented area is not restricted to the Groningen field itself (figure 2.1, blue line), but is larger (red rectangle) and is currently delimited:

- in the West by the borehole **NIW**;
- in the South by the borehole **ENV**;
- in the East and the North by the German border and the North sea.

### 2.1.2 Boreholes

The Northern part of the Netherlands can be considered to be rather noisy (Dost and Haak, 2007, Dost et al., 2017), which in turn poses difficulties in the detection of small seismic events. Therefore, a first borehole (**FSW**) equipped with 5 sensors with a 75 m spacing from 0 to 300 m depth was tested as of 1991. The noise was reduced by a factor of almost 10 in the frequency range 1-10 Hz (Dost and Haak, 2007), leading to the installation of 7 additional borehole seismometers in 1995, containing each 4 three-component sensors with a 50 m spacing down to 200 m depth (**ENM**, **ENV**, **HWF**, **VLW**, **WDB**, **ZLV** and **ZL2**, green crosses in figures 2.1 and 2.3). These boreholes formed at the end of 1995 a regional network covering 40x80 km with an average station spacing of 20 km.

During the years 2009-2010, 3 new boreholes were instrumented (**NIW**, **SPY**, **SUH**) in order to enlarge the network coverage towards the North. Within the individual boreholes, the sensor spacing was reduced to 30 m.

Dost et al. (2017) report that depending on the sites, the SNR in the boreholes was improved by a minimum of 10 dB (for quiet sites) and up to 20-30 dB (for noisy sites) in the frequency range 1-20 Hz.

For simplicity, we name all borehole stations deployed from to, or before, 2010 "old boreholes" or "old borehole network" in this report.

In August 2012, the largest event ( $M_L=3.6$ ) that occurred in the Groningen region until today was recorded. The earthquake caused damage to buildings, and following, a major and massive effort was made to extend the monitoring network further and to reduce the station spacing

The borehole network underwent 3 major upgrades in 1995, 2010 and 2015 and contains 84 stations nowadays.

to only 4-5 km: from 2014 to 2015, 70 new boreholes were instrumented, constituting the **G-network** (red dots in figures 2.1 and 2.3). The sensor configuration of the individual boreholes was the same as in 1995 (i.e. 4 sensors separated by 50 m up to 200 m depth), but accelerometers have been addi-

tionally installed at the surface. Three other boreholes (*N-network*, blue dots in figures 2.1 and 2.3) were also installed in 2016 slightly South of the Groningen field for the monitoring of a gas storage facility there (Dost et al., 2017). However, due to their proximity to the Groningen field, they are also useful for its monitoring.

### 2.1.3 Surface accelerometers

Starting from 1997, surface accelerometers were installed in the Groningen region, primarily at places where felt events have been reported. The network configuration was modified several times until 2013 and the instruments were only installed temporarily. The information on the different deployments are not publicly available; on request more detailed information can be obtained from KNMI (KNMI, pers. comm., 2018). Moreover, for some of these instruments (greyish rows in table 11 in the appendix A.2), the individual sensor timing was not synchronised with GPS time stamps (Kraaijpoel and Dost, 2013) and the sensor orientation was not determined or might have changed throughout the deployment times (KNMI, pers. comm., 2018). For all these reasons, they were not used in the database.

Before 2013, accelerometers have been deployed temporarily in various configurations. Today, 95 accelerometers are installed as part of the B- and G-networks.

Based on a 2012 report of KNMI (Dost et al., 2012), a total of 23 accelerometers were installed in 2010. These instruments are not operational/functional any longer, but some of the previous sensor locations were re-used during the years 2013-2014 when the *B-network* was put in place (yellow stars in figures 2.1 and 2.3).

9 accelerometers were also installed as part of the *G-network* (yellow stars encompassed in red in figures 2.1 and 2.3) in December 2017. Today, a total of 25 independent (i.e. not co-located with a borehole) accelerometers are operational in the Groningen region. Combined with the accelerometers placed at the surface of the boreholes of the *G-network*, there is a total of 95 instruments.

In table 11 in appendix A.2, we listed 39 stations which are not contained in the KNMI station file. This non-exhaustive list is mostly based on phase-picks that we extracted from the Groningen induced seismicity bulletin (section 3.1) and the time span corresponds to the first event and last event for which picks were made. The greyish rows correspond to accelerometers that were named in a document on the seismic instruments operated by KNMI (Dost and Haak, 2002), but which were not used for the data analysis. The yellowish rows correspond to re-used accelerometers when the *B-network* was built. Their locations were provided by KNMI to NORSAR in the framework of the ACISM project and they are represented on a map in figure A.1b. The figure A.1a in appendix A.2 also shows the network status in 2010 as published in Dost et al. (2012). As the accelerometers were not labelled, we corroborated the information obtained from Dost and Haak (2002) and Dost and van Enst (2008) to do so. We were not able to associate the names of only two accelerometers (surrounded and

labelled with a question mark).

Despite our efforts to cross-check the information, there are still 20 temporarily-deployed stations for which no information have been found at all.

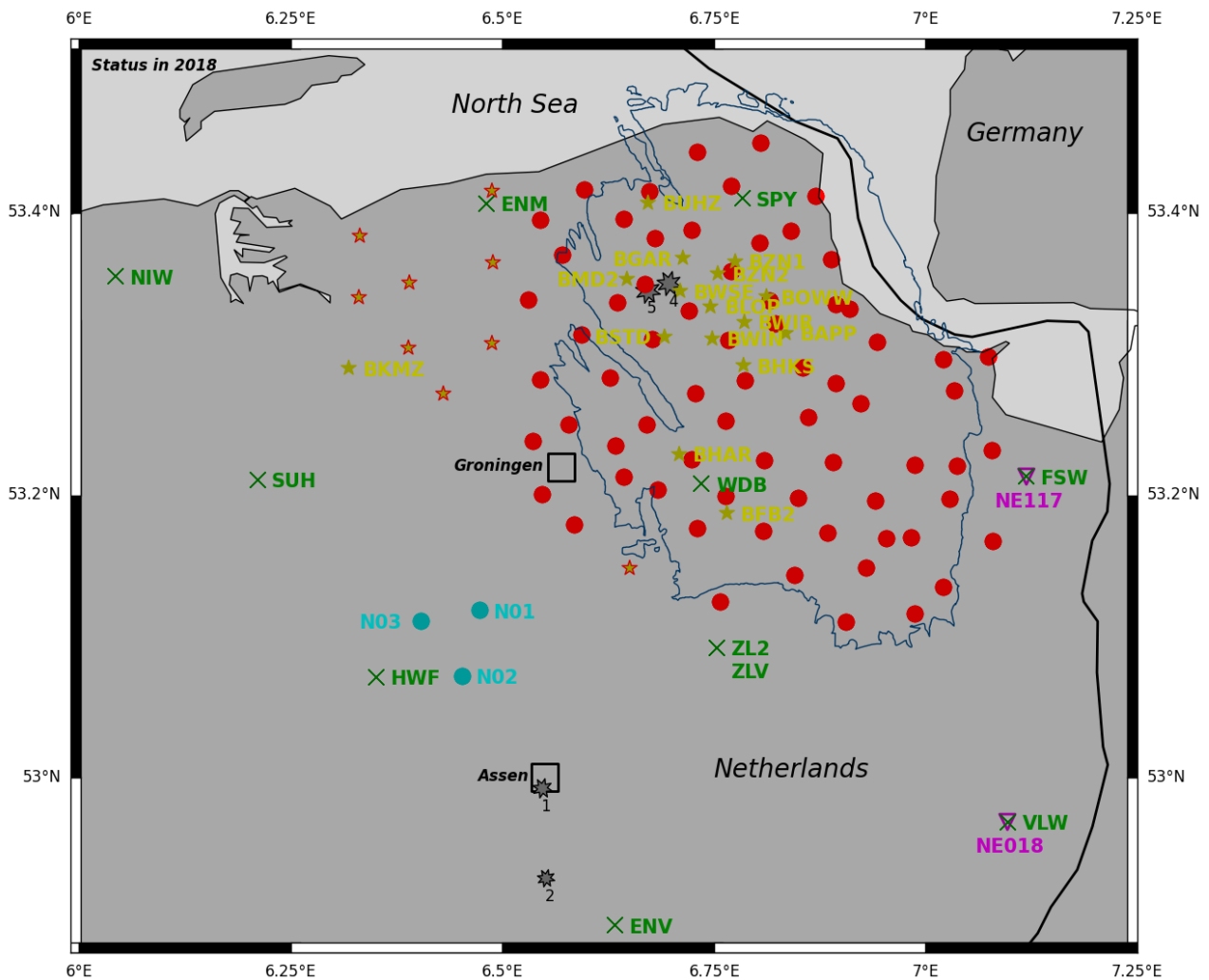


**Fig. 2.3:** Seismic instruments operated by KNMI in the Groningen area in 2018. Same colour- and marker-codes as in figure 2.1. Details are given in Table 10. The dark blue line delimits the Groningen field. The dark grey symbols show the location of the major earthquakes cited in the time-line (numbered from 1 to 5), except the 1989 Kwadijk event (number 4) with is located further West, beyond the map limits.

### 2.1.4 Instrumentation by other institutes

In addition to the instruments operated by KNMI (network code: **NL**), it is worth noting that seismic data were and are also acquired by other institutes in the Groningen area:

- two broadband stations (**NE117** and **NE018**) are part of the NARS network (**NR**) operated by the University of Utrecht (magenta reversed triangles in figures 2.1 and 2.3). The stations are co-located with two boreholes (**VLW** and **FSW**) and were operational already before the 1986

Assen Earthquake. The data are available to KNMI.

- since 2015, more than 350 accelerometers have been gradually placed in public buildings, private home and other facilities by TNO (Netherlands Organisation for Applied Scientific Research), specifically to study the seismic response of the buildings (Dost et al., 2017).
- NAM (Dutch Oil and Gas company) has instrumented deep boreholes with geophones: ZRP-1 (7 geophones from  $\approx 2800$  to 3000 m); SDM-1 (10 geophones from  $\approx 2750$  to 3000 m); HRS-2A (9 geophones from 3086.5 to 3206.5 m depth); ZRP-2 and ZRP-3 (15 geophones each from  $\approx 2700$  to 3000 m depth). In late 2016, only HRS-2A was active (Romijn and Tomic, 2016). Recently (Willacy et al., 2018), NAM has also deployed a dense mobile surface array (400 m between sensors) at various locations.

### 2.1.5 Conclusions

In the past few years, the number and density of seismic instruments in and around the Groningen gas field has been constantly increasing and hence, this site has developed to become one of the best instrumented sites in the world for the monitoring of induced seismicity.

The table 1 summarises the seismic instruments operated by KNMI and others in the entire Netherlands. The sensors which are of interest for the monitoring of the Groningen field are highlighted in red.

In this report, we focus on the data collected by the KNMI. We have tried to provide an overview as complete as possible for the seismic deployment in the Groningen area, but we cannot guarantee that there may be several other short-term deployments of seismic instruments coordinated by other institutions or private interest in the Groningen area.

With more than 100 seismic stations operated by KNMI and an inter-station distance smaller than 5 km, the Groningen area is one of the most thoroughly instrumented sites in the world for the monitoring of induced seismicity.



**Table 1:** Overview of the sensors operated by KNMI in the Netherlands and others in the Groningen area. Grey text either for (1) instruments outside the study area, (2) for non-seismic instruments or (3) for currently non-operational instruments.

| Network   | Number of sensors  | Type of stations   | Description   |
|---|--|--|---|
| EC  | 1  | broadband  | (outside the area of interest)  |
| NA  | 9  | broadband  | (outside the area of interest)  |
| NR  | 7  | broadband  | <b>2</b> in the Groningen area (NE117, NE018) — Utrecht University  |
| NL  | 556 sensors at 177 different sites*<br><br>* One <b>station</b> (=site) can contain several <b>sensors</b> | <ul style="list-style-type: none"> <li>• 42 infrasound</li> <li>• 10 broadbands</li> <li>• <b>96</b> accelerometers</li> <li>• 99 boreholes (398 sensors), of which <b>84</b> are in the Groningen area</li> </ul> | <ul style="list-style-type: none"> <li>• Most broadband seismometers are in the Southern part to monitor natural seismicity;</li> <li>• <b>G-network:</b> <b>70</b> 4-sensor boreholes + accelerometers; <b>9</b> accelerometers without boreholes = <b>359</b> sensors;</li> <li>• <b>N-network:</b> <b>3</b> 4-sensor boreholes + accelerometers = <b>15</b> sensors;</li> <li>• <b>T-network:</b> 7 4-sensor boreholes + accelerometers = 35 sensors;</li> <li>• <b>B-network:</b> <b>17</b> surface accelerometers (<b>16</b> in the Groningen area);</li> <li>• 19 boreholes (2 with 5 sensors (FSW, CHA); the others with 4 sensors), of which <b>11</b> are in the Groningen area (<b>45</b> sensors) = 78 sensors;</li> <li>• 1 4-sensor borehole + accelerometer (<b>SL</b>) = 5 sensors.</li> </ul> |
| ⇒ <b>2018: 437</b> sensors (=112 stations) operated by KNMI in the Groningen area |  |  |   |
| NAM   | Not applicable   | <ul style="list-style-type: none"> <li>• deep downhole (&gt; 3,000 m)</li> <li>• mobile roving surface array</li> </ul>  | <ul style="list-style-type: none"> <li>• Temporary: ZRP-1 (7 geophones); SDM-1 (10 geophones) — not active anymore;</li> <li>• Permanent: ZRP-2, ZRP-3 (15 geophones each) — not operational in Oct. 2016 (Romijn and Tomic, 2016);</li> <li>• HRS-2A: 9 geophones (operational since 5 Oct. 2016 (Romijn and Tomic, 2016)).</li> <li>• Dense receiver spacing: ≈ 400 m</li> </ul>  |
| TNO   | 375  | accelerometers   | In public buildings, private homes and NAM facilities   |

## References

- Dost, B. (2016). *Evolution of the Groningen earthquake monitoring network and event catalogue*. Mmax Expert Workshop, 8 - 10 March 2016, World Trade Centre, Schiphol Airport, the Netherlands.
- Dost, B., F. Goutbeek, T. van Eck, and D. Kraaijpoel (2012). *Monitoring induced seismicity in the North of the Netherlands: status report 2010*. Tech. rep. KNMI.
- Dost, B. and H. Haak (2002). *A comprehensive description of the KNMI seismological instrumentation*. Tech. rep. KNMI.
- Dost, B. and H.W. Haak (2007). "Natural and induced seismicity". In: *Geology of the Netherlands*. Ed. by T.E. Wong. Royal Netherlands Academy of Arts and Sciences, Amsterdam, The Netherlands, pp. 223–239.
- Dost, B., E. Ruigrok, and J. Spetzler (2017). "Development of seismicity and probabilistic hazard assessment for the Groningen gas field". In: *Netherlands Journal of Geosciences* 96.5, s235–s245.
- Dost, B. and J. van Enst (2008). *Proposal for an improved monitoring network for the Groningen field*. Proposal for a joint project KNMI/LOFAR.
- KNMI, pers. comm. (2018). Personal communication.
- Kraaijpoel, D. and B. Dost (2013). "Implications of salt-related propagation and mode conversion effects on the analysis of induced seismicity". In: *Journal of Seismology* 17.1, pp. 95–107.
- Romijn, R. and J. Tomic (2016). *Network status overview*. Groningen Event Location Workshop, 20 October 2016. Presentation by Shell (restricted).
- Willacy, C., E. van Dedem, S. Minisini, J. Li, J.W. Blokland, I. Das, and A. Droujinine (2018). "Application of full-waveform event location and moment-tensor inversion for Groningen induced seismicity". In: *The Leading Edge* 37.2, pp. 92–99.

### 3 Review of existing data

#### 3.1 Induced seismicity catalogue

We base all of our following analyses on the **induced seismicity catalogue** published by KNMI:

- “all\_induced.csv” and “all\_induced.pdf” as downloaded from:  
[www.knmi.nl/kennis-en-datacentrum/dataset/aardbevingscatalogus](http://www.knmi.nl/kennis-en-datacentrum/dataset/aardbevingscatalogus)

At the time of download, this catalogue contained 1485 events ranging from 26/12/1986 to 20/02/2018 and covers all of the Netherlands, including offshore. Since this report is concerned with the induced seismicity at Groningen, we have selected only those events which fall within the boundaries of the Groningen field as defined by the NLOG website ([www.nlog.nl/en/files-interactive-map](http://www.nlog.nl/en/files-interactive-map)) - maintained by TNO and supported by the Dutch Ministry of Economic Affairs. We refer to this filtered catalogue as the *Groningen induced seismicity catalogue*. The filtered catalogue contains 1126 events from 05/12/1991 to 20/02/2018.

The induced seismicity catalogue and the Groningen induced seismicity catalogue are shown in figure 3.1. The induced seismicity catalogue (csv-file) contains the date, origin time, a location name, latitude, longitude, depth, magnitude and a description of the evaluation mode (“manual” for all entries) for all events. The pdf file omits the evaluation mode, but contains a unique event id that can be used for accessing parametric data.

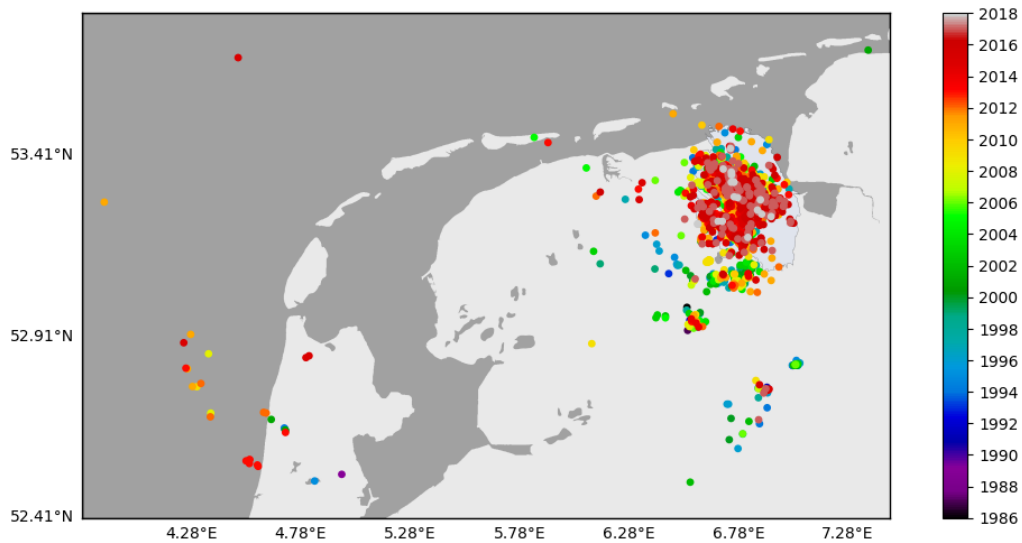
In order to properly assess the Groningen induced seismicity catalogue, we required access to the parametric data associated with each event i.e. the bulletin data. This has been obtained using KNMI’s publicly available FDSN webservices. This provides parametric data for events (i.e. **bulletin data**) and stations, as well as access to waveform data:

- Event data: [rdsa.knmi.nl/fdsnws/event/1/](http://rdsa.knmi.nl/fdsnws/event/1/)
- Station data: <http://rdsa.knmi.nl/fdsnws/station/1/>
- Waveform data: <http://rdsa.knmi.nl/fdsnws/dataselect/1/>

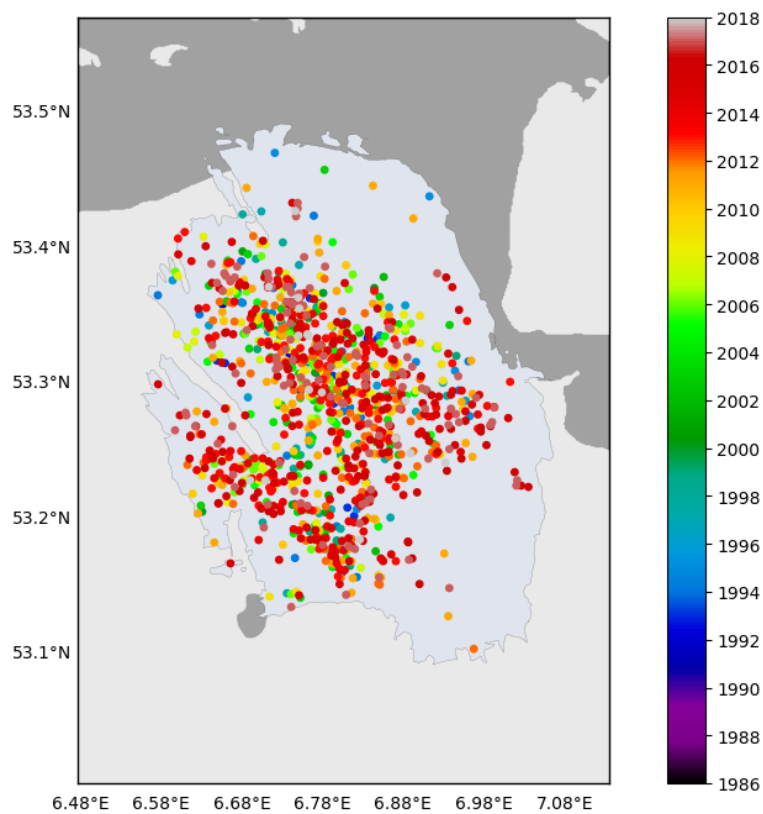
For each analysis within this report, a statement will be made on which of these data sources it is based, the **induced seismicity catalogue** or the **induced seismicity bulletin**.

The bulletin data are in QuakeML format, which is a XML representation of seismological data (Schorlemmer et al., 2012). In the figure 3.2, we present a simplified diagram of the QuakeML event structure and highlight the elements and attributes that are of interest in our analysis.

An additional earthquake catalogue is available from KNMI’s webpage (as NetCDF 4 file downloadable from [https://data.knmi.nl/datasets/aardbevingen\\_catalogus/1?q=aardbeving](https://data.knmi.nl/datasets/aardbevingen_catalogus/1?q=aardbeving)). However, since at the start of the project, we agreed with the Dutch State Supervision of Mines (Staatstoezicht op de



(a)



(b)

**Fig. 3.1:** Map of events from KNMI's induced seismicity catalogue. (a) shows all 1485 events from 1986 to 2018; (b) shows the 1126 events located within the Groningen field, and referred to as the Groningen induced seismicity catalogue. Both plots show timescales from 1986 for comparison purposes, but (b) only contains events from 1991 to 2018.

Mijnen, SodM) to base our work on the induced seismicity catalogue, we disregarded the “complete earthquake catalogue for the Netherlands and near surrounding” from our analysis.

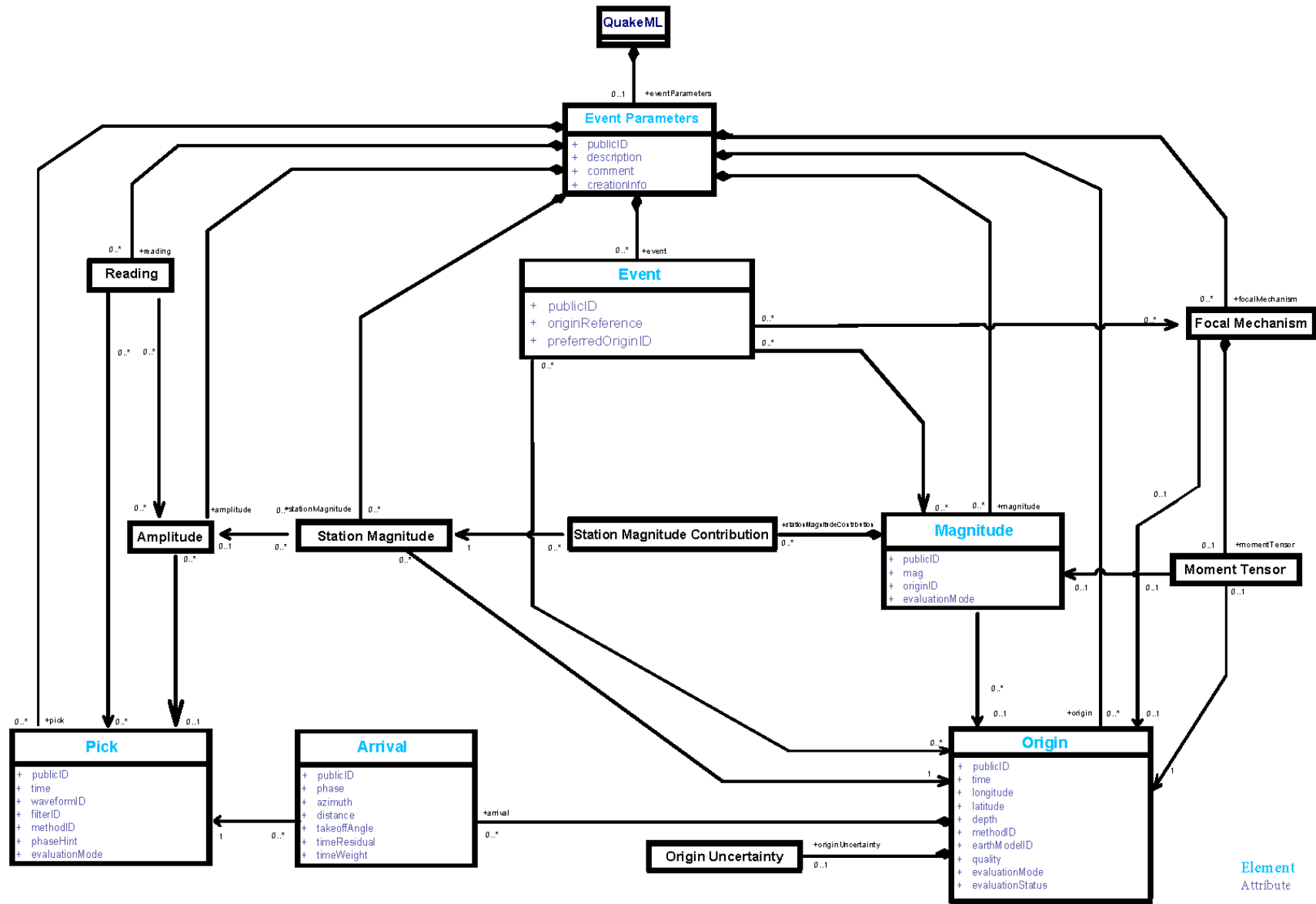


**Fig. 3.2:** Event structure in the QuakeML format, modified and simplified from Schorlemmer et al. (2012), figure 2. In blue, we highlight the elements and the respective list of their attributes that were used in this report. Note that all elements are not available, e.g. moment tensor or focal mechanism. . .

## References

Schorlemmer, D., J. Saul, F. Euchner, J. Becker, R. Buland, A. Heinloo, L. Kamb, P. Kästli, A. Spinuso, and B. Weber (2012). *QuakeML - an XML representation of seismological data, Basic Event Description, Version 1.2*. URL: <http://www.quakeml.org>.

## 3.2 Data completeness

Data completeness refers to the availability of data for analysis in the period of interest. We here analyse how complete the G-network, the B-network, and the original borehole-network waveform data are available on the respective servers of KNMI. This also gives indication to the responsiveness of KNMI to fix potential problems with data transmission or sensor failure. We analyse only the G- and B- networks, located directly above the Groningen field in the time period from 2015-18. We omit older data which is only available through the KNMI internal database.

### 3.2.1 G-network

The G-network consists of up to 350 individual sensors grouped to 5 sensors at different depth levels for each of the 70 locations (section 2.1). For the data completeness analysis presented here, we analyse the time period between January 1<sup>st</sup>, 2015 and February 28<sup>th</sup> 2018. To illustrate G-network completeness, we use data that were already compiled by KNMI, pers. comm. (2018). This consist of binary yes/no information if at any point of a day a gap in data is present.

Figure 3.3 shows an overview of the available data for each of the 350 sensors. Dark colour indicates data is complete (i.e. available) for a particular day, and a light colour indicates a gap in data during the day. Obviously, throughout 2015 many gaps are evident due to the construction of the DSL network. When the new station network was installed, there was a huge delay until the telecommunication company finished the DSL connections. Stations were also able to send their data by 4G, but the coverage in the Groningen field is not good. When the mobile connection was down for only a certain time, data could be send from the internal buffer, but only a finite amount of data could be recovered (KNMI, pers. comm., 2018). From about Q2-2017 onwards, most sensors are complete with only minor outtakes.

Figure 3.4a illustrates this evolution. Whereas for most of 2015 only around 20% of the final network is available, with large variability, data in Q4-17 and Q1-18 are mostly constantly available for all sensors. This means data is complete in this period. Note the dip in data availability during Q2-16, and a general decline in availability between Q3-16 and mid-Q1-17. This indicates problems with the sensors, probably telemetry, which however have been successfully addressed from Q2-17 onwards. Figure 3.4b shows data completeness for each sensor, and figure 3.4c shows histogram data of completeness. It shows that during the analysed period most sensor have at least 70% completeness.

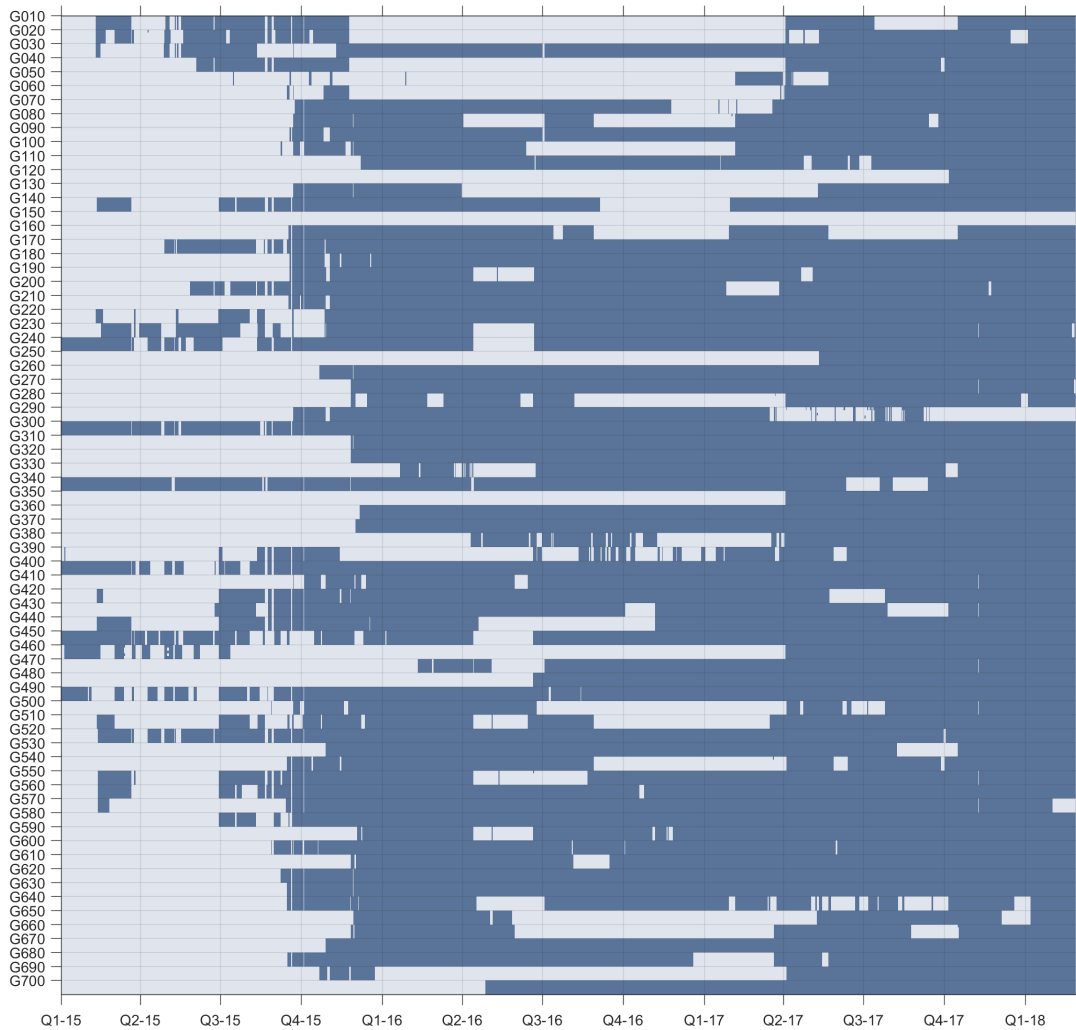


**Fig. 3.3:** Data availability of the G-network. Dark colours indicate data available, whereas light colours indicate missing data at some point during the day.

In figure 3.5, we analyse the duration of down-time of a sensor. Down-time (i.e. gaps in completeness) can be due to technical failure of the sensor, or problems in data transmission. 32% of down-time problems were fixed the next day, 45% within 2 days, and 65% within one week. Only 18% of problems took more than 30 days to fix.

Most gaps in data completeness concern full groups of 5 sensors at the same location, indicating a common problem at the station, potentially with data transmission. However, a small number of gaps are evident at single sensors. Figure 3.6 present a zoom into figure 3.3 for sensor groups G29x and G46x to show the occurrences of these single-sensor gaps.

Figure 3.7 then summarises these gaps by showing histograms of total single-sensor gaps in completeness combined by station groups. It shows that these gaps in completeness are rare.

Overall, data completeness of the G-network is appropriate. Since Q4-2017 data completeness can be described as excellent. Repair times in case of down-time are appropriate given the complexity



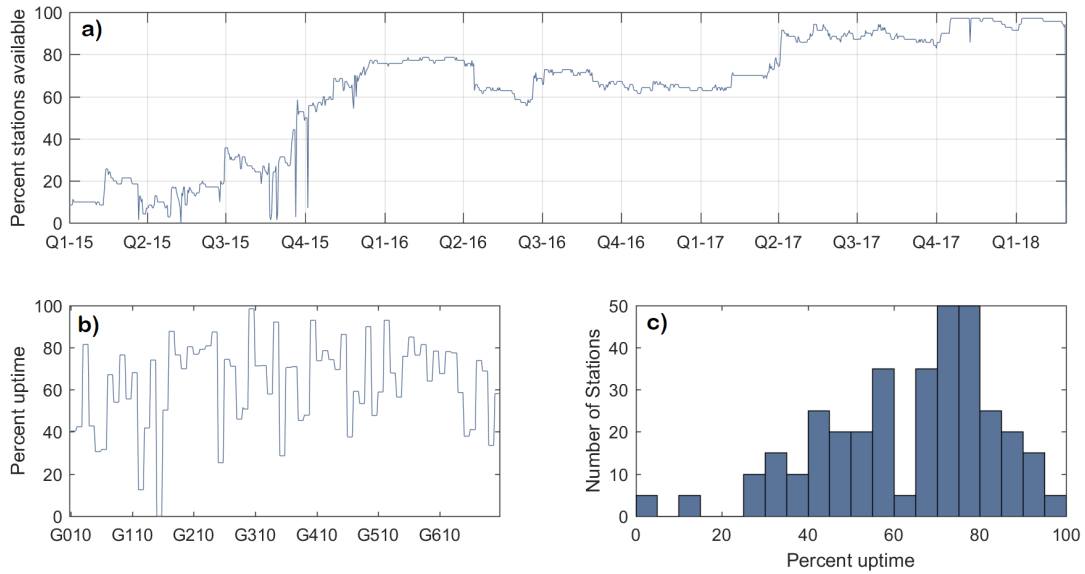


**Fig. 3.4:** Completeness statistics, with a) evolution of data completeness over the analysed period, b) completeness per sensor, and c) histogram of completeness.

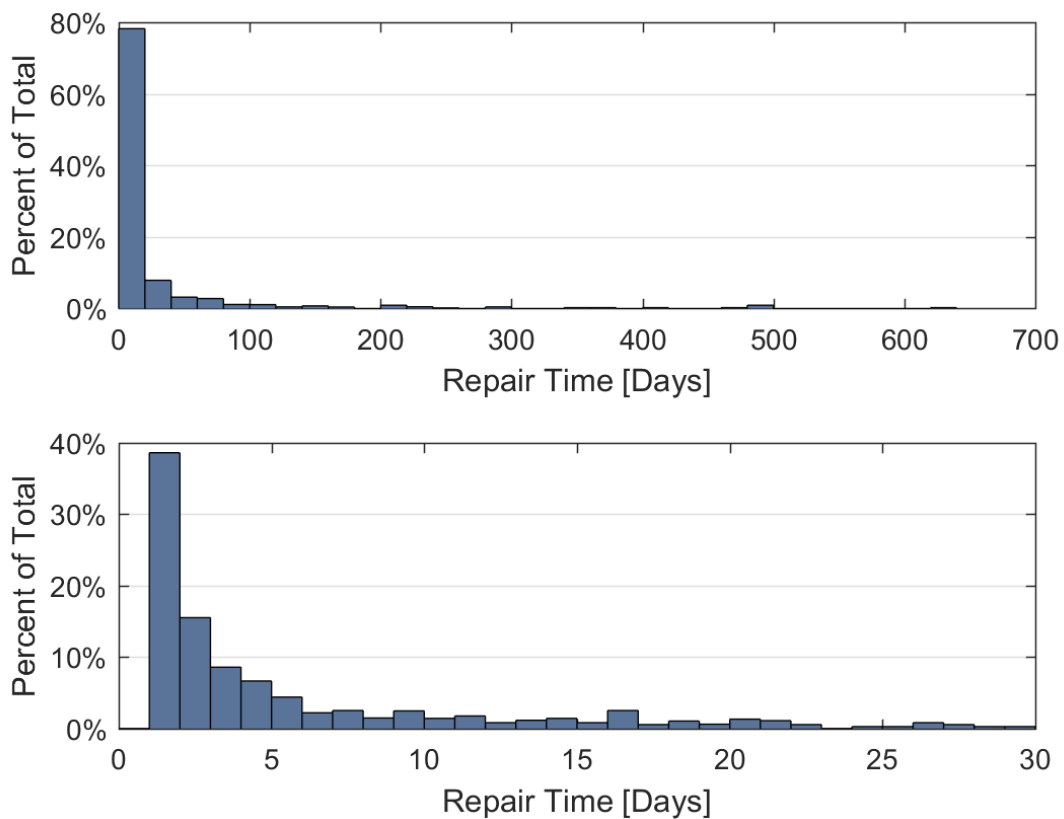


**Fig. 3.5:** Histograms of down-time in the analysed period. Upper panel shows the full dataset, while the lower panel is limited to a maximum of 30 days down-time. Repair or reset of communication was fixed promptly.

and size of the network. Note that this completeness evaluation considers only information from the publicly available sources.

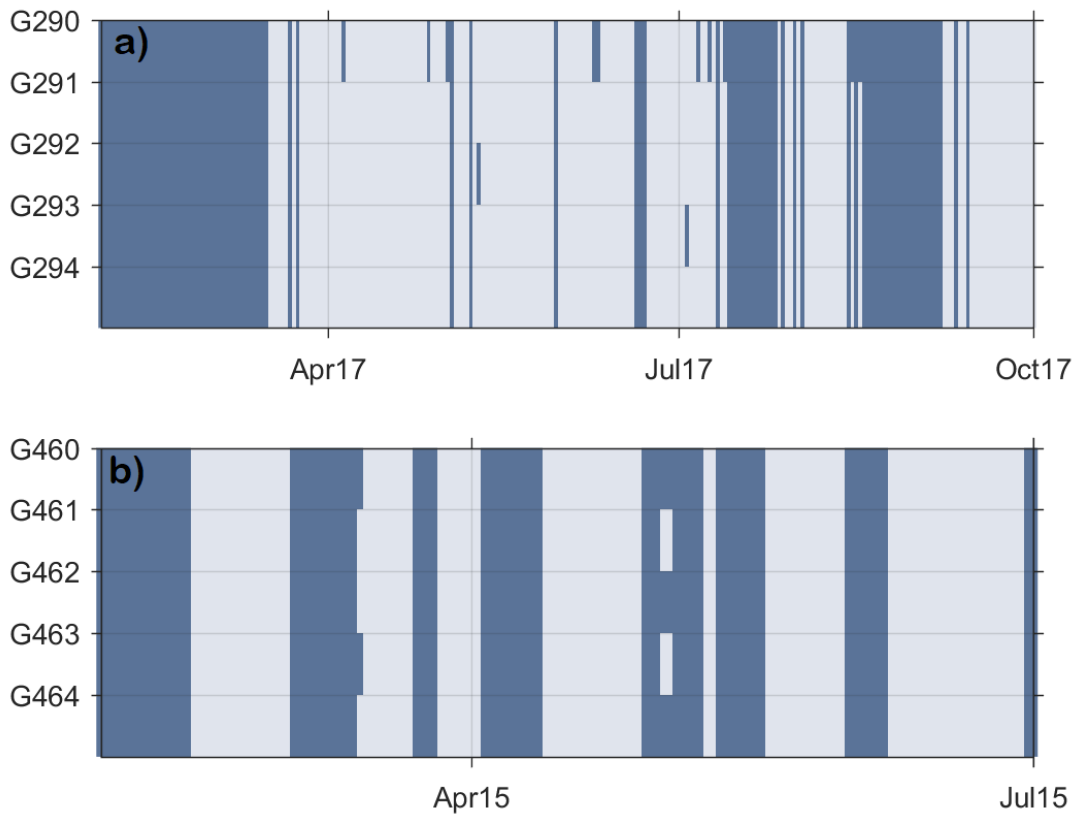


**Fig. 3.6:** Zoom on data completeness presented in figure 3.3 for two sensor groups (G29x and G46x) highlighting gaps in completeness for single sensors of a group.

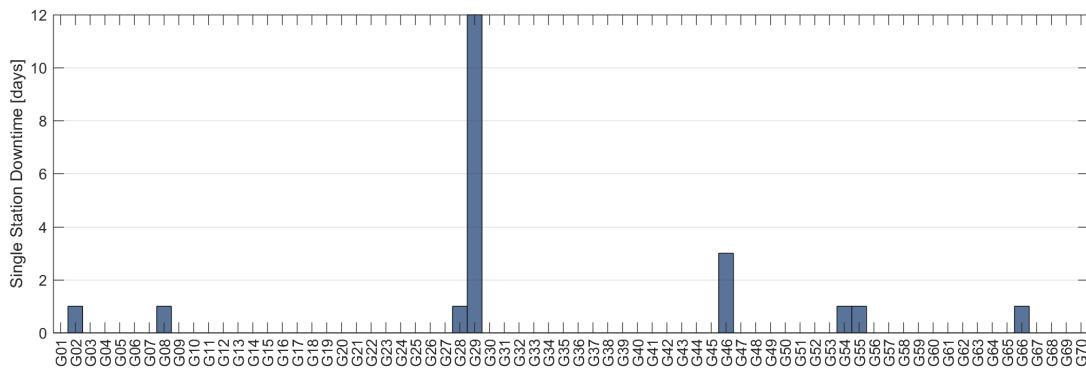


**Fig. 3.7:** Zoom on data completeness presented in figure 3.3 for two sensor groups (G29x and G46x) highlighting gaps in completeness for single sensors of a group.

### 3.2.2 B-network

The B-network consists of accelerometers (section 2.1). Although installation of this network began in September 2013, data completeness information is only publicly available (through ORFEUS) since January 1<sup>st</sup>, 2016. Earlier data is only available through KNMI’s internal database. We restrict our analysis here to the period of publicly available data. A more extended analysis could be added in a

next phase of the review project. We obtained for each sensor (vertical component) the availability information of each day. In the public catalogue, the actual numbers of gaps per day is given, as well as a “percent availability”. The results for the B-network are shown in figure 3.8. Two stations (BMD1 and BONL) are not available at all in the analysed period as they were taken offline in 2014 and 2015, respectively.

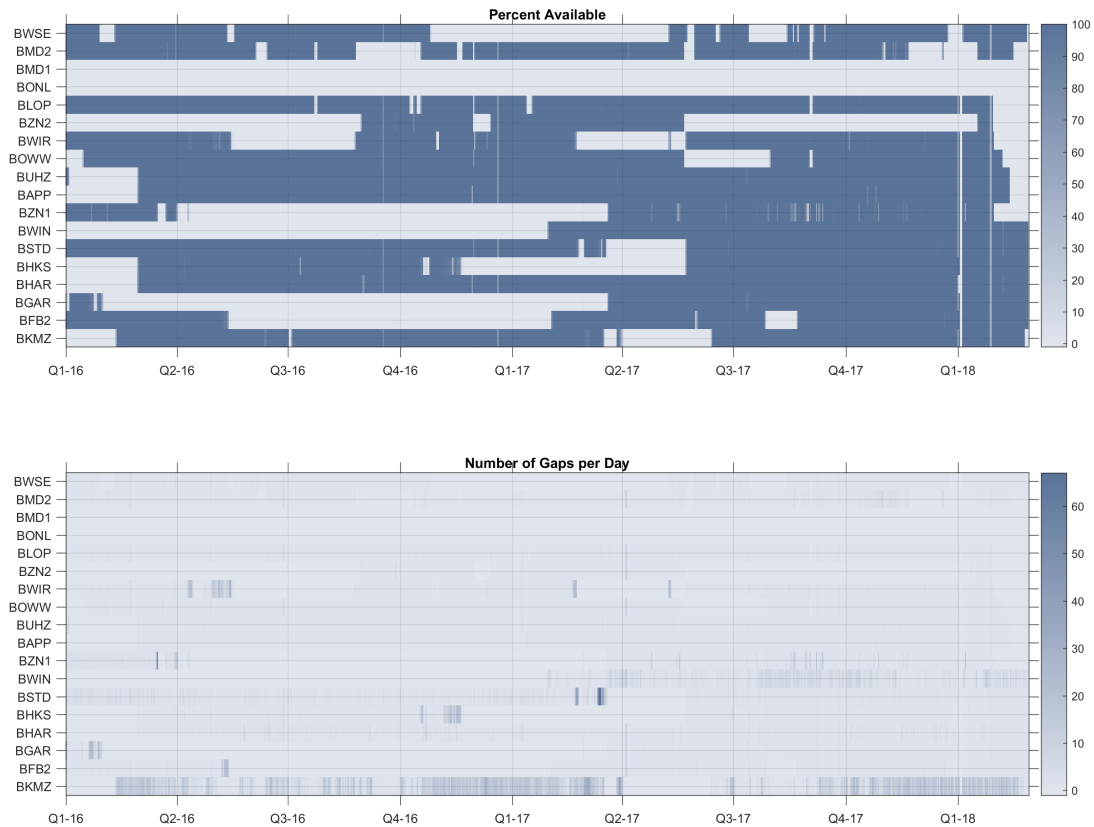


**Fig. 3.8:** Histograms of down-time in the analysed period. Upper panel shows the full dataset, while the lower panel is limited to a maximum of 30 days down-time. Repair or reset of communication was fixed promptly.

In figure 3.9, we show the repair time of the B-network, similar to figure 3.5. B-network repair times are somewhat slower than for the G-network, with 23% of down-times problems were fixed the next day, 35% within 2 days, but similar to the G-network, 65% station problems were fixed within one week.

Figure 3.10 shows a histogram of data gaps per day in the whole B-network. Most gaps are singular problems during the day. Only on 4 occasions, there were more that 40 gaps during the day.

### 3.2.3 Old borehole network

The old borehole network consists of 11 stations, each with 4 levels (section 2.1). We again analyse data completeness in the same period (from January 1st 2016 to February 28th 2018), and use the vertical component as a proxy for the whole sensor. Figure 3.11 shows data availability and data

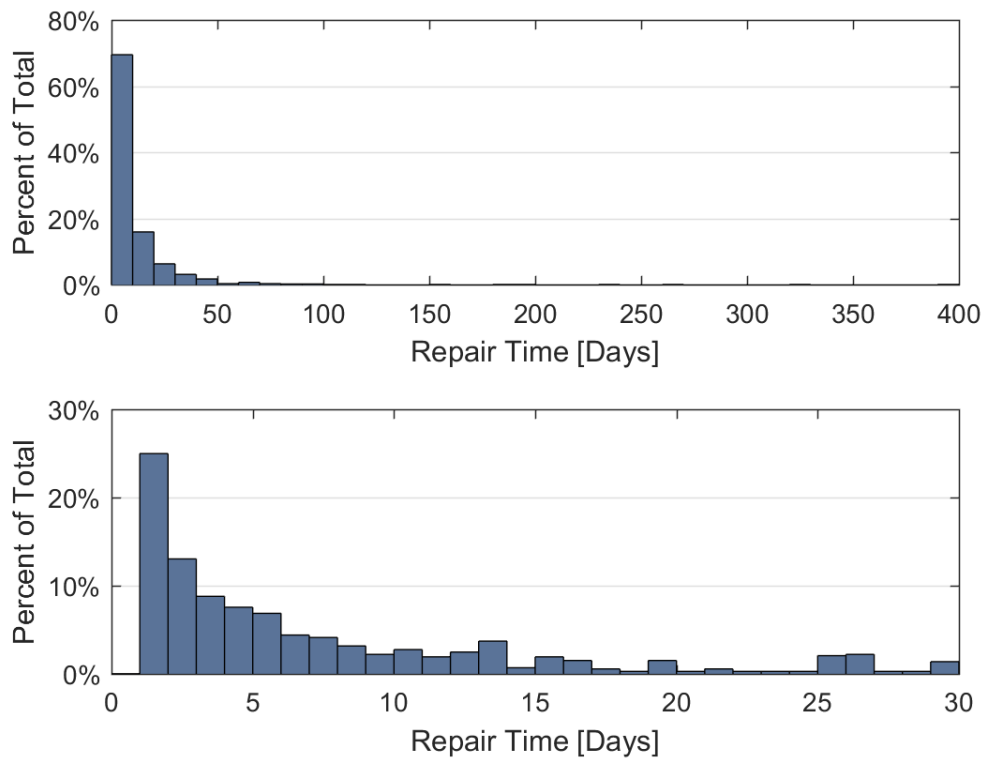


**Fig. 3.9:** Repair times of the B-network.

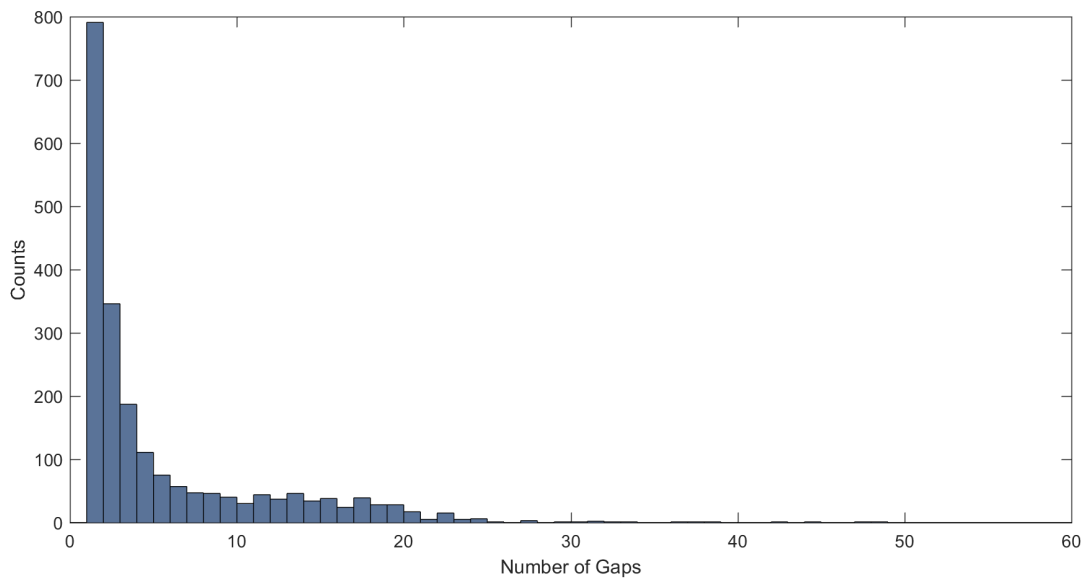


**Fig. 3.10:** Histogram of data gaps per day in the B-network.

gaps.

Channel 4 of FSW apparently failed beyond repair in June 2016. A few other longer gaps are present, but data availability is generally good. Interestingly, station NIW has a long period of many data gaps

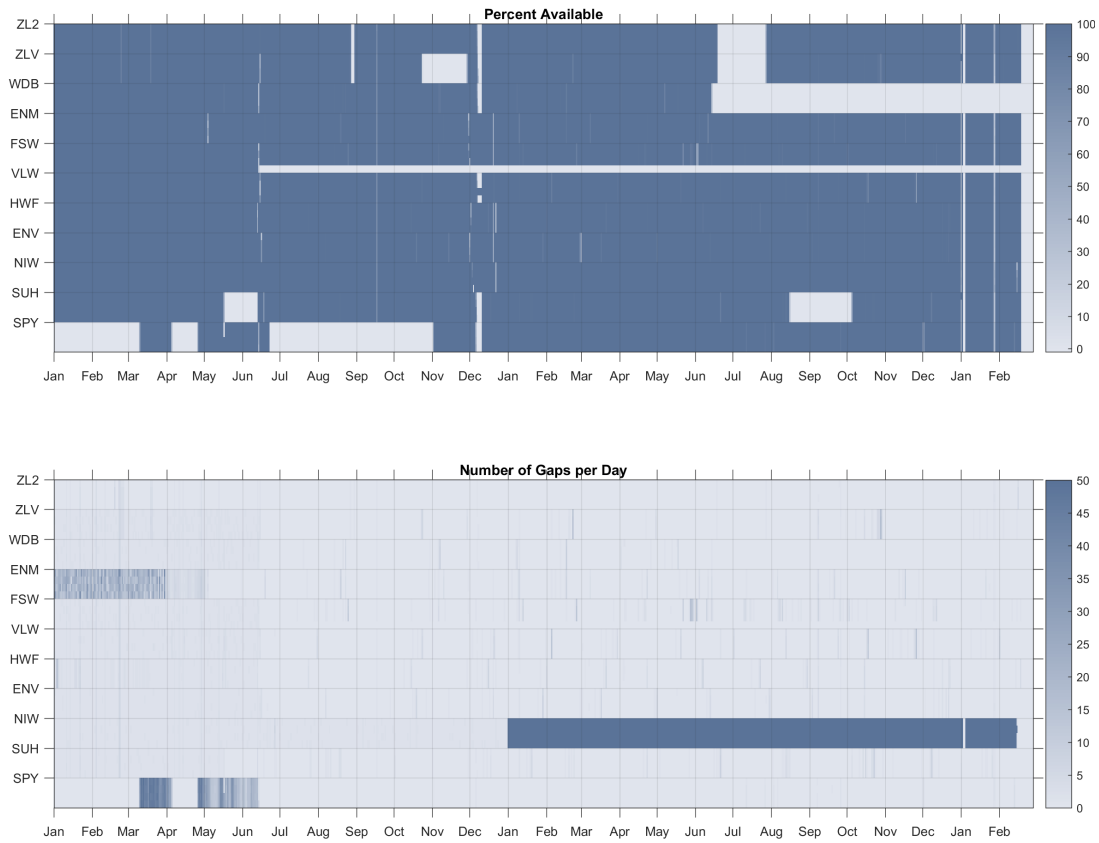
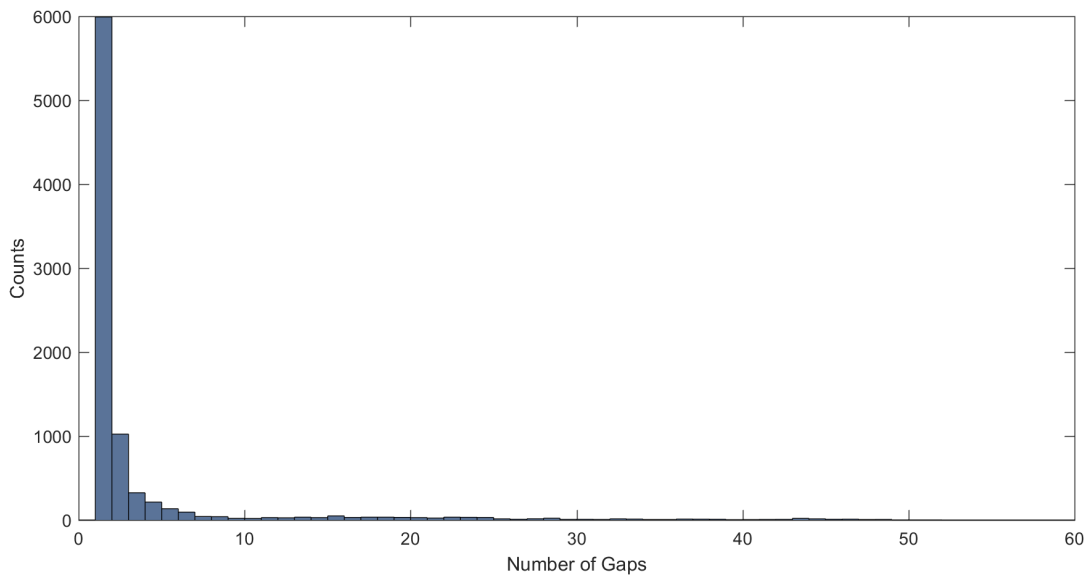


**Fig. 3.11:** Data availability and number of gaps per day for the old borehole network.

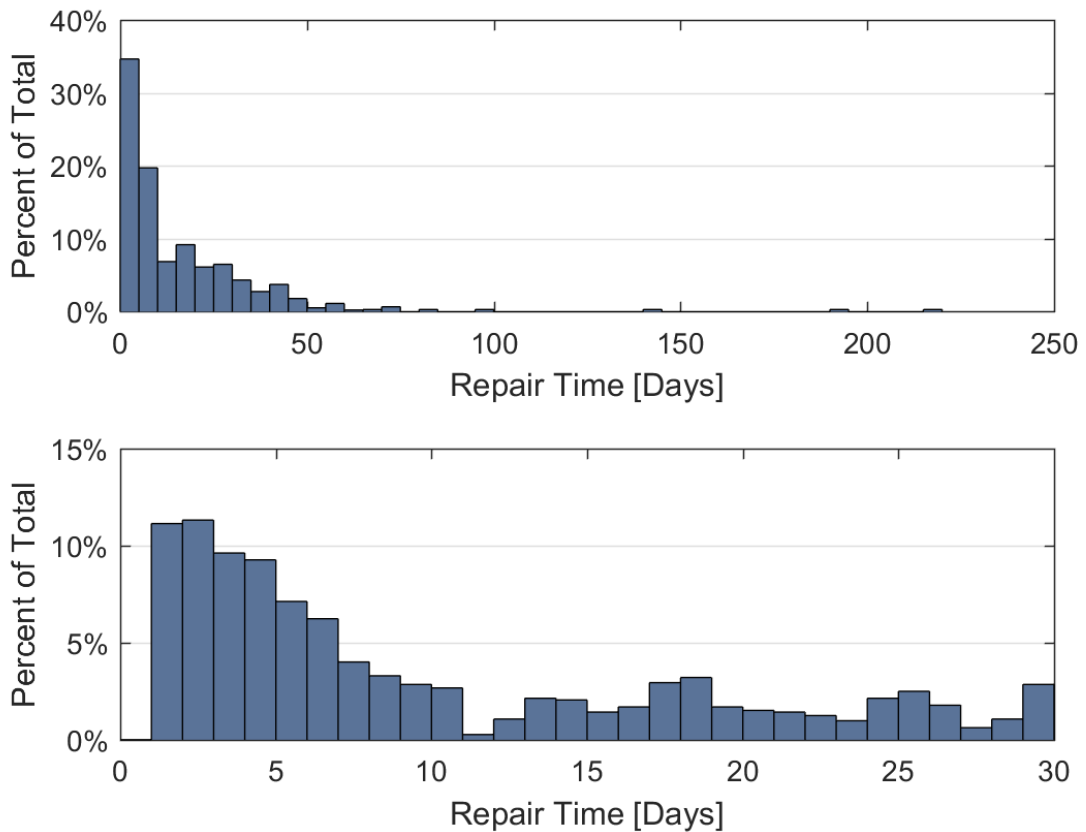
(up to 600) from January 2017 onwards. This is however not reflected in data availability. We assume that the gaps are thus very small, but it may render data processing of this station still difficult. It seems that this problem is fixed since mid-February 2018. Likewise, all levels of station ENM have a varying number of gaps in January-March 2016, which seems to be fixed after that period.

Figure 3.12 shows the histogram of gaps per day, similar to earlier analysis in this section. This borehole network has more problems with small and short data gaps than the other networks, probably related to the age of this network. This highlights the importance of good maintenance and high-quality equipment, and may be used as indicator for expectations for the newer G-network.

Repair times of the old borehole network are also considerably larger than for the other networks (figure 3.13).



**Fig. 3.12:** Number of (short) gaps per day are considerably higher for the old borehole network than for the other networks.



**Fig. 3.13:** Repair times of the original borehole network in the period of 2016-2018.

### 3.3 Data homogeneity

In statistics, homogeneity relates to the assumption that the statistical properties of any part of a dataset are the same as any other part. In meta-analysis, homogeneity measures the differences or similarities between the several studies.

In a review (IRIS, 2003, [https://www.iris.edu/hq/files/programs/gsn/documents/GSN\\_Review.pdf](https://www.iris.edu/hq/files/programs/gsn/documents/GSN_Review.pdf)) of the Global Seismograph Network (GSN) the comments on Network Standardization were as follow:

*“There are voices in the community in favor of homogeneous instrumentation for the future of the GSN. Admittedly, homogeneous instrumentation would ease considerably the task of operating and maintaining the network, and probably would result in some cost reduction. Nevertheless, the Review Committee feels that homogenization is not absolutely necessary. A case can be made for different types of equipment, provided that all instrumentation meet established criteria of performance and compatibility. The GSN ad hoc Design Goals Subcommittee expressed similar views: “. . .efforts toward network-wide standardization of instrument performance, if not instrumentation, should be a priority. . .”. The Review Committee believes that all equipment should pass an established method of quality control and technical specification validation, before deployment in the network. The operating network should not be an arena in which frequent technical innovation leads to unending heterogeneity. The present laissez faire policy that allows unilateral decisions about selection of equipment or protocols, and leads to equipment incompatibility across the GSN, is clearly detrimental to the long-term future of the GSN.”*

In the Groningen area a variety of sensors are used (see section 2.1), reflecting the technological advances and evolution of the requirements. We therefore accept the sensor types as heterogeneous and will focus our investigation on homogeneity on several other aspects that define data homogeneity for such a complex data set as the one for Groningen.

#### 3.3.1 Changes in station location

To assess earthquake catalogues homogeneously, it is important to have consistent sources of input. Information on a moved sensor (while keeping the same sensor name) may be lost in the process of data analysis. Current station locations and names are well documented through several web services (ORFEUS, KNMI, IRIS, etc.). However, we encountered minor gaps in available documentation on historical stations. Notably, the arrival picks are documented with associated station names (section 4.2.6). Several stations in the pick files simply appear to be misspelled compared to available station information (see table 7). Some stations of the B-network were re-used from its temporary precursor. These re-used stations were sometimes moved (see section 2.1), but any move was also associated with a well-documented renaming of that station (KNMI, pers. comm., 2018). Furthermore, 29 temporary stations were deployed in various configurations between 1997 and 2013. Despite our best efforts, we could not find publicly available information on these. KNMI communi-

cated towards us that they “documented changes of the network on paper, but this information is not available in digital form and it will take time to collect a full overview of these changes” (KNMI, pers. comm., 2018). We recommend that KNMI publishes that information together with the other already published material to complete the information database. In general, we find that homogeneity of the Groningen dataset is not affected by station documentation. The complex history of the various networks is well documented.

### 3.3.2 Homogeneity of spatial coverage

As a first step to assess data homogeneity of the Groningen sensor network, we analyse the inter-station distance. Note that for successful event location, picks on at least 3 stations are recommended. Thus, we define network location homogeneity in terms of station distance. We here consider the full network, with all stations as of February 2018 functioning normally. Stations with multiple levels are considered as single station. We then calculate the interstation distances. In figure 3.14, we plot the distance distribution for the three nearest stations to each station within the network.

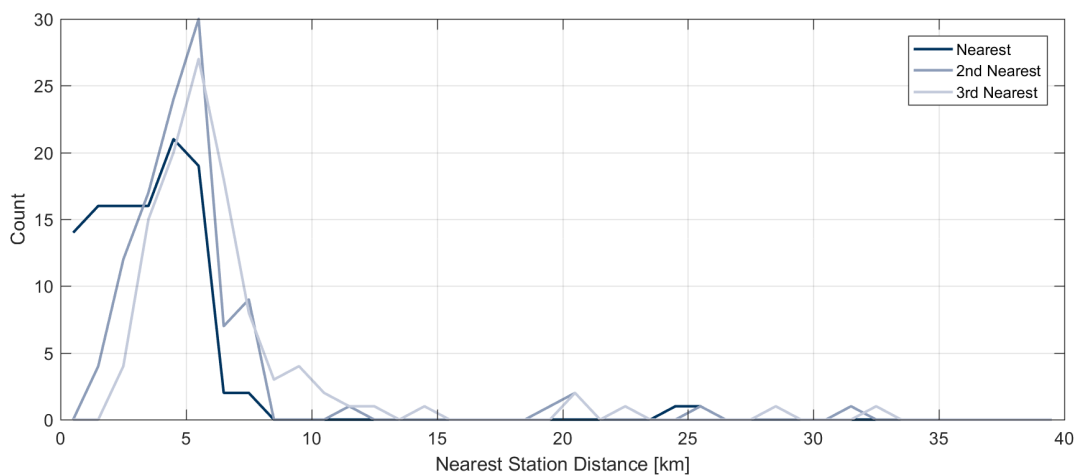
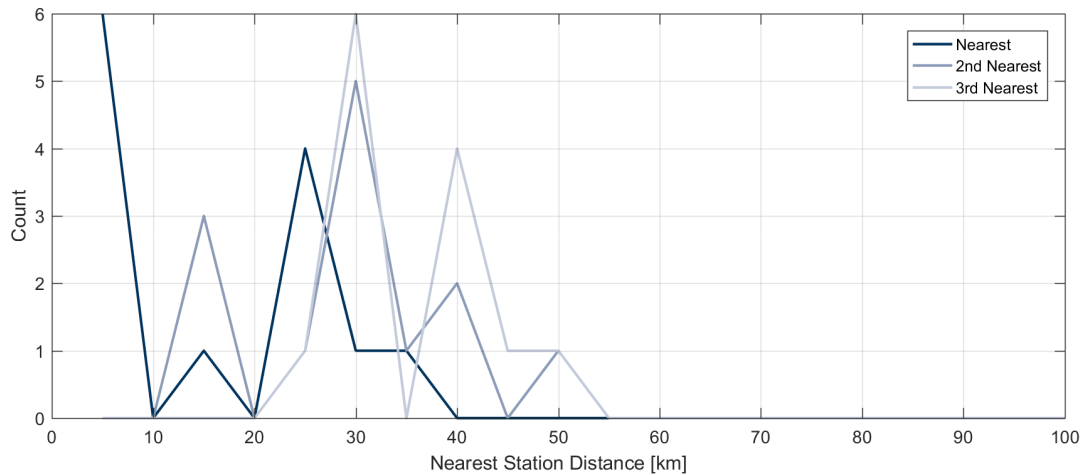


**Fig. 3.14:** Inter-station distances of the stations in the NL-network. Each line represents the number of stations within 1 km distance bins to the three nearest neighbours, respectively.

Interstation distances peak at 4 km and 6 km, for the nearest, 2<sup>nd</sup>, and 3<sup>rd</sup> nearest stations, respectively, then they drop sharply. This indicates that most areas covered by the network have at least 4 stations with homogeneous distances shorter than 6 km. This is a very good result, mainly however due to the dense and rather equally spaced G-network.

Figure 3.15 shows the interstation distances in 5 km bins before September 2013, when the first G-network stations were installed. While the nearest station can often be considered close, with bimodal maxima at 5 km and 25 km, the 2<sup>nd</sup>, and 3<sup>rd</sup> nearest stations are rather distant at around 30 km. This probably inhibits homogeneous event processing.





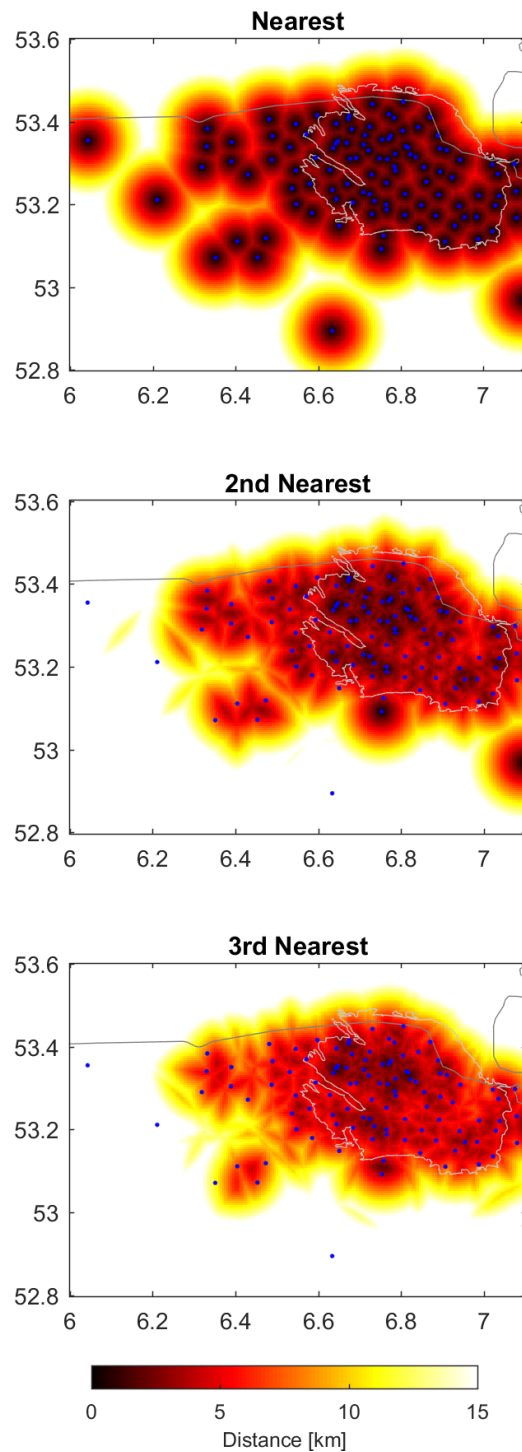
**Fig. 3.15:** Same as figure 3.14, only for stations available before installation of the G-network, i.e. before September 2013.

Figure 3.16 shows the horizontal distance for test locations to the three nearest stations. Dark colours indicate that the nearest station is close-by. The variability of colours is an indicator for station distribution homogeneity. The nearest-station distribution is fairly homogeneous, as should be expected after the installation of the G-network. The 2<sup>nd</sup>, and 3<sup>rd</sup> nearest station distribution can be separated into two areas above the Groningen gas field: around the city of Groningen and in the west of the field, the three nearest are close-by (< 4 km). The eastern part of the field is covered homogeneously as well, albeit with a slightly higher event-station distance. We notice a gap in station distance in the western part of the field, near 53.25°N, 6.95°E, to the west of the town of Wangenborgen.

In figure 3.17, we show the distribution of horizontal event-station distances for the three nearest stations to each event location in the area covered in figure 3.16. This results in a bi-modal distribution with peaks at 2.25 km, 4.00 km, and 4.90 km, respectively. These peaks are followed by a comparatively flat distance distribution at larger distances. The similarity of the curves for the nearest, 2<sup>nd</sup>, and 3<sup>rd</sup> nearest stations indicates good station homogeneity.

### 3.3.3 Homogeneity of catalogue precision

In this section, we analyse the reported precision of catalogue data. We focus on the more relevant data, that is, event location latitude and longitude, and event magnitude. We base our analysis on the 1126 events of the induced seismicity bulletin. Precision is here defined as the number of reported decimal places. Figure 3.18 gives a temporal overview of the reported decimal places for event magnitudes, as well as a histogram of these numbers. We note that before 1999 magnitude was reported with only up to two decimal places, and later with higher precision (with a few low-precision data points between 2010 and 2015). Note that this higher precision does not mean more accurate magnitude estimation. Typically, magnitudes can only be accurately determined with up to 2 decimal places.



**Fig. 3.16:** Maps of nearest-station horizontal distances as of February 2018. Colour scale is clipped at 15 km. The blue dots indicate stations available on that date.

A similar analysis of reported event location gives a more homogeneous distribution of precision (figure 3.19). Interestingly, longitude has been reported with typically more decimal places.

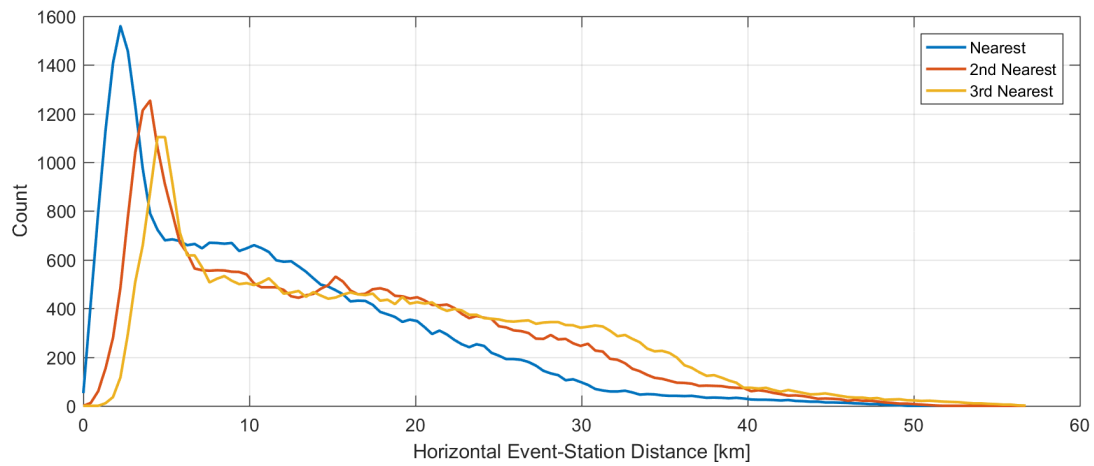


**Fig. 3.17:** Distribution of horizontal event-station distances for the three nearest stations to each event location.

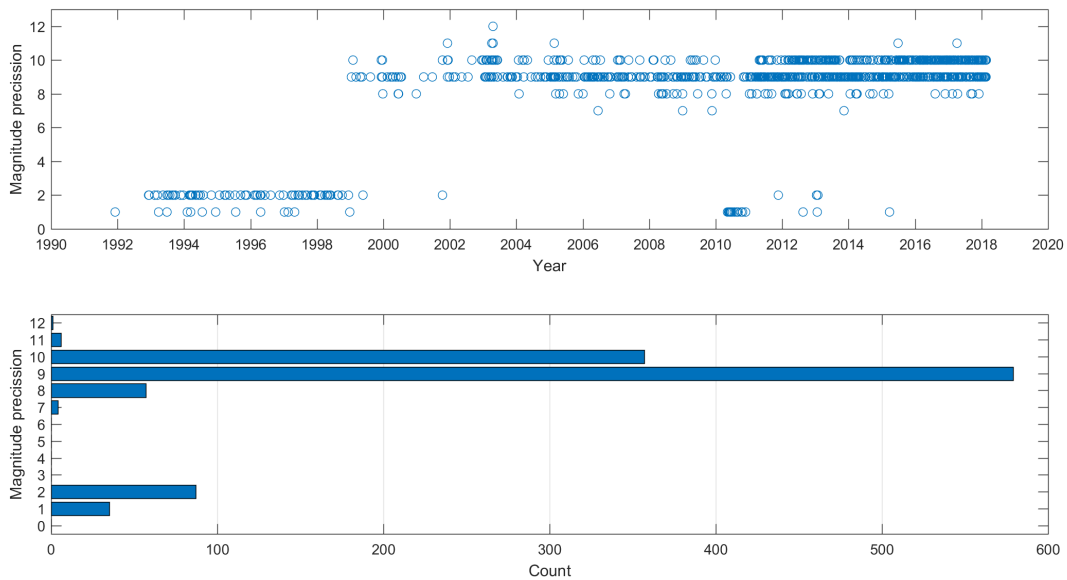


**Fig. 3.18:** Precision of reported magnitudes in terms of decimal places in the induced seismicity bulletin.

In addition, we repeated the analysis for the induced seismicity catalogue. Figures 3.20 and 3.21 show the result of the precision analysis identical to the one performed above for the induced seismicity bulletin. In the catalogue, the magnitudes are all reported with the same precision of 1 decimal place. Precision for latitudes and longitudes is 2 or 3 decimal places, with the occasional single decimal place. No correlation is apparent between precision of latitudes and longitudes. Note that it may well be that values with zeroes as last digits have been truncated.

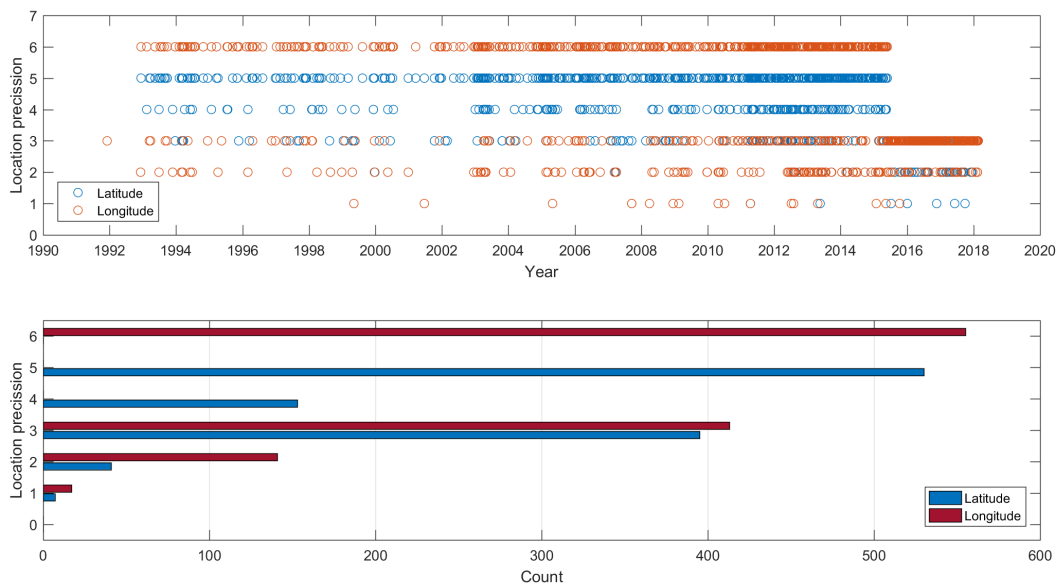


Fig. 3.19: Precision of reported event location in terms of decimal places in the induced seismicity bulletin.

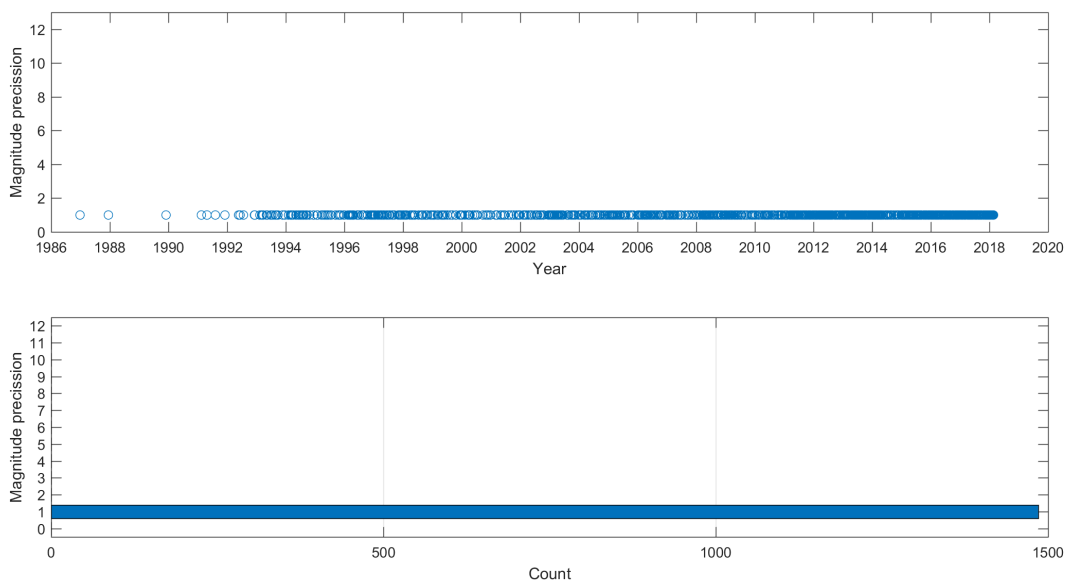
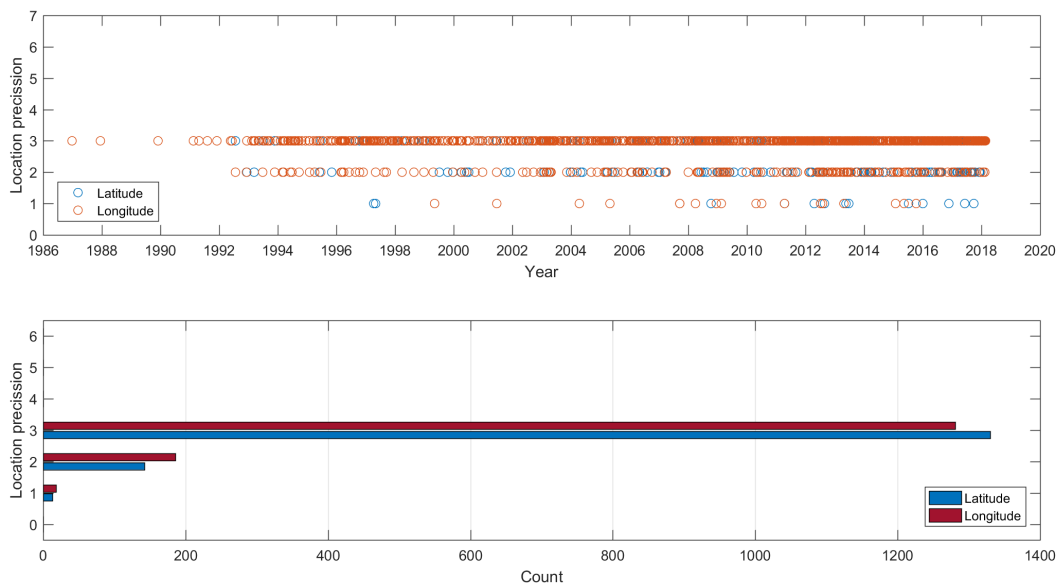


Fig. 3.20: Precision of reported event magnitudes in terms of decimal places in the induced seismicity catalogue.

### 3.3.4 Homogeneity of magnitude computation

Magnitude calculation for the Groningen area is discussed in detail in section 4.3. Magnitudes are consistently reported as local magnitude ( $M_L$ ). This requires a scaling relationship between amplitudes and magnitudes. Different scaling relationships were established in 1988, 1991, 1996, and 2004, respectively. Note that the first two only affect a very small number of events (the catalogue



**Fig. 3.21:** Precision of reported event location in terms of decimal places in the induced seismicity catalogue.

before 1996). The major concern for homogeneity of the catalogue would be the adjusted relation in 2004, since this affects the bulk of the events in the catalogue. However, this adjustment was necessary because of a correction of sensor sensitivities (Dost et al., 2004). Sensitivities and amplitudes are linearly dependent and thus are the scaling relations. We agree with KNMI (Dost et al., 2018) that, despite the two scaling relationships being used, the catalogue after 1996 can be considered as homogeneous in magnitudes.

### 3.3.5 Homogeneity of event detection

Event detection is discussed in detail in section 4.1 and may be affected by the development of the seismic network. In figure 3.22, we represent the cumulative number of stations over time together with the cumulative numbers of events and P-picks (assimilated as detections).

Note that the curve representing the cumulative number of stations does not contain the old accelerometers, which were placed and moved in the period 1997-2013 before the definitive installation of the B-network in 2014. As these accelerometers were not used for detection (Kraaijpoel and Dost, 2013), they will not affect the interpretation of the number of events. However, they may influence the number of picks.

By eye, there seem to be three time periods in which the slope of the cumulative number of events changes:

- 1: from the beginning (December 1991) to January 2003;
- 2: from January 2003 to April 2011;

- 3a-b: from April 2011 to now.

There is also a noticeable change in the cumulative number of P-picks in July 2015 (3b). For each of these periods, we compute the curve slopes and give their respective values (in %) on top of the figure. We observe that, surprisingly, the changes in the curve behaviour do not coincide directly with the changes in the network, except in July 2015, where the increase in the number of picks clearly corresponds to the availability of data recorded by a significant number of new stations in the G-network. However, this increase is not related to an increase in the number of events, which suggests a certain homogeneity in the catalogue completeness since 2011. To understand why the number of detected events has increased in 2003 and 2011, a more thorough analysis needs to be done, for instance by cross-correlating the information with the production rates of the Groningen field.

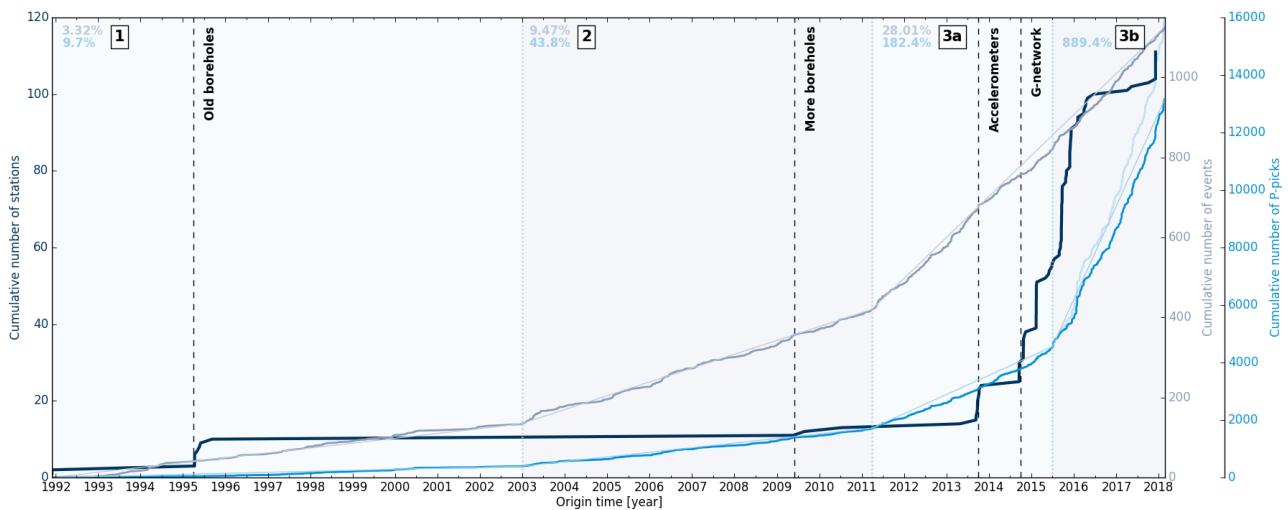


**Fig. 3.22:** Cumulative number of stations (**dark blue**), cumulative number of events (**light gray**) and cumulative number of P-picks (**blue**) over time. For four time periods (corresponding to the shaded areas in the background and numbered from 1 to 3a-b), the slopes of the cumulative number of events and cumulative number of picks are computed and their respective values are given on top in %.

## References

Dost, B., B. Edwards, and J.J. Bommer (2018). "The Relationship between M and ML: A Review and Application to Induced Seismicity in the Groningen Gas Field, The Netherlands". In: *Seismological Research Letters*.

Dost, B., T. Van Eck, and H. Haak (2004). "Scaling of peak ground acceleration and peak ground velocity recorded in the Netherlands". In: *Bollettino di Geofisica Teorica ed Applicata* 45.3, pp. 153–168.

KNMI, pers. comm. (2018). Personal communication.

Kraaijpoel, D. and B. Dost (2013). "Implications of salt-related propagation and mode conversion effects on the analysis of induced seismicity". In: *Journal of Seismology* 17.1, pp. 95–107.

### 3.4 Magnitude of completeness

#### 3.4.1 Context and overview

Estimating the magnitude of completeness  $M_C$  of an earthquake catalogue is important for any seismicity analysis and hazard studies.  $M_C$  is defined as the threshold value above which all earthquakes of equal or larger magnitudes are detected, within a given spatial area and during a specific time period (Rydelek and Sacks, 1989).

$M_C$  is defined as the threshold value above which all earthquakes of equal or larger magnitudes are detected, within a given spatial area and during a specific time period.

Statistical properties of the seismicity cloud such as Gutenberg's b-value can only be assessed above  $M_C$ . An accurate assessment of  $M_C$  is therefore important to avoid biased estimates of Gutenberg-Richter parameters, and/or to avoid overtrimming of catalogue data. In general, the extension and development of the seismic network at Groningen over time significantly improves the detection threshold and hence  $M_C$ . However, this also means that  $M_C$  changes not only in space but also in time, as new seismic stations are added. In particular, a reliable estimation of  $M_C(x,t)$  is required to assess seismicity rate changes, compute magnitude recurrence parameters, and for purposes of earthquake forecasting (Mignan and Woessner, 2012).

#### 3.4.2 Observations and analysis of previous work

From the start of the early network at Groningen in 1995 and later on including the three additional boreholes installed in 2010, the detection and location threshold has been estimated from average noise levels in the boreholes at 200 m depth (see 4.1 for more details; van Eck et al., 2004, Dost et al., 2012). Until 2014, KNMI adopted  $M_C=1.5$  for the North of the Netherlands (Dost et al., 2017). Over time, it was compared to event detection levels and proved to be reasonable (KNMI per. comm.). However, any re-assessment of noise levels was not reported.  $M_C 1.5$  is a rather conservative estimate, as should be expected when no space-time history of  $M_C$  was taken into consideration. Later, an initial analysis of temporal variations of  $M_C$ , using the maximum curvature method MAXC (Wiemer and Wyss, 2000) was performed by NAM (Paleja and Bierman, 2016) for several non-overlapping time periods (see table 2, each including around 200 events). The authors did determine the maximum number of recorded events to estimate  $M_C$ . An overall decrease of  $M_C$  from 1.2 to 0.5 was observed between 2003 and 2016 (see figure 3.23). A re-analysis by KNMI includes a comparison to a synthetic magnitude distribution to evaluate the goodness of fit (R) to a Gutenberg-Richter power law distribution. The approach is described in detail by Wiemer and Wyss (2000). The analysis by KNMI resulted in similar conclusions (Dost et al., 2017). Note that slightly different time periods

Until 2014, KNMI adopted  $M_C=1.5$  for the North of the Netherlands.

were analysed by KNMI as compared to NAM's time periods (see table 2).

**Table 2:** Temporal  $M_C$  for four non-overlapping periods as analysed by NAM and KNMI.

| P | Start t NAM | End t NAM | Start t KNMI | End t KNMI | $M_C$ NAM | $M_C$ KNMI | R KNMI | b KNMI    |
|---|-------------|-----------|--------------|------------|-----------|------------|--------|-----------|
| 1 | 6/4/2003    | 8/5/2009  | 6/4/2003     | 23/2/2009  | 1.2       | 1.2        | 95.6   | 0.94±0.03 |
| 2 | 26/5/2009   | 17/8/2012 | 19/8/2009    | 23/8/2012  | 0.9       | 1.2        | 81.5   | 1.06±0.04 |
| 3 | 23/8/2012   | 23/9/2014 | 23/8/2012    | 21/8/2014  | 0.9       | 0.8        | 96.1   | 0.96±0.04 |
| 4 | 24/9/2014   | 27/9/2016 | 24/9/2014    | 27/9/2016  | 0.6       | 0.5        | 98.2   | 0.85±0.05 |

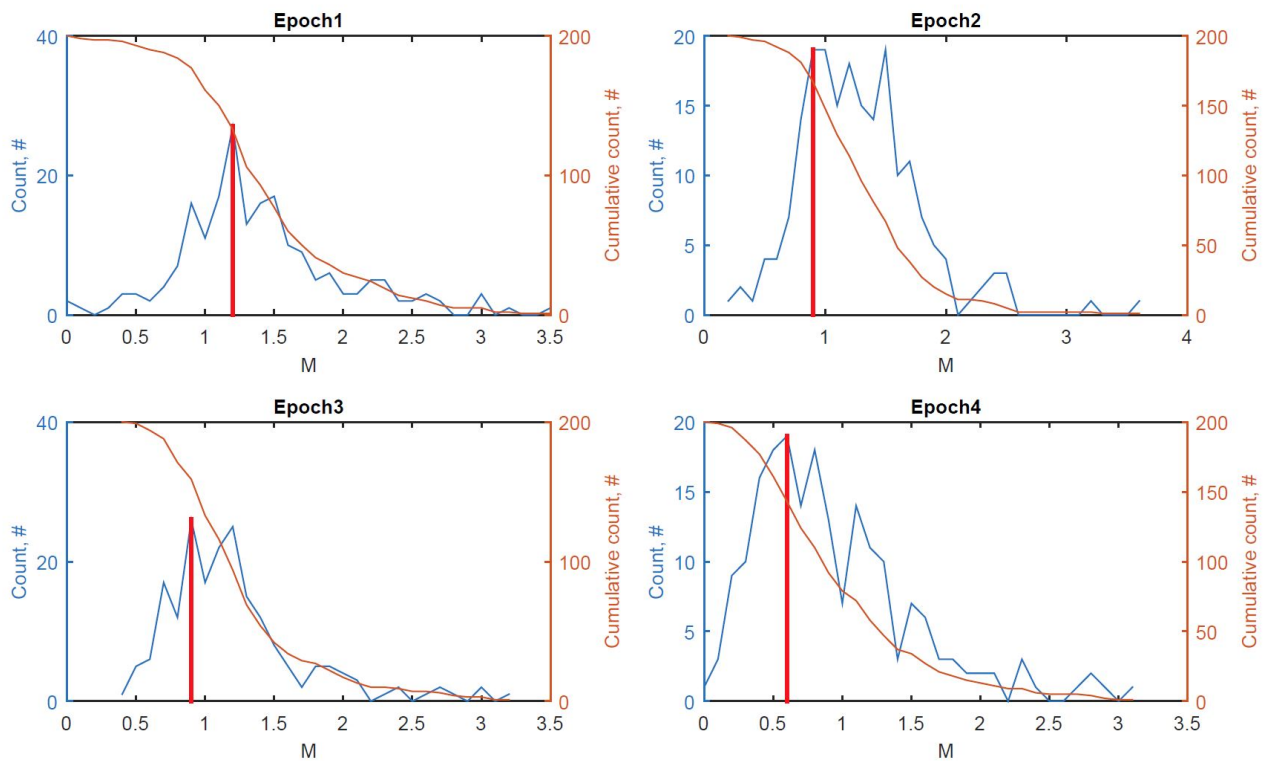


**Fig. 3.23:** Frequency-magnitude distribution (FMD) for the four epochs as analysed by NAM. Figure taken from from Paleja and Bierman (2016). The red line shows the magnitude at which the maximum number of events has been observed.

### 3.4.3 Analysis by NORSAR

NORSAR performed an independent analysis of  $M_C$  applying the same MAXC method as used by NAM and KNMI for the entire Groningen induced seismicity catalogue (see 3.1, figure 3.24) and the four defined time periods of KNMI (figure 3.25). Within the range of aleatoric uncertainty, we obtain an overall result which is comparable to results obtained previously by NAM and KNMI, except for time period 2 (2009 - 2012). Time period 2 also exhibits a larger discrepancy between the values obtained by NAM (0.9) and KNMI (1.2), and shows the lowest R value as determined by KNMI. The cause for this discrepancy becomes clear when looking at the frequency-magnitude distribution FMD for



time period 2 in figure 3.23. We observe several maxima, and no obvious mode in the distribution. NAM chose the first of several maxima as  $M_C$ , resulting in a value of 0.9, which we consider a rather low estimate given that the distribution is broad and several magnitude bins have almost maximum values. If strictly following the methodology applied by NAM, the local maximum with highest magnitude should have been selected, which would lead to an  $M_C$  of 1.5, which is the same as determined by NORSAR. However, the methodology of simply selecting the highest value is quite sensitive to the binning process, and also NORSAR's  $M_C$  estimate of 1.5 is unstable, since it depends on only two M 1.5 events. Again this is due to the small sample distribution of only 200 events in this time interval. A slightly modified time period may result in a drop of  $M_C$  down to about  $M_C$  of 1. Considerable uncertainty in  $M_C$  estimates have also been reported by NAM, using a bootstrapping approach, and are explained similarly by the roughness of the FMD (Paleja and Bierman, 2016), partly due to a small sample size (200 events) per time period. All individual  $M_C$  estimates for a particular time period are well within the errorbars reported in the NAM bootstrapping analysis (Paleja and Bierman, 2016). Nevertheless, NAM's analysis should result in an  $M_C$  of 1.5 for time period 2, as is also suggested by the deviation from a linear Gutenberg-Richer fit at lower magnitudes (figure 3.25, period 2). Overall, KNMI's analysis including a comparison between observed FMD and a synthetic distribution is a good compromise honoring the rather small data set and yielding reasonable estimates.

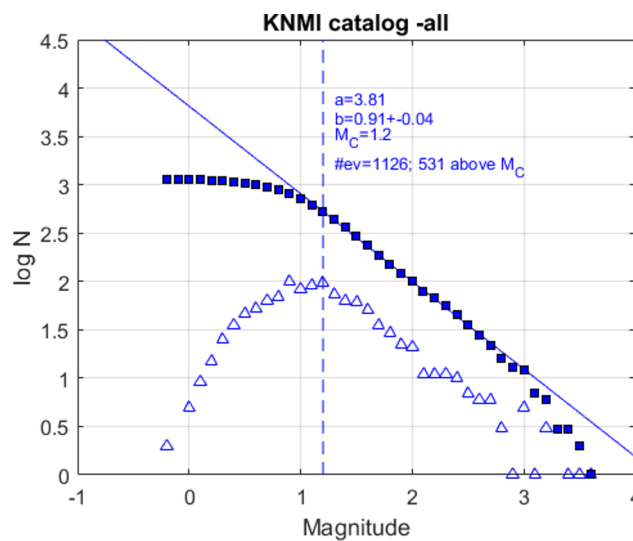


**Fig. 3.24:** Frequency-magnitude distribution of the entire Groningen field induced seismicity.

Common to all studies is a significant decrease in  $M_C$  for the latest time period, despite the large uncertainties. The observed drop in  $M_C$  for the later time period reflects the installation of additional stations hence lowering the detection threshold (see also section 4.1).

All studies observe a decrease in  $M_C$  after September 2014, despite the large uncertainties. The drop in  $M_C$  reflects the installation of additional stations.

Instead of using defined time periods to analyse  $M_C$ , a moving window analysis might be preferable. For this report, NORSAR therefore performed a temporal analysis of  $M_C$  using sliding window with a fixed number of events, moved forward in time by 10 events per analysis step (figure 3.26). By varying the number of events included in the analysis from 200 to 400, we notice how the stability of the  $M_C$  determination improves with a larger sample space. In general, drops in  $M_C$  after 2009 and in 2015 correlate with documented network upgrades. No update for  $M_C$  was provided with data after September 2016, neither from NAM nor from KNMI.

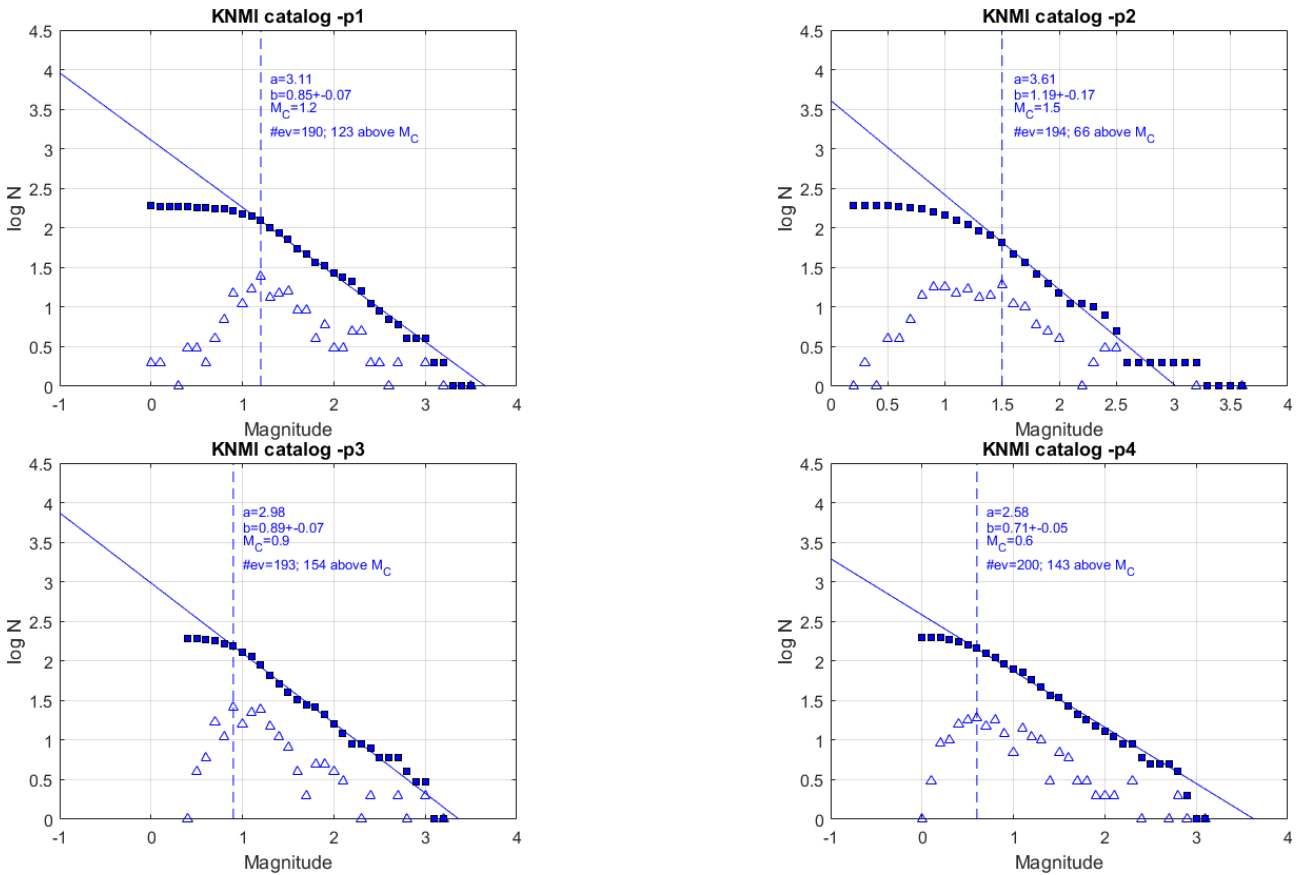


**Fig. 3.25:** Frequency-magnitude distributions and respective  $M_C$  of the Groningen field induced seismicity catalogue for the four time periods defined by KNMI (see table 2) and estimated by NORSAR.

### 3.4.4 Comparison to state-of-the-art and conclusions

The maximum curvature method (MAXC, Wiemer and Wyss, 2000) was used by KNMI and NAM to estimate  $M_C$ . Bootstrapping was applied by NAM for uncertainty estimation. The MAXC method is a fast and straightforward approach to estimate  $M_C$ . The community uses this method widely, although various other methods are available (most are based on the validity of the Gutenberg-Richter law). The community is also aware of the fact that different techniques may provide significantly different results. MAXC is known to underestimate  $M_C$  in the case of gradually curved FMDs (Mignan and Woessner, 2012). However, it has been shown that this may not be the case for a local data set

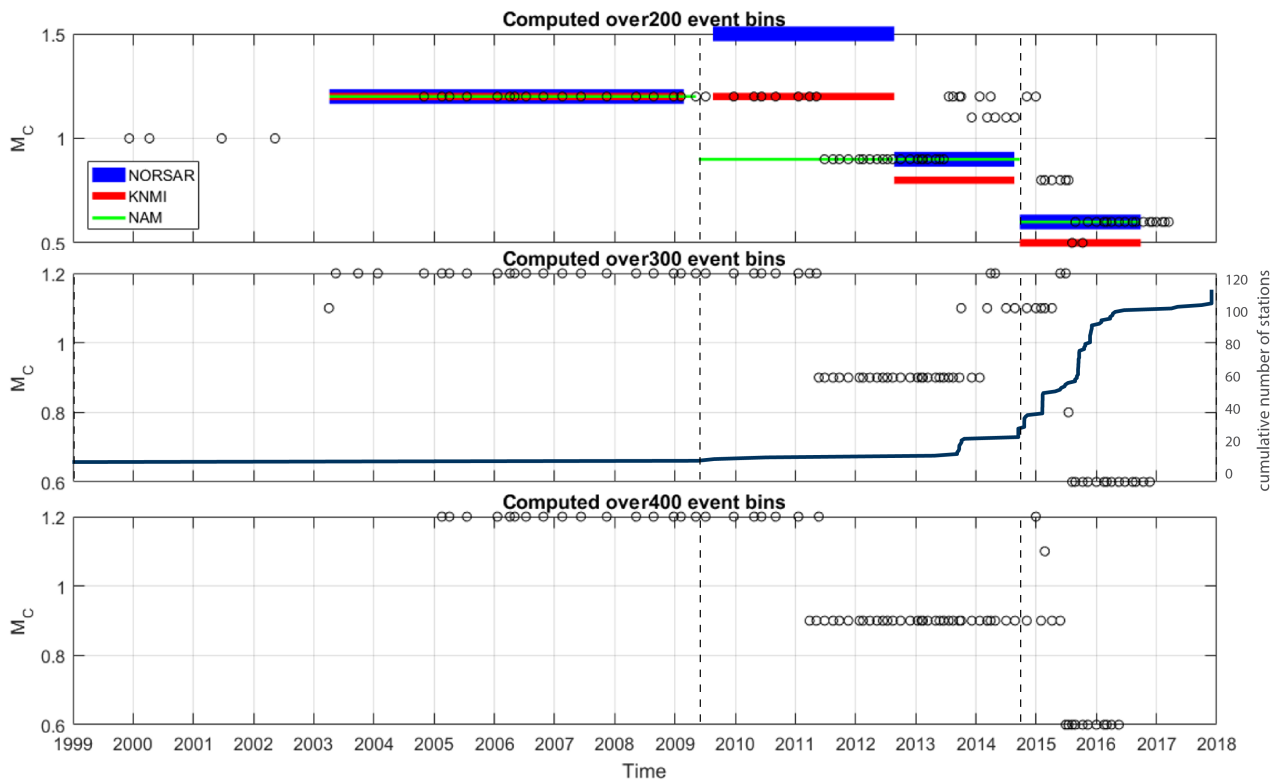


**Fig. 3.26:** Temporal variations of  $M_C$  using 200, 300, and 400 event bins (top, middle, lower panel, respectively) with a 10 event moving window (black circles).  $M_C$  values as estimated by different institutions for the 4 time periods (see table 2) are indicated by different colored bars. The bold dark blue line (middle panel) indicates the cumulative number of stations and the vertical dashed lines mark the beginning time period of larger upgrades of borehole stations.

in which heterogeneities in  $M_C$  are mapped. Another advantage of the MAXC technique is that it requires fewer events than other techniques to reach a stable result (Mignan et al., 2011). However, the used 200 events per time period might be too few events and we may recommend to increase the sample size to at least 300 for a more stable analysis. Additionally, we recommend a moving window approach to estimate  $M_C$  rather than defined time periods. At the present time, there is no consensus on which technique is best suited to compute  $M_C$  and the MAXC method is certainly a valid choice. The analysis performed by KNMI using also synthetic data to estimate  $M_C$  and at the same time optimizing the fit of a Gutenberg-Richter relation to the data might be the best choice for the Groningen analysis.

## References

- Dost, B., F. Goutbeek, T. van Eck, and D. Kraaijpoel (2012). *Monitoring induced seismicity in the North of the Netherlands: status report 2010*. Tech. rep. KNMI.
- Dost, B., E. Ruigrok, and J. Spetzler (2017). "Development of seismicity and probabilistic hazard assessment for the Groningen gas field". In: *Netherlands Journal of Geosciences* 96.5, s235–s245.

- Mignan, A., M.J. Werner, S. Wiemer, C.-C. Chen, and Y.-M. Wu (2011). "Bayesian estimation of the spatially varying completeness magnitude of earthquake catalogs". In: *Bulletin of the Seismological Society of America* 101.3, pp. 1371–1385.
- Mignan, A. and J. Woessner (2012). *Estimating the magnitude of completeness for earthquake catalogs*. Tech. rep. DOI: [10.5078/corssa-00180805](https://doi.org/10.5078/corssa-00180805).
- Paleja, R. and S. Bierman (2016). *Measuring changes in earthquake occurrence rates in Groningen*. Tech. rep.
- Rydelek, P.A. and I.S. Sacks (1989). "Testing the completeness of earthquake catalogues and the hypothesis of self-similarity". In: *Nature* 337, pp. 251–253.
- van Eck, T., F. Goutbeek, H. Haak, and B. Dost (2004). *Seismic hazard due to small shallow induced earthquakes*. Tech. rep. KNMI.
- Wiemer, S. and M. Wyss (2000). "Minimum magnitude of completeness in earthquake catalogs: Examples from Alaska, the western United States, and Japan". In: *Bulletin of the Seismological Society of America* 90.4, pp. 859–869.

## 4 Review of data processing

### 4.1 Event detection

#### 4.1.1 Definitions

In this report, we distinguish between:

- the **detectability**, which describes the ability of the seismic network to detect seismic events in terms of magnitude. Detectability maps are determined theoretically and give an idea of the minimum event magnitude that could be detected under some assumptions.
- the **detection**, which refers to the procedures in place for real data.

#### 4.1.2 Detectability as conducted by KNMI

In the Northern Netherlands, the local population starts to feel earthquakes from about magnitude 1.8 and above. As such, the objective for KNMI was to establish a network that is able to detect all earthquakes that may be felt by people in the Groningen area, and include slightly smaller events as well. The anticipated threshold to detect an event was hence set to magnitude 1.5 (section 3.4). We further define this threshold magnitude as the detectability.

Throughout the development of the seismic network at Groningen, the detectability has been improving. KNMI has evaluated the performance of the network in terms of detectability several times, the first time in 1995 after the installation of the first eleven boreholes (van Eck et al., 2004) and thereafter several times (e.g. in 2010 after the addition of 6 boreholes - Dost et al., 2012). In this section, we only present the methodology that was used by KNMI to produce the detectability maps, as described in van Eck et al. (2004), appendix 3 and Dost et al. (2012), part 3.

To estimate the detectability, the local noise condition at each sensor is the key parameter. However, the noise generally changes with time. For example, diurnal variation and seasonal variation are commonly observed. KNMI has therefore considered to use the average noise value for the computation of the detectability maps. These maps were computed for an SNR of 2 (except if specified otherwise) and the attenuation law that has been used for the borehole stations is given by the equation 4.4 in the section 4.3. Moreover, the detectability maps are produced for single stations, i.e. considering that an event is detected when at least one station records it.

In the figure 4.1a-b, the detectability maps computed and published by KNMI are shown after the installation of the borehole stations in  $\approx 1995$  for a single station, assuming an SNR of 2 (4.1a) and assuming an SNR of 1 (4.1b). The figure 4.1c is an update after the installation of some new boreholes around 2010 (see section 2.1 for more information on the network development) and has to be compared with the figure 4.1a.

As of 1995, the geometry of the seismic network in the Groningen area theoretically allows the detection of seismic events with magnitude lower than 1.5 (and even 1), which was the "target" magnitude defined by KNMI when the site started being instrumented. Since 2010, events smaller than magnitude 1 are detectable in an extended area around Groningen (e.g. including the Harlingen salt mine, West of the field), and smaller than 0.5 locally around the seismic stations.

In 2018, the network geometry is such that all events of magnitude 0.5 or higher are detectable in the Groningen field.

In parallel, location threshold maps were also produced by KNMI (van Eck et al., 2004, Dost et al., 2012, Dost et al., 2017), using exactly the same method but requiring 3 stations instead of 1 (because a minimum of three stations is necessary to locate an event with the circle method). We do not show these maps in this section because we focus on the event detection.

Since 2015, the large upgrade including new borehole and surface stations (**G-network** with a distance of 3 to 4 km between stations) has significantly increased the detectability. To our knowledge, however, we could not find any updated detectability maps, but location threshold maps were published in Dost et al. (2017). The detectability has been re-computed as well, and can be produced by KNMI on request. In any case, the detectability map has lower magnitude levels compared with the location threshold map, meaning that all events of magnitude 0.5 or higher are now theoretically detectable in the whole Groningen field (instead of locally).

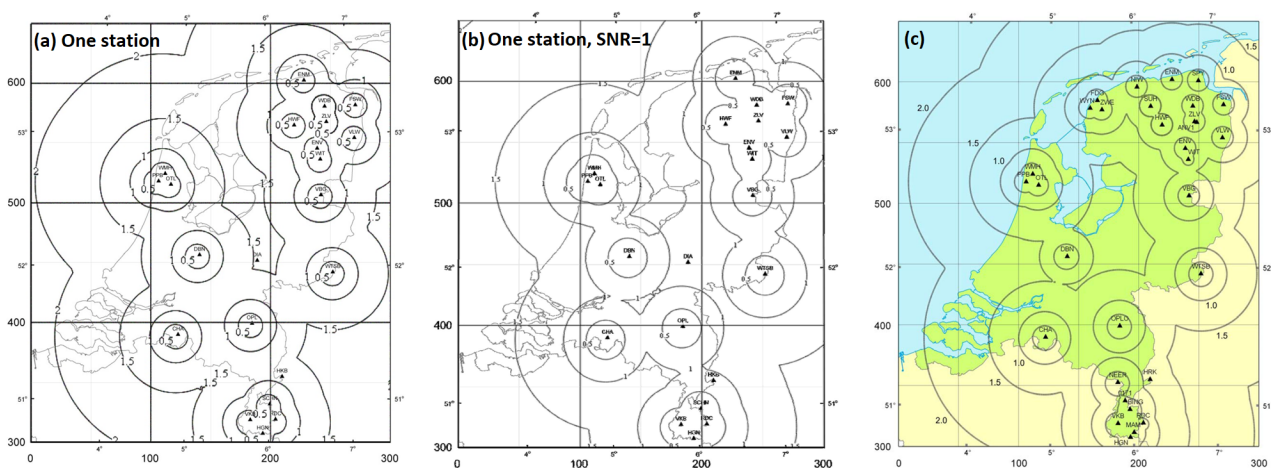


**Fig. 4.1:** Detectability maps. Contours represent the magnitude. (a-b) From van Eck et al. (2004). (c) From Dost et al. (2012).

### 4.1.3 Detection on real data

We now focus on the operational part, meaning how event detection has been performed concretely by KNMI. It is important to note that the detection information is not contained in the event bulletin strictly-speaking. For example, the number of triggers that are necessary to assign to an event, the

detection thresholds associated to each station and the computing parameters are not accessible. However, the information on the phase (P-, S-) picks is available. Hence, we assume that a detection was present in case when a phase pick and identification was provided.

### Generalities and state-of-the-art

In practice, detecting a seismic event means determining its onset. In order to discriminate the signal emitted by an event and the background noise, it is common to compute some objective functions which enhance the signal onset. Among the most popular (and used at Groningen), we can name the STA/LTA (ratio of the Short-Term Average to the Long-Term Average) and the AIC (Akaike Information Criterion).

The **STA/LTA** requires the definition of two windows of different lengths: one long (LTA) and one short (STA). This is one common way of defining the Signal to Noise Ratio (SNR). The LTA basically measures the background noise level and should be about 10 times longer than the STA. The STA, on the other hand, accounts for short duration amplitude changes in the signal. The STA/LTA is computed on a moving time window. When the STA is much higher than the LTA, there is a local maximum, which may be associated to an event if its value is higher than a given threshold.

The **AIC** is a statistical criterion based on the computation of a set of statistical noise models (Akaike, 1973). Broadly-speaking, the AIC measures the variance of the data, which do not match the auto-recursive models. A seismic event has a different statistical signature compared with noise and, as a result, the AIC function will reach a minimum at the time of its onset (St-Onge, 2011).

### Detection at Groningen before 2015

Before 2015, few information is available on how the events were detected, but here are some bullet points on what we could gather:

- Only borehole stations were used for detection purpose. They were run in triggered mode (KNMI, pers. comm., 2018; Kraaijpoel and Dost, 2013). The objective function was *probably* STA/LTA (KNMI, pers. comm., 2018).
- Due to the rather large inter-station distances, a detection on a single station was considered as sufficient to assign an event (KNMI, pers. comm., 2018).
- The accelerometers used to run in pull mode until 2010 and their data were retrieved only when an event was found on the boreholes (KNMI, pers. comm., 2018; Kraaijpoel and Dost, 2013).

Moreover, we found a first reference to the **SeisComp3** software in Dost et al. (2012) where automatic multi-station detection is mentioned as being tested since 2009. This also corresponds to the period when the data transfer was changed to a continuous mode (and not a triggered mode anymore). In general, this new data transfer should not have changed anything related to the continuity of event

detections. Also, we could not find out whether the accelerometers were still running in pull mode or if their data were sent continuously from that time on, and in consequence, whether they were used for event detection purposes.

### Detection at Groningen since 2015 with SeisComp3

Before 2010, KNMI detected events on the borehole stations only in a triggered mode. From 2010, continuous data were available, and since June 2015, KNMI uses the SeisComp3 software.

Since 2015 and the installation of a large number of stations (**G-network**, 70 new sites in total), it has become necessary to take into account more criteria. For example, a detection on a single station is not restrictive enough anymore and would result in a number of false alarms. Thus, a more systematic and stable automatic processing scheme that may also be

suitable for preliminary automatic event location has been implemented. KNMI has chosen to use the SeisComp3 software (Hanka et al., 2010) which is used by more than 200 entities world-wide, including universities, research centres and tsunami and earthquake warning centres (Weber et al., 2015). As mentioned earlier, SeisComp3 has already been tested by KNMI since about 2009, but has become fully operational in June 2015 only (KNMI, pers. comm., 2018).

With respect to detection, SeisComp3 proposes to use either the STA/LTA or the AIC objective functions. From June 2015 to February 2016, KNMI used the STA/LTA with the following computing parameters for the Groningen area (and more generally the Northern Netherlands - different settings are used for the Southern part; KNMI, pers. comm., 2018):

"RMPH(10) » ITAPER(30) » BW(4.5,0,40.0) » STALTA(0.5,10)".

More explanations can be found on the SeisComp3 manual on their meaning. The information that we extracted from the event bulletin also indicates that since February 2016, the STA/LTA has been replaced by the AIC.

All the information on how the picks were made are readable in the QuakeML event structure under the "Pick" field (fig. 3.2). The *evaluation mode* attribute tells if the pick is manual or automatic. In case it is automatic, the "methodID" can be either *Trigger* (for the STA/LTA), which computing settings are detailed in the "filterID" attribute; or *AIC*. Both for manual and automatic picks, the parameters of the filters that are potentially applied are given under "filterID".



Analysis by NORSAR

Our analysis is based on the *Groningen induced seismicity bulletin* (section 3.1).

Overview of the event bulletin in terms of detections:

As specified previously, the information on event detection strictly-speaking is not available before June 2015, when SeisComp3 started being used.

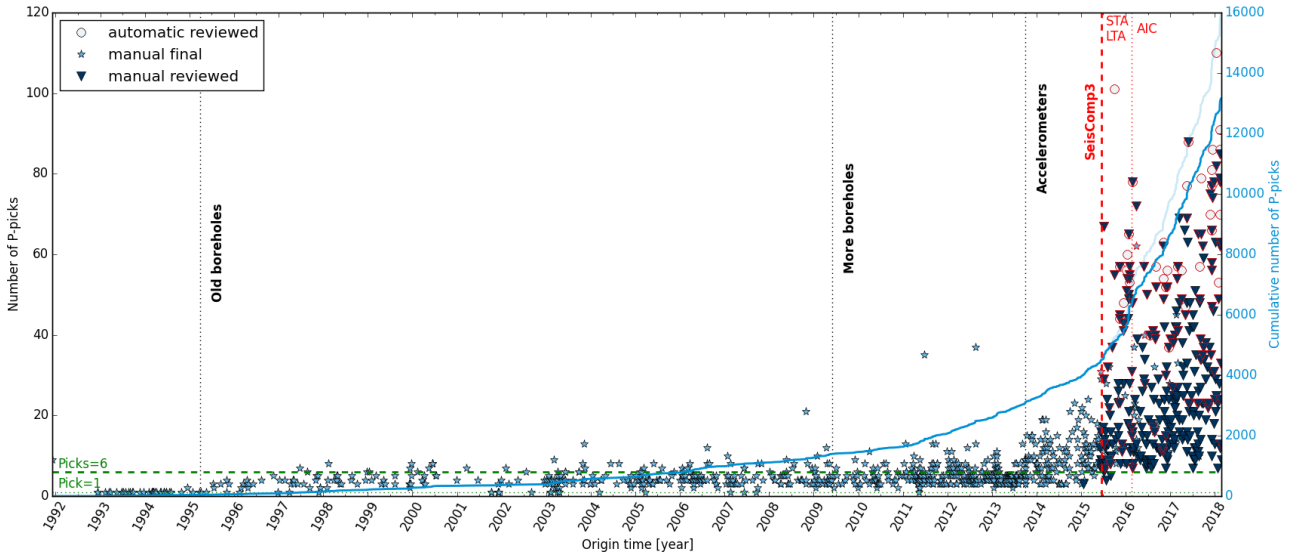


**Fig. 4.2:** Time evolution of the number of P-picks by event extracted from the bulletin. The red dashed line is set for the first event with automatic picks, and the red dotted line represents the change from the STA/LTA to the AIC function. The events for which automatic picks were found are surrounded in red. The blue curve which is superimposed represents the cumulative number of P-picks. After June 2015, the curve is split, depending if the automatic picks are considered (light colour) or not.

The figure 4.2 shows the evolution of the number of P-picks by event over time. Practically, we observe that the number of picks is always higher than 1. Once again, this is because we consider *picks* and not *detections* strictly-speaking. Picks are further used for locating the event and that requires a minimum of 3 picks. Before 1995, a unique borehole (**FSW**) was installed. As of 1995, when seven additional borehole stations were installed, the average number of picks has increased.

In the QuakeML event structure (fig. 3.2), under the "Origin" field, the evaluation mode can be either *automatic* or *manual*, and the evaluation status either *final* or *reviewed*. We use the evaluation mode and status as colour-code in the figure 4.2. Before June 2015, all events were evaluated manually and have a "final" status. The "manual reviewed" events have appeared simultaneously with the "automatic" events around June 2015, when KNMI fully implemented SeisComp3.

Before SeisComp3, the information on detection strictly-speaking are not available from the bulletin. Instead, in order to stay consistent, we use the information on P-picks.

To our best understanding, "automatic" events are the entirely automated and preliminary analysed

events by SeisComp3. "Manual reviewed" may correspond to automatic events reprocessed manually by a KNMI operator, and "manual final" to what is published in the public catalogue of events. However, since 2015, most events belong to only one category, i.e. have only one "origin", and a few events belong to up to 3 categories. Here is a list of a few observations that we made and these would need to be clarified by KNMI:

- after June 2015, not all events are "automatic".
- some of these "automatic" events contain less than 6 automatic picks (see in the figure 4.4). However, a minimum of six triggers is required to assign an event (KNMI, pers. comm., 2018). This suggests that the automatic picks were not always kept as such, but rather improved (or at least modified) manually and re-labelled subsequently as "manual".
- "manual" events may contain automatic picks. For most events, the same picks seem to be used for the "automatic" and "manual" origins (at least, the number of picks is exactly the same). These picks can be a mixture of manual and automatic picks. In other words, it seems that the "automatic" origin does not refer to the SeisComp3 analysis only, but was modified afterwards.

It is not always clear from the bulletin what was analysed manually and automatically.

#### Analysis of the SeisComp3 automatic detections:

In the following paragraph, we consider the automatic picks only. These can be considered as the only pieces of information which relate directly to detections.

In the QuakeML event structure, they correspond to the "Pick" elements which evaluation mode is set to "automatic" (figure 3.2). In the figure 4.3, we summarise the content of the event bulletin. A total of 1126 events were located in the Groningen field. Of these, 88 events (7.8%) contain at least one automatic pick performed by SeisComp3 (fig. 4.3a): 22 with the STA/LTA function and 66 with the AIC (fig. 4.3b). We notice that these detections were performed on the vertical component only (**Z**), where the strongest P-wave onsets are expected. Most automatic picks are made on the G-network stations (which constitute a large majority of the network, see section 2.1), and in a lesser extent on the old borehole network and on the accelerometer B-network (fig. 4.3c). Some events (2.4%) are even detected on stations that are not considered as being part of the Groningen network (T-network stations and **VBG** borehole in the Overijssel region). The magnitude of these particular events is systematically larger than 1.5 (fig. 4.4, dots surrounded in red). Lastly, most automatic picks ( $\approx 88\%$ ) are found on borehole stations (including the G-, N- and old borehole networks) and the figure 4.3d shows that the deepest sensors (number 4) are the most sensitive with more than 90% of the detections. This highlights the importance of such borehole stations for seismic event detection in the Groningen area.

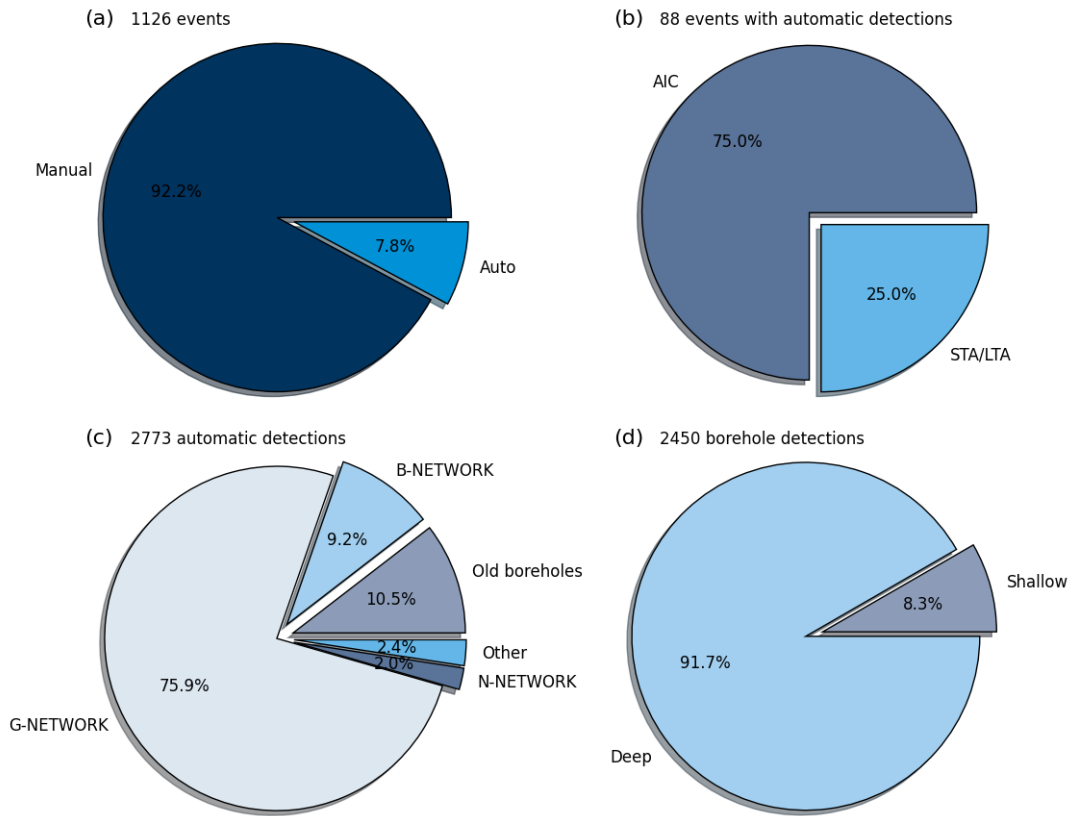


**Fig. 4.3:** (a) Distribution of events containing automatic and/or manual picks. (b) Distribution of the methods used for automatic detections. (c) Distribution of the automatic detections by type of stations. (d) Diagram showing the distribution of the automatic detections by borehole levels: "shallow" corresponds to levels 0 (if that applies), 1, 2, 3 and "deep" to levels 4 and 5 (if that applies).

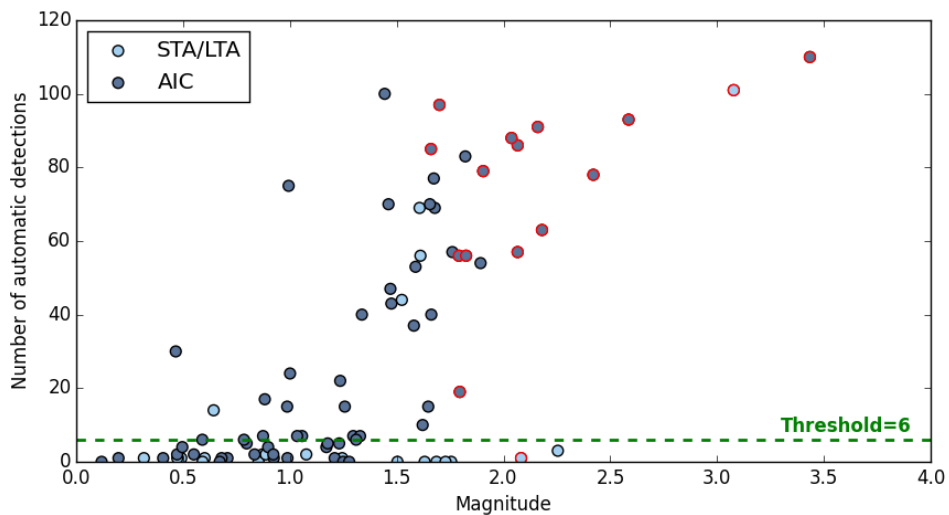


**Fig. 4.4:** Number of automatic detections in function of the event magnitude. Dots surrounded in red show which of the events have detections included originating from sensors placed outside of the Groningen field (T-network, VBG - see figure 2.1, p. 11).

**Detectability applied to real data:**

In figure 4.5, we aim to compare the theoretical detectability map shown in 4.1c with what the real data reflects. In order to ease the comparison, only the events recorded before 2013 are considered. The distances event-station are computed for each possible pair. At each station, for different magnitude ranges, the distance to the farthest event defines the radius of a circle, which delimits the minimum detectable magnitude for this station. The map obtained in figure 4.5 combines the information for all stations available across the Netherlands and for the complete KNMI induced seismicity bulletin (1485 events in total). At first glance, the map seems quite different from the theoretical one. This is very likely due to an heterogeneous distribution of the seismic events in the catalogue, with a large majority of them being located in the Northern part, close to or within the Groningen field, which is the part we are interested in. In this region, the magnitude limits appear to be smaller than the ones predicted by the theory and indicate that even seismic events of magnitude 0.5 occurring outside the Groningen field are visible on the old borehole network (e.g. in the Drenthe region). However, one should remain cautious and keep in mind that this does not guarantee that all seismic events of magnitude 0.5 were found (section 3.4). Also note that to produce the map in figure 4.5, we used all events independently of their signal-to-noise ratios.

The deepest sensors of the borehole stations appear to be the most efficient in detecting events.

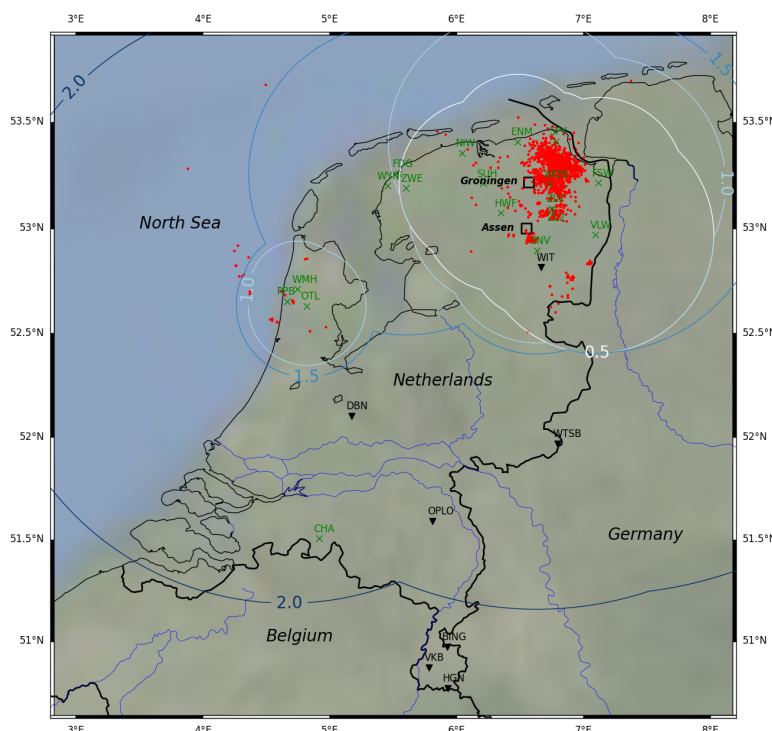


**Fig. 4.5:** Detectability map derived from the complete KNMI induced seismicity bulletin before 2013 (red dots). At that time, only the old borehole network was installed in the Northern part of the Netherlands (broadband seismometers otherwise). Contours are magnitudes. To be compared with figure 4.1c.

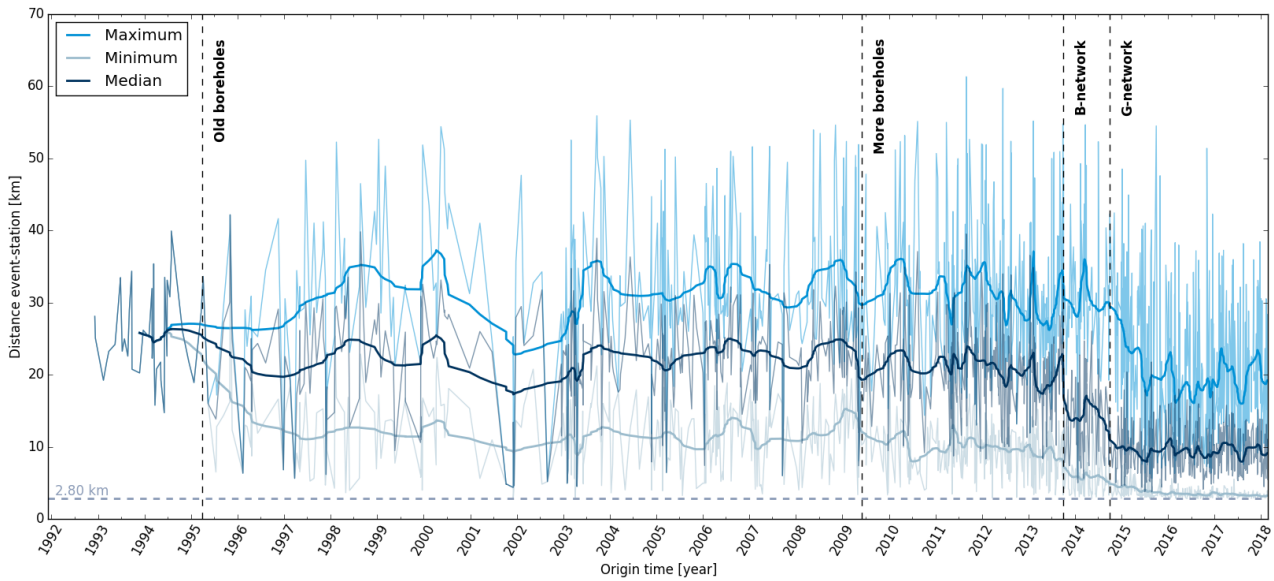


**Fig. 4.6:** Minimum, median and maximum distances of each event to the stations where a P-pick was found over time. The bold curves are obtained by smoothing on a sliding window containing 30 events.

In the figure 4.6, we show the evolution of the minimum, median and maximum distances of each event to the stations where a P-onset was picked. A general observation is that the minimum distance decreased whenever new stations were installed. This is particularly obvious in 1995 and 2013. Currently, the minimum distance curve indicates that the events occurring within the Groningen field are as close as 2.8 km of the nearest stations. Regarding the maximum distance curve, it has been quite constant over time, except since 2013 where a decrease is also observed. This could be explained by a more selective choice of stations for picking, based for instance on signal-to-noise ratio criteria. Moreover, we are unaware of potential changes in the detection threshold values defined for each station, but they might be more restrictive now. Indeed, due to the large number of records available, it may be better not to use all of them, but rather focus on higher-quality signals.

Since the G-network was installed, the minimum distance event-station in the Groningen field has been reduced to 2.8 km only.

The figures 4.7 and 4.8 are other ways of representing the minimum and maximum distances of the events to the stations with the advantage that the maps also include the information on the event magnitude. Each figure contains two plots corresponding to two time periods: before

and after 2013, year from which a major upgrade of the seismic network has been gradually realised. A change is particularly visible in the figure 4.7: the area in the Northern part of the Groningen field where the seismicity occurs ( $>53.25^{\circ}\text{N}$  and  $<53.4^{\circ}\text{N}$ ) is now covered with stations. Because that was not the case before 2013 (only **WDB** and **SPY** within the gas field), it could explain the larger distances measured.

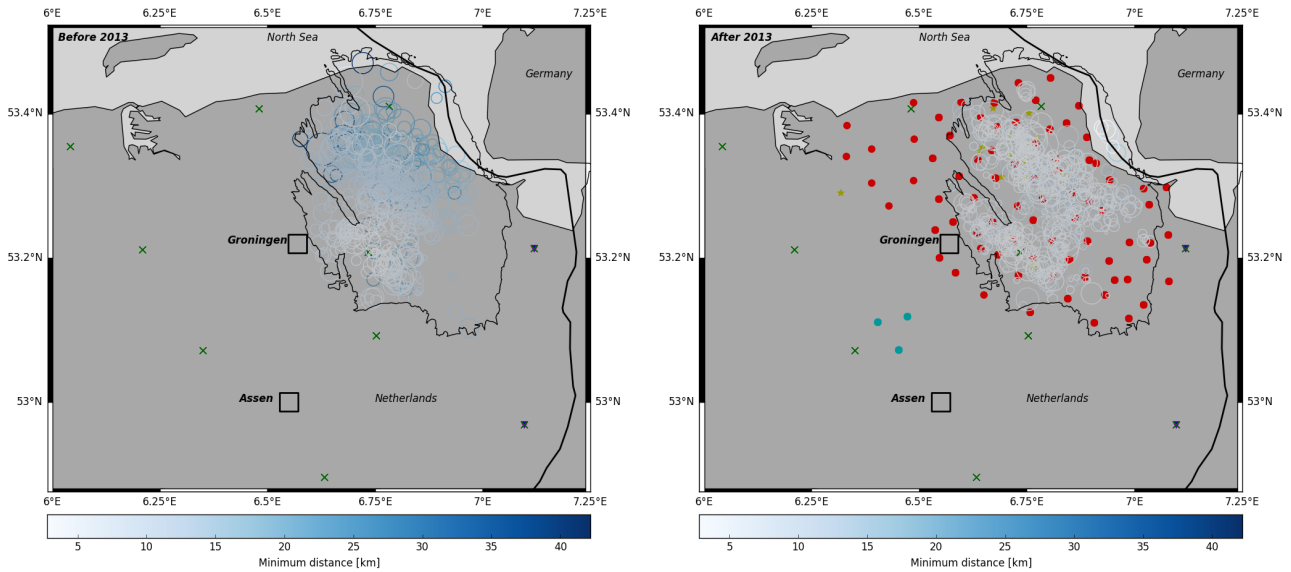


**Fig. 4.7:** Seismicity maps in the Groningen gas field coloured by the minimum distance to the stations. Each circle represents a seismic event and its size is representative of its magnitude. (Left) Seismicity before 2013 recorded by the old boreholes only. (Right) Seismicity after 2013 when the B- and G-networks were progressively installed. To ease the comparison between the two time periods, the colour scale is the same. Station names and symbols are the same as in the figure 2.3 (p. 15 of this report).

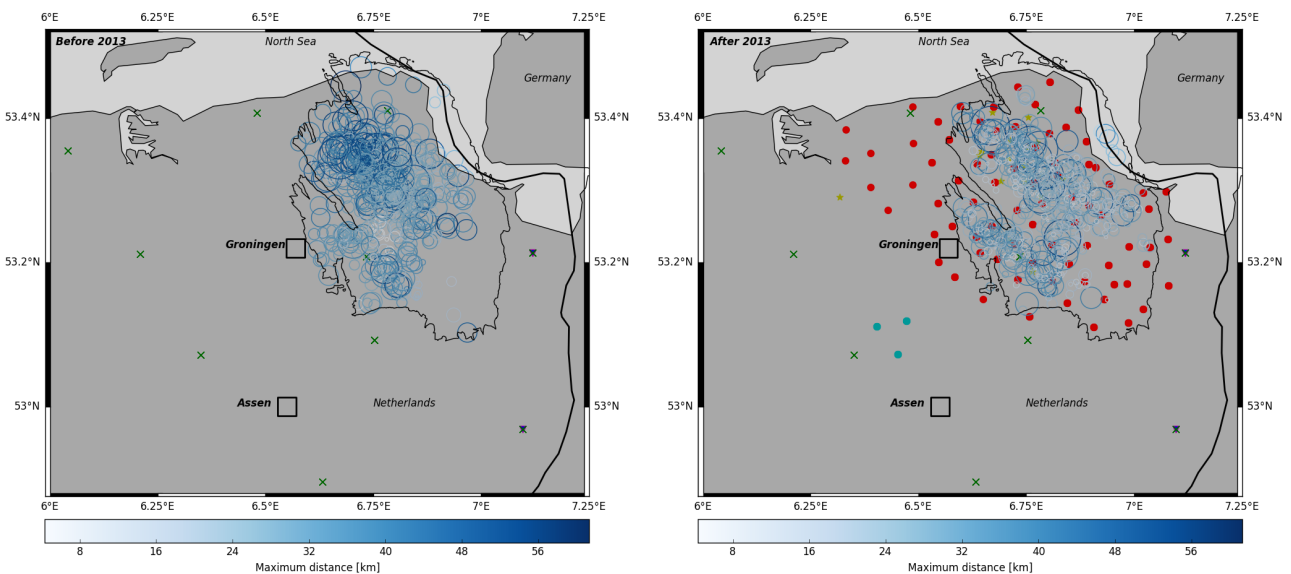


**Fig. 4.8:** Same as figure 4.7, but the events are now coloured by their maximum distance to a station where a P-pick was found.

#### 4.1.4 Other detection algorithms

In addition to the detection process previously described (from which the public KNMI event catalogue is generated), some other methods were tested on the Groningen data in order to detect lower SNR events, among which:

- the **pattern detectors** (more details are given in the section 5.2). Dave Harris (Deschutes Signal Processing LLC) used the matched filter technique in the framework of the ACISM project and keeps providing KNMI with his detection results. These are then added to a private catalogue. For example, recently (DSP, pers. comm., 2018), the detector was applied to 13 months of data from 4 boreholes using the 17 August 2015 Zeerijp event as a master. For this time period, 26 events were reported in the KNMI public event catalogue and 19 new events were found.
- the **migration and stacking** approaches with various implementations such as the coalescence mapping (Drew et al., 2013, Smith et al., 2016), WCEDS (Young et al., 1996, Arrowsmith et al., 2016). These techniques have the advantage of not requiring phase picking of the data and simultaneously detect and locate the events. They exploit the coherent information across the network by (1) correcting the data from the theoretical travel-times from different test locations to the stations (*migration*) and (2) stacking the aligned data for the different test locations. It is also common to simplify the waveforms beforehand, e.g. by using objective functions enhancing the changes in the signals, such as STA/LTA (coalescence mapping, WCEDS, . . .), envelope, kurtosis (Ruigrok et al., 2015), . . .
- the **Hidden Markov Models (HMM)** which simultaneously detect and classify a seismic event. The HMMs are a machine learning technique. Similarly to the pattern detectors, a training set of pre-identified signals (including noise) is required for the implementation. Unlike the pattern detectors, the principle does not rely on the cross-correlation of waveforms, but is a probabilistic approach where the different signal states are each described by a vector of features (e.g. amplitude, polarisation. . .). In the framework of the ACISM project, the HMM method could be successfully applied at Groningen, but the detection of new, noisier events was limited by their SNR (i.e. the method fails in the recognition of very noisy events).

It is important to note that although these methods are powerful, they are also often much more computationally demanding and time consuming. Hence they are more difficult (or not suited to) to implement in real-time.

#### 4.1.5 Conclusions

- KNMI applies standard and well-established methodologies for the seismic event detection in the Groningen field.
- Since June 2015, the automated detection process is fully carried out by the SeisComp3 software. This does not result in a change in the number of events, which suggests that the new implementation has been a done in accordance and in continuation of the previous one, ensuring a certain homogeneity in the catalogue (fig. 3.22 in section 3.3).
- Apart from the real-time implementation, KNMI together with other partners have tested and use more complex algorithms, in particular to search for low-SNR events. Some of these addi-

tional events are part of an internal catalogue which gives material to further scientific investigations.

## References

- Akaike, H. (1973). "Information theory and an extension of the maximum likelihood principle". In: *Second International Symposium on Information Theory, Akademiai Kiado, Budapest*.
- Arrowsmith, S., C. Young, S. Ballard, M. Slinkard, and K. Pankow (2016). *Pickless seismic event detection using WCEDS*. SAND2016-6887 PE. Sandia National Laboratories.
- Dost, B., F. Goutbeek, T. van Eck, and D. Kraaijpoel (2012). *Monitoring induced seismicity in the North of the Netherlands: status report 2010*. Tech. rep. KNMI.
- Dost, B., E. Ruigrok, and J. Spetzler (2017). "Development of seismicity and probabilistic hazard assessment for the Groningen gas field". In: *Netherlands Journal of Geosciences* 96.5, s235–s245.
- Drew, J., R.S. White, F. Tilmann, and J. Tarasewicz (2013). "Coalescence microseismic mapping". In: *Geophysical Journal International* 195.3, pp. 1773–1785.
- DSP, pers. comm. (2018). Personal communication.
- GeoForschungsZentrum (GFZ), Helmholtz Centre Potsdam - (2018). *SeisComp3*. URL: <https://www.seiscomp3.org/> (visited on 04/25/2018).
- Hanka, W., J. Saul, B. Weber, J. Becker, P. Harjadi, M. Fauzi, and GITEWS Seismology Group (2010). "Real-time earthquake monitoring for tsunami warning in the Indian Ocean and beyond". In: *Natural Hazards Earth System Science* 10, pp. 2611–2622.
- KNMI, pers. comm. (2018). Personal communication.
- Kraaijpoel, D. and B. Dost (2013). "Implications of salt-related propagation and mode conversion effects on the analysis of induced seismicity". In: *Journal of Seismology* 17.1, pp. 95–107.
- St-Onge, A. (2011). "Akaike Information Criterion applied to detecting first arrival times on microseismic data". In: *2011 SEG Annual Meeting, San Antonio, Texas*.
- Ruigrok, E., H. Paulssen, and J. Trampert (2015). *Tremor mapping at the Groningen field*. Poster, Schatzalp meeting on Induced Seismicity 2015 in Davos, Switzerland.
- Smith, J., J. Drew, and R. White (2016). *Coalescence Microseismic Mapping*. University of Cambridge.
- van Eck, T., F. Goutbeek, H. Haak, and B. Dost (2004). *Seismic hazard due to small shallow induced earthquakes*. Tech. rep. KNMI.
- Weber, B., D. Rössler, and J. Becker (2015). *Introduction of the key features of SeisComp3*. gempa GmbH, Potsdam, Germany. Oral presentation.
- Young, C., M. Harris, J. Beiriger, S. Moore, J. Trujillo, M. Withers, and Aster R. (1996). *The waveform correlation event detection system project phase 1: issues in prototype development and testing*. Sandia Report SAND96-1916. Sandia National Laboratories.



## 4.2 Event location and uncertainty

### 4.2.1 Overview

Event location methodology is critical for the interpretation of seismicity. Accurate and precise event locations within an earthquake catalogue provide the basis for understanding the seismicity. It allows for the seismicity to be accurately linked to structural features and is the basis for further analysis.

There are multiple factors that will influence the event location. These include:

- the choice of event location algorithm;
- the velocity model;
- the station distribution;
- the data quality.

In this section we shall look at each of these factors, with application to the Groningen induced seismicity catalogue.

The most common methods for earthquake location involve using observed phase arrival-times, their uncertainties and a set of predicted travel-times from a given velocity model, and involves minimising the difference between the observed and the calculated set of travel-times (i.e. the residuals). Since the travel-time does not scale linearly with the event location, there is no direct set of linear equations that can be used to solve the earthquake location problem in a single calculation. Instead, approaches can be divided into one of two methodologies:

- direct search;
- iteratively linearised solution.

Direct searches involve the forward computation of travel-times at potential source locations such that the smallest difference with the observed travel-times can be found (typically the least squares solution for all residuals). Direct searches can be further subdivided into 'regular or deterministic searches' and 'directed searches' (Lomax et al., 2014). The former can involve full grid searches, where the full model space (i.e. all possible event locations) are searched, nested grid-searches, where progressively finer grids are searched, or stochastic/Monte-Carlo type searches, where the random sampling of the model space is used. Such methods allow for a good estimate of the full probability density function, which provides the optimal information for assessing location uncertainty. The drawback is that these methods are computationally intensive and are therefore not typically feasible for large search regions. 'Directed searches' include evolutionary and adaptive searches that iteratively and selectively sample the model space based on certain criteria. This allows for more efficient searches at the expense of reduced sampling of the probability density function, which can

result in events being mislocated. A good review of these methods can be found in Lomax et al. (2014) and Wuestefeld et al. (in press).

Iteratively linearised solutions are based on linearising the earthquake location problem by using a Taylor series expansion around an initial location estimate. This allows the travel-time residuals to vary linearly with small changes in location. Hence, a set of linear equations can be formulated, relating each phase arrival-time observation to the change in earthquake location (from the initial estimate), which can in turn be solved in a linear inversion. The method is repeated iteratively, such that the starting location for the inversion is updated from the previous iteration until a certain stopping criteria (e.g. residual reduction threshold) is reached. Iteratively linearised solutions are extremely quick and efficient and suitable for large regions with simple velocity models. However, the methodology suffers from not being able to effectively sample the misfit of the model space to reliably determine the location uncertainty. Similarly, it is possible for the solution to represent a local minimum in the misfit, and thus mislocates the earthquake, which can be the result of the velocity model, station distribution or the starting location for the inversion.

This overview of earthquake location methods is used as an introduction to KNMI's location methodology in section 4.2.3. We will further expand on earthquake location methodology in section 4.2.10, where an overview of state-of-the-art methods is given, together with their applicability to the induced seismicity at Groningen.

#### 4.2.2 Description of analysed data

The analysis within this section is based on the Groningen induced seismicity catalogue and its associated bulletin data. The bulletin data was retrieved using KNMI's FDSN webservices as described in section 3.1. Station location information that was not available from KNMI was retrieved from ORFEUS and the ISC. We have clearly identified when these supplementary data sources were used.

#### 4.2.3 Current procedures by KNMI

The methodology used by KNMI for earthquake location is recorded as 'Hypocenter' and 'Hypo91' for the Groningen induced seismicity bulletin as shown in figure 4.9. All events up to and including event id, 'knmi2015khoy' (27-05-2015,  $M_L$  2.0) are stated as using the 'Hypo91' method. All events from event id, 'knmi2015kwxl' (04-06-2015,  $M_L$  0.96) are stated as using the 'Hypocenter' method. This change in naming coincides with when KNMI transi-

Standard processing was moved to the SeisComp3 software platform in June 2015 (KNMI, pers. comm., 2018), resulting in changes in naming convention used in the published bulletin. The HYPOCENTRE location algorithm (Lienert et al., 1986; Lienert, 1991) is implemented within this platform.

tioned to using the SeisComp3 software package for standard processing.

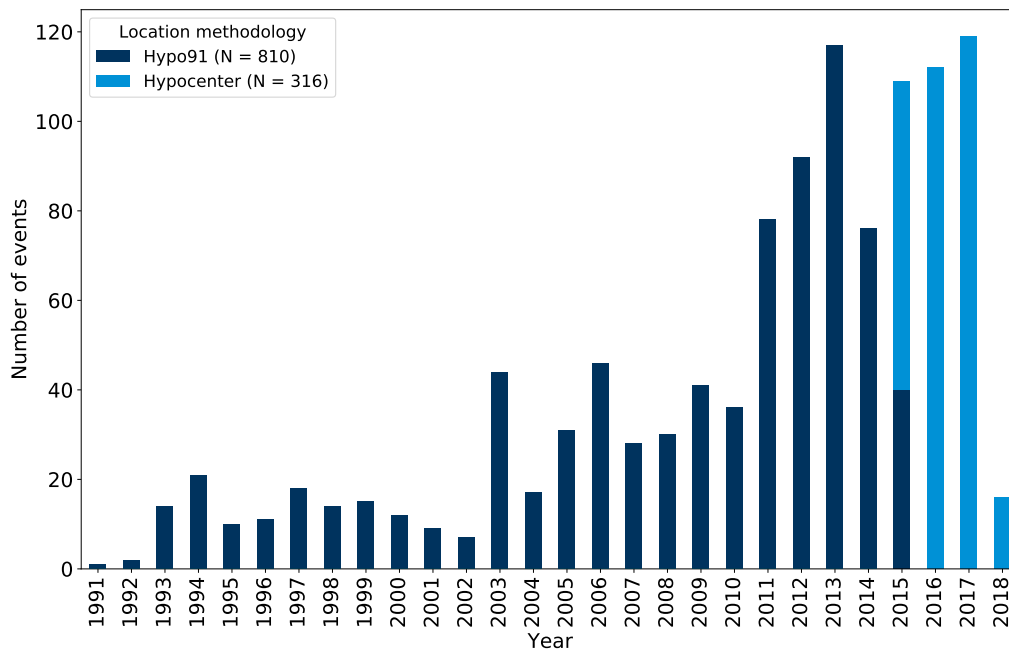


**Fig. 4.9:** Labelling of the event location methodology in KNMI's induced seismicity bulletin.

KNMI, pers. comm. (2018) have stated that the labelling of 'Hypo91' and 'Hypocenter' refer to the same location algorithm - HYPOCENTRE - developed by Lienert et al. (1986), and updated in Lienert (1991). A further update of the algorithm was published by Lienert and Havskov (1995), but no reference is made to this by KNMI based on our findings. It is also reported (KNMI, pers. comm., 2018) that an alternative location algorithm - HYPO71 (Lee and Lahr, 1972) was used between 1991 and approximately 1998, after which the HYPOCENTER algorithm was implemented. Technical reports from KNMI within this period (e.g. KNMI, 1996) also refer to the use of HYPO71.

The HYPO71 location algorithm (Lee and Lahr, 1972) was used by KNMI from 1991 to approximately 1998, while the HYPOCENTER algorithm (Lienert et al., 1986) was its immediate successor. Both methods are iterative linearised inversions. The exact date of change is unknown.

The labelling of the location methodology in the Groningen induced seismicity bulletin may therefore be incorrect/inconsistent for some events. Until approximately 1998, events should be labelled as using HYPO71 (assuming this methodology was used). After this, events should be labelled as having used the HYPOCENTER method. The 'Hypo91' labelling would then be redundant. The exact date of transition from HYPO71 to HYPOCENTER is not well established

within KNMI based on our communication. It was reported to NORSAR that the change was tested such that the new methodology delivers results consistent with the old results.

It should be noted that both location algorithms are iterative linearised inversions, and are fundamentally very similar methods. The HYPOCENTER algorithm is in part designed to address limitations in HYPO71. A comparison table listing the most important features for the two location algorithms is listed within Lienert et al. (1986). One significant feature of the HYPOCENTER algorithm is the adaptive damping, which ensures that any iteration that produces an increase in rms residual is repeated with a higher damping value. This helps to ensure results produced by HYPOCENTER have smaller residuals than HYPO71. Additionally, the depth for HYPOCENTER is initially fixed until a stable lateral location is achieved, after which the depth can then optionally be solved for. In contrast, HYPO71 can have a fixed depth or is solved for with the lateral location simultaneously. As stated by Lienert et al. (1986), HYPO71 tends to leave starting depths unchanged. For KNMI, the difference in how each of these algorithms solve for earthquake depth is moot with regard to induced seismicity at Groningen, since these events are set by KNMI to a default depth of 3 km - corresponding to the average depth of the gas reservoir (Spetzler and Dost, 2017).

From the 1126 events in the Groningen induced seismicity catalogue, only four events have been given depths that are not set at 3 km. These are listed in table 3 and is shown in figure 4.10.

**Table 3:** List of events with depths not set to the default value of 3 km. A map of these events is shown in figure 4.10

| Event id     | Date and time          | Latitude | Longitude | Magnitude ( $M_L$ ) | Depth (m) |
|--------------|------------------------|----------|-----------|---------------------|-----------|
| knmi1994oukb | 1994-07-30 09:18:20.78 | 53.351   | 6.628     | 2.72                | 1000.0    |
| knmi1994oulf | 1994-07-30 09:53:29.68 | 53.365   | 6.577     | 1.27                | 1000.0    |
| knmi2000dagi | 2000-02-12 19:48:10.61 | 53.321   | 6.822     | 1.67                | 3500.0    |
| knmi2008jtdy | 2008-05-18 13:23:46.14 | 53.375   | 6.728     | 2.17                | 2800.0    |

Knowledge of earthquake depths at Groningen is important for understanding the seismic hazard, because the maximum possible magnitude will change depending on the depth of the earthquake due to changes in the lithology and elastic properties. In practice, establishing depths for small magnitude earthquakes recorded on a regional network is not trivial. We discuss this issue further in section 4.2.10. However, it is important to note that without multiple phases (e.g. P and S-waves), and without arrival-time observations from stations close to the epicentre (i.e. at a distance less than the earthquake depth), then the depth will not be resolvable.

KNMI currently fix event depths at 3 km - the average reservoir depth. However, KNMI have also recently shown that there are a minority of events occurring both above and below the reservoir. Establishing correct event depth is important for understanding the seismic hazard at Groningen.

Fixing the depth to 3 km could be considered a limitation in current KNMI procedures, given its im-

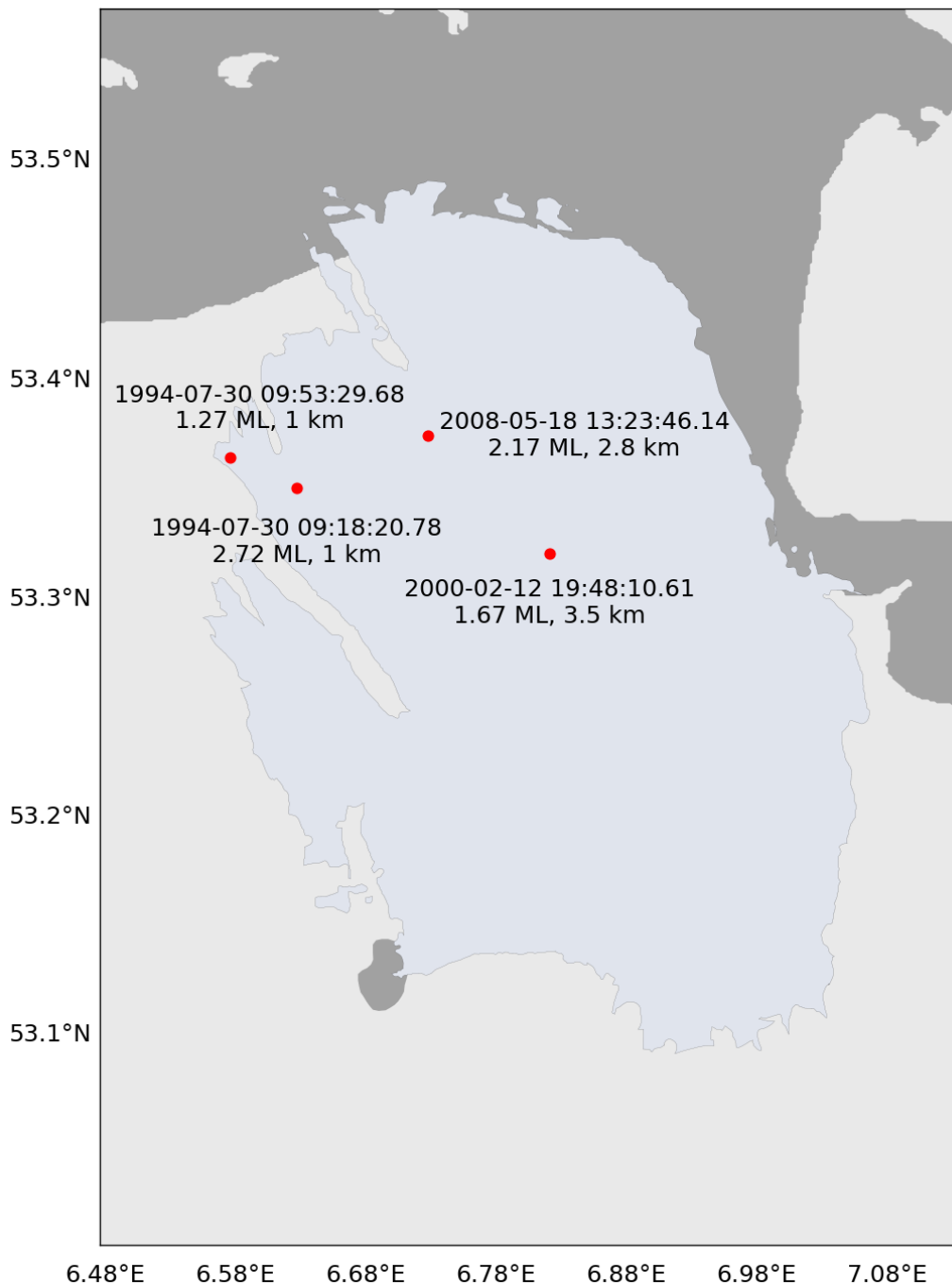


**Fig. 4.10:** Events from the Groningen induced seismicity catalogue with depths not set at the default 3 km. Date, time, magnitude and depth are displayed.

portance. However, it is common practice by seismological observatories (Havskov et al., 2012) and understandable given the difficulties in resolving the depth. Research into Groningen induced seismicity by Pickering (2015) using deep borehole sensors installed by NAM (in wells ZRP and SDM), which have better resolving power for depth, revealed upper and lower bounds of 3020 m and 2822 m respectively, based on one standard deviation from the mean depth (2921 m), from a dataset of 32

events. These values lie within the reservoir, and provide a good basis for using a depth of 3 km when fixing the event depth due to lack of resolvability. Further research by KNMI (Spetzler and Dost, 2017) to better resolve event depths using the increased station network (from February 2014 to July 2016) showed depth ranges between 2200 m and 3500 m, with the majority between 2600 m and 3200 m (reservoir depth). This demonstrates that events (albeit the minority) are occurring outside the reservoir layer. A thorough assessment and reprocessing of the Groningen induced seismicity catalogue is needed to establish which events have the potential to have their depth better constrained using available data.

#### 4.2.4 Velocity model

The choice of velocity model for can dramatically change both the accuracy and the precision of event locations. For the Groningen induced seismicity bulletin, KNMI have reported that only a single 1D velocity model was used for event location - known as the 'Northern Netherlands' model (KNMI, pers. comm., 2018). However, the reported velocity model within the bulletin shows some variation. Figure 4.11 shows the distribution of reported velocity model names with time, and figure 4.12 shows the spatial distribution. These figures show, firstly, that there was a change in name for how the the velocity model was recorded from 'North' to 'Northern\_Netherlands' - this occurs when processing was moved to the SeisComp3 platform in 2015. More significantly, however, is that there are ten events that are labelled as using a velocity model named 'South', and one event that is labelled as using 'Explo'. These events are listed in table 4. Events that use the 'Explo.' velocity model correspond to mining events or NAM dynamite explosions, with the velocity model differing in the near surface. The 'South' velocity model is used for tectonic events in the south of the Netherlands. According to KNMI, neither of these velocity models should be used for events within the Groningen field. It is unclear whether these events have been mislabelled, or whether they were located with the incorrect velocity model.

Due to the effect on event locations, we have also checked additional events from the full induced seismicity catalogue that were located outside but close to the Groningen field. We found no additional events were labelled as using the incorrect velocity model within 10 km of the Groningen field.

For the S-wave arrivals, KNMI have reported that a constant  $V_p/V_s$  value is used for the Northern Netherlands model.

#### 4.2.5 Arrival-time data

Knowledge of the arrival-time data that is used as input into any location algorithm is critical for understanding and assessing the reliability and quality of event locations. For the Groningen induced seismicity bulletin, NORSAR have analysed the arrivals that are associated with each published event

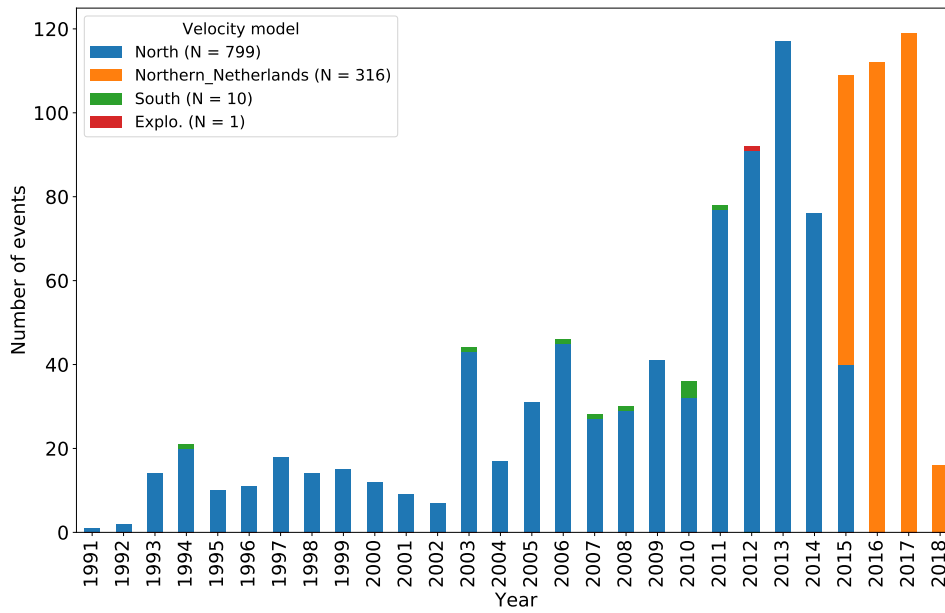


**Fig. 4.11:** Histogram showing the names of the reported velocity model that were used for event location. 'North' and 'Northern\_Netherlands' only represent a name change - the velocity models are identical.

**Table 4:** List of events with velocity models not labelled as using the Northern Netherlands model. All events have fixed depths of 3 km.

| Event id     | Date and time          | Latitude | Longitude | Magnitude ( $M_L$ ) | Velocity model |
|--------------|------------------------|----------|-----------|---------------------|----------------|
| knmi1994kzir | 1994-06-06 04:08:26.16 | 53.156   | 6.823     | 1.03                | South          |
| knmi2003synz | 2003-09-27 13:57:54.15 | 53.348   | 6.697     | 2.71                | South          |
| knmi2006gpwq | 2006-04-05 01:41:09.76 | 53.344   | 6.890     | 1.44                | South          |
| knmi2007bguc | 2007-01-18 22:29:44.29 | 53.274   | 6.767     | 0.88                | South          |
| knmi2008okgj | 2008-07-23 20:05:12.97 | 53.212   | 6.663     | 1.23                | South          |
| knmi2010jvzn | 2010-05-21 02:34:09.18 | 53.281   | 6.870     | 0.90                | South          |
| knmi2010kfxm | 2010-05-26 12:53:59.07 | 53.235   | 6.833     | 0.90                | South          |
| knmi2010knrn | 2010-05-30 18:58:36.12 | 53.238   | 6.678     | 1.50                | South          |
| knmi2010myil | 2010-07-04 01:58:04.72 | 53.251   | 6.800     | 0.80                | South          |
| knmi2011jsds | 2011-05-19 00:09:04.96 | 53.422   | 6.893     | 0.92                | South          |
| knmi2012lpsc | 2012-06-14 03:05:08.38 | 53.254   | 6.922     | 1.72                | Explo.         |

origin. Both the HYPO71 and the HYPOCENTER location algorithms use a 5 level weighting system for each arrival: (0.0, 0.25, 0.5, 0.75, 1.0). Arrivals with a weight of zero, are not used by the location algorithm, while those with values of '1.0' have the strongest influence on the location algorithm. These weights are manually set by the analyst based on a subjective measure of the pick quality KNMI, pers. comm. (2018). The HYPOCENTER method does allow additional weights to be applied

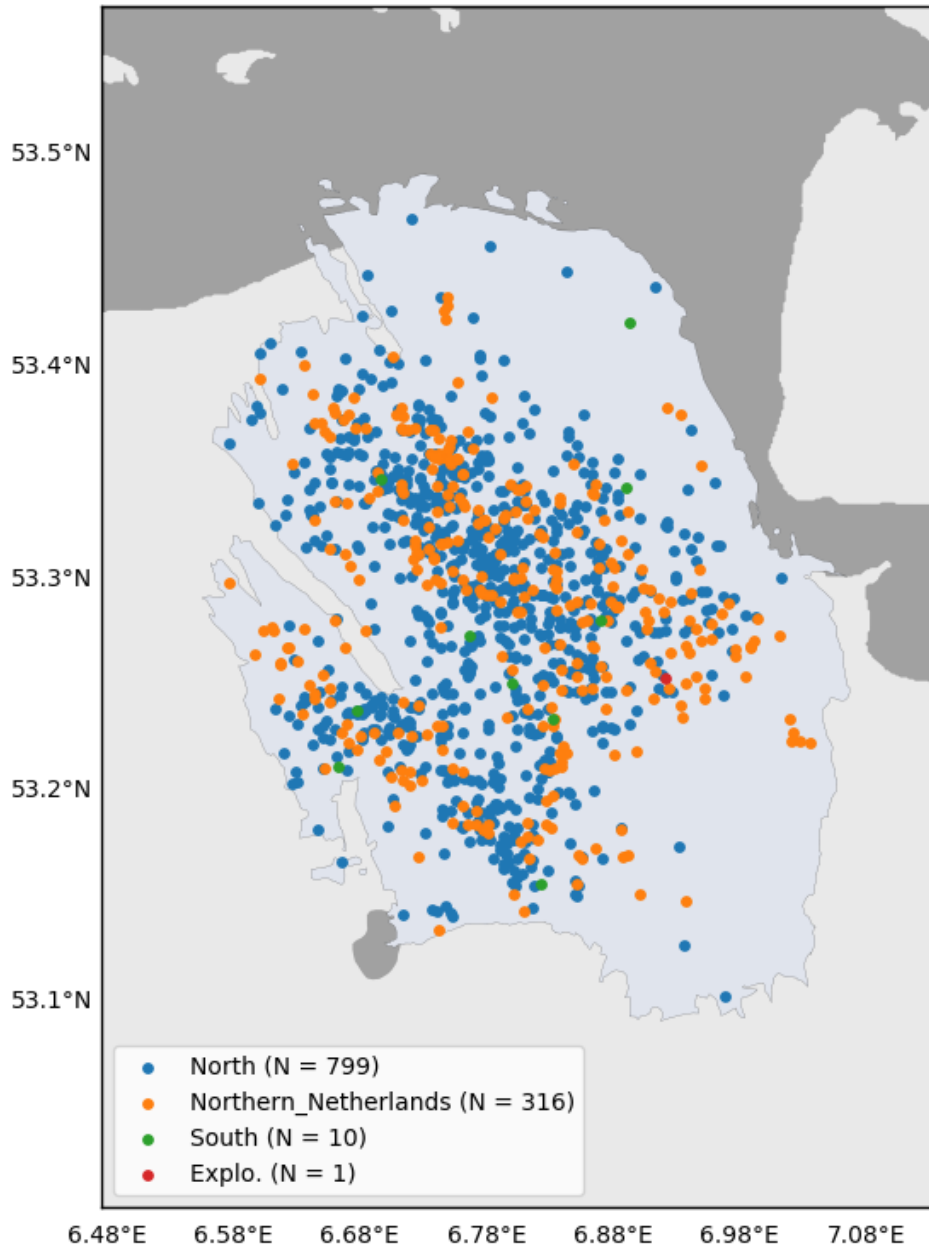


**Fig. 4.12:** Map showing the names of the reported velocity model that were used for each event location. 'North' and 'Northern\_Netherlands' only represent a name change - the velocity models are identical.



based on additional criteria, but it is understood that these have not been implemented (based on the publicly available weight values).

Arrivals are given a weight of either 0, 0.25, 0.5, 0.75 or 1, for use in the location algorithm. This is manually set based on a subjective assessment of data quality.

The Groningen induced seismicity bulletin contains a significant number of arrivals that have been assigned zero weight. These are shown in figure 4.13. NORSAR have excluded these arrivals in the further analysis since they are not used to locate the events. Notably, there is a single event published from 1991, for which all ar-

rivals have been given a weight of zero (Table 5). With all arrivals labelled having zero weight, there is no information available about what arrivals were used to actually locate this event. This is likely due to a labelling error in the bulletin. Similarly, we have also analysed the pick data. All arrivals that have been used for event location, should have corresponding pick data. This includes the pick time used as input for the event location, in addition to information about the station and channels used. We have found that one event in 1997 (Table 6) is missing pick data: out of 8 arrivals (4 P-waves and 4 S-waves), there are only 2 P-wave picks available.

**Table 5:** Details of event with all its published arrivals set to zero weight. This suggests a labelling error for this event's arrivals.

| Event id     | Date and time          | Latitude | Longitude | Magnitude ( $M_L$ ) | Depth (m) |
|--------------|------------------------|----------|-----------|---------------------|-----------|
| knmi1991xtow | 1991-12-05 00:24:55.00 | 53.358   | 6.657     | 2.4                 | 3000.0    |

**Table 6:** Details of event with missing picks. Out of 8 arrivals used for the event location (4 P-wave and 4 S-waves), only information for 2 P-wave picks exist.

| Event id      | Date and time          | Latitude | Longitude | Magnitude ( $M_L$ ) | Depth (m) |
|---------------|------------------------|----------|-----------|---------------------|-----------|
| knmi1997idile | 1997-02-17 07:20:55.23 | 53.387   | 6.752     | 1.6                 | 3000.0    |

The number of non-zero weighted arrivals (i.e. those used for event location) within the Groningen induced seismicity bulletin are shown in figure 4.14. This shows a relatively equal number of P and S-wave arrivals until 2014. From 2014, the station density started to increase with the deployment of the shallow borehole network. Currently, KNMI only use P-wave arrivals to locate events. This is because the quality of the S-waves is regarded as too low quality for accurate arrival-times. With better station coverage from 2014, the number of S-waves used for event location was reduced due to the greater availability of higher quality P-waves. This approach makes sense in the context of fixing event depths to 3 km. However, the increase in station coverage also provides the means to

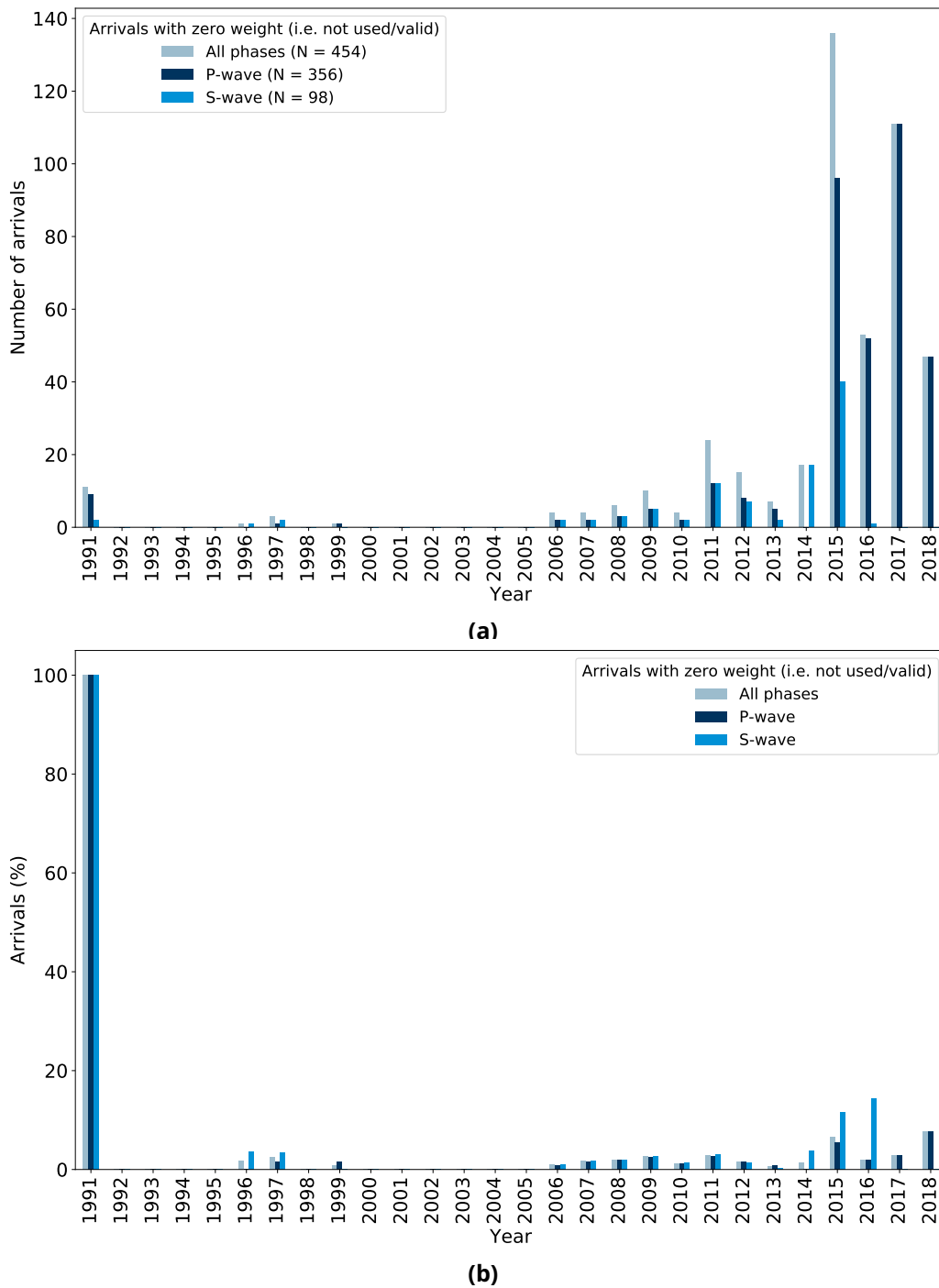


**Fig. 4.13:** Arrivals from the Groningen induced seismicity bulletin with weights set to zero. These arrivals are excluded in further analyses of data quality. (a) shows the absolute number of arrivals set to zero weight per year, while (b) shows the percentage of arrivals per year set to zero weight.

better constrain the event depths, which would significantly benefit from the inclusion of S-waves, depending on data quality.

The number of arrivals per event is shown in figure 4.15. This shows a relatively consistent number

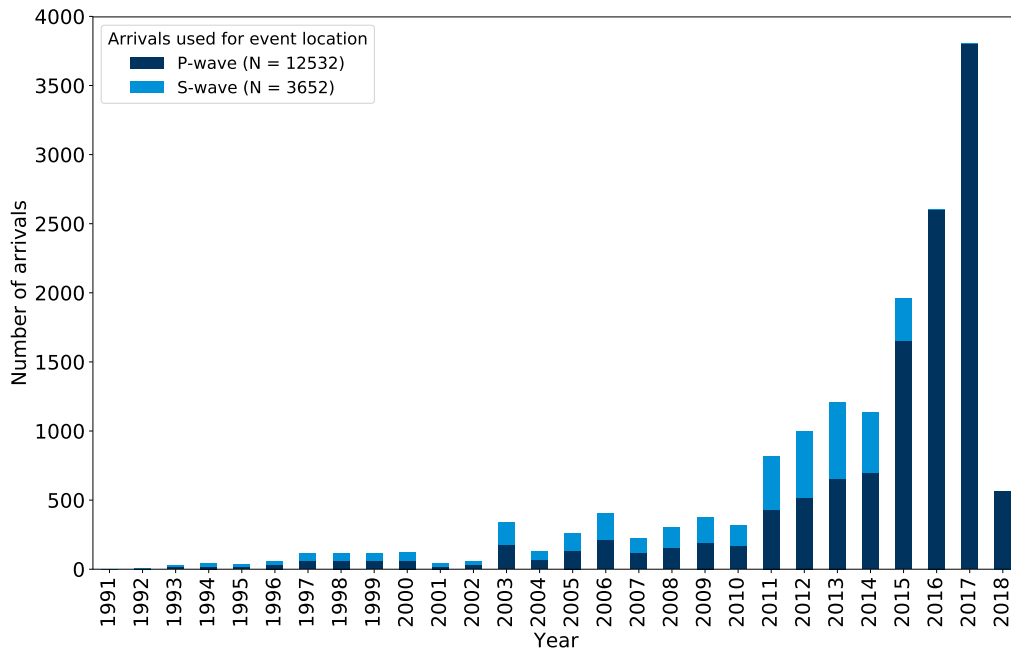


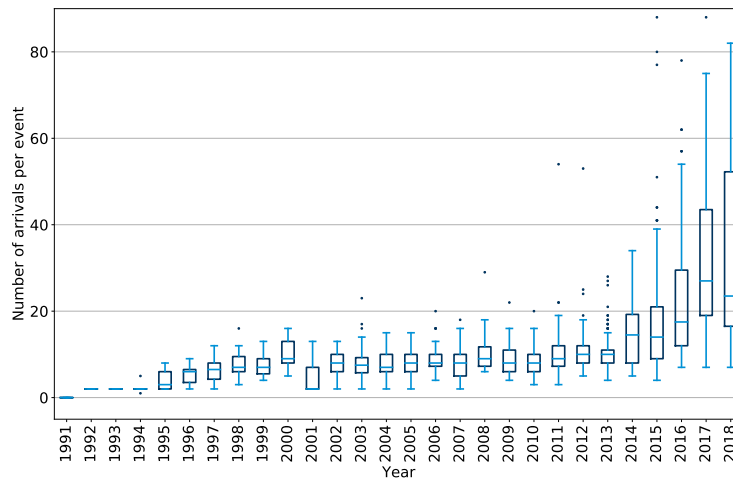
**Fig. 4.14:** Histogram showing the number of arrivals per year used for locating events in the Groningen induced seismicity catalogue.

of arrivals per event from 1995 to 2013. From 2014 with the increases to the station network, the overall number of arrivals per event increases. This is despite the number of S-wave arrivals being completely phased out, as they are overly compensated by the availability of P-wave data.

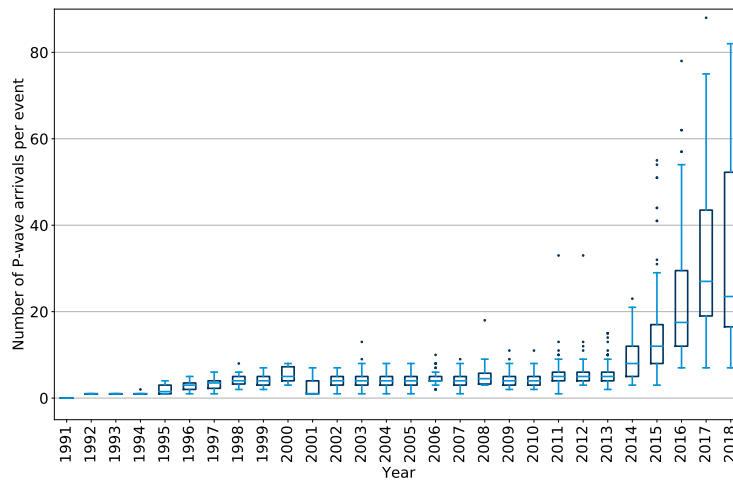
#### 4.2.6 Station contributions

We have also examined which stations are contributing arrival-time data. This is shown in figures 4.16–4.18, which show the station contributions for all arrivals, P-wave arrivals, and S-wave arrivals, respectively. This highlights the benefits that the G-network has brought since 2014 in terms of contributing arrivals. Moreover, it highlights how few stations were contributing prior to the network expansion. From the total of 187 different stations that are labelled as having contributed to arrivals within the Groningen induced seismicity bulletin, only 9 stations have contributed data for at least 10 years. These are ENM4, ENV4, FSW4, HWF4, VBG4, VLW4, WDB4, ZL24, and ZLV4; their location is shown in figure 4.19. It should be noted that ZL24 and ZLV4 have the same latitude and longitude coordinates but represent different depths within a borehole deployment. A map showing all stations, and the total number of arrivals is shown in figure 4.20. A sub-region excluding the most distant stations is shown in figure 4.21, and we also show the effect of the G-network within that figure.

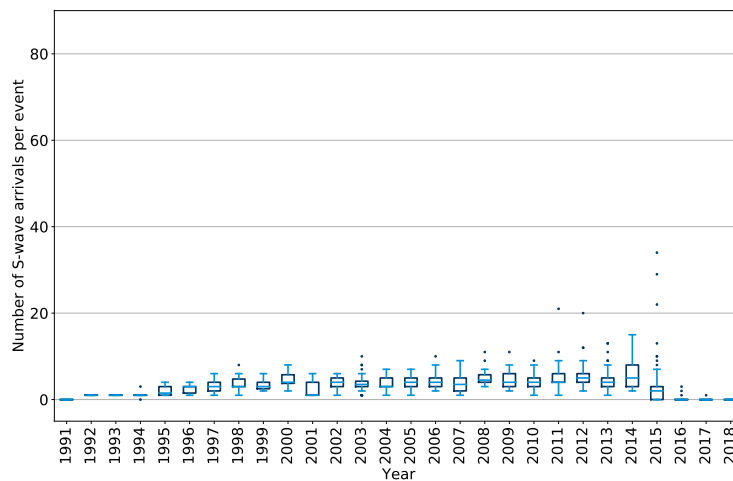
Station coordinates were obtained from KNMI’s publicly available [webservice](#). However, there were 38 stations that had no available information within this webservice, despite the stations being used in the Groningen induced seismicity bulletin. Four of these are stations that have been mislabelled (G30, G34, FSW and WDB), so their coordinates can be determined (using G300, G340, FSW1, and



(a)



(b)



(c)

**Fig. 4.15:** Box plots showing the number of arrivals per event for each year. (a) shows all arrivals; (b) shows P-wave arrivals; and (c) shows S-wave arrivals.

WDB1 respectively). One station belonging to the Belgian network (MEM), could be retrieved from the ORFEUS webservice ([www.orfeus.eu.org](http://www.orfeus.eu.org)), and two stations (BUG and TNS) could be retrieved from the International Seismological Centre's (ISC) station registry ([www.isc.ac.uk/registries/search](http://www.isc.ac.uk/registries/search)). A list of all 38 stations missing from KNMI's station database is shown in table 7, together with the number of events for which they have arrivals, and their total number of arrivals.

38 stations that contribute to arrivals within the Groningen induced seismicity bulletin are not available from KNMI's webservices. 3 of these could be retrieved from alternative sources (ORFEUS, ISC), and 4 were mis-named.

The network code for the 31 stations with no data availability (from any searched public source) are all labelled as 'XX', instead of the Netherlands' usual network code of 'NL'. KNMI have reported that these missing stations are from temporary networks, and that their timing and orientation were such that they were unreliable, so not included into KNMI's station inventory

(KNMI, pers. comm., 2018). However, if the data validity is questionable, it is a cause for concern that it is being used for event locations whilst the station data is not publicly available. KNMI have also reported that a check was done for timing errors at these stations by checking the time synchronisation; timing errors were then accounted for by using P-S times, instead of absolute travel-times. Whilst this is reassuring, it raises further questions about the location methodology, as it is not possible from the bulletin data to determine when arrivals were used using their absolute arrival-times, or using P-S arrival-times e.g. was it only when stations exhibited timing errors, was it every time good quality P and S-wave picks could be made at a station, was it adhoc, or were other criteria applied?

#### 4.2.7 Station distribution

Critical to understanding the location uncertainty is knowledge of the number of station used per event and their distance and azimuthal distribution. We have already shown in figure 4.19, how the stations that are contributing for the most significant time are located largely

Station count, event-station distance, and azimuthal gap are all important metrics for determining the quality of the event location.

outside the Groningen field (i.e. large distances), and with no stations in the north-east. Bondár et al. (2004) determined a set of criteria for local networks such that the epicentral location will be located with a 5 km accuracy (at the 95% confidence level). These criteria are that the event was located:

1. with at least 10 stations, all within 250 km;
2. with an azimuthal gap of less than 110°;
3. a secondary azimuthal gap of less than 160°;
4. at least one station within 30 km from the epicentre

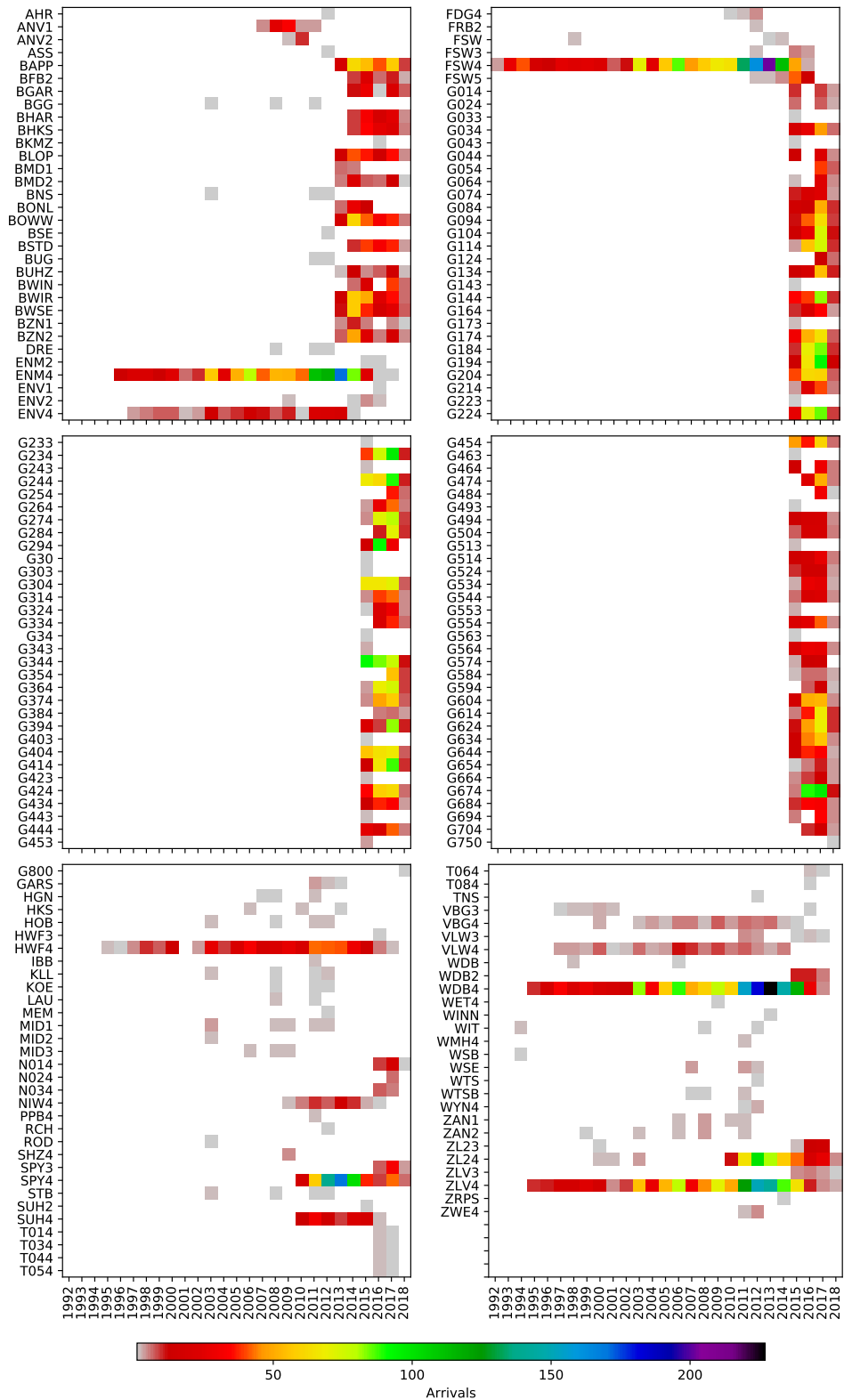


**Fig. 4.16:** Total arrivals per year for each station within the Groningen induced seismicity bulletin. A map of the station locations is shown in figure 4.20.

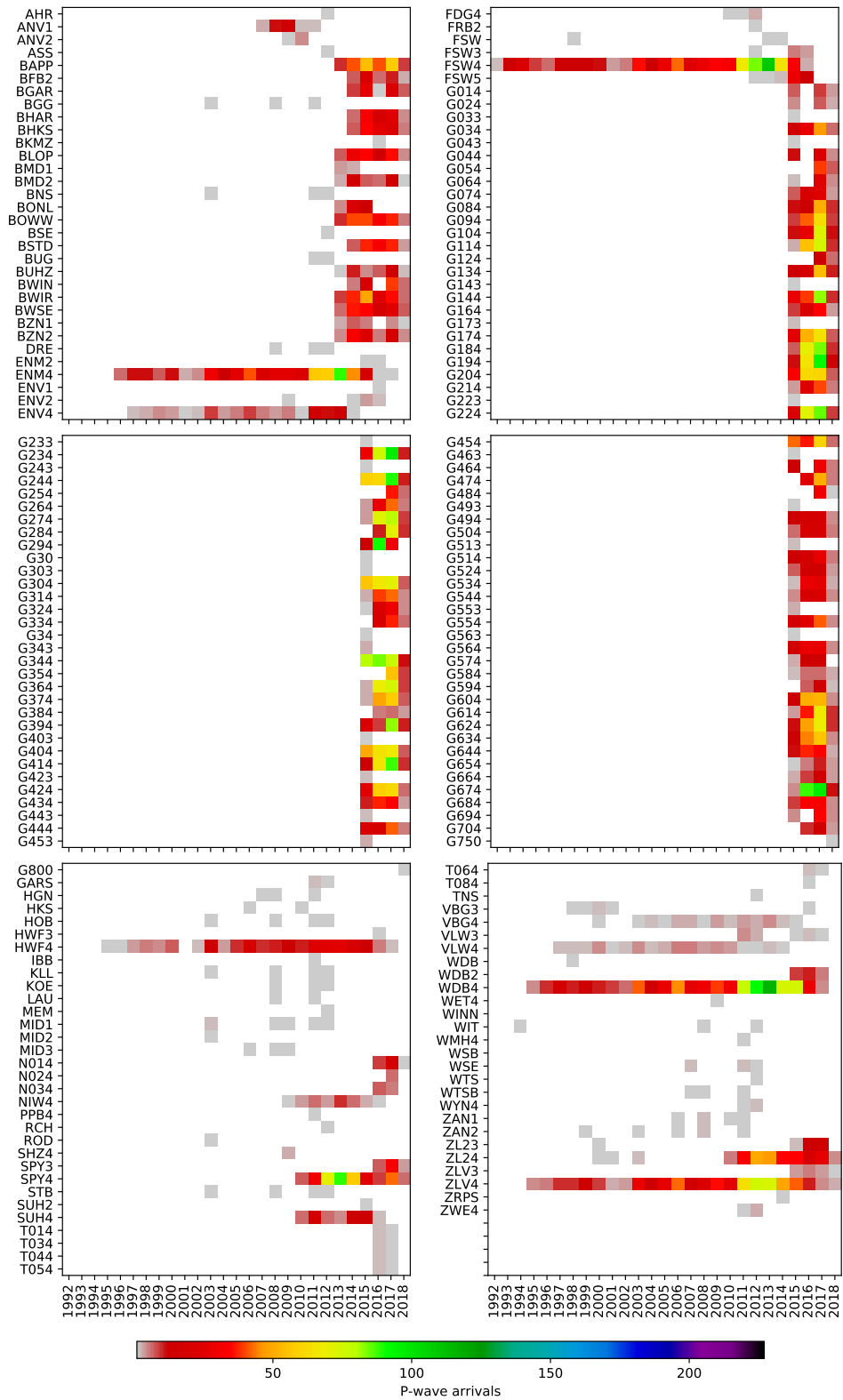


**Fig. 4.17:** Total P-wave arrivals per year for each station within the Groningen induced seismicity bulletin. For comparison purposes, the colour bar is scaled to the maximum from all arrivals (figure 4.16).

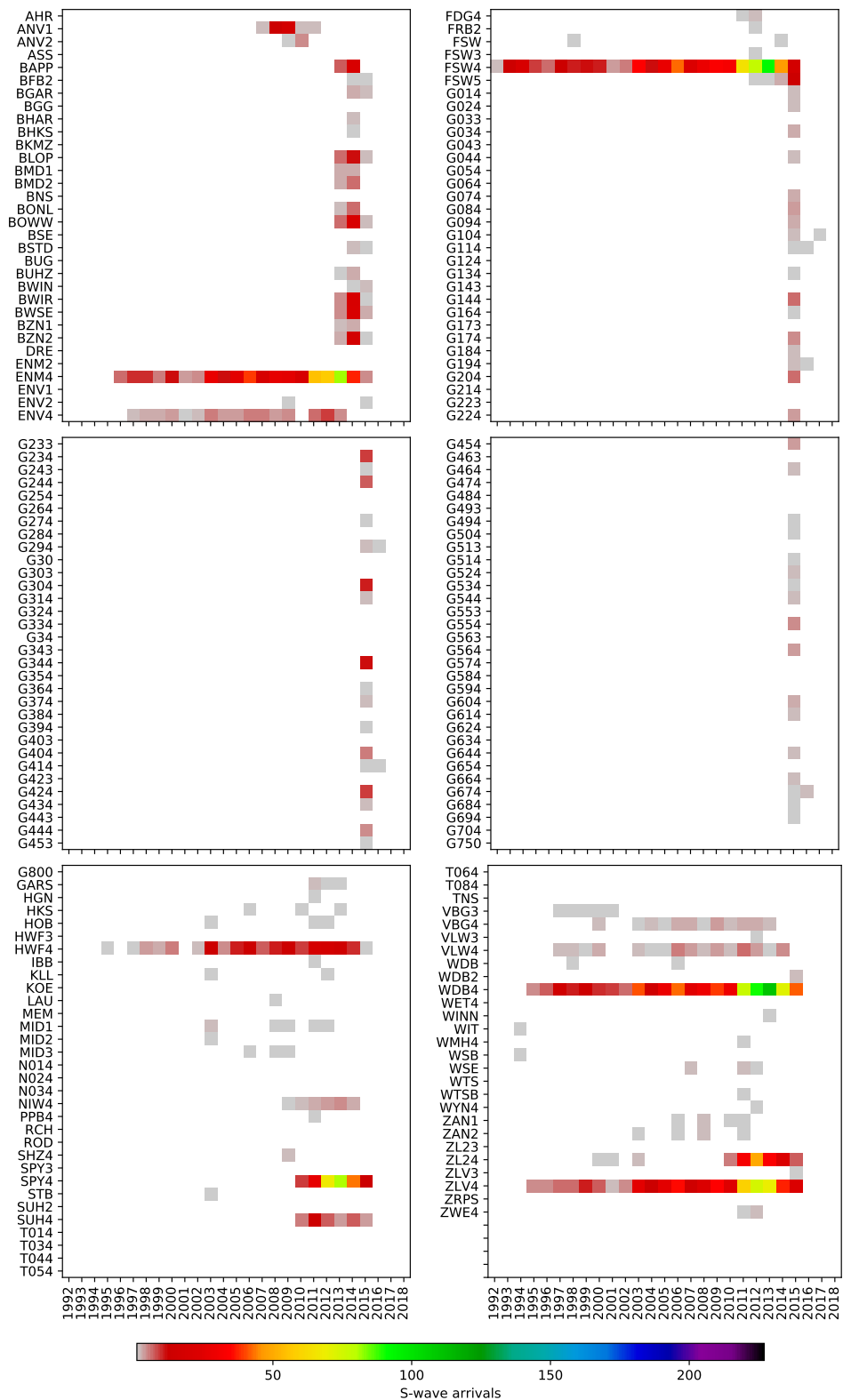


**Fig. 4.18:** Total S-wave arrivals per year for each station within the Groningen induced seismicity bulletin. For comparison purposes, the colour bar is scaled to the maximum from all arrivals (figure 4.16), and it includes stations where there were no S-wave arrivals.



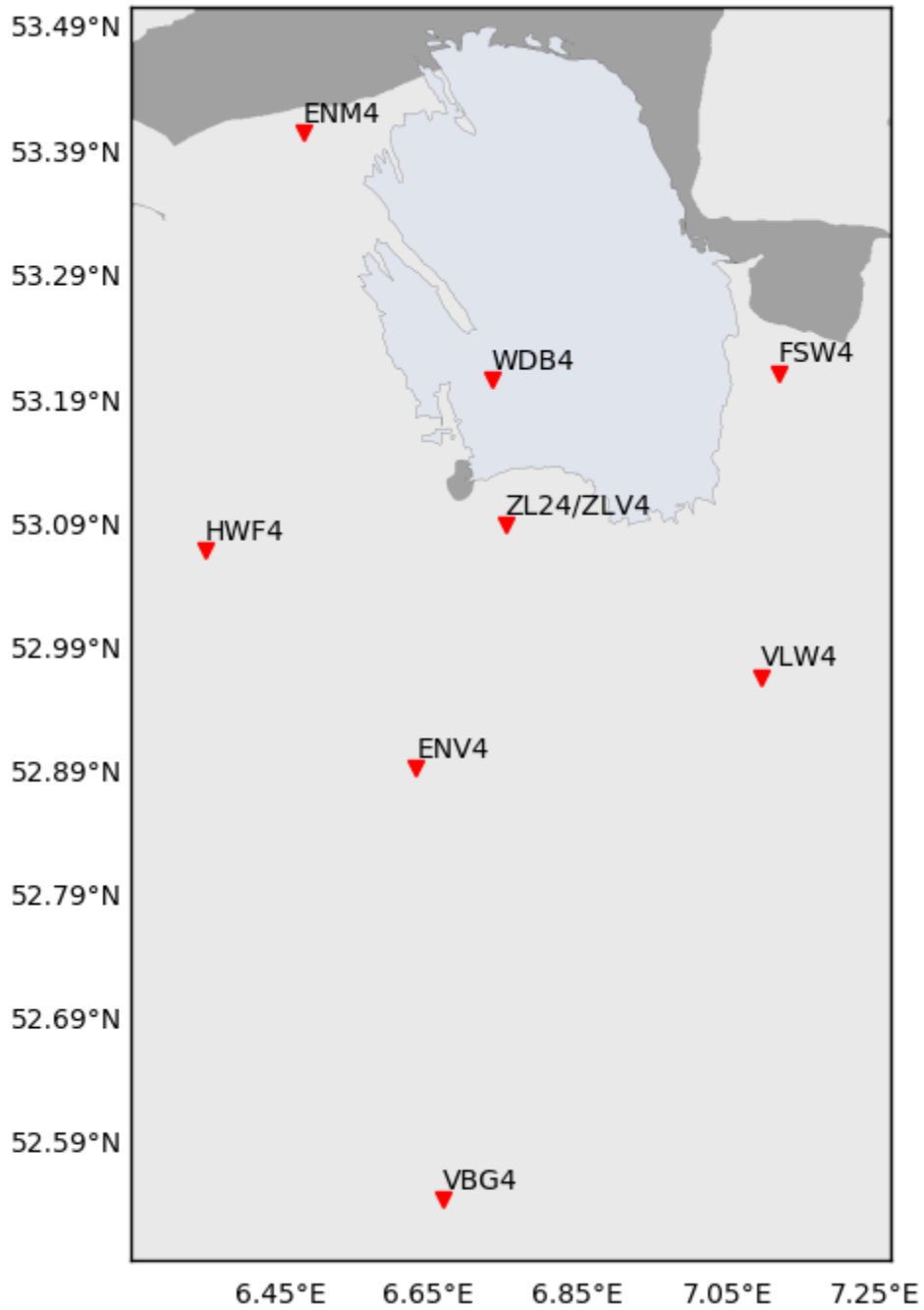


**Fig. 4.19:** Stations contributing to arrivals for at least 10 years (see figure 4.16).

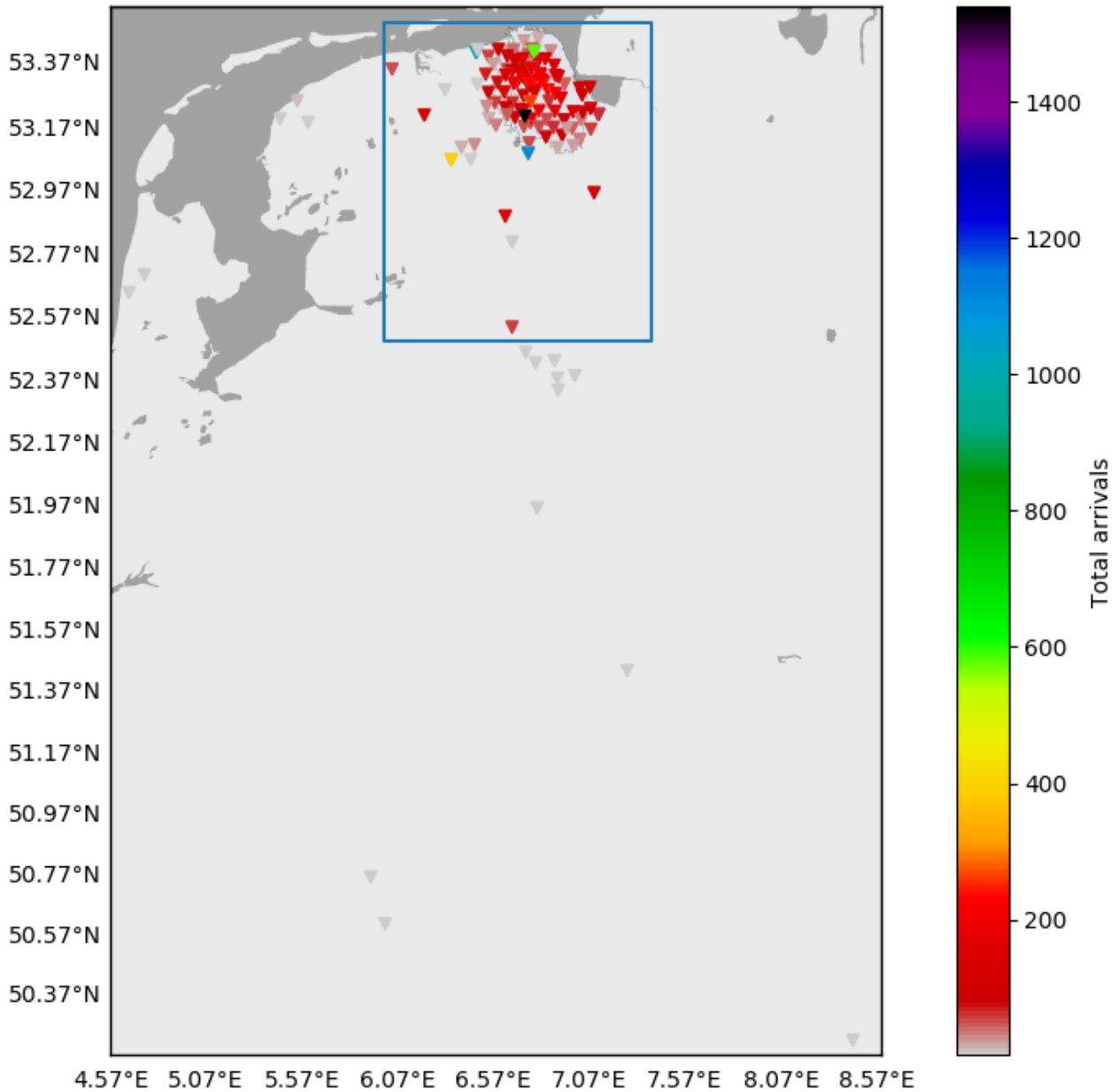


**Fig. 4.20:** Map of all stations contributing to arrivals from the Groningen induced seismicity bulletin. The stations are coloured by total number of arrivals contributed. See figure 4.16 for number of arrivals by year. The blue box shows the zoomed in region shown in figure 4.21. N.B. there are a total of 31 stations contributing arrivals, for which we are unable to obtain station coordinates; thus these cannot be shown in this Figure - see table 7.

**Table 7:** List of 38 stations that are contributing arrivals to the Groningen induced seismicity bulletin with data and information that are not directly available from KNMI's webservices. The station name and network name are as they are labelled in the bulletin. The top seven stations have been grouped into three as they do have available station information from external sources - see text for details.

| Station code | Network code | Number of events with arrivals | Timespan of events (years) | Number of P-wave arrivals | Number of S-wave arrivals | Total arrivals |
|--------------|--------------|--------------------------------|----------------------------|---------------------------|---------------------------|----------------|
| MEM          | BE           | 1                              | 1                          | 1                         | 0                         | 1              |
| BUG          | GR           | 2                              | 2                          | 2                         | 0                         | 2              |
| TNS          | GR           | 1                              | 1                          | 1                         | 0                         | 1              |
| FSW          | XX           | 3                              | 3                          | 3                         | 2                         | 5              |
| G30          | XX           | 1                              | 1                          | 1                         | 0                         | 1              |
| G34          | XX           | 1                              | 1                          | 1                         | 0                         | 1              |
| WDB          | XX           | 2                              | 2                          | 1                         | 2                         | 3              |
| AHR          | XX           | 1                              | 1                          | 1                         | 0                         | 1              |
| ANV1         | XX           | 37                             | 5                          | 35                        | 36                        | 71             |
| ANV2         | XX           | 6                              | 2                          | 6                         | 6                         | 12             |
| ASS          | XX           | 1                              | 1                          | 1                         | 0                         | 1              |
| BGG          | XX           | 3                              | 3                          | 3                         | 0                         | 3              |
| BNS          | XX           | 3                              | 3                          | 3                         | 0                         | 3              |
| BSE          | XX           | 1                              | 1                          | 1                         | 0                         | 1              |
| DRE          | XX           | 3                              | 3                          | 3                         | 0                         | 3              |
| FRB2         | XX           | 1                              | 1                          | 1                         | 1                         | 2              |
| GARS         | XX           | 4                              | 3                          | 3                         | 4                         | 7              |
| HKS          | XX           | 3                              | 3                          | 2                         | 3                         | 5              |
| HOB          | XX           | 4                              | 4                          | 4                         | 3                         | 7              |
| IBB          | XX           | 1                              | 1                          | 1                         | 1                         | 2              |
| KLL          | XX           | 4                              | 4                          | 4                         | 2                         | 6              |
| KOE          | XX           | 3                              | 3                          | 3                         | 0                         | 3              |
| LAU          | XX           | 2                              | 2                          | 2                         | 1                         | 3              |
| MID1         | XX           | 6                              | 5                          | 6                         | 6                         | 12             |
| MID2         | XX           | 1                              | 1                          | 1                         | 1                         | 2              |
| MID3         | XX           | 3                              | 3                          | 3                         | 3                         | 6              |
| RCH          | XX           | 1                              | 1                          | 1                         | 0                         | 1              |
| ROD          | XX           | 1                              | 1                          | 1                         | 0                         | 1              |
| SHZ4         | XX           | 3                              | 1                          | 3                         | 2                         | 5              |
| STB          | XX           | 4                              | 4                          | 4                         | 1                         | 5              |
| WET4         | XX           | 1                              | 1                          | 1                         | 0                         | 1              |
| WINN         | XX           | 1                              | 1                          | 0                         | 1                         | 1              |
| WSB          | XX           | 1                              | 1                          | 0                         | 1                         | 1              |
| WSE          | XX           | 5                              | 3                          | 5                         | 5                         | 10             |
| WTS          | XX           | 1                              | 1                          | 1                         | 0                         | 1              |
| ZAN1         | XX           | 5                              | 4                          | 5                         | 5                         | 10             |
| ZAN2         | XX           | 6                              | 5                          | 6                         | 5                         | 11             |
| ZRPS         | XX           | 1                              | 1                          | 1                         | 0                         | 1              |

The criteria of station to event distances of less than 250 km, is always likely to be satisfied in the case of Groningen, due to the relatively small magnitudes involved, resulting in weak signals at greater distances. Moreover, the last of these criteria helps to constrain the depth of crustal earthquakes.

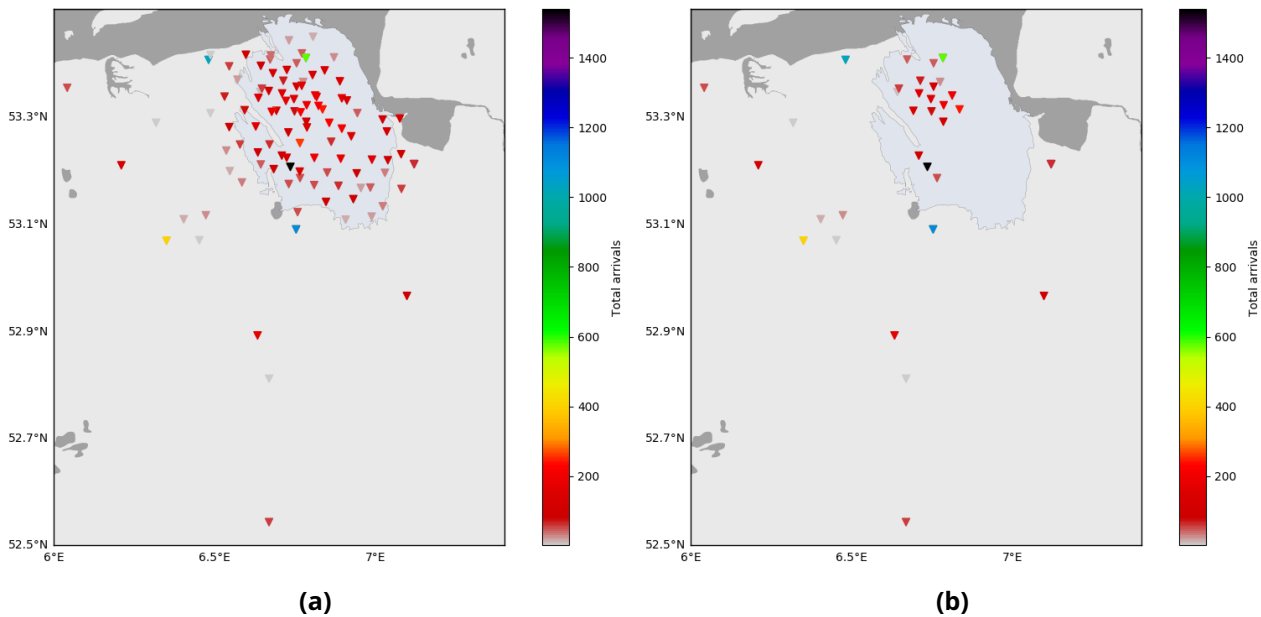


**Fig. 4.21:** Map showing a zoomed in region of figure 4.20. The total number of arrivals per station is shown. (a) shows all stations with the zoomed area; (b) is the same as (a), but excludes the G-network stations. N.B. there are a total of 31 stations contributing arrivals, for which we are unable to obtain station coordinates; thus these cannot be shown in this Figure - see table 7.

Since we are most interested in shallow induced earthquakes, this can be disregarded. Instead, Husen (2010), provide the following additional rules of thumb:

1. you need at least eight travel time arrivals, of which at least one is an S-wave arrival, and at least one was reported from a station within a focal depth's distance from the epicenter for a well constrained hypocentre location (Chatelain et al., 1980);
2. a correctly timed S-wave arrival recorded within 1.4 focal depths distance from the epicenter provides a unique constraint on focal depth (Gomberg et al., 1990).

While the rules pertaining to establishing focal depth are not relevant to directly understanding the existing location uncertainty within the Groningen induced seismicity catalogue, since the event depths are fixed during location, they are still a useful metric to help understand the potential for better establishing event depths.

It should be noted that event location uncertainty (i.e. latitude, longitude and depth uncertainty) is not reported with the Groningen induced seismicity bulletin or catalogue. Only an rms value from the residuals, is recorded, providing a goodness of fit for each event. It is understood that location uncertainties have been computed but they are stored internally at KNMI.

For the Groningen induced seismicity bulletin, an earthquake's origin is reported with different quality metrics. These include 'used station count'. However, the reported used station count does not match with what the station arrivals show. For example, if we count all stations used per event via

the arrivals, including those that have been given a weight of zero (N.B. we have excluded these in our other analyses of the arrivals in this section), then there are differences with the reported station count for 122 events (3 where the reported value is higher than shown by the arrival data, and 119 where the reported value is less). If we compare the reported used station count with the arrivals, with the zero weighted arrivals removed (as we have done for all other analysis of arrivals), then there are differences with the reported station count for 76 events (27 where the reported value is higher than shown by the arrival data, and 49 where the reported value is less). We have done further comparisons, removing arrivals where the residuals are stated as default values (i.e. nan), both with and without the combination of the zero weighted arrivals, but no combination provides a better comparison to the reported station count. N.B. these comparisons do not include the two events where either the picks or the arrivals are missing (see Tables 5 and 6), as we cannot determine the station count for these events. The consequence of the discrepancy is that either the reported arrivals or the reported station count is unreliable.

The KNMI reported 'used station count' is inconsistent with the station count obtained from the reported arrivals. Either the reported arrival data or the used station count is unreliable.

Figures 4.22 and 4.22 show the reported and manually determined station counts for each year. Overall, there is little difference in the statistics between them (despite the difference for 76 events). Significantly, up until 2012, there are cases where the station count (both reported and determined from the arrivals) is less

than 3. For the manually determined station count, this corresponds to 85 events - not including the event with missing arrivals in 1991 (see table 5). The criteria of Bondár et al. (2004), where events should be located with at least 10 stations all within 250 km, is not fulfilled until 2014, with the median station count not reaching this threshold until 2015. The minimum station count for some events has not met this threshold to date.

In addition to station count, the station to event distance is an important metric for determining the quality of the event location. The minimum, maximum and median station to event distances are recorded for the bulletin as 'quality metrics' but only after the processing was moved to the SeisComp3 platform in 2015. However, the individual station to event distances for

Event locations with station counts of less than 3 should be deemed unreliable. There exist 85 events with station counts of less than 3. The 10 station recommendation of Bondár et al. (2004) does not occur until 2014.

each arrival are recorded for the complete bulletin. All of these distances are recorded as epicentral distance in degrees; for ease of comparison, we convert this to kilometres. If we compare the minimum station distance as reported since 2015 (the latest 316 events), with the minimum station distance based on the arrivals (ignoring zero weighted arrivals), there is a discrepancy for two events,

of 20 m and 29 m respectively. These are small discrepancies but suggest possible inconsistencies in the processes. For the maximum station distance, there is a discrepancy for 33 events. These discrepancies range from 0.5 m to 82 km (with a median discrepancy of 5.7 km). For the event with the 82 km discrepancy, the reported maximum distance is 107 m, while the maximum distance recorded within the arrivals is 25 km. This arrival corresponds to station ZL24. Manually checking the station coordinates for ZL24, also provides a maximum station distance of 25 km for this event. This suggests that either the reported maximum distance in the quality metrics is wrong, or that there are missing arrivals.

There are also indications that the reported distances in the arrivals are not always reliable. Analysing the arrivals from all 1126 events, show that there are 57 that have station to event distances of exactly 0 km. Cross-checking with the station coordinates, confirms that this is inaccurate. Therefore to understand the station to event distances, we compute them directly from the available station coordinates, rather than the published distances. This will not take into account the stations for which we have no available coordinates available (see table 7). We plot these station to event distances (both the minimum and maximum) in figure 4.23. The guidelines outlined above by Husen (2010), state the need for at least one observation to be from a station within a focal depths distance from the epicentre, and an S-wave recorded within 1.4 focal depths distance from the epicentre, in order to constrain the focal depth. These values (3 km and 4.2 km respectively) are also plotted in figure 4.23a for reference. We observe that the median minimum distance drops below 4.2 km in 2014, and below 3 km in 2015, due to the expansion of the seismic network. However, this suggests that there is now sufficient station coverage for the depth to be more accurately determined i.e. a fixed depth of 3 km may not be required. Moreover, prior to 2014, whilst the median minimum station distance is much higher than the 3 km and 4.2 km guidelines, there are still events, which fall below these values, providing the potential for better depth constraints for a subset of the events.

Finally the azimuthal gap, strongly influences the lateral location uncertainty. The azimuthal gap is defined as the largest open azimuth between recording stations, and the secondary azimuthal gap is defined as the largest azimuthal gap filled by a single station (Bondár et al., 2004). Both these measurements provide information on the reliability of event locations, with the secondary azimuthal gap less susceptible to outliers that may exist from a single station. We plot the distribution of azimuthal gap in figure 4.25a and the the secondary azimuthal gap in 4.25b, together with the recommended maximum value as suggested by Bondár et al. (2004). It should be noted that the computation of both the primary and secondary azimuthal gaps did not include the stations where coordinates were not available, and for the case of azimuthal gap two stations are required, and for the case of secondary azimuthal gap, three stations are required.

From figure 4.25, we observe that the median azimuthal gap only drops consistently below  $110^\circ$  from 2015, while the median secondary azimuthal gap consistently drops below the recommended  $160^\circ$  in 2009. It is also noticeable that the secondary azimuthal gap shows reasonably acceptable values

throughout the catalogue period. However, these results must be interpreted in tandem with the station count distribution shown in figure 4.23, as events with less than 3 stations skew the statistics - as this has shown to be occurring up until 2015.

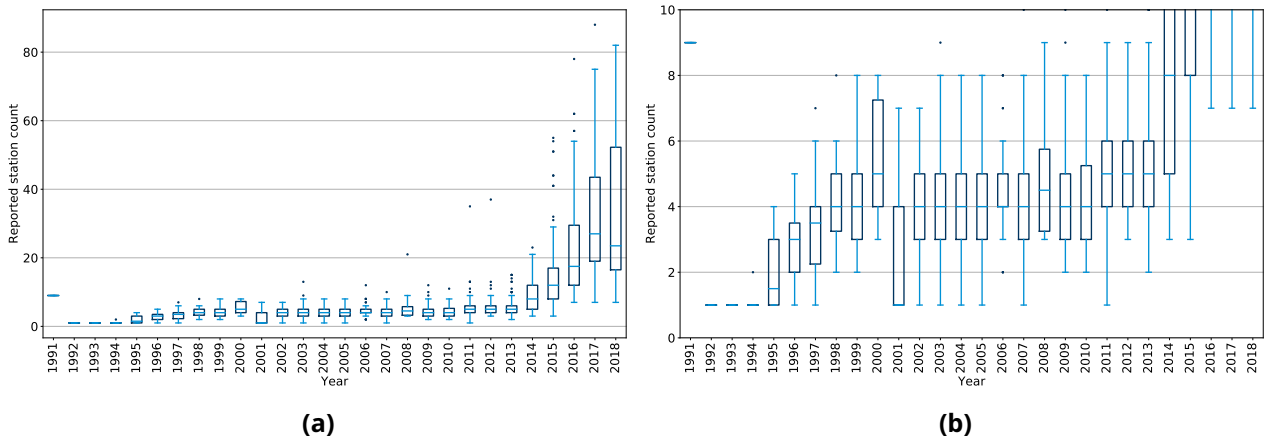


**Fig. 4.22:** Box plot of the station count as reported by KNMI for each year. (b) is a zoom in from 0 to 10 stations of (a). It should be noted that 1) these reported values do not match the station counts determined from the reported that arrivals data; 2) station counts of less than 3 should not be able to determine event locations.

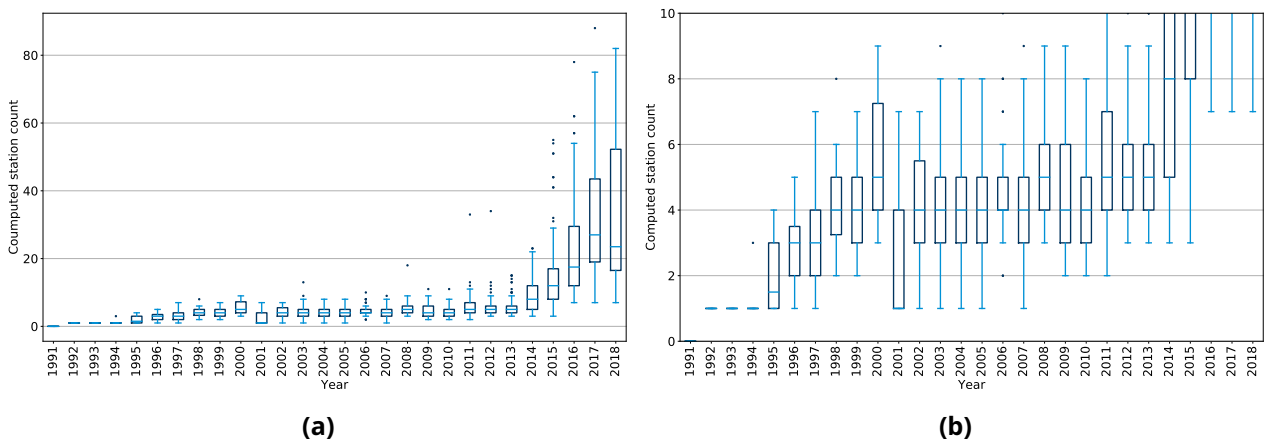
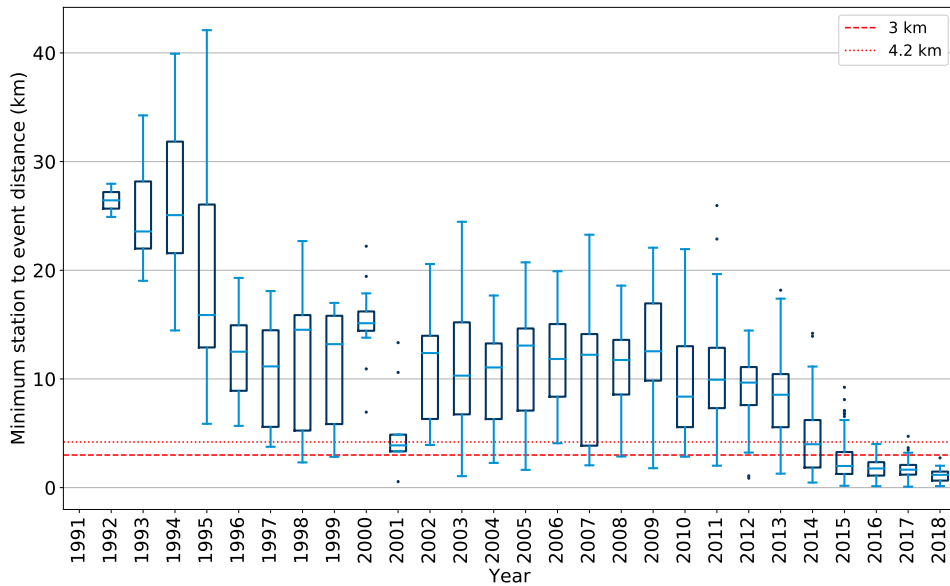


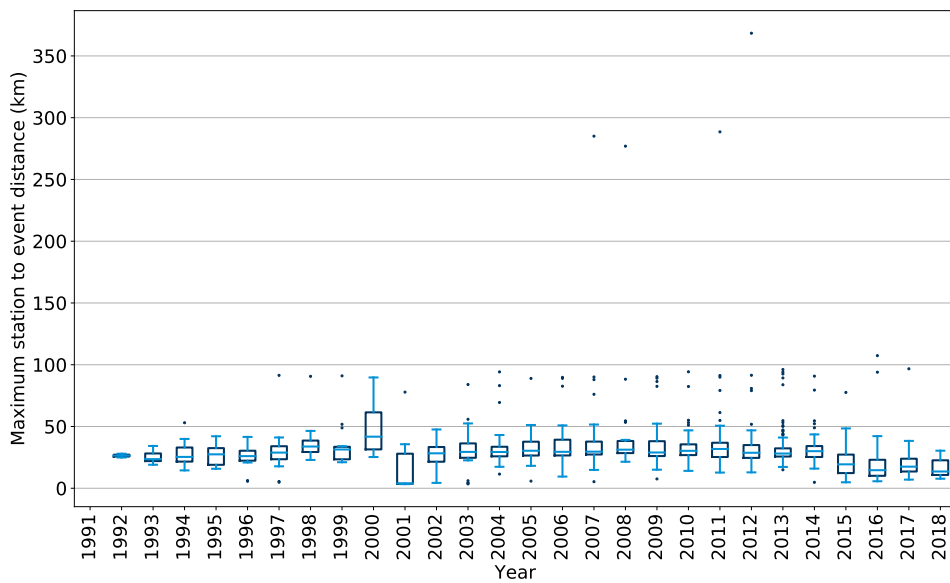
**Fig. 4.23:** Box plot of the station count computed from the arrivals for each year. (b) is a zoom in from 0 to 10 stations of (a). It should be noted that 1) these values do not match the station counts directly by KNMI; 2) station counts of less than 3 should not be able to determine event locations.

### 4.2.8 Station residuals

Directly linked to the arrival-time data that is used for the event location, are the travel-time residuals. This is the difference between the observed and the calculated travel-times after the event has been located. Thus, a travel-time residual close to zero indicates that the arrival-time at a given station is a good match to the velocity model, based on that event location. In analysing the residuals from the Groningen induced seismicity bulletin, we first checked for inconsistencies or possible errors in their



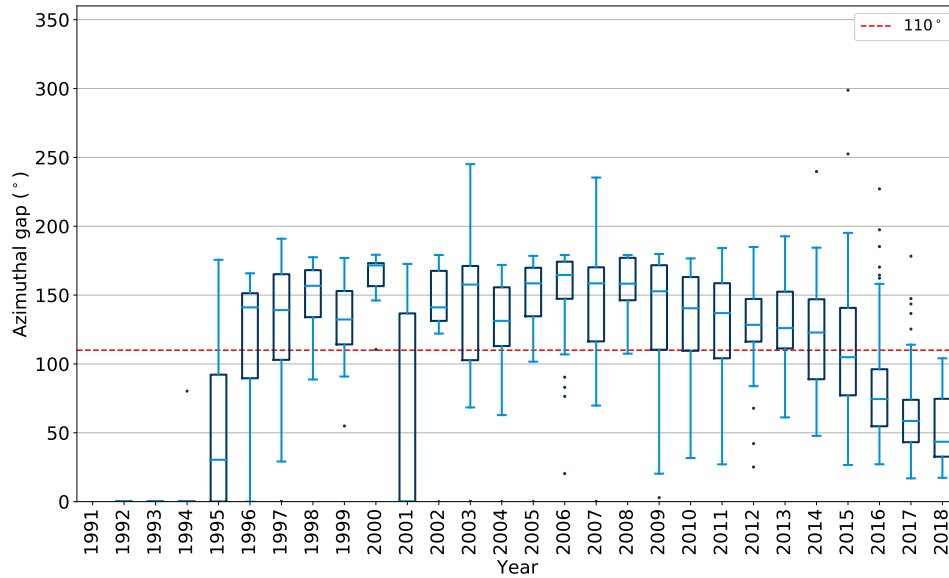
(a)



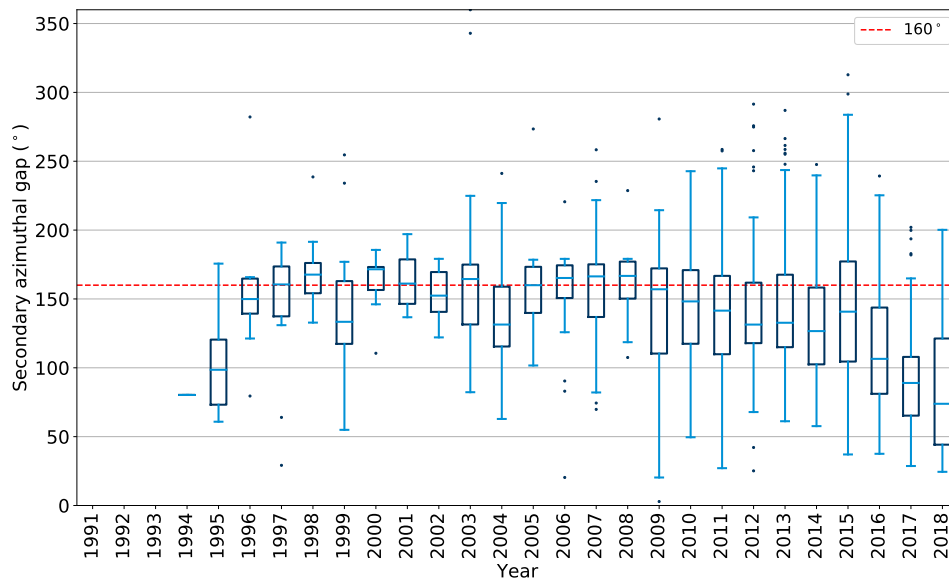
(b)

**Fig. 4.24:** Box plots of: (a) the minimum; and (b) the maximum station to event distances. The dashed and dotted red lines in (a), show a 3 km and 4.2 km epicentral distance respectively. These are key metrics for location uncertainty quality, corresponding to the likely event depth and  $1.4 \times$  the event depth as outlined by Husen (2010).





(a)



(b)

**Fig. 4.25:** Box plots of: (a) the azimuthal gap; and (b) the secondary azimuthal gap for the Groningen induced seismicity bulletin. The recommended maximum values suggested by Bondár et al. (2004) for accurate earthquake locations, are shown as red dashed lines.

values.

Two main peculiarities exist within for the travel-time residual data. Firstly, is the use of default values, where the residual is set to 99.99, which we will refer to as 'NaN' values. Secondly, there are examples where all residuals are set to zero seconds. In the case of Nan residuals, there are no events where all the residuals are set to 'NaN'. However, there are 81 events, where at least one residual is set to 'NaN'. The time distribution of these events is shown in figure 4.26. We also show the 'NaN' residuals in terms of arrivals in figure 4.27. This shows that the problem occurred during the period between 2003 and 2015, suggesting that with the introduction of SeisComp3 the issue was solved. Moreover, it also shows that both P and S-wave were affected but that it only impacted a minority of events within that period - with 2014 showing both the highest number of events and arrivals affected. In addition to the 'NaN' residuals, there exist 48 events where all the residuals are recorded as being zero seconds. If you consider P and S-wave arrivals separately, there are 49 events where all the P-wave residuals are zero seconds, and 52 events where all the S-wave arrivals are set to zero seconds. This is likely to be a error in the bulletin data. The distribution of these events is shown in figure 4.28, and shows that the problem affects a significant percentage of events between 1992 and 1996, and again in 2001, with the problem not existing for events after 2015.

Discarding the 'NaN' residuals and those arrivals where all the residuals are set to zero seconds, we show the distribution of P-wave residuals (figure 4.29) and S-wave residuals (figure 4.30). The P-wave residuals show two significant outliers - one in 2006 and one in 2009 (these are analysed in section 4.2.9), while the S-wave does not contain as large outliers. From Spetzler et al. (2016), we know that KNMI assess the residuals for each event within SeisComp3 as part of their manual QC procedure; but it is not known if such a similar procedure was in place before SeisComp3 was introduced in 2015.

The P-wave residuals also show predominately negative residuals, which are offset by the predominantly positive residuals of the S-waves. With the phasing out of S-wave arrivals from 2015, the P-wave residual tends towards zero seconds. There is also an improvement in the statistical spread of residuals from 2015, indicating higher quality arrival-times.

#### 4.2.9 Pick consistency

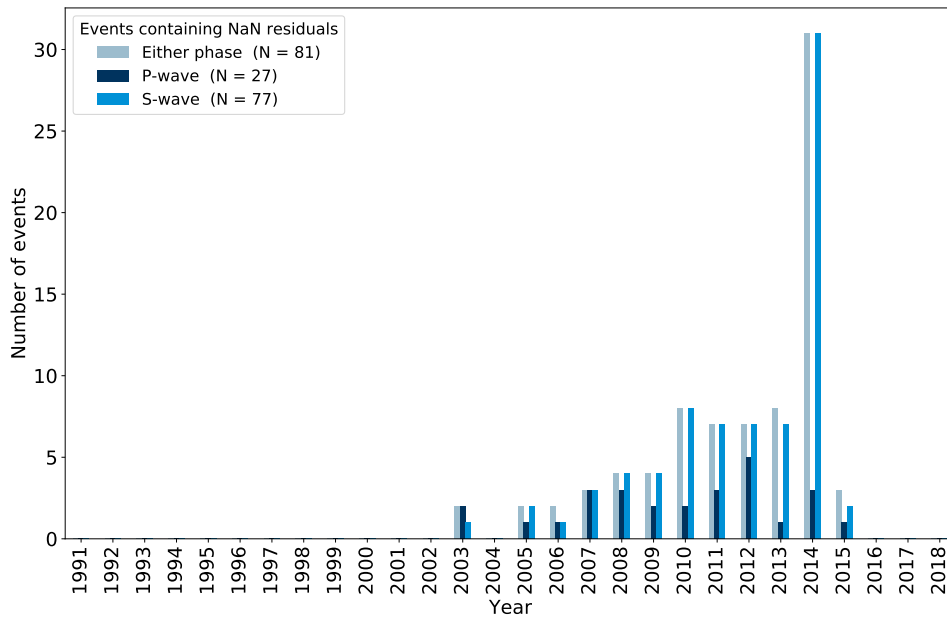
To make an assessment of pick consistency, we follow the method of Chatelain et al. (1980) to generate modified Wadati plots. This compares the time difference of P-wave and S-wave arrivals recorded by pairs of corresponding stations ( $i, j$ ).

$$DTp = P_i - P_j = (x_i - x_j) / V_p \tag{4.1}$$

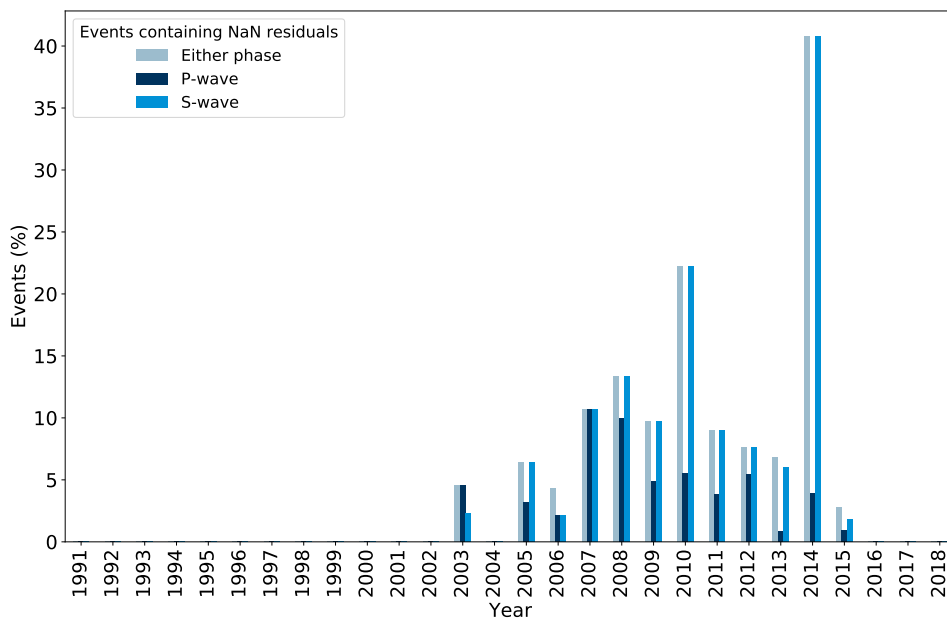
$$DTs = S_i - S_j = (x_i - x_j) / V_s \tag{4.2}$$

$$DTp / DTs = V_p / V_s \tag{4.3}$$

where  $x_i$  is the position of station  $i$ . Plotting DTs versus DTp therefore shows the  $V_p/V_s$  ratio, with

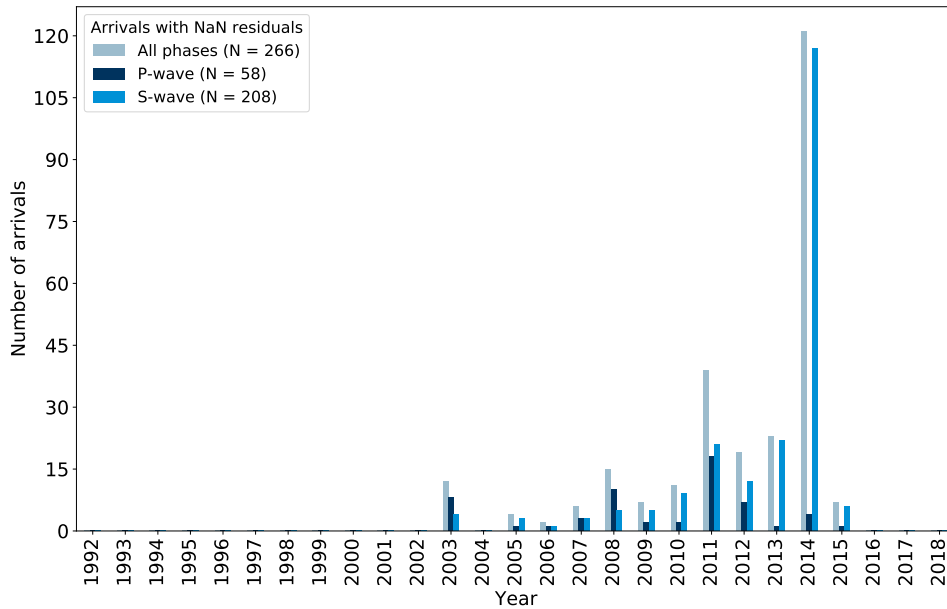


(a)

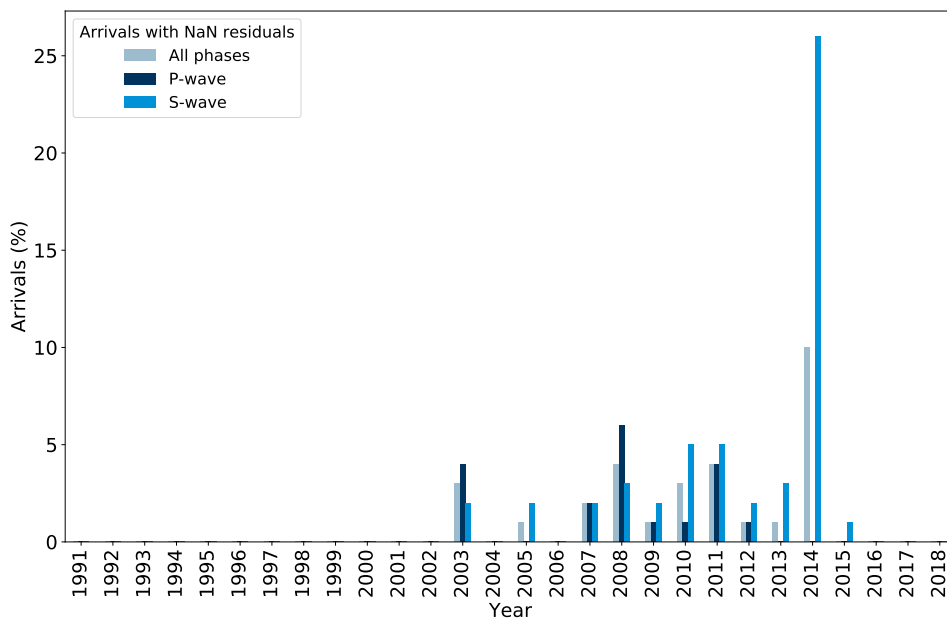


(b)

**Fig. 4.26:** Events containing residuals that are set to default values (i.e. 'NaN'). (a) shows the absolute number of events; (b) shows the percentage of events.

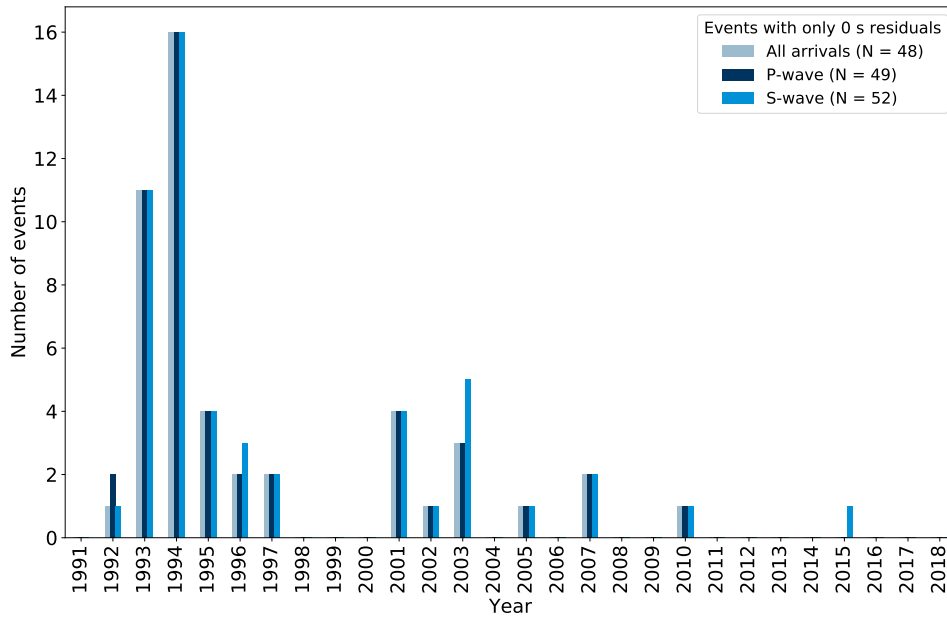


(a)

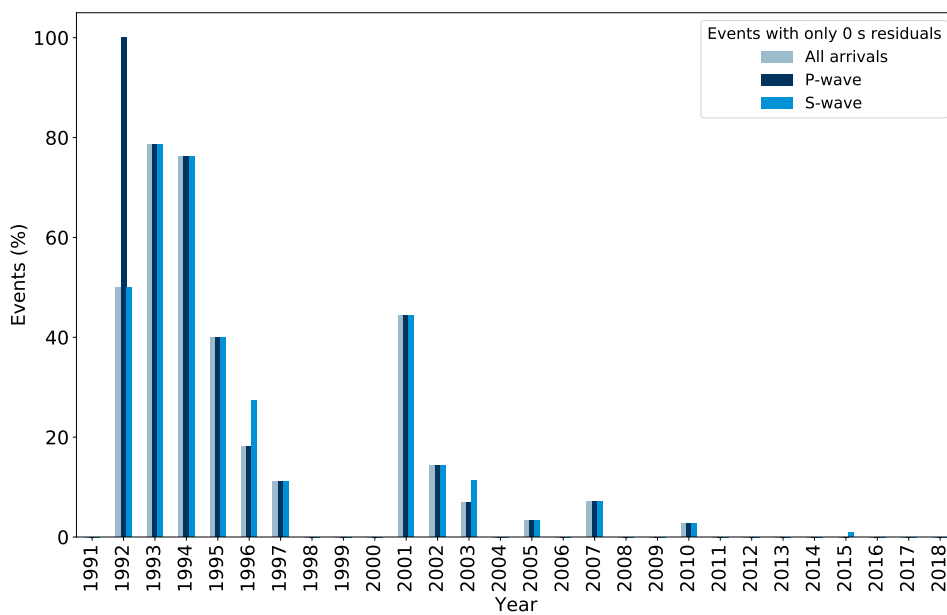


(b)

**Fig. 4.27:** Events containing residuals that are set to default values (i.e. 'NaN'). (a) shows the absolute number of events; (b) shows the percentage of events.

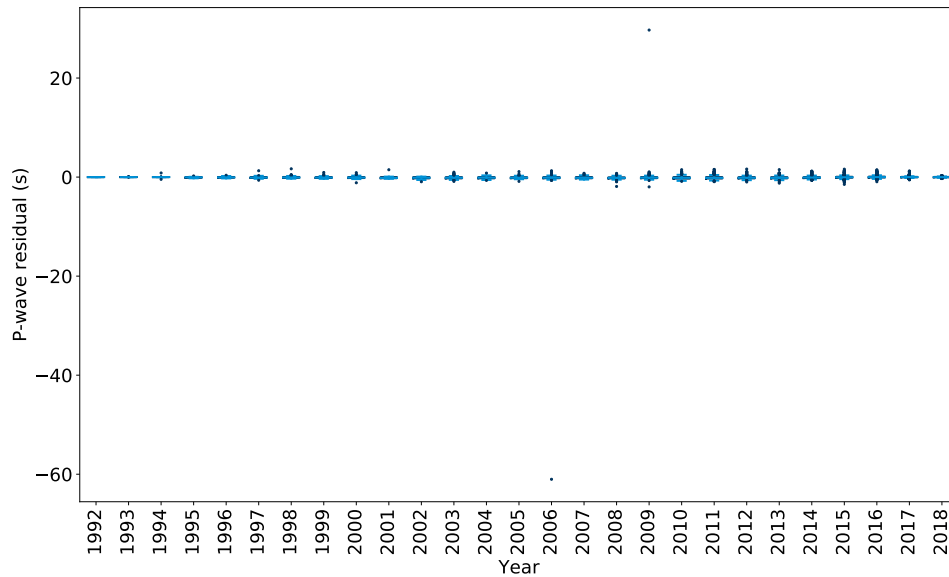


(a)

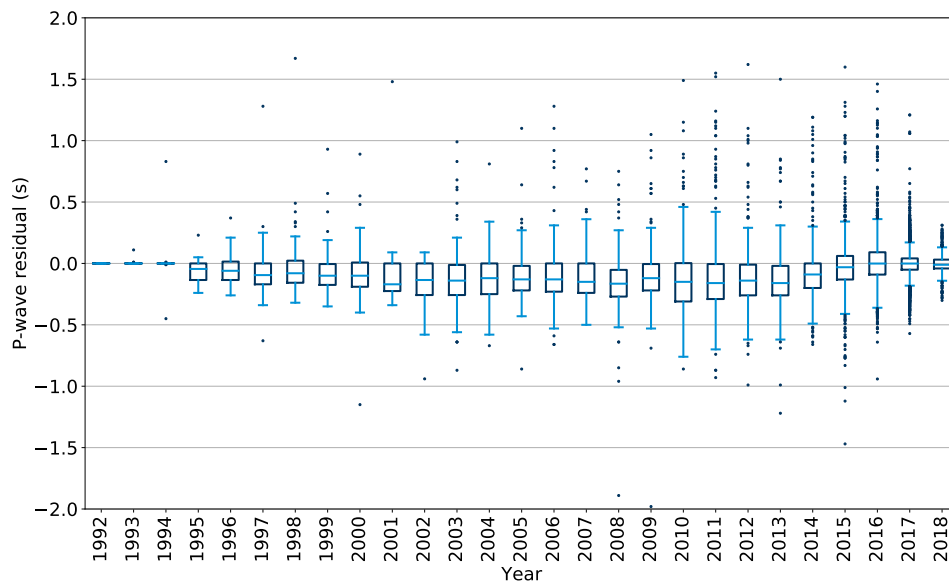


(b)

**Fig. 4.28:** Events where all arrivals have residuals set to zero seconds. (a) shows the absolute number of events; (b) shows the percentage of events.



(a)



(b)

**Fig. 4.29:** P-wave travel-time residuals recorded for the Groningen induced seismicity bulletin. (a) shows the complete set of residuals including outliers; (b) shows the distribution between  $\pm 2$  seconds.

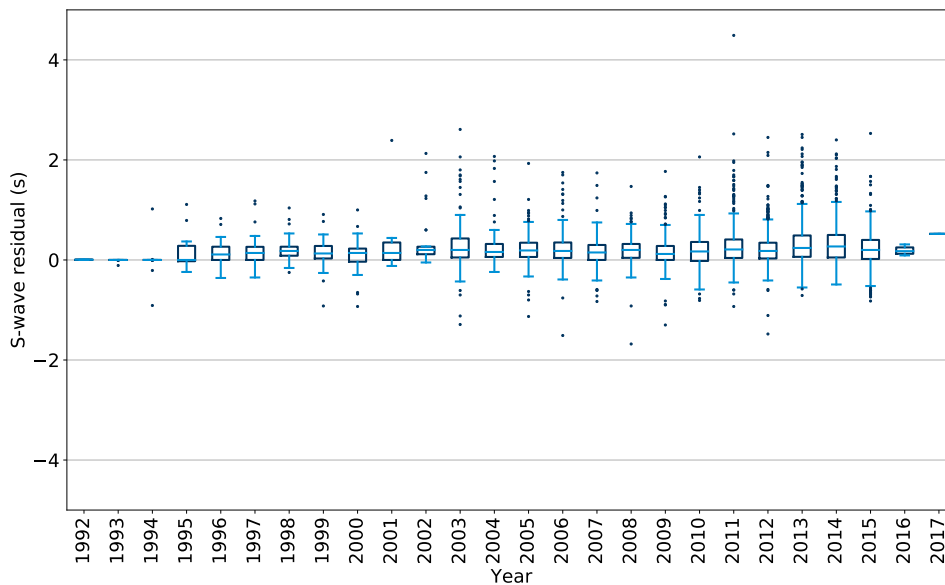


**Fig. 4.30:** *S-wave travel-time residuals recorded for the KNMI induced seismicity catalogue.*

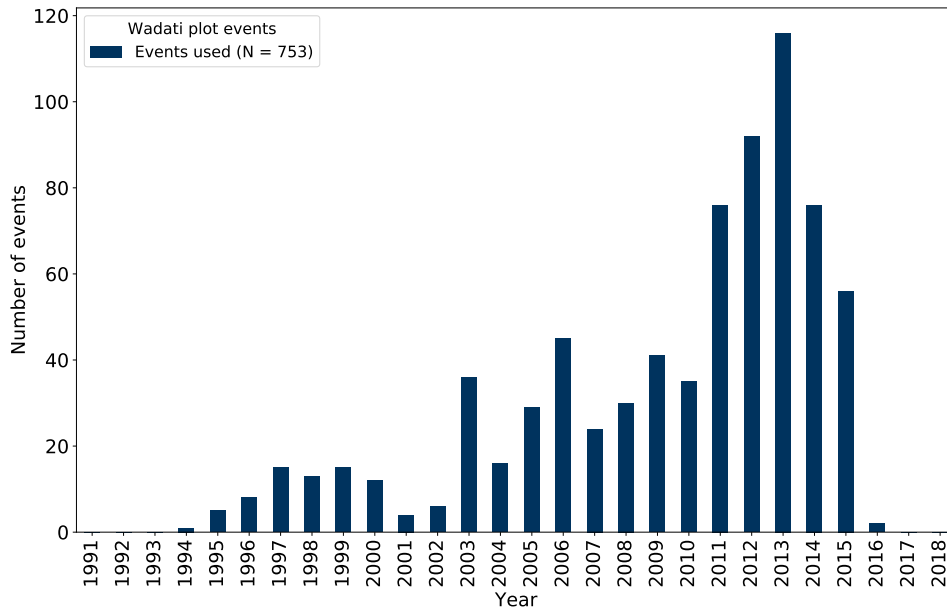
any deviation from the linear trend revealing potential pick errors. Small variations are expected due to velocity heterogeneities. One limitation of this methodology is that it relies on both P and S-wave arrivals existing for each pair of stations. As this is not always the case, and with S-waves arrivals phased out from 2015, the analysis is confined to a subset of the data. In figure 4.31 we show the number and percentage of events used in the analysis, while in figure 4.32 we show the number and percentage of arrivals that are used.

In figure 4.33, we show the modified Wadati plot for the KNMI induced seismicity catalogue. To identify any outliers, we run a robust linear model, with a weight threshold of 0.05 for identifying outliers. The results show that there were 21 outliers, corresponding to 3 events. These events are listed in table 8. The outliers correspond to arrival times from the following stations:

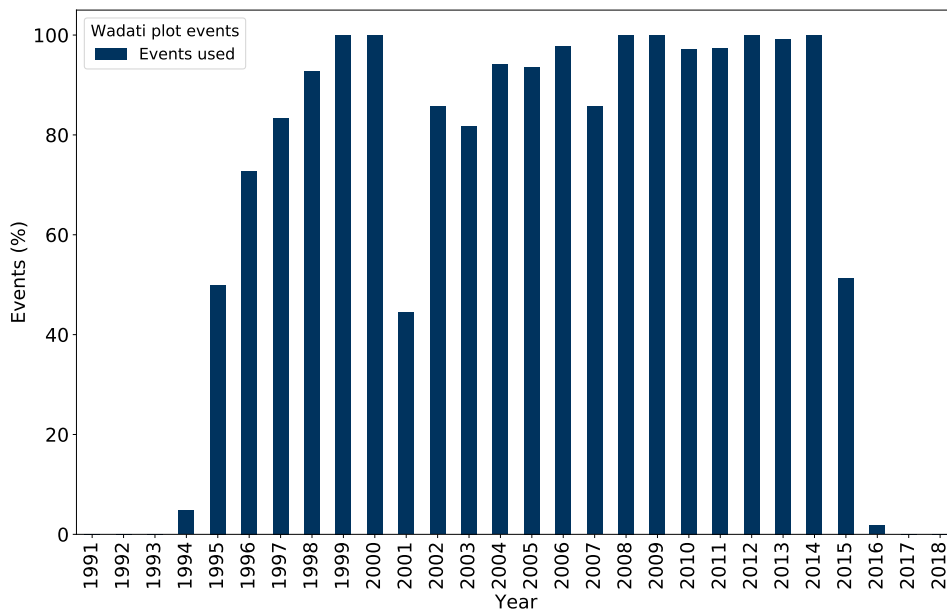
- WDB4, ZL24 (permanent stations)
- MID1, MID3, ZAN2, HOB, KLL, STB, ANV1 (temporary stations)

For WDB4 and ZL24, we can access the waveform data to assess the picks corresponding to the respective Wadati plot outliers. These are shown in figure 4.34. Both the 2003 and 2009 events (Table 8) contain outliers from the temporary stations. The data from these stations are not publicly available from KNMI’s webservices, which means they cannot be independently checked. However, we know that these temporary stations have timing problems associated with them; however, it was reported that where timing errors exist, P-S arrival-times are used instead of the individual arrival-times (KNMI, pers. comm., 2018) - this is something we cannot verify with the information available.

Further analysis of these outliers by cross-checking them with their residuals shows that all but two picks have no valid residual i.e. it is set to 'NaN'. This suggests that it was not used in the location



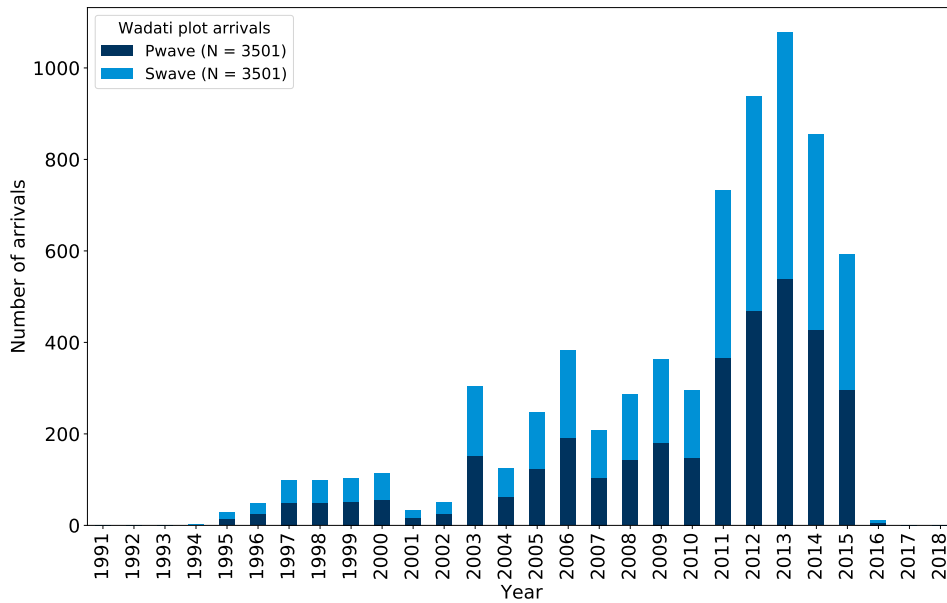
(a)



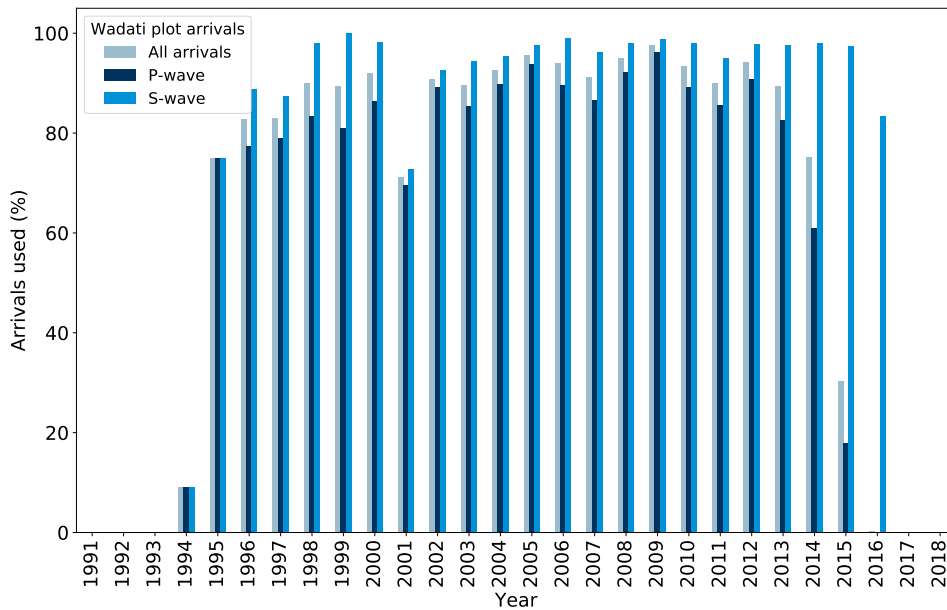
(b)

**Fig. 4.31:** Events used in the modified Wadati plot to analyse pick consistency. Due to the requirement of P-wave and S-wave arrivals at a pair of stations, the analysis represents a subset of events. (a) shows the total number of events used; (b) shows the percentage of events used.





(a)



(b)

**Fig. 4.32:** Arrivals used in the modified Wadati plot to analyse pick consistency. Due to the requirement of P-wave and S-wave arrivals at a pair of stations, the analysis represents a subset of arrivals.(a) shows the total number of events used; (b) shows the percentage of events used.

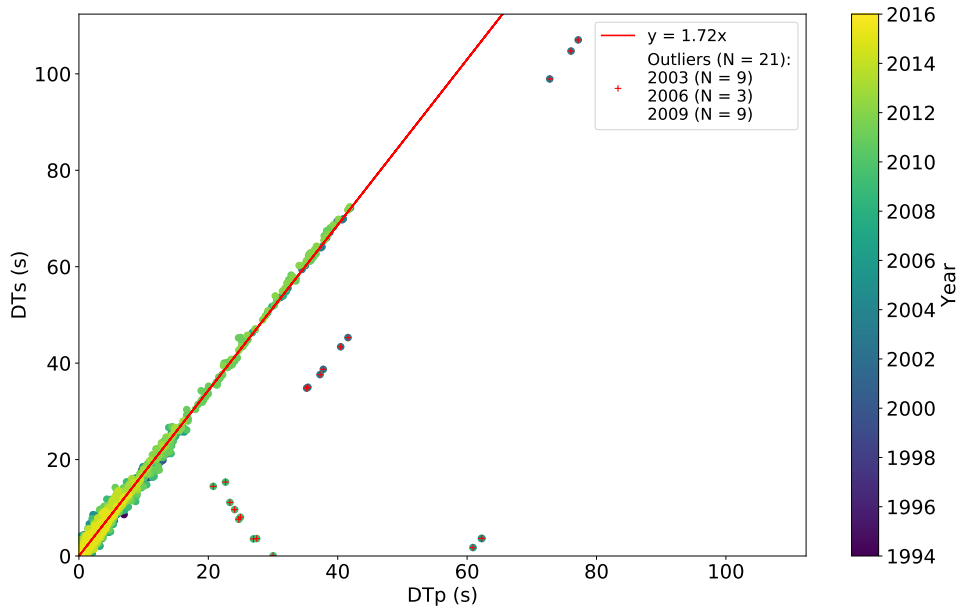


**Fig. 4.33:** Modified Wadati plot for the Groningen induced seismicity bulletin. This provides an assessment of pick consistency.

algorithm, despite not have a weight of zero. The two picks that also have valid residuals correspond to the P-wave residual outliers in figure 4.29a. They are residuals of:

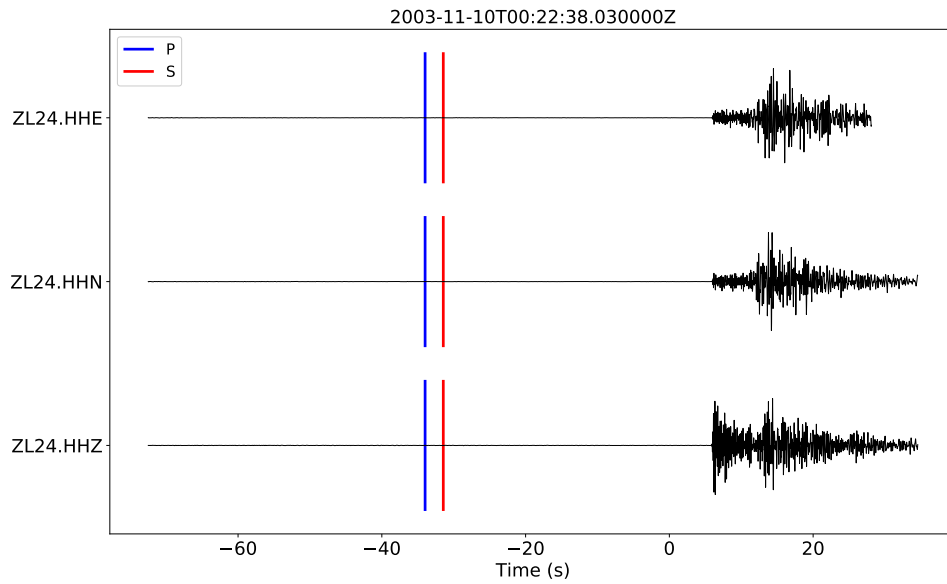
- -61.02 s at station WDB4 (event: 2006-04-05 01:41:09.76)
- 29.69 s at MID1 (event: 2009-04-14 21:05:25.88)

It is impressive that only two picks from the complete bulletin have outliers with valid residuals. With the pick errors corresponding to residual errors, this also suggests that they are not causing a negative effect on the event locations; although verification would be needed by removing those picks to be certain.

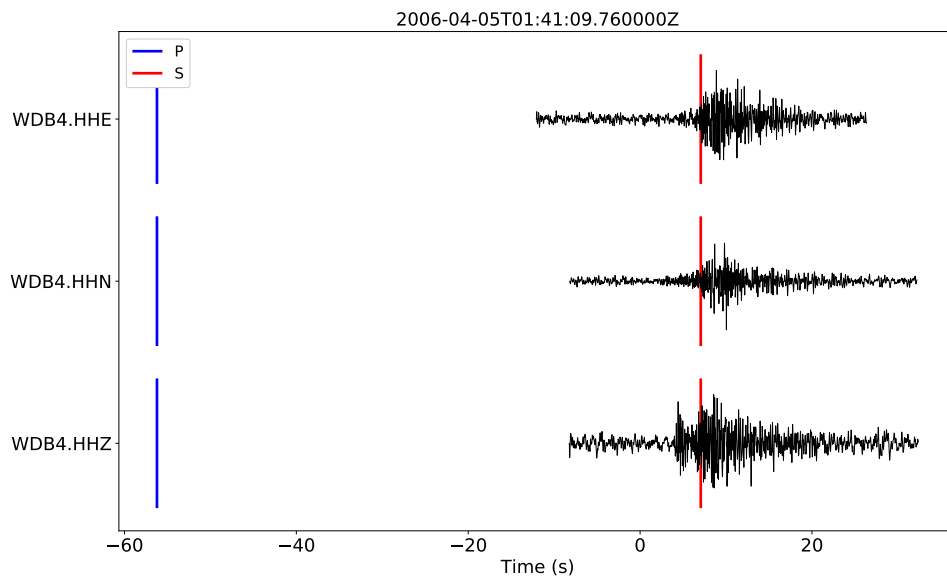
However, there does still remain the question of why/how are residuals set to 'NaN', how can the use of P-S arrival times be identified from the bulletin data, and how are residuals represented for the P-S travel-times? This information is required to make a full assessment on the event location methodology used by KNMI.

**Table 8:** Events containing pick errors identified from the modified Wadati plot in figure 4.33.

| Event id     | Date and time          | Latitude | Longitude | Magnitude ( $M_L$ ) | Depth (m) |
|--------------|------------------------|----------|-----------|---------------------|-----------|
| knmi2003vzxf | 2003-11-10 00:22:38.03 | 53.325   | 6.690     | 2.99                | 3000.0    |
| knmi2006gpwq | 2006-04-05 01:41:09.76 | 53.344   | 6.890     | 1.43                | 3000.0    |
| knmi2009hhuo | 2009-04-14 21:05:25.88 | 53.345   | 6.680     | 2.62                | 3000.0    |



(a)



(b)

**Fig. 4.34:** Waveforms corresponding to pick errors on stations ZL24 in (a) and WDB4 in (a), for an in 2003 and 2006 respectively (see table 8).

#### 4.2.10 Comparison to state-of-the-art

Earthquake location methodology is a topic that is subject to continuous research. There is no single established method that is regarded as optimal. This is in part due to the different variables and requirements involved. For example, station configuration (including azimuthal and depth coverage, total station count, and station to event distance and depth), event depth, data quality, velocity model availability and quality, signal characteristics, and type of failure of the event, are all factors that will influence the choice of location algorithm.

Methods based on relative earthquake locations (e.g. Trugman and Shearer, 2017; Waldhauser and Ellsworth, 2000; Richards-Dinger and Shearer, 2000; Lin and Shearer, 2006) can result in a significant improvement in the resolution of seismicity, revealing fault structures that could otherwise not be seen. Relative location methods can reduce biasing effects due to unmodelled velocity structure, and by using differential travel-times based on cross-correlation techniques there can be a significant improvement in the measurement precision, compared with absolute travel-times. Such methods, while often yielding superior relative event locations for a catalogue of seismicity, the individual absolute event locations are not necessarily more accurate. Since relative location methods require the use of data from multiple events simultaneously, it requires significant effort in terms of data analysis and management - this is typically not practical for routine earthquake monitoring where event locations need to be determined in a short time-frame - although real-time implementations do exist (e.g. Waldhauser, 2009). Moreover, relative event locations will lead to previously located earthquakes changing location each time a new event is added - such behaviour is undesirable for an earthquake catalogue that needs consistency.

While most earthquake location algorithms are based on phase arrival-times directly picked on seismograms, alternative methods exist that rely on scanning through all possible source locations and origin times, then stacking the waveforms after applying a theoretical travel-time correction (e.g. Kao and Shan, 2004; Drew et al., 2013). These methods are often referred to as imaging or migration location techniques. They work particularly well with large number of surface sensors and noisy data, since the stacking power improves the signal to noise ratio, and no picking of phases is required. Moreover, it is possible to process the waveforms to optimise the signal to be stacked - for example using the envelope of the signal, or the signal kurtosis. However, the method is very sensitive to errors in the velocity model, which can greatly affect the ability to detect events and the resolution at which they can be located (i.e. their location uncertainty). Similar to the direct search algorithms that exist for picked data, imaging methods are computationally intensive as they require a extensive grid searches in both space and time to find the optimum location via the maximum stacked amplitude. With the increased station network in place at Groningen, such methods have potential due to their ease of automation and ability to detect events in the presence of noise. However, the lack of precision in the resulting locations is a major drawback, which discourages their use for a robust induced seismicity catalogue, where precise locations are key. It should be noted that Smith et al.

(2016) have experimented with the use of the Coalescence Microseismic Mapping (CMM) method of Drew et al. (2013) for events in the Groningen field. Initial results showed the method used as part of the earthquake location workflow, such that the CMM event locations were used to better constrain the locations derived from a more traditional picking method. It has therefore not been shown thus far to be a complete solution for improving earthquake locations at Groningen.

Improving the depth determination at Groningen is an important factor for monitoring the induced seismicity. If earthquakes are occurring in the basement, there is the potential for higher magnitudes (DeDontney et al., 2016; Vlek, 2018) and thus higher seismic hazard; while events above the reservoir have implications for cap-rock integrity. Unfortunately, constraining event depth can be problematic. There is a trade-off between origin time and depth (i.e. an earlier origin time can be compensated by a deeper source and vice versa). This trade-off will be most apparent when only P-waves are used for event location and station distances from the epicentre are greater than the focal depth. Such behaviour is well illustrated in Husen (2010) and Havskov et al. (2012). When arrivals from stations close to the epicenter are used, a change in event depth has a greater effect on the travel-time, which helps to better constrain the depth. Furthermore, by using a variety of different phases, which travel at different slownesses, then these will add further constraints to the depth determination.

The current procedure of fixing the hypocentre depth during location to 3 km is not ideal in terms of providing an accurate event location. However, as Bondár and Storchak (2011) note, attempting to find a free depth solution is futile when the data have no resolving power for depth. For this reason, the International Seismological Centre follow the procedure in their location algorithm of first assessing if the data provides depth resolution. If it does, then depth determination will be attempted; if not, the depth is fixed to a region-dependent default depth (Bondár and Storchak, 2011). With the increase in station distribution for the Groningen network, the ability to constrain depth has improved, since the likelihood to have stations within 3 km (the expected event depth) has increased. However, the use of multiple phases is more problematic at Groningen since the S-wave characteristics make picking of their arrival time difficult and often impossible to estimate (Spetzler and Dost, 2017). KNMI are actively investigating methods for improving the depth constraint of Groningen events as outlined in Spetzler and Dost (2017). Here, they use a location methodology using the differential travel-times between station pairs for the P-wave, known as the Equal Differential Time (EDT) method, and based on Font et al. (2004), Lomax (2005), and Satriano et al. (2008). This method is insensitive to the origin-time/depth trade-off, and has shown promising results, which may be implemented into the automatic processing of KNMI in the future (KNMI, pers. comm., 2018).

The approach of Spetzler and Dost (2017) was expanded upon in Spetzler and Dost (2018) and used the 3D velocity model generated by NAM. This model contains horizons and elastic properties obtained from 3D active seismic, and covers an area of  $\sim 1716 \text{ km}^2$ . The use of a 3D velocity model has the potential to greatly improve the accuracy of event locations.

#### 4.2.11 Conclusions

The event location methodology used by KNMI has consistently used an iteratively linearised inversion throughout the catalogue period. The exact algorithm changed from HYPO71 to HYPOCENTER, but there are few fundamental differences in how these methodologies work. This change is thought to have taken place in 1998, but the change and the time of change is not well documented. In June 2015, the processing was moved onto the SeisComp3 platform, with the HYPOCENTER algorithm incorporated into this interface.

No location uncertainties are provided in the publicly available catalogue or in the bulletin data. An indication of location uncertainty can be gained from rms residual values, providing a goodness of fit for each event. We understand that location uncertainties have been computed, but they are stored internally at KNMI.

The use of S-waves for locating earthquakes changes with the introduction of the G-network in 2014. From this time, the use of S-waves is phased out, with the event location relying solely on the P-wave arrival-times. Despite this, the number of arrivals used per event significantly increases due to the network expansion.

Analysis of the Groningen induced seismicity bulletin has shown that in addition to the permanent stations, many temporary stations were used for event location. The locations of these stations and their waveform data are not publicly available, making the analysis of event quality limited where these additional data were used. Moreover, these stations are reported as having known timing errors, which were addressed by using S-P arrival-times when the timing errors were identified. However, this is not documented within the bulletin data, where S-P times are used compared with the absolute arrival-times - this makes the interpretation of the arrival-time data difficult.

Throughout the catalogue, the event depth is fixed to 3 km. Establishing the correct depth of the Groningen induced seismicity has important consequences in terms of understanding the seismic hazard. Various metrics exist to assess the quality of the network in terms of the location accuracy. For establishing depth, these include observations from stations within a focal depths distance to the epicentre, and using multiple phases (i.e. both P- and S-wave arrivals). While having stations close to the epicentre is not always possible prior to the network expansion in 2014, we do observe examples from 1997 onwards, where the minimum station to event distances appear sufficient to attempt resolving the event depth. Moreover, the S-wave data are also available (subject to quality) for improving depth resolvability.

We have also assessed both the station count and the azimuthal distribution of the network throughout the catalogue period to better understand the location uncertainty. Up to and including 2011, we observe events with station counts of less than 3 - these are assumed to be errors in the reported bulletin data. For azimuthal coverage, the network performance is much better. Whilst the com-

puted azimuthal and secondary azimuthal gaps do not always meet the recommended guidelines of  $110^\circ$  and  $160^\circ$  respectively, this would have been affected by the missing station information and the shortfalls are low.

Pick consistency for the bulletin data was judged to be good overall, with only two significant outliers corresponding to valid travel-time residuals. However, the data within the bulletin shows inconsistencies in terms of how residuals are recorded. For example, there are cases where arrivals are weighted positively but their residuals are set as default numbers suggesting they are invalid. We also observe events where all residuals are set to zero seconds.

In comparison to state-of-the-art methods for event location, there is the potential for the current procedures at KNMI to be improved. While many state of the art methods are not appropriate for routine processing, event depth resolvability should be a priority. With the availability of a 3D velocity model for Groningen, the event location accuracy also has the potential to be improved.

## References

- Bondár, I., S.C. Myers, E.R. Engdahl, and E.A. Bergman (2004). "Epicentre accuracy based on seismic network criteria". In: *Geophysical Journal International* 156.3, pp. 483–496. ISSN: 0956540X. DOI: [10.1111/j.1365-246X.2004.02070.x](https://doi.org/10.1111/j.1365-246X.2004.02070.x).
- Bondár, I. and D. Storchak (2011). "Improved location procedures at the International Seismological Centre: Improved location procedures at the ISC". In: *Geophysical Journal International* 186.3, pp. 1220–1244. ISSN: 0956540X. DOI: [10.1111/j.1365-246X.2011.05107.x](https://doi.org/10.1111/j.1365-246X.2011.05107.x).
- Chatelain, J.L., S.W. Roecker, D. Hatzfeld, and P. Molnar (1980). "Microearthquake seismicity and fault plane solutions in the Hindu Kush Region and their tectonic implications". In: *Journal of Geophysical Research: Solid Earth* 85.B3, pp. 1365–1387. ISSN: 0148-0227. DOI: [10.1029/JB085iB03p01365](https://doi.org/10.1029/JB085iB03p01365).
- DeDontney, N. et al. (2016). *Maximum Magnitude of Induced Earthquakes in the Groningen Gas Field*. Tech. rep. Nederlandse Aardolie Maatschappij BV.
- Drew, J., R.S. White, F. Tilmann, and J. Tarasewicz (2013). "Coalescence microseismic mapping". In: *Geophysical Journal International* 195.3, pp. 1773–1785.
- Font, Y., H. Kao, S. Lallemand, C.-S. Liu, and L.-Y. Chiao (2004). "Hypocentre determination offshore of eastern Taiwan using the Maximum Intersection method". In: *Geophysical Journal International* 158.2, pp. 655–675.
- Gomberg, J.S., K.M. Shedlock, and S.W. Roecker (1990). "The effect of S-wave arrival times on the accuracy of hypocenter estimation". In: *Bulletin of the Seismological Society of America* 80.6a, p. 1605.
- Havskov, J., P. Bormann, and J. Schweitzer (2012). "New Manual of Seismological Observatory Practice 2 (NMSOP-2)". eng. In: ed. by P. Bormann. Potsdam: Deutsches GeoForschungsZentrum GFZ. Chap. Seismic source location, pp. 1–36. DOI: [10.2312/GFZ.NMSOP-2](https://doi.org/10.2312/GFZ.NMSOP-2).
- Husen, S. (2010). "CORSSA". In: chap. Earthquake Location Accuracy.

- Kao, H. and S-J Shan (2004). "The Source-Scanning Algorithm: mapping the distribution of seismic sources in time and space". In: *Geophysical Journal International* 157.2, pp. 589–594. ISSN: 0956540X. DOI: [10.1111/j.1365-246X.2004.02276.x](https://doi.org/10.1111/j.1365-246X.2004.02276.x).
- KNMI (1996). *Seismische analyse van de aardbevingen bij Middlestum op 30 Juli 1994, Annen op 16 Augustus, Annen op 31 Januari 1995*. Tech. rep. KNMI.
- KNMI, pers. comm. (2018). Personal communication.
- Lee, W.H.K. and J.C. Lahr (1972). *HYP071: a computer program for determining hypocenter, magnitude, and first motion pattern of local earthquakes*. Tech. rep.
- Lienert, B.R. (1991). *Report on modifications made to Hypocenter*. Tech. rep. Insitute of Solid Earth Physics, University of Bergen.
- Lienert, B.R., E. Berg, and L.N. Frazer (1986). "HYPOCENTER: An earthquake location method using centered, scaled, and adaptively damped least squares". In: *Bulletin of the Seismological Society of America* 76.3, p. 771.
- Lienert, B.R. and J. Havskov (1995). "A Computer Program for Locating Earthquakes Both Locally and Globally". In: *Seismological Research Letters* 66.5, p. 26. DOI: [10.1785/gssr1.66.5.26](https://doi.org/10.1785/gssr1.66.5.26).
- Lin, G. and P. Shearer (2006). "The COMLOC Earthquake Location Package". In: *Seismological Research Letters* 77.4, pp. 440–444. ISSN: 0895-0695. DOI: [10.1785/gssr1.77.4.440](https://doi.org/10.1785/gssr1.77.4.440).
- Lomax, A. (2005). "A Reanalysis of the Hypocentral Location and Related Observations for the Great 1906 California Earthquake". In: *Bulletin of the Seismological Society of America* 95.3, pp. 861–877. ISSN: 0037-1106. DOI: [10.1785/0120040141](https://doi.org/10.1785/0120040141).
- Lomax, A., A. Michelini, and A. Curtis (2014). "Encyclopedia of Complexity and Systems Science". In: ed. by R.A. Meyers. Springer New York. Chap. Earthquake Location, Direct, Global-Search Methods, pp. 1–33. DOI: [10.1007/978-3-642-27737-5\\_150-2](https://doi.org/10.1007/978-3-642-27737-5_150-2).
- Pickering, M. (2015). *An estimate of the earthquake hypocenter locations in the Groningen Gas Field*. Tech. rep. Nederlandse Aardolie Maatschappij BV.
- Richards-Dinger, K.B. and P.M. Shearer (2000). "Earthquake locations in southern California obtained using source-specific station terms". In: *Journal of Geophysical Research: Solid Earth* 105.B5, pp. 10939–10960. ISSN: 0148-0227. DOI: [10.1029/2000JB900014](https://doi.org/10.1029/2000JB900014).
- Satriano, C., A. Lomax, and A. Zollo (2008). "Real-Time Evolutionary Earthquake Location for Seismic Early Warning". In: *Bulletin of the Seismological Society of America* 98.3, pp. 1482–1494. ISSN: 0037-1106. DOI: [10.1785/0120060159](https://doi.org/10.1785/0120060159).
- Smith, J., J. Drew, and R. White (2016). *Coalescence Microseismic Mapping*. University of Cambridge.
- Spetzler, J. and B. Dost (2017). "Hypocentre estimation of induced earthquakes in Groningen". In: *Geophysical Journal International* 209.1, pp. 453–465.
- Spetzler, J. and B. Dost (2018). *Hypocenter estimation of induced earthquakes in Groningen*. NAC (Nederlands Aardwetenschappelijk Congres), Veldhoven, 15 - 16 March. Poster presentation.
- Spetzler, J., B. Dost, and E. Ruigrok (2016). *Seiscomp3 analysis of the Froombosch Event on February 25, 2016*. Groningen Event Location Workshop, 20 October 2016. Oral presentation.



- Trugman, D.T. and P.M. Shearer (2017). "GrowClust: A Hierarchical Clustering Algorithm for Relative Earthquake Relocation, with Application to the Spanish Springs and Sheldon, Nevada, Earthquake Sequences". In: *Seismological Research Letters* 88.2a, pp. 379–391. ISSN: 0895-0695. DOI: 10.1785/0220160188.
- Vlek, C. (2018). "Induced Earthquakes from Long-Term Gas Extraction in Groningen, the Netherlands: Statistical Analysis and Prognosis for Acceptable-Risk Regulation". In: *Risk Analysis*.
- Waldhauser, F. (2009). "Near-Real-Time Double-Difference Event Location Using Long-Term Seismic Archives, with Application to Northern California". In: *Bulletin of the Seismological Society of America* 99.5, pp. 2736–2748. ISSN: 0037-1106. DOI: 10.1785/0120080294.
- Waldhauser, F. and W.L. Ellsworth (2000). "A double-difference earthquake location algorithm: method and application to the northern Hayward fault, California". In: *Bulletin of the Seismological Society of America* 90.6, pp. 1353–1368.
- Wuestefeld, A., S. Greve, S.P. Näsholm, and V. Oye (in press). "Benchmarking earthquake location algorithms: A synthetic comparison". In: *Geophysics*.

### 4.3 Magnitude computation

#### 4.3.1 Context and overview

For all induced events in the Groningen region, the determination of the local magnitude  $M_L$  at KNMI is part of the standard processing and the basis for the Groningen seismic hazard and risk models. Mainly for larger events in the Groningen field ( $M_L > 2.5$ ) also moment magnitudes  $M_W$  have been determined. Scaling relations between  $M_L$  and  $M_W$  have been developed for the whole range of Groningen seismicity (Dost et al., 2018).

The determination of the local magnitude  $M_L$  at KNMI is part of the standard processing for all induced events in the Groningen region and  $M_L$  is the basis for the Groningen seismic hazard and risk models.

#### 4.3.2 Magnitude types

##### Local magnitude $M_L$

In the standard KNMI analysis  $M_L$  is determined, using the KNMI borehole network stations (Dost et al., 2004, Dost et al., 2018). The local magnitude is defined as  $M_L = \log(A_{wa}) - \log(A_0)$  (Richter, 1935), where  $A_{wa}$  is the maximum amplitude in mm recorded on a simulated Wood-Anderson seismograph and  $\log(A_0)$  is the attenuation function. In order to simulate a Wood-Anderson seismograph an additional Wood-Anderson (WA) filter is applied, that includes a 0.8 Hz high pass filter.

Despite the limitations of  $M_L$ , it is widely adopted as the magnitude of choice for regional earthquakes. Several well known shortcomings of  $M_L$  are:

- Saturation of larger magnitudes due to the Wood-Anderson filter response (acts as high-pass filter above 1 Hz).
- A local re-calibration of the attenuation correction is necessary.
- $M_L$  is only consistent locally and large regional differences may exist, which makes it difficult to compare. Often systematic differences exist between different agencies.

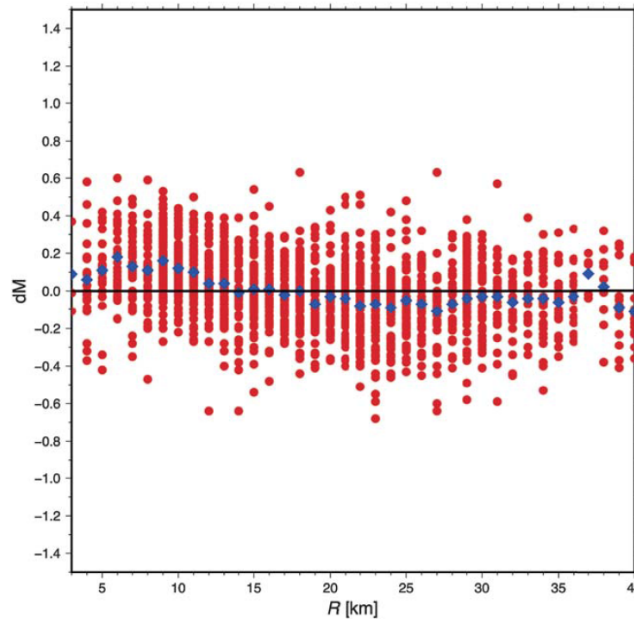


**Fig. 4.35:** Difference between calculated station magnitude and average magnitude ( $dM$ ) for events recorded in the period 2010 to 2015 as a function of hypocentral distance  $R$ . Mean values are indicated in blue. Figure taken from Dost et al. (2018)

In Groningen, in the early times (1986-1992),  $M_L$  was calculated using a reference station (WTS) of the KNMI network (Dost et al., 2018). The attenuation relation of Ahorner (1983) was used, in which  $\log(A_0) = -1.90 \log(R) + 0.35$ , where  $R$  is the hypocentral distance. A first attenuation relation for the North of the Netherlands could be determined using the Assen array, a small aperture array of vertical component receivers around the city of Assen installed in 1988. In 1991,  $M_L$  could be determined from borehole data at station FSW by extrapolating the previous attenuation relation. After the borehole network in Groningen became operational in 1995, a new attenuation relation was derived for the North of the Netherlands in 1996 (Dost et al., 2004) from amplitude measurements at the deepest level in the boreholes (generally at 200 m depth, except for FSW where it is 225 m):

$$M_L = \log(A_{wa}) + 1.33 \log(R) + 0.00139 R + 0.424 \tag{4.4}$$

where  $R$  is the hypocentral distance in km. The second term in equation 4.4  $1.33 \log(R)$  implies that the geometrical spreading is faster than the usually assumed  $1/R$ . 157 events between 1995 and mid 1996 were included in estimating the attenuation function. For each station  $A_{wa}$  is measured as the

average maximum displacement amplitude (half peak-to-peak) of the two horizontal components after application of the Wood-Anderson (WA) filter. In 2004, equation 4.4 had been modified from its original form as determined in 1996 by subtracting a constant -0.5 (0.424 instead of 0.924 previously), accounting for an error in the sensitivity of the borehole sensors (Dost et al., 2004). In other words, magnitudes before and after 2004 have been estimated using the same relation but with the application of a different constant since different sensitivities were used to convert to Wood-Anderson amplitudes. Until the recent extension of the network from 2015 onwards, the eight-station borehole network in the northeastern Netherlands was used for  $M_L$  calculations, and the average over all usable stations was taken. For smaller events, the S/N ratio of stations at larger distance may not have been sufficient to calculate magnitudes and in such cases less than 8 borehole stations were used.

Dost et al. (2018) noted that the difference in  $M_L$  using the new general relation (equation 4.4) compared to the previous relation based on the Assen array is small (around 0.1-0.2 magnitude units). In addition, amplitude station corrections have been calculated and are less than 0.1 magnitude units. However, these station corrections were not used in the magnitude estimation.

Dost et al. (2018) also observed a minor distance dependence at hypocentral distances  $R$  less than 10-15 km (see figure 4.35), which may suggest a reconsideration of the used attenuation relation. Such corrections of the attenuation function at short distances ( $R < 20$  km) have been found necessary in other regions, such as for example Switzerland (Edwards et al., 2015), where a mean difference of almost up to 1 magnitude unit compared to larger distances was observed. However, the observed distance dependence at  $R < 15$  km in Groningen with a mean difference of 0.12 magnitude units was evaluated by KNMI as being small compared to the observed standard deviation at these distances (Dost et al., 2018).

The attenuation function of equation (4.4) applies to a larger region than only the Groningen area. Despite the change of the attenuation function in 2004, accounting for different sensor sensitivities used in the processing before and after, the resulting catalogue can be considered consistent. We only consider local magnitudes determined before 1996 as inconsistent with the rest of the catalogue, from 1996 until today. These early magnitudes were determined using either the calibration with reference station WTS, the Assen array, or the first borehole station FSW. However, as noted by Dost et al. (2018), the difference to the relation based on the Assen array is small ( $< 0.2$  magnitude units). The attenuation function has also not been updated after more records became available in recent years. However, Dost et al. (2018) show that the assumptions are still valid when including newer data.

In our analysis, we evaluate the consistency of the catalogue further and check whether changes in data processing, or recent extensions of the borehole network could potentially be a source of magnitude inconsistency.

For this purpose, we compare mean  $M_L$  over time as shown in figure 4.36 to check for obvious vari-

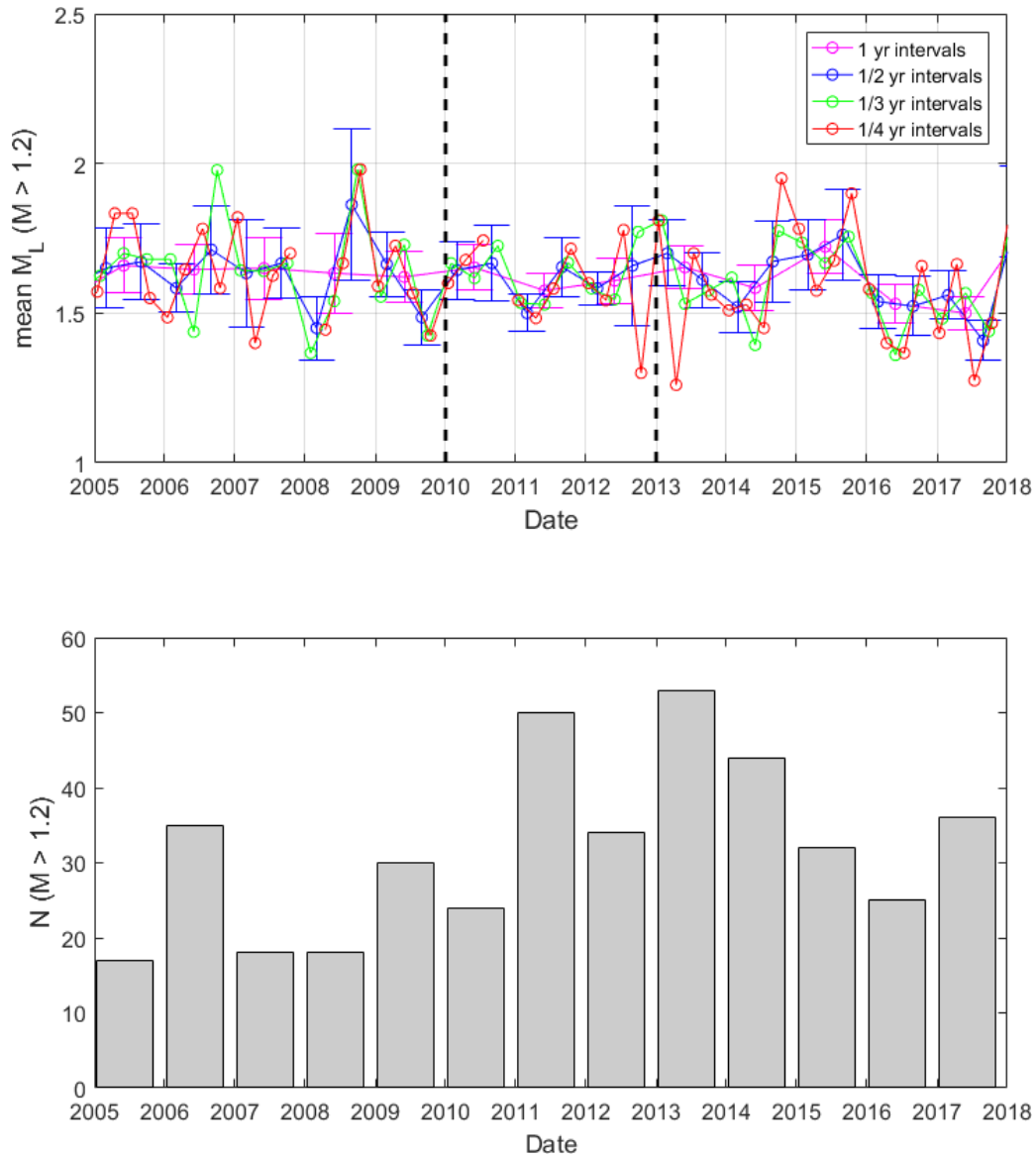


**Fig. 4.36:** Top: Mean  $M_L$  over time for all  $M_L > 1.2$ . Several time interval lengths are shown. Two time periods where a change to the processing has been applied are marked by the black dashed lines. Bottom: Number of events per year.

ations with time. To remove the effect of network upgrades, we include only events with  $M_L > 1.2$ , i.e., above the highest magnitude of completeness determined by NORSAR’s moving window analysis, as discussed in 3.4. To account for random temporal variations of the seismicity, we perform this analysis over various interval lengths ranging from three months to one year (figure 4.36). We observe an overall constant mean value of  $M_L$  over the whole time period within the range of expected random statistical variation, especially when looking at the one-year average (pink line). Two time periods are of particular interest: a) In 2010 the data processing was switched from manual to automated processing. The required number of triggers has been increased to six. The switch from manual to automated data processing should not have affected the catalogue, since all events in the

catalogue are reprocessed manually. Only the first detection is performed automatically. We observe no obvious change in mean  $M_L$  around 2010 (4.36). b) Since 2013 all automatic as well as standard manual processing has been performed using SeisComp3. Again, no change in mean  $M_L$  can be seen in figure 4.36.

### Moment magnitude

The moment magnitude  $M_W$  is based on a physical quantity and provides a reliable magnitude estimate without saturation effects.  $M_W$  is estimated from the seismic moment  $M_0$ , following  $M_W = 2/3 \log(M_0) - 10.7$  (Hanks and Kanamori, 1979). The seismic moment,  $M_0$ , can be derived from the low-frequency component of spectra of P and S waves (e.g., Abercrombie, 1995). For Groningen, S waves are used for the moment magnitude analysis since they typically have higher amplitudes. Methods rely on determining the long-period displacement plateau  $\Omega_0$  of the spectrum, accounting for anelastic attenuation and site effects. The recorded plateau values are subsequently used to determine geometrical spreading, amplification and seismic moment. The low-frequency spectral level can be expressed in terms of  $M_0$  (Boatwright, 1984) as

$$\Omega_0 = \frac{2\Theta}{4\pi\rho_0^{1/2}\rho_S^{1/2}V_0^{-1/2}V_S^{5/2}}g(R)M_0, \quad (4.5)$$

where  $\Theta$  denotes the average radiation pattern,  $\rho_S$  the density at the source ( $2.6\text{ kg/m}^3$ , Kraaijpoel and Dost, 2013),  $\rho_0$  the density at the surface ( $2.1\text{ kg/m}^3$ , Kraaijpoel and Dost, 2013),  $V_S$  the S wave velocity at the source ( $2009\text{ m/s}$ , Dost et al., 2018) and  $V_0$  the S wave velocity at the surface ( $200\text{ m/s}$ , Kruiver et al., 2017). The term  $g(R)$  describes the geometrical spreading. The Brune source model (Brune, 1970), modified by Boatwright, 1978, was used by KNMI to estimate the best fitting parameters for  $\Omega_0$ , the spectral corner frequency  $f_c$ , and the  $t^*$ -operator by using a grid search. A more detailed description of the processing is given in Dost et al. (2018).

To evaluate the sensitivity of individual  $M_W$  estimates, KNMI compared the obtained  $M_W$  results to results using a slightly different approach in spectral  $M_W$  estimation following Edwards et al. (2010). This approach is based on a simultaneous fitting of source-, propagation-, and receiver terms and hence a different, distance-dependent geometrical spreading function is used. However, the approach leads to overall very similar results and a comparison of the  $M_W$  values obtained by the two different approaches revealed a 1:1 scaling (figure 6 of Dost et al., 2018).

### 4.3.3 Magnitude scaling relations

Within the context of the Groningen seismic hazard and risk models, both, the compaction-based seismicity model (e.g., Bourne et al., 2014) and the ground-motion models (GMM) are being developed in terms of  $M_L$ , but with the assumption of these magnitudes being equivalent to  $M_W$ . Although this assumption represents a reasonable starting point (Deichmann, 2006), it has been a

clear goal of KNMI to either confirm this assumed equivalence or else to replace it with a validated empirical relationship.

In order to determine a first scaling relation between  $M_L$  and  $M_W$ ,  $M_W$  was estimated for a total of 34 events using accelerometer data (Dost et al., 2016, figure 4.37). These first results on the scaling relation between  $M_L$  and  $M_W$  indicated an overall linear relation with  $M_W - M_L = b M_L + a$ , with  $a = 0.327 \pm 0.186$  and  $b = -0.169 \pm 0.071$ . For  $M_L > 2.5$ , a relation of  $M_W = M_L - 0.2$  (Dost et al., 2016) has been determined as can be seen in figure 4.37. However, personal communication with KNMI in preparation of this report revealed that an error in  $M_W$  estimation due to a mistake in the scaling of the spectra was discovered by KNMI following the work of Dost et al. (2016). Therefore the  $M_W$  estimates as shown in figure 4.37 are not correct. This applies in particular to the highest magnitude events (two events of  $M_L$  3.5 and 3.6), and hence the depicted scaling relation for  $M_L > 2.5$  (red line in figure 4.37) should be dismissed. The mistake was corrected in any subsequent work.

Scaling relations between  $M_L$  and  $M_W$  have been developed for the whole range of Groningen seismicity, which is in agreement with recent theoretical and empirical publications on scaling relations elsewhere.

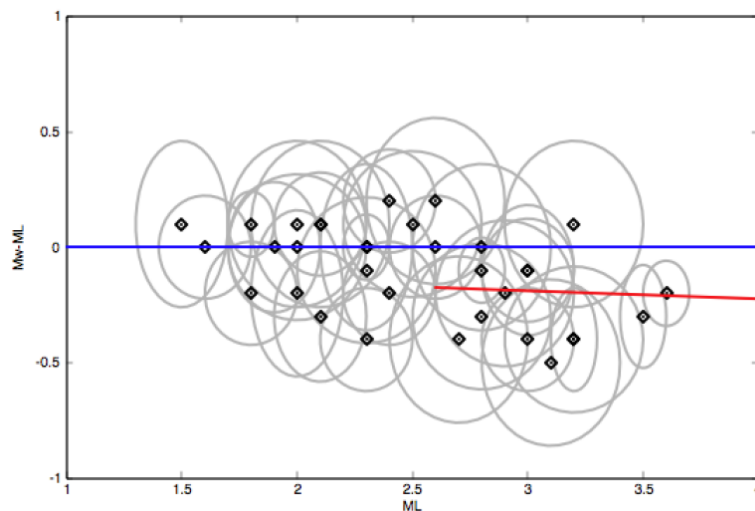


**Fig. 4.37:**  $M_W - M_L$  as a function of  $M_W$  for selected events. Uncertainties are shown as ellipses. Blue line denotes a 1:1 scaling between  $M_L$  and  $M_W$ . A linear regression for  $M_L > 2.5$ , taking into account uncertainties in both parameters, is shown in red. Figure taken from Dost et al. (2016).

The dataset was later on expanded to 116 events and a re-assessment of the above described scaling relation was performed by Dost et al. (2018). In this re-analysis the detected mistake in the scaling of the spectra was corrected. For events of magnitude  $M_L > 2$  both  $M_L$  and  $M_W$  are similar with a 1:1 relation (see figure 4.38). The data does not show the previously determined offset of 0.2. In addition, a clear deviation from 1:1 scaling can be observed at magnitudes below 2. Hence, following the lines

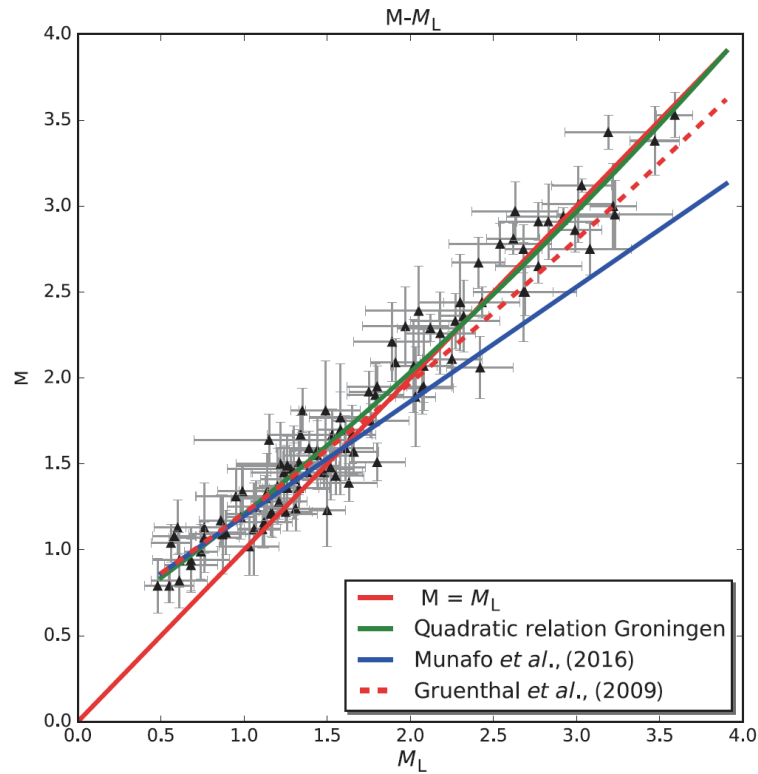


**Fig. 4.38:**  $M_W$  as a function of  $M_L$ . The proposed quadratic relation is shown in green line. Other relations from other studies are shown in red dashed line and in blue line. Error bars indicate the standard deviation of the magnitudes. Figure taken from Dost et al. (2018).

of Grünthal et al., 2009, Dost et al., 2018 fitted a quadratic relation to the data using a least-squares optimization:

$$M_W = 0.056262 M_L^2 + 0.65553 M_L + 0.4968. \tag{4.6}$$

#### 4.3.4 Comparison to state-of-the-art and conclusions

All applied methods to estimate  $M_L$  and  $M_W$  are state of the art, and reflect, or consider recent theoretical and empirical publications on scaling relations elsewhere.

For a further assessment, we first note that the initial analysis presented in Dost et al. (2016) and summarized in figure 4.37 is based on very few data points (34 events), which we do not see as sufficient in providing a reliable and convincing relationship between  $M_W$  and  $M_L$ . We will therefore concentrate on the results presented in Dost et al., 2018 based on the larger catalogue.

Based on the theoretical considerations brought forward by (Deichmann, 2006), the scientific community has generally accepted that, for intermediate magnitudes above about 3,  $M_L = M_W$  up to the point where  $M_L$  is known to saturate, due to the Wood-Anderson filter (around magnitude 6). At lower magnitudes (roughly below 3, depending on study), a similar break in scaling has been observed by many authors (e.g., Grünthal et al., 2009, Goertz-Allmann et al., 2011), including observations from

Groningen (figure 4.38). Only recently, this widely observed break in scaling could be explained theoretically (Munafò et al., 2016; Deichmann, 2017). From these theoretical considerations, it is expected that  $M_L = 3/2 M_W + C$  for  $M < 2$ . Between these two theoretically expected linear scaling regimes is a transition. The magnitude range at which the transition occurs depends on the attenuation properties and source characteristics of the region of interest and needs to be determined empirically. No theory exists to prescribe the functional form of the transition. A quadratic form is often used for the convenience of having the lowest number of fitting parameters after a linear relation.

The estimated quadratic relation between  $M_L$  and  $M_W$  for small magnitude events (equation 4.6) is in good agreement with what has been estimated from other studies at other sites (e.g. Grünthal et al., 2009, Goertz-Allmann et al., 2011). However, this is strictly valid only within the fitting range of the measured magnitudes. Furthermore this relation is consistent with the listed theoretical considerations: (i) it exhibits a slope very close to 2/3 at the low magnitude end, as also observed by Munafò et al., 2016, and (ii) leads to a data-consistent 1:1 slope at the high magnitude end.

Alternatively, one could have chosen a piecewise continuous function, forcing a linear 2/3 fit at low magnitudes and a linear 1:1 fit at high magnitudes with a quadratic function in between (see, e.g., Goertz-Allmann et al., 2011 for an example in Switzerland). A piecewise continuous scaling relation as, e.g., presented in Goertz-Allmann et al., 2011 can be forced to honour any theoretical expectations. The problem with this approach, however, is that the catalogue presented in Dost et al., 2018 may not contain enough data at the low magnitudes to sufficiently constrain a linear fit. It may therefore be worth trying to further expand the catalogue of moment magnitude estimates with newer data, since the network was upgraded. It can be expected that the lower detection threshold in newer data may allow to add more moment magnitude estimates for events below magnitude 2, hence increasing the statistical base for determination of the low-magnitude scaling.

It should be emphasized that the seismicity in the region is nonstationary, and time-dependent b-values are required in the hazard analysis, based mainly on  $M_L < 2.5$ . Therefore, measured  $M_L$  values should ideally be converted to  $M_W$ , using a suitable scaling relation, before a reliable b-value can be determined.

## References

- Abercrombie, R.E. (1995). "Earthquake source scaling relationships from -1 to 5 ML using seismograms recorded at 2.5-km depth". In: *Journal of Geophysical Research: Solid Earth* 100.B12, pp. 24015–24036.
- Ahorner, L. (1983). "Historical seismicity and present-day microearthquake activity of the Rhenish Massif, Central Europe". In: *Plateau Uplift*. Springer, pp. 198–221.
- Boatwright, J. (1978). "Detailed spectral analysis of two small New York State earthquakes". In: *Bulletin of the Seismological Society of America* 68.4, pp. 1117–1131.



- Boatwright, J. (1984). "Seismic estimates of stress release". In: *J. of Geoph. Res.* 89.B8, pp. 6961–6968.
- Bourne, S.J., S.J. Oates, J. van Elk, and D. Doornhof (2014). "A seismological model for earthquakes induced by fluid extraction from a subsurface reservoir". In: *Journal of Geophysical Research: Solid Earth* 119.12, pp. 8991–9015.
- Brune, J.N. (1970). "Tectonic stress and the spectra of seismic shear waves from earthquakes". In: *Journal of geophysical research* 75.26, pp. 4997–5009.
- Deichmann, N. (2006). "Local magnitude, a moment revisited". In: *Bulletin of the Seismological Society of America* 96.4A, pp. 1267–1277.
- Deichmann, N. (2017). "Theoretical basis for the observed break in ML/M w scaling between small and large earthquakes". In: *Bulletin of the Seismological Society of America* 107.2, pp. 505–520.
- Dost, B., B. Edwards, and J.J. Bommer (2016). *Local and Moment Magnitudes in the Groningen Field*. Tech. rep. KNMI.
- Dost, B., B. Edwards, and J.J. Bommer (2018). "The Relationship between M and ML: A Review and Application to Induced Seismicity in the Groningen Gas Field, The Netherlands". In: *Seismological Research Letters*.
- Dost, B., T. Van Eck, and H. Haak (2004). "Scaling of peak ground acceleration and peak ground velocity recorded in the Netherlands". In: *Bollettino di Geofisica Teorica ed Applicata* 45.3, pp. 153–168.
- Edwards, B., B. Allmann, D. Fäh, and J. Clinton (2010). "Automatic computation of moment magnitudes for small earthquakes and the scaling of local to moment magnitude". In: *Geophysical Journal International* 183.1, pp. 407–420.
- Edwards, B., T. Kraft, C. Cauzzi, P. Kästli, and S. Wiemer (2015). "Seismic monitoring and analysis of deep geothermal projects in St Gallen and Basel, Switzerland". In: *Geophysical Journal International* 201.2, pp. 1022–1039.
- Goertz-Allmann, B.P., B. Edwards, F. Bethmann, N. Deichmann, J. Clinton, D. Fäh, and D. Giardini (2011). "A new empirical magnitude scaling relation for Switzerland". In: *Bulletin of the Seismological Society of America* 101.6, pp. 3088–3095.
- Grünthal, G., R. Wahlström, and D. Stromeyer (2009). "The unified catalogue of earthquakes in central, northern, and northwestern Europe (CENEC)-updated and expanded to the last millennium". In: *Journal of Seismology* 13.4, pp. 517–541.
- Hanks, T. and H. Kanamori (1979). "A magnitude moment scale". In: *J. geophys. Res.* 84, pp. 2348–2351.
- Kraaijpoel, D. and B. Dost (2013). "Implications of salt-related propagation and mode conversion effects on the analysis of induced seismicity". In: *Journal of Seismology* 17.1, pp. 95–107.
- Kruiver, P.P., E. van Dedem, R. Romijn, G. de Lange, M. Korff, J. Stafleu, J.L. Gunnink, A. Rodriguez-Marek, J.J. Bommer, J. van Elk, et al. (2017). "An integrated shear-wave velocity model for the Groningen gas field, The Netherlands". In: *Bulletin of Earthquake Engineering* 15.9, pp. 3555–3580.
- Munafò, I., L. Malagnini, and L. Chiaraluce (2016). "On the relationship between  $M_W$  and  $M_L$  for small earthquakes". In: *Bull. Seismol. Soc. Am.* 106, pp. 2402–2408.

Richter, C.F. (1935). "An instrumental earthquake magnitude scale". In: *Bulletin of the Seismological Society of America* 25.1, pp. 1-32.

## 4.4 Stress drop computation

### 4.4.1 Context and overview

The stress drop  $\Delta\sigma$  of an earthquake is a measure of how much stress is released along a fault during an earthquake. This is an important source parameter, which defines the theoretical form of the source spectrum. It is typically estimated from the corner frequency  $f_C$  of the displacement spectrum following Brune's relation:

$$\Delta\sigma = \frac{7}{16} M_0 \left( \frac{f_C}{0.37 v_S} \right)^3 \quad (4.7)$$

where  $v_S$  is the shear-wave velocity at the source. The higher the stress drop of an event, the higher the corner frequency of the source displacement spectrum. Translated into acceleration (multiplication by  $\omega^2$ ), this means that the higher the corner frequency, the higher the spectral acceleration amplitude of the event, and accordingly, the higher will be the predicted ground motion for the event. An estimate of stress drop is therefore required for a reliable prediction of ground motions.

In its original definition, stress drop relates to the difference in shear stress before and after the earthquake. In practice, however, when stress drop is inverted empirically from displacement spectra through equation 4.7, it has more the character of a parameter to describe the functional form of the source spectrum for further analysis, such as ground motion prediction equations (GMPE's). It is therefore sometimes also referred to as stress parameter (e.g., in Bommer et al., 2016) to express the more empirical use of it and to avoid over-interpretation.

In its original definition, stress drop relates to the difference in shear stress before and after the earthquake.

Uncertainties in determining stress drop are typically large and can easily span orders of magnitudes. Often, epistemic uncertainties between different studies are not reconcilable and generally depend on the underlying assumptions of the utilized inversion method, and, not the least, the available bandwidth and magnitude range of the data.

### 4.4.2 Observations and analysis of previous work

The dataset is too small and the uncertainties of stress drop estimates too large to derive a statistically significant trend.

KNMI used the Brune source model (Brune, 1970), modified by Boatwright (1978) to estimate the best fitting parameters for the low-frequency spectral level  $\Omega_0$ , the spectral corner frequency  $f_c$ , and the  $t^*$ -operator (describing attenuation along the travel path) using a grid search. A

more detailed description of the processing is given in Dost et al. (2016) and Dost et al. (2018).

34 events have been analysed by Dost et al. (2016), and they conclude that the majority of events show a comparatively low stress drop estimate of  $\Delta\sigma < 20$  bar ( $< 2$  MPa). The individual estimates are depicted in figure 4.39 (taken from Dost et al. (2016)) and exhibit, as expected, a large scatter with values ranging from 0.1 to 50 bar (0.01 to 5 MPa). Uncertainties depicted by vertical error bars have been estimated using the approach of Viegas et al. (2010). Data from only one reference station has been analysed. An increase of  $\Delta\sigma$  with moment magnitude  $M_W$  may be observed (figure 4.39). However, it is acknowledged by Dost et al. (2016) that the dataset is too small and the uncertainties too large to derive a statistically significant trend.

$\Delta\sigma$  of 85 recordings were also analysed by Bommer et al. (2016) using the same method of Edwards et al. (2008). Estimates of event-specific  $\Delta\sigma$  in this analysis are overall similar to those found by Dost et al., 2016, with values ranging range from 0.1 to 50 bars (0.01 to 5 MPa). Bommer et al. (2016) report an event average of 7 bars (0.7 MPa), and a record average of 9 bars (0.9 MPa, see figure 4.40). Error bars were again determined using the method of Viegas et al. (2010). Stress drop estimates given in Bommer et al. (2016) are apparently a subset of stress drop estimates reported by DeDontney et al. (2016) for magnitudes  $> 2.5$ , although the individual estimates appear to differ somewhat. DeDontney et al. (2016) furthermore state a "best-fitting single value" of 3 MPa (30 bar), which appears inconsistent with the average reported by Bommer et al. (2016).

Finally, Kraaijpoel and Dost (2013) estimated stress drop for the largest recorded events and also concluded with comparatively low stress drop values.

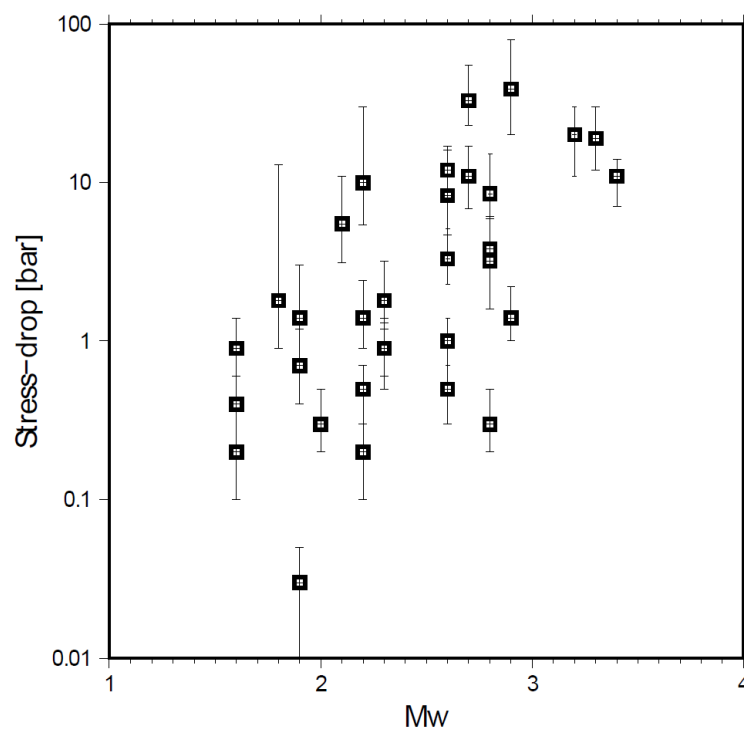


**Fig. 4.39:** Overview of stress drop measurements for 34 Groningen events. Figure taken from Dost et al. (2016).

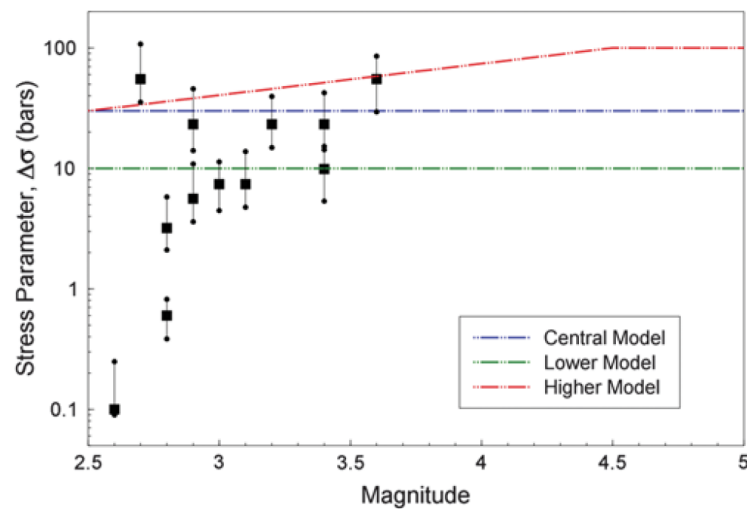


**Fig. 4.40:** Individual stress parameter estimates, with vertical bars indicating confidence intervals using the procedure of Viegas et al. (2010), compared with the three stress parameter models defined for ground-motion simulations. Figure taken from Bommer et al. (2016).

#### 4.4.3 Comparison to state-of-the-art and conclusions

Of the studies presented above, which are reporting stress drop results (Bommer et al., 2016, Dost et al., 2016, Kraaijpoel and Dost, 2013, DeDontney et al., 2016), all use the same method of Edwards et al. (2008) for stress drop estimation, and come to similar conclusions. All conclude that the obtained stress drop estimates can be considered low in comparison to average tectonic earthquakes, although no quantitative comparison is given. Bommer et al. (2016) attribute these comparatively low stress drop values to the generally lower hypocentral depth of induced earthquakes compared to tectonic earthquakes. Lower stress drop estimates for shallow earthquakes can arise from a number of causes. One possible reason is the generally lower shear wave velocity at the source, if the shear wave velocity in equation 4.7 is not varied according to hypocentral depth, or a depth variation is unknown (see, e.g., Allmann and Shearer, 2009). In Groningen, the hypocentral depths are very similar and the shear wave velocity well known.

Furthermore, all evaluated studies appear to be consistent in the use of definitions (stress drop according to Brune as defined in equation 4.7), and parameters such as shear wave velocity. Other possible reasons for differing stress drop estimates could arise from the underlying assumptions on attenuation and geometrical spreading. We note for example, that the geometrical spreading of  $R^{-1}$  assumed by Bommer et al., 2016 is not consistent with the best-

All studies conclude that stress drop estimates in Groningen can be considered low in comparison to average tectonic earthquakes, although no quantitative comparison is given.

fitting geometrical spreading observed from the attenuation relation of  $R^{-1.33}$  determined for the Groningen area (see equation 4.4 in section 4.3).

Although generally consistent with Bommer et al., 2016, the results presented in Dost et al., 2016 have been obtained from only one reference station. When using only one station, source radiation effects can not be averaged out, and the resulting stress drop estimates may be biased for individual events due to radiation pattern effects, leading to larger scatter. Bommer et al., 2016 use recordings at several stations for their analysis. However the azimuthal coverage of the analysed data for individual events is not reported. The events analysed by Kraaijpoel and Dost (2013) were recorded by at least three accelerometers each.

The two most common sources of epistemic uncertainty and bias in stress drop estimates are a limited bandwidth of the analysed data and the well known trade-off between source corner frequency and travel-path attenuation.

A model-dependent method such as the method of Edwards et al. (2008) is known to have difficulties resolving the trade-off between source- and attenuation effects. For example, Goertz-Allmann and Edwards (2013) showed that the assumption of a frequency-independent  $Q$  can result in a lower stress drop estimate. The same study concluded that the assumption of a frequency-dependence of  $Q$  yields overall more consistent results, even though independent data constraining an actual frequency-dependence of  $Q$  in their study region is scarce.

Stress-drop studies are in particular prone to suffer from lack of bandwidth in the underlying waveform data. This may stem either from a limited recording bandwidth imposed by instrument responses or sampling rates, or from a lack of effective bandwidth due to various sources of noise. A typical noise source at the very low frequencies affecting spectral estimates of larger earthquakes are the ocean microseisms leading to low signal-to-noise (SNR) ratios below 1 Hz. More problematic in Groningen with its high population density is cultural noise at high frequencies, which starts to severely limit the SNR at frequencies above 50 Hz (figure 3 in Dost et al., 2018). This leads NORSAR to believe that the bandwidth is too limited in Groningen to unambiguously resolve the mentioned trade-offs. This could explain why stress drop estimates for lower magnitudes tend to be lower, even though this trend is not observed at a statistically significant level due to the small sample size.

As discussed in the beginning of this section, stress drop estimates can have an effect on ground motion predictions. Considering the mentioned uncertainties of the stress drop estimates, a conservative approach should be used for any ground motion prediction. This is the case, as Bommer et al. (2016) determine a  $\Delta\sigma$  of 30 bars (3 MPa) for the best-fitting simulation model, which is significantly higher than the 7 bars (0.7 MPa) event average. The value of 3 MPa is also consistent with the "best-fitting single value" stress drop of 3 MPa reported by DeDontney et al., 2016.

In light of this, NORSAR recommends to analyse the sensitivity of the obtained stress drop results with respect to underlying assumptions such as frequency-independent  $Q$ , and attempt a verification

of the obtained stress drop estimates with an independent method. However, owed to the comparatively small size of the catalogue at Groningen, the options for independent spectral analysis methods are limited and need to be carefully evaluated with respect to sample size, coverage, and reliability.

More advanced methods for source parameter estimation are based on Empirical Green's function analysis (e.g. Shearer et al., 2006, Hough, 1997, Viegas et al., 2010) to remove path effects. However, these methods depend either on collocated events, or a suitable source-receiver geometry and associated wave path coverage. The catalogue utilized so far for estimating source parameters (< 50 events) is likely too small to ensure a suitable wave path coverage. The determination of collocated events requires the use of a correlation-based method, which has so far resulted in only very limited numbers of collocated events in the Groningen area (see section 5.2).

## References

- Allmann, B.P. and P.M. Shearer (2009). "Global variations of stress drop for moderate to large earthquakes". In: *Journal of Geophysical Research: Solid Earth* 114.B1.
- Boatwright, J. (1978). "Detailed spectral analysis of two small New York State earthquakes". In: *Bulletin of the Seismological Society of America* 68.4, pp. 1117–1131.
- Bommer, J.J., B. Dost, B. Edwards, P.J. Stafford, J. van Elk, D. Doornhof, and M. Ntinalexis (2016). "Developing an application-specific ground-motion model for induced seismicity". In: *Bulletin of the Seismological Society of America* 106.1, pp. 158–173.
- Brune, J.N. (1970). "Tectonic stress and the spectra of seismic shear waves from earthquakes". In: *Journal of geophysical research* 75.26, pp. 4997–5009.
- DeDontney, N. et al. (2016). *Maximum Magnitude of Induced Earthquakes in the Groningen Gas Field*. Tech. rep. Nederlandse Aardolie Maatschappij BV.
- Dost, B., B. Edwards, and J.J. Bommer (2016). *Local and Moment Magnitudes in the Groningen Field*. Tech. rep. KNMI.
- Dost, B., B. Edwards, and J.J. Bommer (2018). "The Relationship between M and ML: A Review and Application to Induced Seismicity in the Groningen Gas Field, The Netherlands". In: *Seismological Research Letters*.
- Edwards, B., A. Rietbrock, J. J. Bommer, and B. Baptie (2008). "The acquisition of source, path, and site effects from microearthquake recordings using Q tomography: Application to the United Kingdom". In: *Bulletin of the Seismological Society of America* 98.4, pp. 1915–1935.
- Goertz-Allmann, B.P. and B. Edwards (2013). "Constraints on crustal attenuation and three-dimensional spatial distribution of stress drop in Switzerland". In: *Geophysical journal international* 196.1, pp. 493–509.
- Hough, S.E. (1997). "Empirical Green's function analysis: Taking the next step". In: *Journal of Geophysical Research: Solid Earth* 102.B3, pp. 5369–5384.
-

- Kraaijpoel, D. and B. Dost (2013). "Implications of salt-related propagation and mode conversion effects on the analysis of induced seismicity". In: *Journal of Seismology* 17.1, pp. 95-107.
- Shearer, P.M., G.A. Prieto, and E. Hauksson (2006). "Comprehensive analysis of earthquake source spectra in southern California". In: *Journal of Geophysical Research: Solid Earth* 111.B6.
- Viegas, G., R.E. Abercrombie, and W.Y. Kim (2010). "The 2002 M5 Au Sable Forks, NY, earthquake sequence: Source scaling relationships and energy budget". In: *Journal of Geophysical Research: Solid Earth* 115.B7.



## 5 Review of advanced data analyses

### 5.1 Event relocation

Various event relocation methodologies are being actively investigated for use at Groningen. In particular, an improvement to the depth estimates for the induced seismicity at Groningen is required, as this directly impacts the seismic hazard. If earthquakes are occurring in the basement, there is the potential for higher magnitudes (DeDontney et al., 2016; Vlek, 2018); while events above the reservoir have implications for cap-rock integrity. The current procedure at KNMI is to fix event depths at 3 km.

In addition to better constraining event depths, being able to better tie event locations to fault structures provides additional valuable information for assessing the seismic hazard at Groningen.

Work by KNMI to improve the depth constraint at Groningen is described by Spetzler and Dost (2017). One of the major difficulties in constraining event depth is that there is a trade-off between the origin time of the earthquake and its depth. This means a change in event depth can simply be represented by a change in event origin time. Depth can be better constrained by:

- using multiple phases that travel with different velocities;
- using observations that are close to the event epicentre.

These constraints are incorporated into the guidance provided by Bondár et al. (2004) and Husen (2010), for establishing accurate event locations, which we assess in section 4.2.

In Spetzler and Dost (2017), the benefit of using observations close to the event epicentre is shown in the travel-time curves (Figure 5.1). This shows the travel-time curves for three different source depths. At epicentral distances between 0 and  $\sim 3$  km, there are observable differences in the travel-times, which indicate that event depths can be better constrained. From 3 km to 8.5 km, the travel-times for the three different source depths are less distinguishable. After  $\sim 8.5$  km, there is a significant change in the travel-times for the three source depths as diving waves become the first arrival for the deeper sources. It should be noted that these travel-times are based on the NAM 3D velocity model, not the 1D 'Northern Netherlands' model that is used in the current KNMI location procedures. For Spetzler and Dost (2017), they investigate the potential benefits of using a location methodology that uses the differential travel-times between station pairs for the P-wave. This is known as the Equal Differential Time (EDT) method, and is based on Font et al. (2004), Lomax (2005), and Satriano et al. (2008). This method is insensitive to the origin-time/depth trade-off. In addition, the minimisation involves a global grid search, rather than an iterative linearised inversion, making the location less susceptible to mislocation, compared to the current KNMI procedures. They process 87 events from February 2014 to July 2016 using the EDT method in combination with 1D profiles from the NAM 3D velocity model. The results of their relocation methodology estimates depths of between 2200 m and 3500, with the majority between 2600 m and 3200 m - still in the reservoir interval. The results also

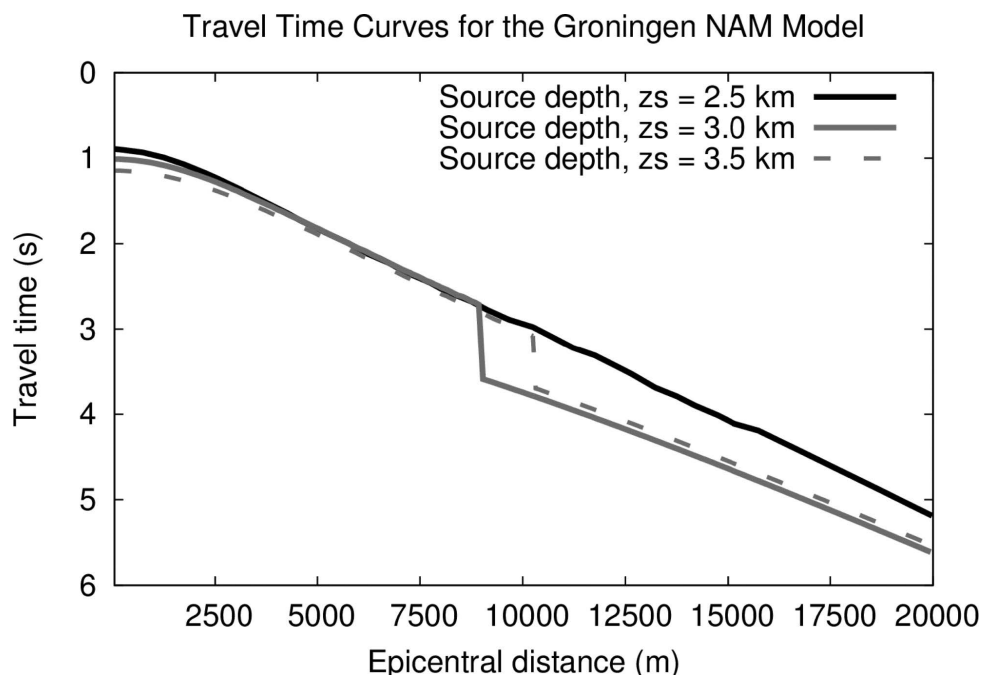


**Fig. 5.1:** Travel-time curves for a source depth at 2500, 3000 and 3500 m. Taken from Spetzler and Dost (2017).

show changes to the lateral locations of events.

Spetzler and Dost (2017) state that as a rule of thumb, at least 3–4 stations with epicentral distances shorter than 5–8 km must be available in order to obtain an estimate of the event depth using the EDT method. However, the lateral location can still be established if the station coverage (distance and azimuth) is not optimal. For events prior to 2014, it is stated that the network is too sparse to apply the EDT methodology.

Earlier work done by Pickering (2015), used the deep borehole sensors installed by NAM in wells ZRP and SDM. These wells provide better resolving power for depth and using a global grid search for a dataset of 32 events, revealed upper and lower bounds of 3020 m and 2822 m respectively, based on one standard deviation from the mean depth (2921 m). While this showed that the event depths were largely constrained to the reservoir, variation still exists in the event depths and the size of the dataset was limited.

An alternative assessment of event locations at Groningen is provided by Wuestefeld et al. (in press). Using the case of the ZRP and SDM downhole wells and a 1D velocity model from Groningen, they show the variation that exists between different location algorithms and minimisation schemes using synthetic locations. This includes comparing the EDT minimisation with the standard least squares approach, in addition to a new '1Plus' minimisation. This is done for six different location algorithms (all direct search methods - see section 4.2 and Lomax et al. (2014) for an overview). The results revealed variations of over 500 m in depth (at the 95% confidence level) using a directed grid search, while a full grid search, naturally provides the best solution in terms of depth. Moreover, the EDT min-

imisation as used by Spetzler and Dost (2017), was shown to provide more accurate event locations as compared to the standard least squares approach.

Work by Utrecht university and KNMI (Jagt et al., 2017), has also looked at improving the lateral earthquake locations at Groningen such that the fault structures may be better delineated. As described in section 5.2, events were first clustered using cross-correlation. However, this resulted in only ~10% of events recorded at station WDB being grouped into one of six clusters, due to highly variable waveforms. The clustered events, which occurred prior to the expanded seismic network being deployed at Groningen, were then relocated relative to master events that were recorded by the dense network - and thus much better resolved. During the relocation, arrival-times from the master event and the clustered event must be present on the same station. Therefore, the relocation itself does not use data from the new network. The methodology is similar to the double-difference approach of Waldhauser and Ellsworth (2000), with travel-time differences between pairs of events providing the input data to determine their relative locations. In the standard approach by Waldhauser and Ellsworth (2000), all events move relative to each other, while Jagt et al. (2017), keep the master event locations fixed. Moreover, Jagt et al. (2017) use a grid search around the master event to search for all possible locations for the clustered events. Such an approach is usually unfeasible for relocation methodologies, but since the number of clustered events is so low, and the search region is constrained by the master events, then the approach brings more stability to the relocations.

Another way to enhance earthquake locations in the Groningen field are full waveform methods. Two of those, simultaneously inverting for source mechanism and event locations, are described in section 5.4.

## References

- Bondár, I., S.C. Myers, E.R. Engdahl, and E.A. Bergman (2004). "Epicentre accuracy based on seismic network criteria". In: *Geophysical Journal International* 156.3, pp. 483–496. ISSN: 0956540X. DOI: [10.1111/j.1365-246X.2004.02070.x](https://doi.org/10.1111/j.1365-246X.2004.02070.x).
- DeDontney, N. et al. (2016). *Maximum Magnitude of Induced Earthquakes in the Groningen Gas Field*. Tech. rep. Nederlandse Aardolie Maatschappij BV.
- Font, Y., H. Kao, S. Lallemand, C.-S. Liu, and L.-Y. Chiao (2004). "Hypocentre determination offshore of eastern Taiwan using the Maximum Intersection method". In: *Geophysical Journal International* 158.2, pp. 655–675.
- Husen, S. (2010). "CORSSA". In: chap. Earthquake Location Accuracy.
- Jagt, L., E. Ruigrok, and H. Paulssen (2017). "Relocation of clustered earthquakes in the Groningen gas field". In: *Netherlands Journal of Geosciences* 96.5, s163–s173.
- Lomax, A. (2005). "A Reanalysis of the Hypocentral Location and Related Observations for the Great 1906 California Earthquake". In: *Bulletin of the Seismological Society of America* 95.3, pp. 861–877. ISSN: 0037-1106. DOI: [10.1785/0120040141](https://doi.org/10.1785/0120040141).
-

- Lomax, A., A. Michelini, and A. Curtis (2014). "Encyclopedia of Complexity and Systems Science". In: ed. by R.A. Meyers. Springer New York. Chap. Earthquake Location, Direct, Global-Search Methods, pp. 1–33. DOI: [10.1007/978-3-642-27737-5\\_150-2](https://doi.org/10.1007/978-3-642-27737-5_150-2).
- Pickering, M. (2015). *An estimate of the earthquake hypocenter locations in the Groningen Gas Field*. Tech. rep. Nederlandse Aardolie Maatschappij BV.
- Satriano, C., A. Lomax, and A. Zollo (2008). "Real-Time Evolutionary Earthquake Location for Seismic Early Warning". In: *Bulletin of the Seismological Society of America* 98.3, pp. 1482–1494. ISSN: 0037-1106. DOI: [10.1785/0120060159](https://doi.org/10.1785/0120060159).
- Spetzler, J. and B. Dost (2017). "Hypocentre estimation of induced earthquakes in Groningen". In: *Geophysical Journal International* 209.1, pp. 453–465.
- Vlek, C. (2018). "Induced Earthquakes from Long-Term Gas Extraction in Groningen, the Netherlands: Statistical Analysis and Prognosis for Acceptable-Risk Regulation". In: *Risk Analysis*.
- Waldhauser, F. and W.L. Ellsworth (2000). "A double-difference earthquake location algorithm: method and application to the northern Hayward fault, California". In: *Bulletin of the Seismological Society of America* 90.6, pp. 1353–1368.
- Wuestefeld, A., S. Greve, S.P. Näsholm, and V. Oye (in press). "Benchmarking earthquake location algorithms: A synthetic comparison". In: *Geophysics*.

## 5.2 Cross-correlation of waveforms

### 5.2.1 Overview

In seismology, waveform cross-correlation can be used in a wide range of possibilities, e.g.:

- event detection (e.g. Harris, 1991, Young et al., 1996, Gibbons and Ringdal, 2006);
- event clustering (e.g. Got et al., 1994, Dyer et al., 2010);
- sensor orientation (e.g. Zha et al., 2013);
- wave velocities determination (e.g. Poupinet et al., 1984, Brenguier et al., 2007, Duputel et al., 2009, Mordret et al., 2013, Taira et al., 2015).

The Groningen data have been used for each of these four main application domains and we give a brief overview of what has been done for each of them in the next paragraphs.

### 5.2.2 Cross-correlation for event detection

The detection methods based on waveform cross-correlation are generically called **pattern detectors**. They exploit the fact that if an event is well-recorded on a given station network, the waveforms from an event located in the vicinity of a previous event are very similar (Geller and Mueller, 1980).

The pattern detectors require a set (or at least one) of well-identified signals (the so-called *master*

*events*) which can then be used as templates for cross-correlation on continuous data. In that sense, the methods cannot be applied blindly from scratch and presuppose a relatively good knowledge of the dataset, especially for the identification and selection of the template events. Then pattern detectors can be used as a complement of more traditional detectors (such as e.g. STA/LTA, see section 4.1) and are particularly well-suited for the detection of low-SNR events.

At Groningen, in the framework of the ACISM project, different pattern detectors have been tested and applied both by NORSAR (multi-template correlation detectors) and Deschutes Signal Processing LLC (matched field processing). The latter technique is slightly more complex than classical correlation detectors. It consists in splitting the data into a large number of narrow bands and comparing the spatial structure of the templates and that of the data in each of the narrow bands. For that reason, the technique allows for more variability in the source mechanisms. Matched field processing is still applied to the Groningen seismic data by Dave Harris so far (e.g. Harris, 2018) whose results are sent to KNMI and collected to be part of a private catalogue (DSP, pers. comm., 2018).

### 5.2.3 Cross-correlation for event clustering

A **cluster** is generally defined as a group of elements presenting some similarities. In seismology, event clustering consists in finding several groups of events with similar waveform. The similarity measurement between two events is given by the normalised cross-correlation coefficient (value between 0 and 1). The higher the values, the more similar the events.

Seismic event clustering is a way of characterising the seismicity, and potentially highlights different types of events (then grouped in different clusters) with different mechanisms. This eventually gives information on the faults and processes involved in the seismicity generation. More importantly, the event clusters can be used as inputs for precise event relocation via the double-difference method (Waldhauser and Ellsworth, 2000) (see section 5.1).

At Groningen, a clustering analysis was performed by Jagt et al. (2017) using 4.5 years of data recorded by the North and vertical components of the bottom sensor of the borehole station **WDB**. The cross-correlation matrices resulting from the analysis are presented in figure 5.2a-b and the corresponding seismicity map coloured by event clusters is shown in figure 5.2c. An observation is that each identified cluster contains co-located events, with the exception of the cluster 1's events (in red) which are more widely distributed and expand up to 13 km.

To summarise, the major result of the paper is that only a limited number of clusters containing a limited number of events are observed (approximately 10% of the total number of events considered in the study). According to the authors, this suggests that many faults or fault segments are active in the Groningen area, resulting in a variety of source mechanisms, and by extension of waveforms.

NORSAR also performed a cluster analysis in the framework of the ACISM project and came to a similar conclusion, with a few number of well defined clusters.

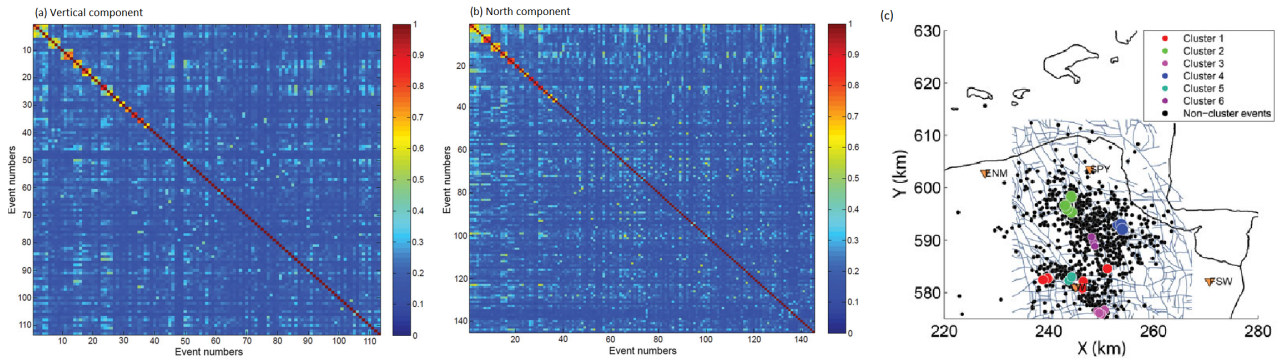


**Fig. 5.2:** (a-b) Sorted cross-correlation matrices for events recorded on WDB4 and filtered between 1 and 8 Hz: (a) Vertical component; (b) North component. (c) Location of the event clusters (coloured) identified on the vertical component of WDB4 as well as non-clustered events (black). The background shows the fault network. Taken from Jagt et al., 2017.

### 5.2.4 Cross-correlation for sensor orientation

Knowing the seismic sensor orientations is a key pre-requisite for detailed data analysis and most notably, for moment tensor determination (section 5.3). However, the orientation of deep borehole stations is unknown and needs to be computed, usually by using either checkshots or teleseismic events.

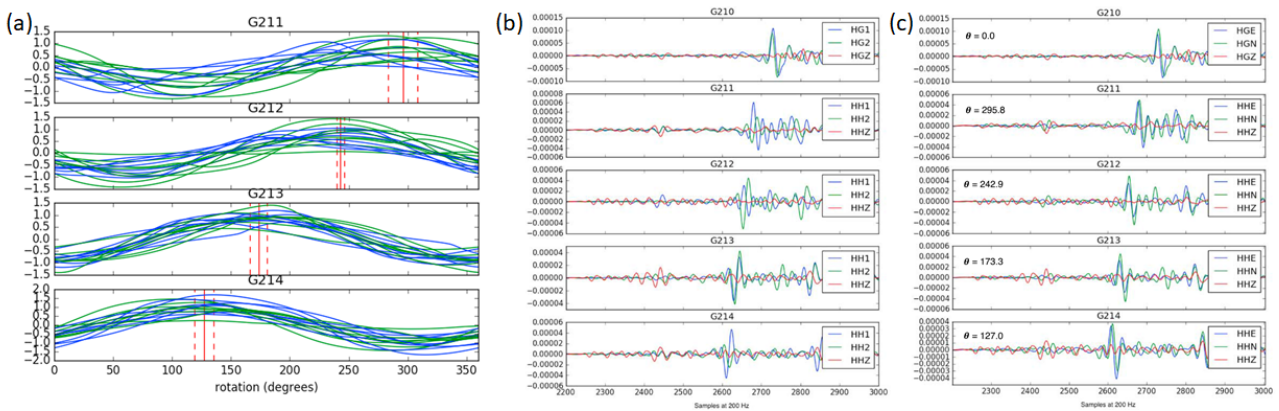


**Fig. 5.3:** Example of orientation results obtained by Hofman et al. (2017) for the borehole **G21**. (a) Sine functions showing the maximum cross-correlation coefficient in function of the sensor rotation angle  $\theta$  for an optimised lag-time. (b) Example of an event before rotation. (c) Same event as (b) after correction from the estimated  $\theta$  angles. The waveform on top is recorded by the surface accelerometer (reference).

In the paper published by Hofman et al. (2017), the orientation of almost all the sensors constituting the G-network were determined by taking advantage of the accelerometers placed at the same time at the surface which orientations are presumably known. For that purpose, the authors used local seismicity and recovered the sensor orientations based on the similarity between the horizontal channels of the borehole sensors and the accelerometers. An example of a successful orientation for the borehole **G21** is shown in figure 5.3.

### 5.2.5 Cross-correlation for wave velocities determination

In seismology, for many years, the signal recorded between the seismic events was not used and even often cut out (e.g. triggered mode). Nowadays, together with the growing of data storage capacities, it has been shown that continuous records contain a lot more information. In particular, the past few years have seen the emergence of a new technique which consists in cross-correlating the ambient noise for pairs of sensors (Shapiro and Campillo (2004), Roux et al. (2005)). This method, also called noise interferometry, enables to retrieve the medium response (or Green’s function) between two sensors and allows building wave velocity models (e.g. Brenguier et al. (2007), Mordret et al. (2013)). Eventually, the method also has a huge potential for tracking the velocity changes and modifications of the medium that may occur with time (e.g. Duputel et al. (2009), Taira et al. (2015)).

Two recent studies (Hofman et al., 2017, Zhou and Paulssen, 2017) have been using interferometry to determine the wave velocities in the Groningen field. To be mentioned too, a larger-scale study has also been carried out by Yudistira et al. (2017) for the whole Netherlands.

The work by Zhou and Paulssen (2017) includes exclusively seismic data from the deep downhole SDM-1 operated by NAM where 10 geophones are placed between 2,750 and 3,017 m depth. The P- and S-wave velocities that they determine using noise interferometry present a good match with the velocity logs provided by NAM (figure 5.4a).

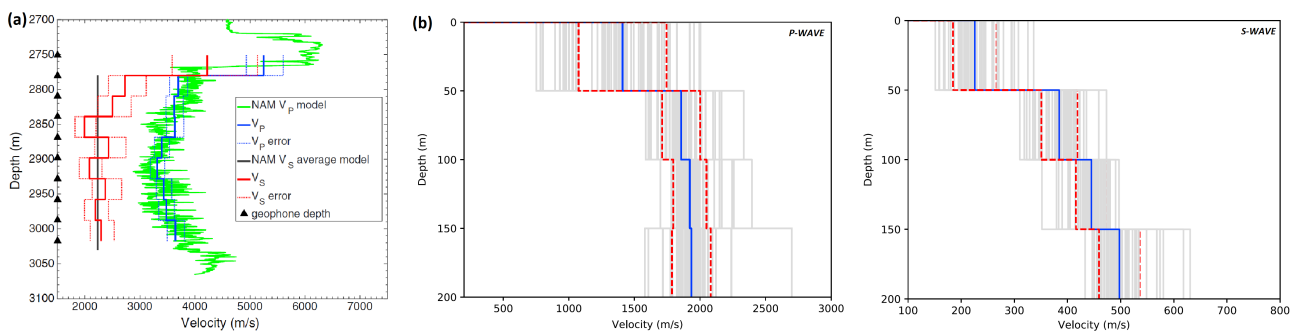


**Fig. 5.4:** (a) P- and S-wave interval velocities retrieved by Zhou and Paulssen (2017) at SDM-1 deep downhole. (b) P- and S-wave interval velocities (respectively left and right) retrieved by Hofman et al. (2017) for 60 boreholes of the G-network. Blue line: mean velocity. Red lines: one standard-deviation from the mean.

On the other hand, Hofman et al. (2017) used the seismic data from 60 stations of the G-network, including each a surface accelerometer and 4 deeper sensors down to 200 m. Their approach also relies on interferometry, but instead of using noise, they decided to use the records of local seismic events of  $M_L \geq 1.5$ . The P- and S-wave interval velocities computed in their analysis are presented in the figure 5.4b. The authors also produced interpolated velocity maps at the different investigated depths. As underlined in their conclusions, Hofman et al. (2017) present the first detailed analysis of the near-surface P-wave velocity model in the Groningen field, so that no comparison is possible with potential previous studies. Their results for the S-wave velocities, however, are consistent with

previous studies based on lithology and/or surface wave inversion.

## References

- Brenguier, F., N.M. Shapiro, M. Campillo, A. Nercessian, and V. Ferrazzini (2007). "3D surface wave tomography of the Piton de la Fournaise volcano using seismic noise correlations". In: *Geophysical Research Letters* 34.2.
- DSP, pers. comm. (2018). Personal communication.
- Duputel, Z., V. Ferrazzini, F. Brenguier, N. Shapiro, M. Campillo, and A. Nercessian (2009). "Real time monitoring of relative velocity changes using ambient seismic noise at the Piton de la Fournaise volcano (La Réunion) from January 2006 to June 2007". In: *Journal of Volcanology and Geothermal Research* 184.1, pp. 164–173.
- Dyer, B.C., U. Schanz, T. Spillmann, F. Ladner, and M.O. Häring (2010). "Application of microseismic multiplet analysis to the Basel geothermal reservoir stimulation events". In: *Geophysical Prospecting* 58, pp. 791–807.
- Geller, R.J. and C.S. Mueller (1980). "Four similar earthquakes in central California". In: *Geophysical Research Letters* 7.10, pp. 821–824.
- Gibbons, S.J. and F. Ringdal (2006). "The detection of low magnitude seismic events using array-based waveform correlation". In: *Geophysical Journal International* 165.1, pp. 149–166.
- Got, J.-L., J. Fréchet, and F.W. Klein (1994). "Deep fault plane geometry inferred from multiplet relative relocation beneath the south flank of Kilauea". In: *Journal of Geophysical Research: Solid Earth* 99.B8, pp. 15375–15386.
- Harris, D.B. (1991). "A waveform correlation method for identifying quarry explosions". In: *Bulletin of the Seismological Society of America* 81, pp. 2395–2418.
- Harris, D.B. (2018). *Detections from the 2015 Zeerijp master event*. PPT sent to KNMI in March 2018.
- Hofman, L.J., E. Ruigrok, B. Dost, and H. Paulssen (2017). "A shallow seismic velocity model for the Groningen area in the Netherlands". In: *Journal of Geophysical Research: Solid Earth* 122.10, pp. 8035–8050.
- Jagt, L., E. Ruigrok, and H. Paulssen (2017). "Relocation of clustered earthquakes in the Groningen gas field". In: *Netherlands Journal of Geosciences* 96.5, s163–s173.
- Mordret, A., M. Landès, N. M. Shapiro, S. C. Singh, P. Roux, and O. I. Barkved (2013). "Near-surface study at the Valhall oil field from ambient noise surface wave tomography". In: *Geophysical Journal International* 193.3, pp. 1627–1643.
- Poupinet, G., W.L. Ellsworth, and J. Fréchet (1984). "Monitoring Velocity Variations in the Crust Using Earthquake Doublets: An Application to the Calaveras Fault, California". In: *Journal of Geophysical Research* 89, pp. 5719–5731.
- Roux, P., K.G. Sabra, P. Gerstoft, W. A. Kuperman, and M.C. Fehler (2005). "P-waves from cross-correlation of seismic noise". In: *Geophysical Research Letters* 32.19.



- Shapiro, N.M. and M. Campillo (2004). "Emergence of broadband Rayleigh waves from correlations of the ambient seismic noise". In: *Geophysical Research Letters* 31.7.
- Taira, T., F. Brenguier, and Q. Kong (2015). "Ambient noise-based monitoring of seismic velocity changes associated with the 2014 Mw 6.0 South Napa earthquake". In: *Geophysical Research Letters* 42.17, pp. 6997–7004.
- Waldhauser, F. and W.L. Ellsworth (2000). "A double-difference earthquake location algorithm: method and application to the northern Hayward fault, California". In: *Bulletin of the Seismological Society of America* 90.6, pp. 1353–1368.
- Young, C., M. Harris, J. Beiriger, S. Moore, J. Trujillo, M. Withers, and Aster R. (1996). *The waveform correlation event detection system project phase 1: issues in prototype development and testing*. Sandia Report SAND96-1916. Sandia National Laboratories.
- Yudistira, T., H. Paulssen, and J. Trampert (2017). "The crustal structure beneath The Netherlands derived from ambient seismic noise". In: *Tectonophysics* 721, pp. 361–371.
- Zha, Y., C. Webb Spahr, and W. Menke (2013). "Determining the orientations of ocean bottom seismometers using ambient noise correlation". In: *Geophysical Research Letters* 40.14, pp. 3585–3590.
- Zhou, W. and H. Paulssen (2017). "P and S velocity structure in the Groningen gas reservoir from noise interferometry". In: *Geophysical Research Letters* 44.23, pp. 11, 785–11, 791.

### 5.3 Focal mechanism computation using P- and S-wave amplitudes and polarities

#### 5.3.1 Context and overview

Source mechanisms - be it as focal mechanisms or moment tensors - are not reported in the KNMI induced earthquake catalogue. However, some relevant work has been performed at KNMI. Due to the often limited azimuthal coverage of the network before 2015, focal mechanisms have been computed (Dost et al., 2012) and published (Kraaijpoel and Dost, 2013) for only four events. This work will be described in section 5.3.2. All mechanisms show normal faulting at a steeply dipping fault. In addition, three of the four events indicate a similar direction for the strike of the fault (approx. 290°). For the Huizinge event on August 16, 2012, an attempt was made as well to recover the focal mechanism, but no stable solution could be found (Dost and Kraaijpoel, 2013). In the following, the concept of earthquake source mechanisms and focal mechanisms will be explained shortly.

#### Earthquake source mechanisms

Knowledge on the source mechanism of an earthquake is important input to:

- distinguish between different styles of faulting, even if the fault themselves are not mapped
- understand the causes of seismicity and enhance the insight into the geological, tectonic and geomechanical processes occurring within the subsurface
- seismic hazard assessment

- the discrimination of tectonic earthquakes and induced fault reactivation
- and, in case that full waveforms are inverted, the inversion for a source mechanism may be accompanied by an improved earthquake location that in turn may help delineate faults.

In order to study the geometry of the fault on which an earthquake occurred as well as the direction and amount of slip it involved, the amplitudes and shapes of the radiated seismic waves are employed as recorded on seismograms at various distances and azimuths (Stein and Wysession, 2009). The simplest method uses first motion (P-wave) polarities. Other approaches employ P-wave and/or S-wave amplitudes or P/S amplitude ratios. More sophisticated techniques use the full waveforms of body and or surface waves (Stein and Wysession, 2009). Two common models to represent earthquake source mechanisms are the focal mechanism and the moment tensor. In literature, the distinction between focal mechanisms and moment tensors is not always clear; however, we will employ the term “focal mechanism” as synonym for pure shear faulting. We will also term the double couple component of a moment tensor as “focal mechanisms” (see also explanation below).

### Focal mechanisms

Focal mechanisms represent the geometry of faulting during an earthquake assuming that only shear faulting occurred (Stein and Wysession, 2009). The fault is assumed to be a planar surface across which relative motion took place during the earthquake and the source mechanism is described with the help of three angles, the strike angle (the direction of the fault compared to the North direction, the dip angle (the orientation of the fault with respect to the surface) and the rake angle (the direction of motion on the fault plane; Stein and Wysession, 2009). However, the analysis of the seismograms cannot distinguish between the actual fault plane and the auxiliary plane situated at right angles to it. Additional information (e.g., geologic, geodetic, location of aftershocks) is required to solve this problem (Stein and Wysession, 2009). Another way to mathematically describe earthquake source mechanisms are moment tensors (see below). In section 5.3.2, focal mechanisms computed by KNMI will be analysed in more detail.

### Moment tensors

The seismic moment tensor is a generalized approach to describe seismic sources, including sources that cannot be reduced to shear faulting. To this end, equivalent body forces are employed that yield the same seismic radiation, but do not describe the actual fracture process (Stein and Wysession, 2009). Thus, they can also be used to describe single forces (e.g., generated by impacts, landslides and eruptions) and volumetric changes (e.g., explosions and collapses). Moment tensors are mathematically represented by a tensor

$$M = \begin{pmatrix} m_{xx} & m_{xy} & m_{xz} \\ m_{yx} & m_{yy} & m_{yz} \\ m_{zx} & m_{zy} & m_{zz} \end{pmatrix}, \quad (5.1)$$

where each of the nine components describes a force couple. This tensor is symmetric and contains only six independent components ( $m_{xy} = m_{yx}$ ,  $m_{xz} = m_{zx}$  and  $m_{yz} = m_{zy}$ ). A shear fracture, as described in the previous paragraph, is expressed mathematically as double couple (only two of the off-diagonal components are non-zero and equal, more precisely a pair of dependent components, either  $m_{xy}$  and  $m_{yx}$  or  $m_{xz}$  and  $m_{zx}$  or  $m_{yz}$  and  $m_{zy}$ ). Explosive or implosive sources are defined by an isotropic moment tensor, where all three diagonal elements are non-zero and equal (Stein and Wysession, 2009). Another class of non-double couple seismic sources (which cannot be described by simple shear faulting) are compensated linear vector dipoles (CLVDs), which are mathematically described by sets of three force dipoles that are compensated, with one dipole -2 times the magnitude of the others (Stein and Wysession, 2009). However, sources with large CLVD components are rare and usually only present in complicated tectonic environments (Stein and Wysession, 2009). When moment tensors are computed from seismograms, they usually are decomposed in several tensors for interpretation. Most often, the decomposition is into an isotropic, a CLVD and a double couple moment tensor, but other decompositions are possible (for example in an isotropic, a major and a minor double couple). However, both moment tensor decompositions and their interpretations are not unique (Stein and Wysession, 2009). This is analogous to the way that a vector can be decomposed into various sums of vectors with different magnitudes (Stein and Wysession, 2009).

Focal mechanisms derived by KNMI using P- and S-wave amplitudes and polarities will be described in section 5.3.2. Source mechanisms computed by NAM employing full waveforms will be explained in section 5.4.2, whereas source mechanisms calculated by KNMI using full waveforms will be presented in section 5.4.3.

### 5.3.2 Double couple mechanisms computed by KNMI

Due to the often limited azimuthal coverage of the network before 2015, focal mechanisms have been computed (Dost et al., 2012) and published (Kraaijpoel and Dost, 2013) for only four events located in the western part of the Groningen field (for results, see Table 9 reproduced from Kraaijpoel and Dost, 2013). The motivation for this work was a better association of earthquakes to specific faults, since the strike and dip of the source mechanism should be consistent with the fault geometry. Due to the limited azimuthal coverage of the region by the shallow borehole network, accelerometer data was employed to provide additional constraints (Kraaijpoel and Dost, 2013).

For this work, originally five events were selected based on their magnitude ( $M_L > 2.2$ ; Dost et al., 2012) and the availability of at least three accelerograms recorded at short distances ( $< 8$  km; Kraaijpoel and Dost, 2013). For one of the events (090201), no stable solution could be found (Dost et al., 2012), such that only the results for the four remaining events were published (Kraaijpoel and Dost, 2013). The following description is extracted from the reviewed paper by Kraaijpoel and Dost (2013).

A particular problem is posed by the presence of the Zechstein salt layer above the reservoir. The presence of salt layers is a well-known challenge for imaging and interpretation in reflection seismology (Ogilvie and Purnell, 1996; Lu et al., 2003). A similar problem is encountered in earthquake analysis, since firstly, it leads to defocussing of seismic energy, which has implications for the amplitudes of the seismic waves and the understanding of the observed source radiation pattern. Secondly, it results in strong conversions from P- to S-wave energy at the bottom of the salt layer, leading to the presence of strong S-wave precursors in the seismograms (Kraaijpoel and Dost, 2013).

**Input data** As input data for the focal mechanism computation, P-wave first motion directions and P/S amplitude ratios were employed. Due to the complexity of the recorded signals, S-wave polarities were not included in the inversion.

**Velocity model** In order to project measured data back onto the focal sphere of the earthquake source, the propagation of seismic waves through the medium has to be understood. To this end, a velocity model is required. Kraaijpoel and Dost (2013) employed P-wave velocities from the VELMOD-1 model, a comprehensive seismic velocity model for the Netherlands (van Dalen et al., 2006). The VELMOD-1 model contains nine main lithostratigraphic units (North Sea supergroup, Chalk group, Rijnland group, Upper and lower Germanic trias groups, Zechstein group, Upper Rotliegend group, Limburg group) and the P-wave velocity is assumed to increase linearly with depth, albeit with a different gradient in each layer. Depths of horizons separating the units were taken from the Geological Atlas of the Subsurface of the Netherlands (Duin et al., 2006). To obtain S-wave velocities, Castagna's relation for siliciclastic rocks has been applied (Castagna et al., 1985). Densities were assumed to be constant over each unit and were taken from Roest and Kuilman (1993). Since the layering was approximately horizontal in the area of interest, a 1-D velocity model was assumed (Kraaijpoel and Dost, 2013). The velocity model was only specified for depths shallower than 3.5 km, since larger depths were expected to be not relevant for the study (Kraaijpoel and Dost, 2013).

**Inversion** The inversion for a double couple mechanism was performed employing the FOCMEC program (Snook, 1984). The parameter space comprising strike, dip and rake angles was searched for potential solutions in 5° increments. Kraaijpoel and Dost (2013) note that the application of the VELMOD-1 velocity model (as compared to the averaged regional North Netherlands model routinely used by KNMI for event location) was especially important to obtain correct take-off angles of P- and S-rays at the source, which are an important input to the inversion. For the VELMOD-1 model, take-off angles, measured with respect to the vertical, were increased substantially for fixed epicentral distances (Kraaijpoel and Dost, 2013).

**Results and interpretation** The resulting focal mechanism are given in Table 9.

**Table 9:** *Focal mechanisms published by KNMI reproduced from Kraaijpoel and Dost (2013)*

| Event ID (date) | $M_L$ | $M_W$         | Strike/dip/rake (°) |
|-----------------|-------|---------------|---------------------|
| 060808          | 3.5   | $3.4 \pm 0.2$ | 285/70/-120         |
| 081030          | 3.2   | $3.1 \pm 0.2$ | 285/75/-120         |
| 090414          | 2.6   | $2.7 \pm 0.2$ | 320/66/-105         |
| 090508          | 3.0   | $2.9 \pm 0.1$ | 295/60/-105         |

The discrimination between fault and auxiliary plane was presumably performed by accounting for regional geology. The fault planes have been interpreted such that the rake angle, which indicates a right-lateral movement in all cases, fits the character of the west Groningen fault (Frikken, 1999) separating the Groningen High from the Lauwerszee Trough (Dost and Haak, 2007). Interpreted in this manner, all mechanisms show normal faulting at a steeply dipping (60° - 70°) fault. Apart from the event occurring on the 14<sup>th</sup> April 2014, the strike angles are similar (approx. 290°).

**Additional computations** Apart from the focal mechanisms, seismic moments, magnitudes, source radii, stress drops and average displacements at depths have been computed for these four events from spectra corrected for instrument response, absorption and scattering. In addition, the seismic attenuation Q was calculated for the event occurring on the 8<sup>th</sup> August 2006 (Kraaijpoel and Dost, 2013).

The complexity of waveforms, especially of the S-wave arrival, was investigated by ray tracing. Synthetic waveforms were generated by convolution with a Berlage wavelet and compared to the measured accelerograms. Thus, a significant contribution of phases converted from P-to-S at the bottom of the salt layer or reflected at the bottom of the reservoir was revealed. Especially at short epicentral distances, S-wave precursors may be mistaken for S-wave direct arrivals, which may lead to mislocation of events and misinterpretation of S-wave polarities (Kraaijpoel and Dost, 2013).

### 5.3.3 Comparison to state-of-the-art and conclusions

“For the previous shallow borehole network, potentially only larger events can be analysed due to the large interstation distances. However, at large distances, waveforms become more and more complicated due to reflections and reverberations, and thus, amplitude picking is almost impossible due to the difficulties in phase identification. These problems can be circumvented by employing the accelerometers, which are located closer to the regions of interest. However, since the accelerometers were installed with the aim of measuring peak accelerations, their orientation has not been taken sufficiently care of and additionally, may have changed over time. Such changes are difficult to assess in retrospect, since only triggered data were recorded and thus, no teleseismic events can be used for orienting the stations” (KNMI, pers. comm., 2018).

From our own experience in the ACISM project, we can confirm the complexity of seismic waveforms recorded in the Groningen field. For any study on source mechanisms, it is paramount that both the instrument response as well as the station orientation is well known. With respect to the analysis of the four events described above, we confirm that it was executed thoroughly and according to the state-of-the-art at that time. Especially, great care was taken in producing a velocity model that was more sophisticated than the North Netherlands velocity model used for event location. S-wave velocities and densities were computed from P-wave velocities. Densities usually do not have a very strong influence on amplitudes of seismic waves. Since S-wave amplitudes were only employed in a P-to-S ratio and not as time traces, the influence of the S-wave velocity model is restricted to differences in amplitudes for transmitted, reflected and converted waves. As long as the  $v_P/v_S$  ratio does not deviate too strongly from reality, errors in the velocity model, when S-wave velocities are retrieved from P-wave velocities, should counterbalance each other. Thus, the derivation of both densities and S-wave velocities from P-wave velocities was adequate, since no further information was available.

We can affirm that an inversion for focal mechanisms of earthquakes occurring in the Groningen field before the installation of the G-network and therefore using the accelerometer data is only feasible in particular cases and requires extraordinary diligence when analysing the data. Due to the missing orientation information for the accelerometers, we advise against any attempt to retrieve further focal mechanisms for past events that occurred before a sufficient number of stations of the G-network was installed. Further, due to the complexity of the wavefield, we advise against the use of first motion P- and S-polarities or amplitudes in focal mechanism inversion for events in the Groningen field. Instead, we recommend employing full waveform analysis methods as presented in section 5.4.

## References

- Castagna, J.P., M.L. Batzle, and R.L. Eastwood (1985). "Relationships between compressional-wave and shear-wave velocities in clastic silicate rocks". In: *Geophysics* 50.4, pp. 571–581.
- Dost, B., F. Goutbeek, T. van Eck, and D. Kraaijpoel (2012). *Monitoring induced seismicity in the North of the Netherlands: status report 2010*. Tech. rep. KNMI.
- Dost, B. and H.W. Haak (2007). "Natural and induced seismicity". In: *Geology of the Netherlands*. Ed. by T.E. Wong. Royal Netherlands Academy of Arts and Sciences, Amsterdam, The Netherlands, pp. 223–239.
- Dost, B. and D. Kraaijpoel (2013). *The August 2016, 2012 earthquake near Huizinge (Groningen)*. Tech. rep. KNMI.
- Duin, E.J.T., J.C. Doornenbal, R.H.B. Rijkers, J.W. Verbeek, and T.E. Wong (2006). "Subsurface structure of the Netherlands-results of recent onshore and offshore mapping". In: *Netherlands Journal of Geosciences* 85.4, pp. 245–276.

- Frikken, H. W. (1999). "Reservoir-geological aspects of productivity and connectivity of gasfields in the Netherlands". PhD thesis. TU Delft, Delft University of Technology.
- KNMI, pers. comm. (2018). Personal communication.
- Kraaijpoel, D. and B. Dost (2013). "Implications of salt-related propagation and mode conversion effects on the analysis of induced seismicity". In: *Journal of Seismology* 17.1, pp. 95–107.
- Lu, R.S., D.E. Willen, and I.A. Watson (2003). "Identifying, removing, and imaging PS conversions at salt-sediment interfaces". In: *Geophysics* 68.3, pp. 1052–1059.
- Ogilvie, J.S. and G.W. Purnell (1996). "Effects of salt-related mode conversions on subsalt prospecting". In: *Geophysics* 61.2, pp. 331–348.
- Roest, J.P.A. and W. Kuilman (1993). *Geomechanische analyse van de lichte aardschokken in het Eleveld reservoir*. Tech. rep. TU Delft.
- Snoke, J.A. (1984). "A program for focal mechanism determination by combined use of polarity and SVP amplitude ratio data". In: *Earthquake Notes* 55, p. 15.
- Stein, S. and M. Wysession (2009). *An Introduction to Seismology, Earthquakes, and Earth Structure*. John Wiley & Sons.
- van Dalfsen, W., J.C. Doornenbal, S. Dortland, and J.L. Gunnink (2006). "A comprehensive seismic velocity model for the Netherlands based on lithostratigraphic layers". In: *Netherlands Journal of Geosciences* 85.4, pp. 277–292.

## 5.4 Full waveform inversion for event location and source mechanism

### 5.4.1 Context and overview

Modelling of full waveform propagation in the Groningen area velocity model results in complex waveforms. Both Shell (Willacy et al., 2018) and KNMI (Spetzler and Dost, 2017) discovered that wave propagation for sources at reservoir level apart from the P-to-S conversion at the base of the Zechstein salt layer and the defocussing of seismic energy when waves are travelling through the salt layer (see section 5.3.2), the wavefield is further complicated by guided waves at reservoir level and diving waves below the reservoir. Additionally, free surface reverberations, internal multiples and interface conversions were detected (Spetzler and Dost, 2017), all of which require a thorough understanding when identifying seismic phases for use in event location algorithms or source mechanism inversions. Thus, it may be more efficient to employ full waveforms in order to circumvent the problem of phase identification. Source mechanisms employing full waveforms computed by Shell will be explained in section 5.4.2, whereas those calculated by KNMI will be presented in section 5.4.3.

### 5.4.2 Source mechanisms computed by Shell

We will base our subsequent description on the two papers authored by Shell Global Solutions International B.V. and Shell International Exploration & Production Inc. that are publicly available: Li et al. (2016) and Willacy et al. (2018). The method that is employed is based on the PhD thesis by

Li (2013) and has been applied to seismicity induced by stress changes due to water injection and gas/oil extraction before (Li et al., 2011).

The method is employing full waveforms and computes event locations and a source mechanisms simultaneously. The best fit between synthetically computed and observed seismograms will only be achieved at the correct event location and assuming the correct source mechanism (Li et al., 2016). First, a grid search is performed over all candidate locations to find an optimum match of event location and double couple. This is achieved in several steps by an algorithm denoted as FAMA (“Fast Alignment and Matching Algorithm”; Li et al., 2016):

1. for each candidate location, an approximate correction for origin time is applied based on approximate travel time picks on synthetic and observed seismograms;
2. for each candidate location, all potential double couple mechanisms (with a resolution of 5° in strike, dip and rake angles) are tested by comparing synthetically calculated seismograms employing these mechanism with the observed seismograms;
3. for each of these trial solutions, the delay times at each receiver that maximize the normalised cross-correlation between synthetic and observed seismograms are found;
4. the cross-correlation maxima for all receivers are stacked;
5. the optimum pair of event location and double couple is identified by searching for the global maximum.

The reason to perform a cross-correlation to align synthetic and observed seismograms is to avoid a phase mismatch that does not result from an erroneous source mechanism, but from deviations between the assumed velocity model and the true subsurface structure (Li et al., 2016).

In order to avoid cycle-skipping during cross-correlation (pairing seemingly corresponding parts of waveforms with each other, but skipping one or more wavelengths), a constraint can be introduced exploiting that delay times for neighbouring receivers in the same borehole should not deviate too much from each other (Li et al., 2016). However, while inverting for source mechanisms for the Groningen field using data recorded on the shallow borehole network, only the seismograms recorded on the deepest sensors at 200 m depth were employed (Shell, pers. comm., 2018), probably leading to an omission of the constraint on delay times.

In order to be able to quickly compute synthetic seismograms for all candidate event locations and potential double couple mechanisms, a Green’s functions database is computed once (Li et al., 2016) employing the reciprocal strain Green’s tensor (Zhao et al., 2006). Further, the time-consuming cross-correlation between synthetic and observed seismograms can be exchanged by a summation reducing the computational cost from  $O(n \log n)$  to  $O(n)$  (Li et al., 2016), where  $n$  denotes the number of seismograms and  $O$  is the “big O notation” describing the limiting behaviour of a function.



In a second step, an inversion for a full moment tensor is performed, retaining the double couple found by the FAMA algorithm, but computing the waveform residual based on a full moment tensor and introducing a back azimuth constraint in addition. Event location and delay times seem to be adapted a second time during this inversion. Thus, the final objective function is (Li et al., 2016):

$$\begin{aligned}
 R_t &= R_W + R_{M_{ij}} + R_\theta + R_{\Delta\tau^n} \\
 &= \|d_n(t - T_0^{init} - \Delta\tau^n) - G_{ni,j}(t)M_{ij}\|_2 \\
 &\quad + \beta \|M_{ij} - M_{DC}^{FAMA}\|_2 + \gamma \|W(\theta_{obs} - \theta_{syn})\|_2 + \eta \|\Delta\tau^n\|_2,
 \end{aligned} \tag{5.2}$$

where  $R_t$ ,  $R_W$ ,  $R_{M_{ij}}$ ,  $R_\theta$  and  $R_{\Delta\tau^n}$  describe different terms of the objective function penalizing the difference between synthetic and observed waveforms, the deviation of the full moment tensor from the reference double couple, the deviation between synthetic and observed back azimuths as well as the required time shifts between synthetic and observed waveforms, respectively (Li et al., 2016).

Within the  $R_W$  term,  $n$  is the number of seismograms,  $t$  is time,  $T_0^{init}$  is the approximate correction for origin time, which is applied at the start of the grid search,  $\Delta\tau^n$  are the optimized delay times,  $G_{ni,j}$  are the Green's functions and  $M_{ij}$  is the full moment tensor that is searched for (the product of  $G_{ni,j}$  and  $M_{ij}$  results in the synthetic seismograms). Within the  $R_{M_{ij}}$  term,  $M_{DC}^{FAMA}$  is the double couple source mechanism identified by the FAMA algorithm and within the  $R_\theta$  term,  $W(\theta_{obs} - \theta_{syn})$  describes the difference between observed and synthetic azimuths, usually derived from P-wave arrivals (Li et al., 2016).

$\|\cdot\|_2$  is the  $L_2$  norm and  $\beta$ ,  $\gamma$  and  $\eta$  are weights that may be automatically scaled with magnitude to balance with the  $R_W$  term.  $\beta$  can also be used to adjust the amount of the non-double couple component that is allowed during inversion (depending on expectations for the environment in which the induced seismicity is observed; Li et al., 2016). According to Li et al. (2016),  $\gamma$  and  $\eta$  are usually chosen such that  $R_\theta$  and  $R_{\Delta\tau^n}$  become only weak constraints.

Willacy et al. (2018) describe the application of the method to data recorded by the shallow borehole network as follows: seismometer orientations have been obtained by check-shots. P- and S-arrivals are picked automatically, since only approximate P- and S-wave arrival times are required to align synthetic and observed seismograms. Data have been rotated to the eigenvector coordinate system estimated from the P-wave polarization and have been band-pass filtered to 1-2-7-10 Hz (most likely corresponding to the cut-off frequencies of the bandpass filter including a taper). One long time window is chosen containing both P- and S-waves (Shell, pers. comm., 2018). A Shell in-house full waveform modelling FD algorithm was used to compute a Green's functions database employing the detailed NAM 3-D velocity model. Absorbing boundary conditions were applied, therefore surface multiples are not present in the synthetic seismograms. Green's functions were generated over a grid of candidate source locations with 50 x 50 x 50 m intergrid point distance and for a 12 x 12 km aperture around each receiver (Willacy et al., 2018). Event depths are restricted between 2.5 and 3.5 km (Shell, pers. comm., 2018). In case that an event location or receiver is not located exactly on a

grid point, the nearest gridpoint is chosen (Shell, pers. comm., 2018). Despite the objective function including the  $R_{M_{ij}}$  term describing a deviation from a double couple solution, Willacy et al. (2018) state that the inversion was restricted to double couple sources. The grid search over strike, dip and rake angles was performed in  $5^\circ$  increments for strike and rake and  $3^\circ$  increments for the dip angle (Shell, pers. comm., 2018). In case an event would possess a large non-double component, it would be recognized from the output of the second step of the inversion and alternative inversion parameters allowing for larger non-double components could be explored (Shell, pers. comm., 2018). For quality control, an interactive application has been developed that allows scenario testing over all candidate source locations and source mechanism grids (Willacy et al., 2018).

The method has been applied to 100 events recorded by the shallow borehole network between 2015 and 2017 (Willacy et al., 2018). All events have been located within the reservoir. A strong correlation between earthquake locations and major faults within the Rotliegend reservoir is recognisable. The resulting double couple mechanisms are consistent and mainly show normal faulting (Willacy et al., 2018). A subset of mechanisms that indicates strike-slip faulting is located at the junction to other faults. These results support the hypothesis that fault reactivation by reservoir compaction is the principle cause for induced seismicity (Willacy et al., 2018). Compared to the KNMI catalogue, event locations differ horizontally by as much as 2 km, on average between 300 and 400 m (Shell, pers. comm., 2018). Results are delivered to NAM and after approval by NAM, subsequently to KNMI (Shell, pers. comm., 2018). In case event locations or source mechanisms differ from KNMI's own results, data are reprocessed by KNMI and results compared carefully (KNMI, pers. comm., 2018).

In addition, Willacy et al. (2018) present tests restricting the number of wells contributing to the inversion from eight to two wells. Although the resulting event locations vary only by a small amount horizontally (approx. 100 m), the source mechanisms defined by dip, strike and rake angles become nonunique (Willacy et al., 2018). In the same test, errors in event depth became as large as 300 m, which makes it difficult to unambiguously locate the earthquake at reservoir depth.

#### **5.4.3 Source mechanisms computed by KNMI**

Before 2015, KNMI did not yet explore any full waveform methods to simultaneously locate events and recover source mechanisms. Within the ACISM project, however, NORSAR and cooperation partner GFZ adapted an open access code for probabilistic moment tensor inversion ("Grond", developed by Heimann et al., GFZ Potsdam) to seismometer data recorded by the shallow borehole stations. After completion of the project, recommendations for parameters settings and input data were delivered to KNMI, who continue to apply this code to recent events. This is currently work in progress and early results are shared with NAM. Multiple publications are planned for the near future, but have not been published so far (KNMI, pers. comm., 2018).

**Grond** Grond is a full waveform probabilistic optimisation method for moment tensor inversion implemented as open source code in a seismic source optimisation framework (<http://gitext.gfz-potsdam.de/heimann/grond/>). The optimisation algorithm is a Monte Carlo directed global search approach, with the non-standard ability to simultaneously and efficiently optimise an ensemble of perturbed objective functions. Perturbations are generated employing a Bayesian bootstrap methodology. Since it is based on a plethora of forward computed models rather than on an inversion in the mathematical sense, it contains extensive methods to compute and represent errors, which is a big advancement in moment tensor studies. Therefore, parameter trade-offs, uncertainties, and ambiguities on the retrieved results can be analysed.

One point in parameter space defines one potential source model (including mechanism, magnitude, location and origin time). During the optimisation, new candidate models are generated and evaluated iteratively according to a flexible, user-specified schedule. For each new model, the objective functions are evaluated, leading to N misfit values, one for each bootstrap entity. The L1 norm is used to measure the mismatch between observation and modelled seismograms. The weighted misfit contributions from all stations and phase observations are combined into a global misfit value and are normalised for convenience. For each bootstrap entity, a fixed size set of K best performing models is maintained (*high score list* and *high score populations*). The algorithm is capable of tracking multiple or irregularly shaped minima.

Synthetic waveforms are modelled based on pre-calculated Green's functions for efficient use during the inversion. The inversion algorithm is flexible in terms of input data; an arbitrary set of data fitting targets can be used, employing time traces, amplitude spectra, cross-correlation traces, envelopes, absolute amplitudes and P/S ratios. Full waveforms or windowed body wave phases are automatically or manually selected and compared with modelled seismograms. Different filter and weights are associated to different targets. A host of quality checks is implemented to analyse data and metadata quality (e.g. station orientation, transfer functions) before performing the inversion and channels can accordingly be blacklisted for the inversion. Pre-processing of the data (azimuthal correction, restitution, timing correction, filtering, windowing) is automated; data and instrument responses can be downloaded from FDSN web services.

A more detailed description of the optimisation routine and an application to regional distances is given in Dahm et al. (2018). The algorithm has also been applied to earthquakes recorded at local and teleseismic distances (Cesca et al., 2017).

**Recommendations from the ACISM project** NORSAR applied the grond algorithm to invert full waveforms for event location and moment tensor for events recorded within the Groningen field during the ACISM project. The original aim was to invert the 2006, 2008 and 2009 events described in Kraaijpoel and Dost (2013), but since it emerged that the knowledge on the corresponding data was incomplete (data being affected by timing problems, orientations of horizontal components are

unknown, polarity of vertical components is unclear, see also section 5.3.2), a more recent event (11<sup>th</sup> of March 2017 12:52:48.00) was selected. Location and depth were defined as 53.35°N, 6.761°E and 2.8 km depth by KNMI.

If information on earthquake source mechanisms is supposed to be extracted from data, both the properties of the recording instruments as well as the properties of the medium between source and receivers need to be known. During the ACISM project, we experimented with computing synthetic seismograms for waves propagating through 3-D media (namely, the 3-D velocity model prepared by NAM) employing SW4 as well as SPECFEM3D. SW4 is based on a finite difference method and is developed by the Lawrence Livermore National Lab (<https://computation.llnl.gov/projects/serpentine-wave-propagation>), whereas SPECFEM3D is based on the spectral-element method (<https://geodynamics.org/cig/software/specfem3d/#users>) and is developed in a cooperation between Princeton University (USA), CNRS and University of Marseille (France) and ETH Zürich (Switzerland). However, the computation and usage of 3-D Green's function databases for moment tensor inversion was not tested in the course of the ACISM project. Instead, we generated a 1-D velocity model averaged from NAM's 3-D velocity model within a circle of 10 km radius for the region of interest and compared results to the application of the Northern Netherlands model that is used by KNMI for event location and the model presented in Kraaijpoel and Dost (2013). In addition, a new Q model was developed based on studies by Hofman et al. (2017). In their work as of today, KNMI follows the example of the ACISM project to generate separate 1-D velocity models for different regions of interest by averaging NAM's 3-D velocity model.

We inverted P-waves in the frequency range of 2 to 4 Hz and S-waves in the frequency range 1 to 3 Hz. Despite the removal of the instruments' response function, amplitudes may be distorted in frequency bands lower than the eigenfrequency of the instruments (which is 4.5 Hz for the shallow borehole geophones). However, KNMI stated that according to their tests, the amplitude of the secondary microseism could be retrieved correctly down to 0.4 Hz after instrument response deconvolution (KNMI, pers. comm., 2018). We weighed S-wave contributions with half the weight of P-wave contributions. We ran 64 000 inversion steps with 100 perturbation chains (bootstrap entities), resulting in 6 400 000 tested source models. From each perturbation chain, the 10 best models were kept yielding 1000 source models to compute statistics.

The main findings from the multitude of synthetic tests that were performed are:

1. It is advisable to invert both P- and S-waves, but in separate time windows due to the complexity of the wavetrain.
2. When employing the Grond algorithm, it is advisable to use data from different instruments within the same borehole, if available, due to the bootstrap method used to perturb the objective functions.
3. Different kinds of input data (amplitude spectra, time traces with or without shift, cross-correlation

traces, envelopes, absolute amplitudes) should be combined in a sensible way, since their information content may be complementary.

4. Synthetic waveforms are complex for all three velocity models tested.
5. It is sufficient to invert the S-wave as recorded on the T component, as the S-wave recorded on the R component does not contain new information content. Instead, its inversion is challenging, since it comprises many converted waves directly after the P-wave onset and is more influenced by uncertainties in the velocity model than waves recorded on the T component.

For the moment tensor inversion, we restricted the input to data from stations with less than 10 km distance (due to complexity of the velocity model) and excluded data from channels with uncertain orientation. Due to the large number of stations, sufficient data is available despite these limitations. We only employed data recorded on geophones within the shallow boreholes, since for these instruments, the orientation of components had been reviewed by KNMI.

The main findings inverting for a deviatoric moment tensor (excluding the volumetric information) can be summarised as follows:

1. The influence of the velocity model is more significant than the influence of input data types.
2. The preferable combination of input data leading to the lowest misfit is a combination of time traces (allowing for a shift accounting for modelling errors), cross-correlation traces and amplitude spectra.
3. For all three velocity models, we obtain a shift in location 1 km to the South.
4. For the averaged 1-D velocity model, the depth of the event (3 km) fits the reservoir depth. For the Northern Netherlands velocity model, a source depth of 2.6 km is retrieved, whereas the Kraaijpoel and Dost (2013) velocity model favours event depths of almost 4 km.
5. For the averaged 1-D velocity model, the source mechanism indicates normal faulting with slightly right-lateral slip as was also obtained for the events described in Kraaijpoel and Dost (2013) occurring at distances between 1.4 km and 5.3 km from the event inverted here. For both other velocity models, the double couple implies strike-slip faulting, but can be considered as unstable due to a large CLVD component exceeding the double couple component.
6. When the Northern Netherlands or the (Kraaijpoel and Dost, 2013) velocity model is applied, there is ambiguity in event location and other inversion parameters indicating that not all data can be fitted simultaneously with these velocity models. This is not the case for the more complex averaged velocity model containing also the anhydrite floater and basal floater layer.

When allowing for a full moment tensor, results from the Northern Netherlands and the Kraaijpoel and Dost (2013) velocity model do not appear to be trustworthy. Solutions obtained applying the averaged 1-D velocity model potentially indicate a more complex behaviour involving normal faulting

and a simultaneous collapse. However, the discussion if gas extraction may lead to isotropic components in the source mechanism is still controversial. Thus, the credibility of the isotropic component needs to be confirmed by inversion of further events in the same area.

We concluded that since the averaged 1-D velocity model employed in a deviatoric moment tensor inversion provided the least scatter in location and other inversion parameters, the smallest variability in CLVD component and the best agreement between mean and best solution, it represented our preferred velocity model. For moment tensor inversion, the presence of both high velocity layers (anhydrite floaters and basal anhydrite layer) seemed to be imperative to model waveforms as correctly as possible. Further, the new network of shallow borehole stations emerged to be very useful for moment tensor inversion. The density of stations is sufficient to enable the choice of only the best quality input data. KNMIs work on orientation of instrument components during the course of the ACISM project was substantial to obtain correct input data for the moment tensor inversion. Finally, the variety in solutions that is available when employing a probabilistic moment tensor inversion illustrates the spectrum of potential solutions and indicates the reliability of the best solution.

#### **5.4.4 Comparison to state-of-the-art and conclusions**

While seismic moment tensors have become a basic tool to analyse earthquake sources and are calculated by a number of agencies for global and regional earthquakes, parameter uncertainties are rarely computed (Musta and Tkali, 2015). Especially in the case of earthquakes with significant non-double couple components, the uncertainties are important, since the amount of double couple, CLVD and isotropic components may vary significantly already for small perturbations of parameters (Zahradnik et al., 2008).

In addition, the source location is usually determined by seismic wave arrival times and thus, is identical to the hypocentre, but not necessarily the centroid, on which the moment tensor solution depends (Musta and Tkali, 2015). (The earthquake hypocentre denotes the starting point of the rupture, the earthquake centroid is the centre of energy release. The distance between hypocentre and centroid is in the order of the fault size; e.g. for an earthquake of magnitude 1, the fault size can be approximated to 40 m, for an earthquake of magnitude 2 to 100 m and an earthquake of magnitude 4 to 1 km.) Further, the location estimate determined from moment tensor inversion, especially the depth, is often less sensitive to uncertainties in crustal structure (Zahradnik et al., 2008). For both reasons, it is advisable to include the centroid (earthquake location) as parameter in the inversion, as is done by both algorithms described above.

In order to solve for uncertainties, Bayesian or probabilistic inversions are increasingly applied in geophysical and also seismological problems. Bayes' approach was first applied in terms of the Akaike Bayesian information criterion by Ide et al. (1996) and Yagi and Fukahata (2008) to invert for slip distribution earthquakes. The Bayesian inversion has been employed to invert wave polarities (Zollo and

Bernard, 1991; Walsh et al., 2009) and waveforms of local (Wéber, 2006), regional (Lee et al., 2011) and teleseismic (Duputel et al., 2012) events. In addition, it can be used for tomographic studies (Bodin et al., 2012), fault rupture models (Monelli et al., 2009) and source time functions (Debski, 2008). Hence, we regard the application of probabilistic algorithms for moment tensor inversion as technically mature and state-of-the-art.

The computation of Green's functions for 3-D media, as performed by Shell, instead of the usage of simpler 1-D velocity models, is certainly non-standard and should be considered as beyond state-of-the-art. It requires extraordinary knowledge of the subsurface, which is the case for the Groningen field (Romijn, 2017), as well as adequate computational resources.

From our perspective, the application of the Grond algorithm, which KNMI already has started to employ with, has several important advantages:

- The python source code is open, examinable, changeable and therefore adaptable, as compared to in-house code developed by Shell.
- In addition to event location and source mechanism, the magnitude is computed.
- Instead of a grid search, a sophisticated search algorithm is employed, reducing computational costs substantially.
- The algorithm is flexible in terms of input data with different information content; an arbitrary set of data fitting targets can be used, employing time traces, amplitude spectra, cross-correlation traces, envelopes, absolute amplitudes and P/S ratios.
- No travel-time picks are required to align observed and synthetic seismograms.
- The code allows for interpolation of Green's functions in between gridpoints of the pre-computed Green's function database.
- The approach additionally opens the possibility to simulate ground motions for earthquake scenarios, as it is requested more and more by regulators for hazard and risk studies.

Further, in addition to obtaining a single source mechanism, a whole range of nearly equivalent source mechanism is obtained, such that parameter trade-offs, uncertainties and ambiguities on the retrieved results can be analysed. Interactive quality control is also available within Shell's algorithms and allows to display the performance of the objective functions (e.g. for different location and strike, dip, rake angles), but Grond is moreover suited to analyse alternative solutions and map parameter trade-offs. In addition, a great advantage of the bootstrap method employed by Grond over other approaches in error propagation is that it implicitly accounts for modelling errors that may affect every station and phase differently (Dahm et al., 2018).

Further, we recommend:

- to invert P- and S-wave windows separately, instead of integrating both in a common time window. Due to the complexity of the waveform and the inaccuracy of the velocity model, phases in between P- and S-onset may be easily modelled.
- not to use absorbing boundary conditions at the surface of the velocity model during computation of Green's functions, since this may lead to a difference in waveforms for synthetic and observed seismograms.
- to invert at least for a deviatoric moment tensor, since when restricting the source mechanism to a double couple mechanism, noise in the data may distort the orientation of the fault planes (Jechumtálová and Sílený, 2005).
- to at least test for a full moment tensor and compare results for several events.

So far, the Grond algorithm has not been applied to Green's function databases computed for 3-D velocity models, although it is prepared to handle them. The computation of Green's functions in 3-D media is feasible, but computationally expensive. So far, results obtained in the ACISM project employing an average 1-D velocity model generated from the 3-D velocity model for the region of interest are promising. Nevertheless, the difference in source mechanism when employing a 1-D versus a 3-D velocity model should be analysed in more detail. In addition, a comprehensive and systematic comparison between event locations obtained by the EDT method (Spetzler and Dost, 2017) and the inversion by Grond is desirable, as is the comparison between event locations and source mechanisms obtained by Shell and the Grond algorithm. Both comparisons are under way at KNMI, but are not yet open to the public.

We strongly recommend KNMI to use full waveform methods for full moment tensor inversion on a larger population of earthquakes in the Groningen region. The Grond algorithm, which is currently applied and further tested by KNMI, including its probabilistic methods, is setting the state-of-the-art. Further, a 3D Green's function database should be developed independently from Shell's, to compare 1D with 3D source mechanism solutions. All results should be compared in the greatest detail possible to Shell's and potentially other researcher's findings.

## References

- Bodin, T., M. Sambridge, H. Tkali, P. Arroucau, K. Gallagher, and N. Rawlinson (2012). "Transdimensional inversion of receiver functions and surface wave dispersion". In: *Journal of Geophysical Research: Solid Earth* 117.B2.
- Cesca, S., S. Heimann, M. Kriegerowski, J. Saul, and T. Dahm (2017). "Moment Tensor Inversion for Nuclear Explosions: What Can We Learn from the 6 January and 9 September 2016 Nuclear Tests, North Korea?" In: *Seismological Research Letters* 88.2A, pp. 300–310.



- Dahm, T., S. Heimann, S. Funke, S. Wendt, I. Rappsilber, D. Bindi, T. Plenefisch, and F. Cotton (2018). "Seismicity in the block mountains between Halle and Leipzig, Central Germany: centroid moment tensors, ground motion simulation and felt intensities of two  $M \approx 3$  earthquakes in 2015 and 2017". In: *Journal of Seismology*.
- Debski, W. (2008). "Estimating the earthquake source time function by Markov Chain Monte Carlo sampling". In: *Pure and Applied Geophysics* 165.7, pp. 1263–1287.
- Duputel, Z., L. Rivera, Y. Fukahata, and H. Kanamori (2012). "Uncertainty estimations for seismic source inversions". In: *Geophysical Journal International* 190.2, pp. 1243–1256.
- Hofman, L.J., E. Ruigrok, B. Dost, and H. Paulssen (2017). "A shallow seismic velocity model for the Groningen area in the Netherlands". In: *Journal of Geophysical Research: Solid Earth* 122.10, pp. 8035–8050.
- Ide, S., M. Takeo, and Y. Yoshida (1996). "Source process of the 1995 Kobe earthquake: determination of spatio-temporal slip distribution by Bayesian modeling". In: *Bulletin of the Seismological society of America* 86.3, pp. 547–566.
- Jechumtálová, Z. and J. Sílený (2005). "Amplitude ratios for complete moment tensor retrieval". In: *Geophysical Research Letters* 32.22.
- KNMI, pers. comm. (2018). Personal communication.
- Kraaijpoel, D. and B. Dost (2013). "Implications of salt-related propagation and mode conversion effects on the analysis of induced seismicity". In: *Journal of Seismology* 17.1, pp. 95–107.
- Lee, E.-J., P. Chen, T.H. Jordan, and L. Wang (2011). "Rapid full-wave centroid moment tensor (CMT) inversion in a three-dimensional earth structure model for earthquakes in Southern California". In: *Geophysical Journal International* 186.1, pp. 311–330.
- Li, J. (2013). "Study of induced seismicity for reservoir characterization". PhD thesis. Massachusetts Institute of Technology.
- Li, J., H. Kuehl, A. Droujinine, and J.-W. Blokland (2016). "Microseismic and induced seismicity simultaneous location and moment tensor inversion: Moving beyond picks with a robust full-waveform method". In: *2016 SEG International Exposition and Annual Meeting*. Society of Exploration Geophysicists.
- Li, J., H. Zhang, H. Sadi Kuleli, and M. Nafi Toksoz (2011). "Focal mechanism determination using high-frequency waveform matching and its application to small magnitude induced earthquakes". In: *Geophysical Journal International* 184.3, pp. 1261–1274.
- Monelli, D., P.M. Mai, S. Jónsson, and D. Giardini (2009). "Bayesian imaging of the 2000 Western Tottori (Japan) earthquake through fitting of strong motion and GPS data". In: *Geophysical Journal International* 176.1, pp. 135–150.
- Musta, M. and H. Tkali (2015). "Point source moment tensor inversion through a Bayesian hierarchical model". In: *Geophysical Journal International* 204.1, pp. 311–323.
- Romijn, R. (2017). *Groningen velocity model 2017 - Groningen full elastic velocity model September 2017*. Tech. rep. Nederlandse Aardolie Maatschappij BV.

- Shell, pers. comm. (2018). Personal communication.
- Spetzler, J. and B. Dost (2017). "Hypocentre estimation of induced earthquakes in Groningen". In: *Geophysical Journal International* 209.1, pp. 453–465.
- Walsh, D.d, R. Arnold, and J. Townend (2009). "A Bayesian approach to determining and parametrizing earthquake focal mechanisms". In: *Geophysical Journal International* 176.1, pp. 235–255.
- Wéber, Z. (2006). "Probabilistic local waveform inversion for moment tensor and hypocentral location". In: *Geophysical Journal International* 165.2, pp. 607–621.
- Willacy, C., E. van Dedem, S. Minisini, J. Li, J.W. Blokland, I. Das, and A. Droujinine (2018). "Application of full-waveform event location and moment-tensor inversion for Groningen induced seismicity". In: *The Leading Edge* 37.2, pp. 92–99.
- Yagi, Y. and Y. Fukahata (2008). "Importance of covariance components in inversion analyses of densely sampled observed data: an application to waveform data inversion for seismic source processes". In: *Geophysical Journal International* 175.1, pp. 215–221.
- Zahradnik, J., J. Jansky, and V. Plicka (2008a). "Detailed waveform inversion for moment tensors of M 4 events: Examples from the Corinth Gulf, Greece". In: *Bulletin of the Seismological Society of America* 98.6, pp. 2756–2771.
- Zahradnik, J., E. Sokos, G.-A. Tselentis, and N. Martakis (2008b). "Non-double-couple mechanism of moderate earthquakes near Zakynthos, Greece, April 2006; explanation in terms of complexity". In: *Geophysical Prospecting* 56.3, pp. 341–356.
- Zhao, L., P. Chen, and T.H. Jordan (2006). "Strain Green's tensors, reciprocity, and their applications to seismic source and structure studies". In: *Bulletin of the Seismological Society of America* 96.5, pp. 1753–1763.
- Zollo, A. and P. Bernard (1991). "Fault mechanisms from near-source data: joint inversion of S polarizations and P polarities". In: *Geophysical Journal International* 104.3, pp. 441–451.

## A Station network

### A.1 List of stations (2018)

**Table 10:** List of permanent seismic stations operated by KNMI in the Groningen area sorted by installation date. See map in figure 2.3. The number of sensors in each borehole is indicated in brackets. \* needs to be replaced by the sensor level (from 0 or 1 to 4 or 5) to get the full name of each sensor.

| Network | Station | Latitude  | Longitude | Depth (m)        | Start Date              | Type of Station     | Other     |
|---------|---------|-----------|-----------|------------------|-------------------------|---------------------|-----------|
| NR      | NE117   | 53.213402 | 7.119599  | 0                | 01/01/1970              | broadband           |           |
| NR      | NE018   | 52.968219 | 7.097177  | 0                | 01/01/1970              | broadband           |           |
| NL      | ZL2*    | 53.0921   | 6.7533    | 25-75-125-175    | 12/04/1995              | borehole (4)        |           |
| NL      | ZLV*    | 53.0921   | 6.7533    | 50-100-150-200   | 12/04/1995              | borehole (4)        |           |
| NL      | WDB*    | 53.2083   | 6.7355    | 47-97-147-197    | 12/04/1995              | borehole (4)        |           |
| NL      | ENM*    | 53.4064   | 6.4817    | 50-100-150-200   | 12/04/1995              | borehole (4)        |           |
| NL      | FSW*    | 53.2135   | 7.1195    | 0-75-150-225-300 | 05/05/1995              | borehole (5)        |           |
| NL      | VLW*    | 52.9682   | 7.0972    | 50-100-150-200   | 23/05/1995              | borehole (4)        |           |
| NL      | HWF*    | 53.071    | 6.3512    | 50-100-150-200   | 02/06/1995              | borehole (4)        |           |
| NL      | ENV*    | 52.8944   | 6.6337    | 50-100-150-200   | 09/09/1995              | borehole (4)        |           |
| NL      | NIW*    | 53.3548   | 6.043     | 30-60-90-120     | 20/05/2009              | borehole (4)        |           |
| NL      | SUH*    | 53.2113   | 6.211     | 30-60-90-120     | 26/08/2009              | borehole (4)        |           |
| NL      | SPY*    | 53.4098   | 6.7838    | 30-60-90-120     | 08/07/2010              | borehole (4)        |           |
| NL      | BWSE    | 53.34442  | 6.70989   | 0                | 24/04/2013              | accelerometer       | B-NETWORK |
| NL      | BMD2    | 53.35325  | 6.6472    | 0                | 10/09/2013              | accelerometer       | B-NETWORK |
| NL      | BMD1    | 53.34726  | 6.64225   | 0                | 11/09/2013 - 11/03/2014 | accelerometer       | B-NETWORK |
| NL      | BONL    | 53.40014  | 6.75483   | 0                | 19/09/2013 - 23/08/2015 | accelerometer       | B-NETWORK |
| NL      | BLOP    | 53.33391  | 6.74663   | 0                | 23/09/2013              | accelerometer       | B-NETWORK |
| NL      | BZN2    | 53.35683  | 6.75474   | 0                | 23/09/2013              | accelerometer       | B-NETWORK |
| NL      | BWIR    | 53.32257  | 6.7861    | 0                | 24/09/2013              | accelerometer       | B-NETWORK |
| NL      | BOWW    | 53.34053  | 6.8125    | 0                | 01/10/2013              | accelerometer       | B-NETWORK |
| NL      | BUHZ    | 53.40704  | 6.67266   | 0                | 07/10/2013              | accelerometer       | B-NETWORK |
| NL      | BAPP    | 53.31482  | 6.83539   | 0                | 07/10/2013              | accelerometer       | B-NETWORK |
| NL      | BZN1    | 53.36567  | 6.77512   | 0                | 24/10/2013              | accelerometer       | B-NETWORK |
| NL      | BWIN    | 53.3112   | 6.74837   | 0                | 17/09/2014              | accelerometer       | B-NETWORK |
| NL      | BSTD    | 53.312297 | 6.692137  | 0                | 17/09/2014              | accelerometer       | B-NETWORK |
| NL      | BHKS    | 53.29195  | 6.78502   | 0                | 17/09/2014              | accelerometer       | B-NETWORK |
| NL      | BHAR    | 53.22916  | 6.70898   | 0                | 17/09/2014              | accelerometer       | B-NETWORK |
| NL      | BGAR    | 53.36786  | 6.71359   | 0                | 17/09/2014              | accelerometer       | B-NETWORK |
| NL      | BFB2    | 53.18751  | 6.76549   | 0                | 17/09/2014              | accelerometer       | B-NETWORK |
| NL      | G34*    | 53.25252  | 6.76508   | 0-50-100-150-200 | 23/10/2014              | borehole (4) + acc. | G-NETWORK |
| NL      | G45*    | 53.199535 | 6.764478  | 0-50-100-150-200 | 23/10/2014              | borehole (4) + acc. | G-NETWORK |
| NL      | G30*    | 53.27917  | 6.895145  | 0-50-100-150-200 | 23/10/2014              | borehole (4) + acc. | G-NETWORK |
| NL      | G49*    | 53.17647  | 6.730598  | 0-50-100-150-200 | 23/10/2014              | borehole (4) + acc. | G-NETWORK |
| NL      | G39*    | 53.22525  | 6.724121  | 0-50-100-150-200 | 24/10/2014              | borehole (4) + acc. | G-NETWORK |
| NL      | G40*    | 53.22501  | 6.809874  | 0-50-100-150-200 | 24/10/2014              | borehole (4) + acc. | G-NETWORK |
| NL      | G46*    | 53.19783  | 6.849796  | 0-50-100-150-200 | 31/10/2014              | borehole (4) + acc. | G-NETWORK |
| NL      | G24*    | 53.289974 | 6.856169  | 0-50-100-150-200 | 12/11/2014              | borehole (4) + acc. | G-NETWORK |
| NL      | G01*    | 53.442535 | 6.731191  | 0-50-100-150-200 | 10/02/2015              | borehole (4) + acc. | G-NETWORK |
| NL      | G22*    | 53.31035  | 6.677621  | 0-50-100-150-200 | 10/02/2015              | borehole (4) + acc. | G-NETWORK |
| NL      | G02*    | 53.44901  | 6.805842  | 0-50-100-150-200 | 10/02/2015              | borehole (4) + acc. | G-NETWORK |
| NL      | G03*    | 53.415886 | 6.597559  | 0-50-100-150-200 | 10/02/2015              | borehole (4) + acc. | G-NETWORK |
| NL      | G44*    | 53.204193 | 6.683958  | 0-50-100-150-200 | 11/02/2015              | borehole (4) + acc. | G-NETWORK |
| NL      | G51*    | 53.1732   | 6.88481   | 0-50-100-150-200 | 11/02/2015              | borehole (4) + acc. | G-NETWORK |
| NL      | G14*    | 53.358604 | 6.770835  | 0-50-100-150-200 | 11/02/2015              | borehole (4) + acc. | G-NETWORK |
| NL      | G42*    | 53.221687 | 6.988649  | 0-50-100-150-200 | 11/02/2015              | borehole (4) + acc. | G-NETWORK |
| NL      | G57*    | 53.13513  | 7.022222  | 0-50-100-150-200 | 12/02/2015              | borehole (4) + acc. | G-NETWORK |
| NL      | G52*    | 53.16989  | 6.983663  | 0-50-100-150-200 | 12/02/2015              | borehole (4) + acc. | G-NETWORK |
| NL      | G55*    | 53.143345 | 6.846056  | 0-50-100-150-200 | 12/02/2015              | borehole (4) + acc. | G-NETWORK |
| NL      | G56*    | 53.14844  | 6.930871  | 0-50-100-150-200 | 12/02/2015              | borehole (4) + acc. | G-NETWORK |
| NL      | G23*    | 53.30949  | 6.767527  | 0-50-100-150-200 | 16/02/2015              | borehole (4) + acc. | G-NETWORK |
| NL      | G17*    | 53.336197 | 6.636346  | 0-50-100-150-200 | 29/04/2015              | borehole (4) + acc. | G-NETWORK |
| NL      | G20*    | 53.335297 | 6.895165  | 0-50-100-150-200 | 28/05/2015              | borehole (4) + acc. | G-NETWORK |
| NL      | G04*    | 53.41469  | 6.67472   | 0-50-100-150-200 | 04/06/2015              | borehole (4) + acc. | G-NETWORK |
| NL      | G43*    | 53.231853 | 7.079074  | 0-50-100-150-200 | 25/06/2015              | borehole (4) + acc. | G-NETWORK |
| NL      | G58*    | 53.110264 | 6.907052  | 0-50-100-150-200 | 30/06/2015              | borehole (4) + acc. | G-NETWORK |
| NL      | G05*    | 53.418438 | 6.771304  | 0-50-100-150-200 | 16/07/2015              | borehole (4) + acc. | G-NETWORK |
| NL      | G50*    | 53.174526 | 6.809343  | 0-50-100-150-200 | 28/08/2015              | borehole (4) + acc. | G-NETWORK |
| NL      | G60*    | 53.297935 | 7.075193  | 0-50-100-150-200 | 28/08/2015              | borehole (4) + acc. | G-NETWORK |
| NL      | G62*    | 53.38698  | 6.841949  | 0-50-100-150-200 | 08/09/2015              | borehole (4) + acc. | G-NETWORK |

|    |      |            |           |                  |            |                     |           |
|----|------|------------|-----------|------------------|------------|---------------------|-----------|
| NL | G10* | 53.37847   | 6.804435  | 0-50-100-150-200 | 08/09/2015 | borehole (4) + acc. | G-NETWORK |
| NL | G63* | 53.33143   | 6.910878  | 0-50-100-150-200 | 15/09/2015 | borehole (4) + acc. | G-NETWORK |
| NL | G06* | 53.411095  | 6.870878  | 0-50-100-150-200 | 15/09/2015 | borehole (4) + acc. | G-NETWORK |
| NL | G64* | 53.220726  | 7.038012  | 0-50-100-150-200 | 15/09/2015 | borehole (4) + acc. | G-NETWORK |
| NL | G54* | 53.124283  | 6.757957  | 0-50-100-150-200 | 15/09/2015 | borehole (4) + acc. | G-NETWORK |
| NL | G68* | 53.235077  | 6.63466   | 0-50-100-150-200 | 16/09/2015 | borehole (4) + acc. | G-NETWORK |
| NL | G21* | 53.313374  | 6.593737  | 0-50-100-150-200 | 17/09/2015 | borehole (4) + acc. | G-NETWORK |
| NL | G16* | 53.338528  | 6.531397  | 0-50-100-150-200 | 17/09/2015 | borehole (4) + acc. | G-NETWORK |
| NL | G18* | 53.330624  | 6.721702  | 0-50-100-150-200 | 18/09/2015 | borehole (4) + acc. | G-NETWORK |
| NL | G19* | 53.337814  | 6.817032  | 0-50-100-150-200 | 18/09/2015 | borehole (4) + acc. | G-NETWORK |
| NL | G09* | 53.387764  | 6.724525  | 0-50-100-150-200 | 18/09/2015 | borehole (4) + acc. | G-NETWORK |
| NL | G13* | 53.34894   | 6.668564  | 0-50-100-150-200 | 22/09/2015 | borehole (4) + acc. | G-NETWORK |
| NL | G29* | 53.281406  | 6.786966  | 0-50-100-150-200 | 22/09/2015 | borehole (4) + acc. | G-NETWORK |
| NL | G41* | 53.223434  | 6.891867  | 0-50-100-150-200 | 22/09/2015 | borehole (4) + acc. | G-NETWORK |
| NL | G08* | 53.395447  | 6.643896  | 0-50-100-150-200 | 22/09/2015 | borehole (4) + acc. | G-NETWORK |
| NL | G07* | 53.39458   | 6.545769  | 0-50-100-150-200 | 24/09/2015 | borehole (4) + acc. | G-NETWORK |
| NL | G69* | 53.212837  | 6.643776  | 0-50-100-150-200 | 22/10/2015 | borehole (4) + acc. | G-NETWORK |
| NL | G26* | 53.28208   | 6.545806  | 0-50-100-150-200 | 22/10/2015 | borehole (4) + acc. | G-NETWORK |
| NL | G53* | 53.167362  | 7.08012   | 0-50-100-150-200 | 29/10/2015 | borehole (4) + acc. | G-NETWORK |
| NL | G67* | 53.32134   | 6.822783  | 0-50-100-150-200 | 29/10/2015 | borehole (4) + acc. | G-NETWORK |
| NL | G32* | 53.24981   | 6.57919   | 0-50-100-150-200 | 27/11/2015 | borehole (4) + acc. | G-NETWORK |
| NL | G31* | 53.296196  | 7.021759  | 0-50-100-150-200 | 27/11/2015 | borehole (4) + acc. | G-NETWORK |
| NL | G27* | 53.28318   | 6.628118  | 0-50-100-150-200 | 27/11/2015 | borehole (4) + acc. | G-NETWORK |
| NL | G61* | 53.381855  | 6.681333  | 0-50-100-150-200 | 27/11/2015 | borehole (4) + acc. | G-NETWORK |
| NL | G66* | 53.179398  | 6.585236  | 0-50-100-150-200 | 27/11/2015 | borehole (4) + acc. | G-NETWORK |
| NL | G65* | 53.169216  | 6.95428   | 0-50-100-150-200 | 30/11/2015 | borehole (4) + acc. | G-NETWORK |
| NL | G37* | 53.273952  | 7.035     | 0-50-100-150-200 | 02/12/2015 | borehole (4) + acc. | G-NETWORK |
| NL | G59* | 53.116028  | 6.987698  | 0-50-100-150-200 | 04/12/2015 | borehole (4) + acc. | G-NETWORK |
| NL | G36* | 53.26505   | 6.924454  | 0-50-100-150-200 | 07/12/2015 | borehole (4) + acc. | G-NETWORK |
| NL | BKMZ | 53.290115  | 6.318887  | 0                | 08/12/2015 | accelerometer       | B-NETWORK |
| NL | G11* | 53.366917  | 6.889139  | 0-50-100-150-200 | 08/12/2015 | borehole (4) + acc. | G-NETWORK |
| NL | G33* | 53.24991   | 6.670763  | 0-50-100-150-200 | 22/01/2016 | borehole (4) + acc. | G-NETWORK |
| NL | N03* | 53.11103   | 6.404509  | 0-50-100-150-200 | 04/02/2016 | borehole (4) + acc. | N-NETWORK |
| NL | N02* | 53.071995  | 6.452966  | 0-50-100-150-200 | 04/02/2016 | borehole (4) + acc. | N-NETWORK |
| NL | G47* | 53.19635   | 6.941322  | 0-50-100-150-200 | 28/03/2016 | borehole (4) + acc. | G-NETWORK |
| NL | G28* | 53.27221   | 6.729164  | 0-50-100-150-200 | 28/03/2016 | borehole (4) + acc. | G-NETWORK |
| NL | G38* | 53.200512  | 6.547563  | 0-50-100-150-200 | 11/04/2016 | borehole (4) + acc. | G-NETWORK |
| NL | N01* | 53.11851   | 6.473259  | 0-50-100-150-200 | 14/04/2016 | borehole (4) + acc. | N-NETWORK |
| NL | G70* | 53.2385392 | 6.5367816 | 0-50-100-150-200 | 28/04/2016 | borehole (4) + acc. | G-NETWORK |
| NL | G48* | 53.19726   | 7.028954  | 0-50-100-150-200 | 21/06/2016 | borehole (4) + acc. | G-NETWORK |
| NL | G35* | 53.254936  | 6.862136  | 0-50-100-150-200 | 04/04/2017 | borehole (4) + acc. | G-NETWORK |
| NL | G25* | 53.308117  | 6.943312  | 0-50-100-150-200 | 12/05/2017 | borehole (4) + acc. | G-NETWORK |
| NL | G12* | 53.36992   | 6.57139   | 0-50-100-150-200 | 05/10/2017 | borehole (4) + acc. | G-NETWORK |
| NL | G750 | 53.307755  | 6.487526  | 0                | 04/12/2017 | accelerometer       | G-NETWORK |
| NL | G760 | 53.350715  | 6.390067  | 0                | 04/12/2017 | accelerometer       | G-NETWORK |
| NL | G770 | 53.340286  | 6.330437  | 0                | 04/12/2017 | accelerometer       | G-NETWORK |
| NL | G780 | 53.364822  | 6.489397  | 0                | 04/12/2017 | accelerometer       | G-NETWORK |
| NL | G790 | 53.383557  | 6.331927  | 0                | 04/12/2017 | accelerometer       | G-NETWORK |
| NL | G710 | 53.148299  | 6.650657  | 0                | 04/12/2017 | accelerometer       | G-NETWORK |
| NL | G740 | 53.304267  | 6.389409  | 0                | 04/12/2017 | accelerometer       | G-NETWORK |
| NL | G730 | 53.271889  | 6.430106  | 0                | 04/12/2017 | accelerometer       | G-NETWORK |

A.2 List of "missing" stations

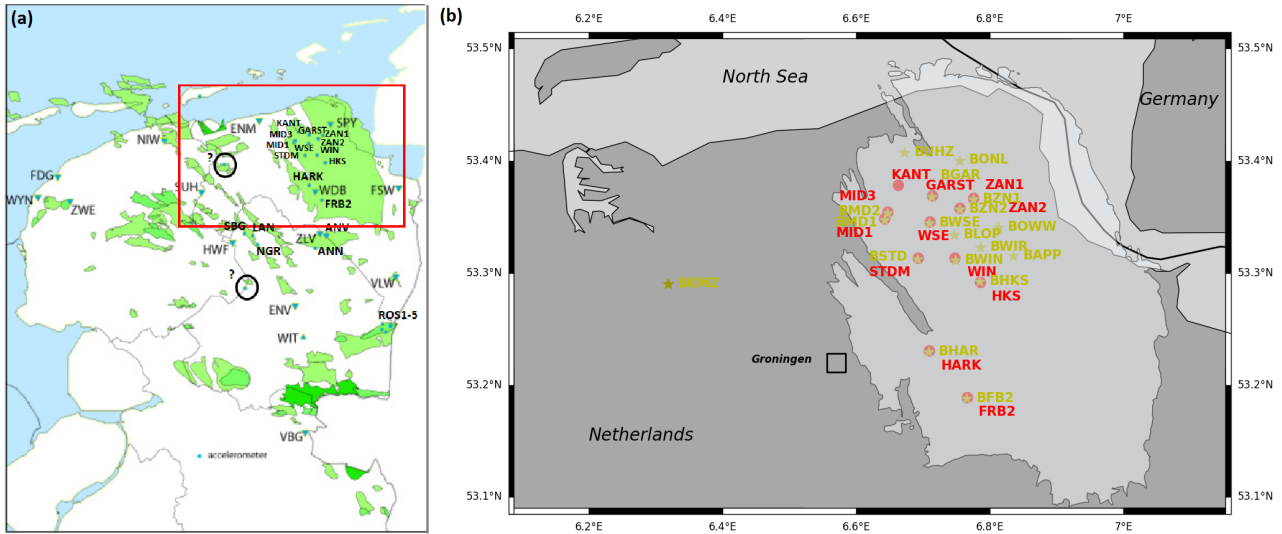


**Fig. A.1:** (a) 2010 network status modified from Dost et al. (2012). Borehole stations are marked as triangles and accelerometers as squares. By cross-checking the information from different reports and articles, we added some station names. The red square delimits approximately the region plotted on (b). (b) Map of some old accelerometers (red markers) which were replaced by the B-network accelerometers (yellow markers).

**Table 11:** List of stations that have been temporarily deployed. Grey rows show stations which were not used in the database. We found references to the 34 remaining stations in the event database (section 4.2.6).

|    | Station name       | (Latitude, Longitude) | Time span               | Additional information              |
|----|--------------------|-----------------------|-------------------------|-------------------------------------|
| 1  | ANN                | ?                     | ?                       | accelerometer (Dost and Haak, 2002) |
| 2  | AHR                | ?                     | 2012-08-16              |                                     |
| 3  | ANV1               | close to ZLV          | 2007-06-23 / 2011-07-23 | borehole (Dost and van Enst, 2008)  |
| 4  | ANV2               | close to ZLV          | 2009-11-18 / 2010-08-29 | borehole (Dost and van Enst, 2008)  |
| 5  | ASS                | ?                     | 2012-08-16              |                                     |
| 6  | BGG                | ?                     | 2003-11-10 / 2011-06-27 |                                     |
| 7  | BNS                | ?                     | 2003-11-10 / 2012-08-16 |                                     |
| 8  | BSE                | ?                     | 2012-08-16              |                                     |
| 9  | DRE                | ?                     | 2008-10-30 / 2012-08-16 |                                     |
| 10 | FRB2 ⇒ <b>BFB2</b> | (53.1886, 6.7662)     | 2012-08-16              | accelerometer                       |
| 11 | GARS ⇒ <b>BGAR</b> | (53.369, 6.7142)      | 2011-06-27 / 2013-09-04 | accelerometer                       |
| 12 | HARK ⇒ <b>BHAR</b> | (53.2302, 6.7097)     | ?                       | accelerometer                       |
| 13 | HKS ⇒ <b>BHKS</b>  | (53.2919, 6.7855)     | 2006-08-08 / 2013-09-04 | accelerometer                       |
| 14 | HOB                | ?                     | 2003-11-10 / 2012-08-16 |                                     |
| 15 | IBB                | ?                     | 2011-06-27              |                                     |
| 16 | KANT               | (53.3784, 6.6627)     | 2011-06-27 / 2012-08-16 | accelerometer                       |
| 17 | KLL                | ?                     | 2003-11-10 / 2012-08-16 |                                     |
| 18 | KOE                | ?                     | 2008-10-30 / 2012-08-16 |                                     |
| 19 | LAN                | ?                     | ?                       | accelerometer (Dost and Haak, 2002) |
| 20 | LAU                | ?                     | 2008-10-30 / 2011-06-27 |                                     |
| 21 | MID1 ⇒ <b>BMD1</b> | (53.3485, 6.6427)     | 2003-03-03 / 2012-08-16 | accelerometer                       |
| 22 | MID2               | ?                     | 2003-03-03              |                                     |
| 23 | MID3 ⇒ <b>BMD2</b> | (53.3543, 6.6475)     | 2006-08-08 / 2011-01-19 | accelerometer                       |
| 24 | NGR                | ?                     | ?                       | accelerometer (Dost and Haak, 2002) |
| 25 | RCH                | ?                     | 2012-08-16              |                                     |
| 26 | ROD                | ?                     | 2003-11-10              |                                     |
| 27 | ROS1-5             | ?                     | ?                       | accelerometer (Dost and Haak, 2002) |
| 28 | SBG                | ?                     | ?                       | accelerometer (Dost and Haak, 2002) |
| 29 | SHZ4               | ?                     | 2009-12-04              |                                     |
| 30 | STB                | ?                     | 2003-11-10 / 2012-08-16 |                                     |
| 31 | STDM ⇒ <b>BSTD</b> | (53.3133, 6.6927)     | 2011-01-19 / 2012-08-16 | accelerometer                       |
| 32 | WET4               | ?                     | 2009-12-04              |                                     |
| 33 | WINN ⇒ <b>BWIN</b> | (53.3132, 6.7478)     | 2008-10-30 / 2013-09-04 | accelerometer                       |
| 34 | WSB                | ?                     | 1994-12-13              |                                     |
| 35 | WSE ⇒ <b>BWSE</b>  | (53.3457, 6.7103)     | 2007-01-26 / 2012-08-16 | accelerometer                       |
| 36 | WTS                | ?                     | 2012-08-16              |                                     |
| 37 | ZAN1 ⇒ <b>BZN1</b> | (53.3669, 6.7755)     | 2006-08-08 / 2011-06-27 | accelerometer                       |
| 38 | ZAN2 ⇒ <b>BZN2</b> | (53.358, 6.7553)      | 1999-08-10 / 2011-08-31 | accelerometer                       |
| 39 | ZRPS               | ?                     | 2014-02-13              |                                     |

### A.3 Instruments and orientation

Seismic records are easily accessible via the [KNMI dataportal](#). However, if externals want to analyse the data thoroughly, some additional information must be provided, such as (1) the instrument response and (2) the sensor orientations. Indeed, they are necessary for magnitude computation, focal mechanism determination or simply for remaining consistent.

#### Station metadata

The instrument response is accessible for each station via the [KNMI dataportal](#), for example by using the `ObsPy` python package (Beyreuther et al., 2010, Krischer et al., 2015). In case an instrument is replaced with a new instrument, the instrument response is updated for the corresponding operational period of the sensor. Technically, this change is realised through a modification of the location flag in the station code, which considers the relevant time interval (increment by one: empty field for the current period, and then 00, 01, 02. . .).

#### Sensor orientation

The sensor orientations are not yet part of the metadata, i.e. also changes of sensor orientation are not automatically updated. However, according to the KNMI, the work to determine the sensor orientation is mostly conducted and is in its final phase. [This information will be made available by KNMI soon after their internal review. A detailed documentation about the methods used is also being written and will be released at that time.](#) The following bullet points describe briefly how the work was performed for the different networks (KNMI, pers. comm., 2018):

- **For the borehole sensors of the G-network:** the method developed by Hofman et al. (2017) was initially used and this method relies on the cross-correlation of the borehole records with the surface accelerometer records (more details in the section 5.2). However, the intrinsic assumption was that the surface accelerometers were properly oriented, but it turned out later that this was not always the case. Hence, the orientation was finally performed by combining 3 data attributes : (1) P and SP phases from local events; (2) guided waves from local explosions and (3) check shots (processed by NAM).
- **For the accelerometers of the G-network:** the method used is derived from Hofman et al. (2017). Once the borehole sensor orientation have been determined (previous bullet point), the very consistent polarisation of the S-wave of local events across the borehole array are exploited to update the accelerometer orientations.
- **For the accelerometers of the B-network:** the prominent phases of teleseismic events were used. The orientation of the G-network stations are used as reference.
- **For the old borehole network:** originally, their orientation was determined using checkshots

at short distances. However, the analysis of some teleseismic phases revealed that most vertical components were flipped. The corrections are not available yet in the metadata, but this information will be updated by KNMI together with the orientation information of the sensors after internal review.

#### A.4 Data transmission

- Until 2010, all available stations were operated in triggered mode: only the data corresponding to events detected by the borehole stations were selected and sent to the KNMI data centre (section 4.1);
- Since 2010, continuous data are sent to the KNMI data centre in real-time. To our best understanding, this procedure includes an automated multi-station detection and followed by a preliminary event location, performed with the [SeisComp3](#) software. Subsequently, the automatic results are quality controlled and fine-tuned manually.
- At the beginning of 2017, the newly installed G-network was not fully operational yet (Dost et al., 2017). The real-time data transmission was done via wireless network (3G), because the DSL (Digital Subscriber Line) was not possible in such a short time frame. This resulted in some variability in the data availability (section 3.2, figures 3.3 & 3.4).

#### References

- Beyreuther, M., R. Barsch, L. Krischer, T. Megies, Y. Behr, and J. Wassermann (2010). "ObsPy: A Python Toolbox for Seismology". In: *Seismological Research Letters* 81.3, p. 530.
- Dost, B., F. Goutbeek, T. van Eck, and D. Kraaijpoel (2012). *Monitoring induced seismicity in the North of the Netherlands: status report 2010*. Tech. rep. KNMI.
- Dost, B. and H. Haak (2002). *A comprehensive description of the KNMI seismological instrumentation*. Tech. rep. KNMI.
- Dost, B., E. Ruigrok, and J. Spetzler (2017). "Development of seismicity and probabilistic hazard assessment for the Groningen gas field". In: *Netherlands Journal of Geosciences* 96.5, s235–s245.
- Dost, B. and J. van Enst (2008). *Proposal for an improved monitoring network for the Groningen field*. Proposal for a joint project KNMI/LOFAR.
- GeoForschungsZentrum (GFZ), Helmholtz Centre Potsdam - (2018). *SeisComp3*. URL: <https://www.seiscomp3.org/> (visited on 04/25/2018).
- Hofman, L.J., E. Ruigrok, B. Dost, and H. Paulssen (2017). "A shallow seismic velocity model for the Groningen area in the Netherlands". In: *Journal of Geophysical Research: Solid Earth* 122.10, pp. 8035–8050.
- KNMI (2018). *Seismic & Acoustic Data Portal*. URL: <http://rdsa.knmi.nl/dataportal/> (visited on 04/25/2018).



KNMI, pers. comm. (2018). Personal communication.

Krischer, L., T. Megies, R. Barsch, M. Beyreuther, T. Lecocq, C. Caudron, and J. Wassermann (2015). "ObsPy: a bridge for seismology into the scientific Python ecosystem". In: *Computational Science & Discovery* 8.1, p. 014003.

*ObsPy - A Python framework for Seismology* (2018). URL: <https://docs.obspy.org/> (visited on 04/25/2018).

## B Reviewed papers on the Groningen gas field consulted during project

- Almagro Vidal, C., D. Draganov, J. van der Neut, G. Drijkoningen, and K. Wapenaar (2014). "Retrieval of reflections from ambient noise using illumination diagnosis". In: *Geophysical Journal International* 198.3, pp. 1572–1584.
- Bommer, J.J., B. Dost, B. Edwards, P.P. Kruiver, M. Ntinalexis, A. Rodriguez-Marek, P.J. Stafford, and J. van Elk (2017a). "Developing a model for the prediction of ground motions due to earthquakes in the Groningen gas field". In: *Netherlands Journal of Geosciences* 96.5, s203–s213.
- Bommer, J.J., B. Dost, B. Edwards, P.J. Stafford, J. van Elk, D. Doornhof, and M. Ntinalexis (2016). "Developing an application-specific ground-motion model for induced seismicity". In: *Bulletin of the Seismological Society of America* 106.1, pp. 158–173.
- Bommer, J.J., P.J. Stafford, B. Edwards, B. Dost, E. van Dedem, A. Rodriguez-Marek, P.P. Kruiver, J. van Elk, D. Doornhof, and M. Ntinalexis (2017b). "Framework for a ground-motion model for induced seismic hazard and risk analysis in the Groningen gas field, the Netherlands". In: *Earthquake Spectra* 33.2, pp. 481–498.
- Bommer, J.J. and J. van Elk (2017). "Comment on "The maximum possible and the maximum expected earthquake magnitude for production-induced earthquakes at the gas field in Groningen, The Netherlands" by Gert Zöller and Matthias Holschneider". In: *Bulletin of the Seismological Society of America* 107.3, pp. 1564–1567.
- Bourne, S.J. and S.J. Oates (2017). "Development of statistical geomechanical models for forecasting seismicity induced by gas production from the Groningen field". In: *Netherlands Journal of Geosciences* 96.5, s175–s182.
- Bourne, S.J., S.J. Oates, J.J. Bommer, B. Dost, J. van Elk, and D. Doornhof (2015). "A Monte Carlo Method for Probabilistic Hazard Assessment of Induced Seismicity due to Conventional Natural Gas Production". In: *Bulletin of the Seismological Society of America* 105.3, pp. 1721–1738.
- Bourne, S.J., S.J. Oates, and J. van Elk (2018). "The exponential rise of induced seismicity with increasing stress levels in the Groningen gas field and its implications for controlling seismic risk". In: *Geophysical Journal International*.
- Bourne, S.J., S.J. Oates, J. van Elk, and D. Doornhof (2014). "A seismological model for earthquakes induced by fluid extraction from a subsurface reservoir". In: *Journal of Geophysical Research: Solid Earth* 119.12, pp. 8991–9015.
- Buijze, L., P.A.J. van den Bogert, B.B.T. Wassing, and J. Orlic B. and ten Veen (2017). "Fault reactivation mechanisms and dynamic rupture modelling of depletion-induced seismic events in a Rotliegend gas reservoir". In: *Netherlands Journal of Geosciences* 96.5, s131–s148.
- Crowley, H., R. Pinho, B. Polidoro, and J. van Elk (2017). "Developing fragility and consequence models for buildings in the Groningen field". In: *Netherlands Journal of Geosciences* 96.5, s247–s257.

- Daniilidis, A., L. Doddema, and R. Herber (2016). "Risk assessment of the Groningen geothermal potential: from seismic to reservoir uncertainty using a discrete parameter analysis". In: *Geothermics* 64, pp. 271–288.
- de Jager, J. and C. Visser (2017). "Geology of the Groningen field—an overview". In: *Netherlands Journal of Geosciences* 96.5, s3–s15.
- de Waal, J.A., A.G. Muntendam-Bos, and J.P.A. Roest (2015). "Production induced subsidence and seismicity in the Groningen gas field-can it be managed?" In: *Proceedings of the International Association of Hydrological Sciences* 372, p. 129.
- de Waal, J.A., A.G. Muntendam-Bos, and J.P.A. Roest (2017). "From checking deterministic predictions to probabilities, scenarios and control loops for regulatory supervision". In: *Netherlands Journal of Geosciences* 96.5, s17–s25.
- deCrook, T. (1996). "A seismic zoning map conforming to Eurocode 8, and practical earthquake parameter relations for the Netherlands". In: *Geologie en Mijnbouw* 75.1, pp. 11–18.
- Dost, B., B. Edwards, and J.J. Bommer (2018). "The Relationship between M and ML: A Review and Application to Induced Seismicity in the Groningen Gas Field, The Netherlands". In: *Seismological Research Letters*.
- Dost, B. and H.W. Haak (2007). "Natural and induced seismicity". In: *Geology of the Netherlands*. Ed. by T.E. Wong. Royal Netherlands Academy of Arts and Sciences, Amsterdam, The Netherlands, pp. 223–239.
- Dost, B., E. Ruigrok, and J. Spetzler (2017). "Development of seismicity and probabilistic hazard assessment for the Groningen gas field". In: *Netherlands Journal of Geosciences* 96.5, s235–s245.
- Dost, B., T. Van Eck, and H. Haak (2004). "Scaling of peak ground acceleration and peak ground velocity recorded in the Netherlands". In: *Bollettino di Geofisica Teorica ed Applicata* 45.3, pp. 153–168.
- Drijkoningen, G.G., J. Brouwer, J. Kooijman, G. Steenbergen, B. Dost, and A. Huijgen (2006). "4C Seismic Monitoring on Land in The Netherlands-Results for Acquisition Design". In: *68th EAGE Conference and Exhibition incorporating SPE EUROPEC 2006*.
- Duin, E.J.T., J.C. Doornenbal, R.H.B. Rijkers, J.W. Verbeek, and T.E. Wong (2006). "Subsurface structure of the Netherlands-results of recent onshore and offshore mapping". In: *Netherlands Journal of Geosciences* 85.4, pp. 245–276.
- Gunnink, J.L., D. Maljers, S.F. van Gessel, A. Menkovic, and H.J. Hummelman (2013). "Digital Geological Model (DGM): a 3D raster model of the subsurface of the Netherlands". In: *Netherlands Journal of Geosciences* 92.1, pp. 33–46.
- Gussinklo, H.J., H.W. Haak, R.C.H. Quadvlieg, P.M.F.M. Schutjens, and L. Vogelaar (2001). "Subsidence, tremors and society". In: *Netherlands Journal of Geosciences* 80.1, pp. 121–136.
- Hettema, M.H.H., B. Jaarsma, B.M. Schroot, and G.C.N. van Yperen (2017). "An empirical relationship for the seismic activity rate of the Groningen gas field". In: *Netherlands Journal of Geosciences* 96.5, s149–s161.

- Hofman, L.J., E. Ruigrok, B. Dost, and H. Paulssen (2017). "A shallow seismic velocity model for the Groningen area in the Netherlands". In: *Journal of Geophysical Research: Solid Earth* 122.10, pp. 8035–8050.
- Horrent, C., D. Jongmans, and T. Camelbeeck (1995). "Local ground motion variations observed in the region of Roermond, the Netherlands, from aftershocks of the April 1992 earthquake". In: *Geologie en Mijnbouw* 73, pp. 323–323.
- Jagt, L., E. Ruigrok, and H. Paulssen (2017). "Relocation of clustered earthquakes in the Groningen gas field". In: *Netherlands Journal of Geosciences* 96.5, s163–s173.
- Jansen, J.-D. and R. Herber (2017). "Research into induced seismicity in the Groningen field—further studies". In: *Netherlands Journal of Geosciences* 96.5, s279–s284.
- Ketelaar, V.B.H. (2009). "Subsidence due to hydrocarbon production in the Netherlands". In: *Satellite radar interferometry: Subsidence monitoring techniques*, pp. 7–26.
- Kettermann, M., S. Abe, A.F. Raith, J. de Jager, and J.L. Urai (2017). "The effect of salt in dilatant faults on rates and magnitudes of induced seismicity—first results building on the geological setting of the Groningen Rotliegend reservoirs". In: *Netherlands Journal of Geosciences* 96.5, s87–s104.
- Kortekaas, M. and B. Jaarsma (2017). "Improved definition of faults in the Groningen field using seismic attributes". In: *Netherlands Journal of Geosciences* 96.5, s71–s85.
- Kraaijpoel, D. and B. Dost (2013). "Implications of salt-related propagation and mode conversion effects on the analysis of induced seismicity". In: *Journal of Seismology* 17.1, pp. 95–107.
- Kruiver, P.P., E. van Dedem, R. Romijn, G. de Lange, M. Korff, J. Stafleu, J.L. Gunnink, A. Rodriguez-Marek, J.J. Bommer, J. van Elk, et al. (2017a). "An integrated shear-wave velocity model for the Groningen gas field, The Netherlands". In: *Bulletin of Earthquake Engineering* 15.9, pp. 3555–3580.
- Kruiver, P.P., A. Wiersma, F.H. Kloosterman, G. de Lange, M. Korff, J. Stafleu, F.S. Busschers, R. Harting, J.L. Gunnink, R.A. Green, et al. (2017b). "Characterisation of the Groningen subsurface for seismic hazard and risk modelling". In: *Netherlands Journal of Geosciences* 96.5, s215–s233.
- Muntendam-Bos, A.G., J.P.A. Roest, and H.A. de Waal (2017). "The effect of imposed production measures on gas extraction induced seismic risk". In: *Netherlands Journal of Geosciences* 96.5, s271–s278.
- Muntendam-Bos, A.G., J.P.A. Roest, and J.A. de Waal (2015). "A guideline for assessing seismic risk induced by gas extraction in the Netherlands". In: *The Leading Edge* 34.6, pp. 672–677.
- Nepveu, M., K. van Thienen-Visser, and D. Sijacic (2016). "Statistics of seismic events at the Groningen field". In: *Bulletin of Earthquake Engineering* 14.12, pp. 3343–3362.
- Noorlandt, R., P.P. Kruiver, M.P.E. de Kleine, M. Karaoulis, G. de Lange, A. Di Matteo, J. von Ketelhodt, E. Ruigrok, B. Edwards, A. Rodriguez-Marek, et al. (2018). "Characterisation of ground motion recording stations in the Groningen gas field". In: *Journal of Seismology*, pp. 1–19.
- Orlic, B. and B.B.T. Wassing (2013). "A study of stress change and fault slip in producing gas reservoirs overlain by elastic and viscoelastic caprocks". In: *Rock mechanics and rock engineering* 46.3, pp. 421–435.

- Paulssen, H., B. Dost, and T. van Eck (1992). "The April 13, 1992 earthquake of Roermond (The Netherlands); first interpretation of the NARS seismograms". In: *Geologie en Mijnbouw* 71, pp. 91–91.
- Remmelts, G., E.J.Th. Duin, B. Pinet, and C. Bios (1990). "Results of a regional deep seismic survey in the Netherlands". In: *The Potential of Deep Seismic Profiling for Hydrocarbon Exploration. Editions Technip, Paris*, pp. 335–343.
- Rodriguez-Marek, A., P.P. Kruiver, P. Meijers, J.J. Bommer, B. Dost, J. van Elk, and D. Doornhof (2017). "A Regional Site-Response Model for the Groningen Gas Field". In: *Bulletin of the Seismological Society of America* 107.5, pp. 2067–2077.
- Sijacic, D., F. Pijpers, M. Nepveu, and K. van Thienen-Visser (2017). "Statistical evidence on the effect of production changes on induced seismicity". In: *Netherlands Journal of Geosciences* 96.5, s27–s38.
- Sleeman, R. and T. van Eck (1999). "Robust automatic P-phase picking: an on-line implementation in the analysis of broadband seismogram recordings". In: *Physics of the earth and planetary interiors* 113.1-4, pp. 265–275.
- Sleeman, R. and T. van Eck (2003). "Single station real-time P and S phase pickers for seismic observatories". In: *Methods and Applications of Signal Processing in Seismic Network Operations*. Springer, pp. 173–194.
- Spetzler, J. and B. Dost (2017). "Hypocentre estimation of induced earthquakes in Groningen". In: *Geophysical Journal International* 209.1, pp. 453–465.
- Spica, Z.J., M. Perton, N. Nakata, X. Liu, and G.C. Beroza (2017). "Site characterization at Groningen gas field area through joint surface-borehole H/V analysis". In: *Geophysical Journal International* 212.1, pp. 412–421.
- Spiers, C.J., S.J.T. Hangx, and A.R. Niemeijer (2017). "New approaches in experimental research on rock and fault behaviour in the Groningen gas field". In: *Netherlands Journal of Geosciences* 96.5, s55–s69.
- Stafleu, J., D. Maljers, J.L. Gunnink, A. Menkovic, and F.S. Busschers (2011). "3D modelling of the shallow subsurface of Zeeland, the Netherlands". In: *Netherlands Journal of Geosciences* 90.4, pp. 293–310.
- van der Meulen, M.J., J.C. Doornenbal, J.L. Gunnink, J. Stafleu, J. Schokker, R.W. Vernes, F.C. van Geer, S.F. van Gessel, S. van Heteren, R.J.W. van Leeuwen, et al. (2013). "3D geology in a 2D country: perspectives for geological surveying in the Netherlands". In: *Netherlands Journal of Geosciences* 92.4, pp. 217–241.
- van Eck, T., F. Goutbeek, H. Haak, and B. Dost (2006). "Seismic hazard due to small-magnitude, shallow-source, induced earthquakes in The Netherlands". In: *Engineering Geology* 87.1-2, pp. 105–121.
- van Eijs, R.M.H.E., F.M.M. Mulders, M. Nepveu, C.J. Kenter, and B.C. Scheffers (2006). "Correlation between hydrocarbon reservoir properties and induced seismicity in the Netherlands". In: *Engineering Geology* 84.3-4, pp. 99–111.

- van Eijs, R.M.H.E. and O. van der Wal (2017). "Field-wide reservoir compressibility estimation through inversion of subsidence data above the Groningen gas field". In: *Netherlands Journal of Geosciences* 96.5, s117–s129.
- van Elk, J., D. Doornhof, J.J. Bommer, S.J. Bourne, S.J. Oates, R. Pinho, and H. Crowley (2017). "Hazard and risk assessments for induced seismicity in Groningen". In: *Netherlands Journal of Geosciences* 96.5, s259–s269.
- van Gelderen, M., R. Haagmans, and M. Bilker (1999). "Gravity changes and natural gas extraction in Groningen". In: *Geophysical Prospecting* 47.6, pp. 979–993.
- van Gent, H., S. Back, J.L. Urai, and P. Kukla (2010). "Small-scale faulting in the Upper Cretaceous of the Groningen block (The Netherlands): 3D seismic interpretation, fault plane analysis and regional paleostress". In: *Journal of Structural Geology* 32.4, pp. 537–553.
- van Gent, H., J.L. Urai, and M. de Keijzer (2011). "The internal geometry of salt structures—A first look using 3D seismic data from the Zechstein of the Netherlands". In: *Journal of Structural Geology* 33.3, pp. 292–311.
- van Gent, H.W., S. Back, J.L. Urai, P.A. Kukla, and K. Reicherter (2009). "Paleostresses of the Groningen area, the Netherlands - Results of a seismic based structural reconstruction". In: *Tectonophysics* 470.1-2, pp. 147–161.
- van Oeveren, H., P. Valvatne, L. Geurtsen, and J. van Elk (2017). "History match of the Groningen field dynamic reservoir model to subsidence data and conventional subsurface data". In: *Netherlands Journal of Geosciences* 96.5, s47–s54.
- van Thienen-Visser, K. and J.N. Breunese (2015). "Induced seismicity of the Groningen gas field: History and recent developments". In: *The Leading Edge* 34.6, pp. 664–671.
- van Thienen-Visser, K. and P.A. Fokker (2017). "The future of subsidence modelling: compaction and subsidence due to gas depletion of the Groningen gas field in the Netherlands". In: *Netherlands Journal of Geosciences* 96.5, s105–s116.
- van Wees, J.D., L. Buijze, K. van Thienen-Visser, M. Nepveu, B.B.T. Wassing, B. Orlic, and P.A. Fokker (2014). "Geomechanics response and induced seismicity during gas field depletion in the Netherlands". In: *Geothermics* 52, pp. 206–219.
- van Wees, J.-D., P.A. Fokker, K. van Thienen-Visser, B.B.T. Wassing, S. Osinga, B. Orlic, S.A. Ghouri, L. Buijze, and M. Pluymaekers (2017a). "Geomechanical models for induced seismicity in the Netherlands: inferences from simplified analytical, finite element and rupture model approaches". In: *Netherlands Journal of Geosciences* 96.5, s183–s202.
- van Wees, J.-D., S. Osinga, K. van Thienen-Visser, and P.A. Fokker (2017b). "Reservoir creep and induced seismicity: inferences from geomechanical modeling of gas depletion in the Groningen field". In: *Geophysical Journal International* 212.3, pp. 1487–1497.
- Visser, C.A. and J.L. Solano Viota (2017). "Introduction to the Groningen static reservoir model". In: *Netherlands Journal of Geosciences* 96.5, s39–s46.
-

- Vlek, C. (2018). "Induced Earthquakes from Long-Term Gas Extraction in Groningen, the Netherlands: Statistical Analysis and Prognosis for Acceptable-Risk Regulation". In: *Risk Analysis*.
- Willacy, C., E. van Dedem, S. Minisini, J. Li, J.W. Blokland, I. Das, and A. Droujinine (2018). "Application of full-waveform event location and moment-tensor inversion for Groningen induced seismicity". In: *The Leading Edge* 37.2, pp. 92–99.
- Yudistira, T., H. Paulssen, and J. Trampert (2017). "The crustal structure beneath The Netherlands derived from ambient seismic noise". In: *Tectonophysics* 721, pp. 361–371.
- Zhou, W. and H. Paulssen (2017). "P and S velocity structure in the Groningen gas reservoir from noise interferometry". In: *Geophysical Research Letters* 44.23, pp. 11, 785–11, 791.
- Zöller, G. and M. Holschneider (2016). "The maximum possible and the maximum expected earthquake magnitude for production-induced earthquakes at the gas field in Groningen, The Netherlands". In: *Bulletin of the Seismological Society of America* 106.6, pp. 2917–2921.
- Zurek, B., W. Burnett, N. Dedontney, G. Gist, et al. (2017). "The effect of modeling kinematic finite faults on deterministic formulation of ground motion prediction equations-Groningen, an induced seismicity case study". In: *2017 SEG International Exposition and Annual Meeting*. Society of Exploration Geophysicists.

## C KNMI reports on the Groningen gas field consulted during project

- Dost, B., M. Caccavale, T. van Eck, and D. Kraaijpoel (2013). *Report on the expected PGV and PGA values for induced earthquakes in the Groningen area*. Tech. rep. KNMI.
- Dost, B., B. Edwards, and J.J. Bommer (2016). *Local and Moment Magnitudes in the Groningen Field*. Tech. rep. KNMI.
- Dost, B., F. Goutbeek, T. van Eck, and D. Kraaijpoel (2012). *Monitoring induced seismicity in the North of the Netherlands: status report 2010*. Tech. rep. KNMI.
- Dost, B. and H. Haak (2002). *A comprehensive description of the KNMI seismological instrumentation*. Tech. rep. KNMI.
- Dost, B. and D. Kraaijpoel (2013). *The August 2016, 2012 earthquake near Huizinge (Groningen)*. Tech. rep. KNMI.
- Dost, B. and J. Spetzler (2015). *Probabilistic seismic hazard analysis for induced earthquakes in Groningen; update 2015*. Tech. rep. KNMI.
- Dost, B. and J. Spetzler (2016). *Probabilistic seismic hazard analysis for induced earthquakes in Groningen, update June 2016*. Tech. rep. KNMI.
- Dost, B. and J. Spetzler (2017). *Probabilistic seismic hazard analysis for induced earthquakes in Groningen, update June 2017*. Tech. rep. KNMI.
- Dost, B. and J. van Enst (2008). *Proposal for an improved monitoring network for the Groningen field*. Tech. rep. KNMI.
- Haak, H.W. (1993). *Summary of the final report on a multidisciplinary study of the relationship between gas production and earthquakes in the northern part of the Netherlands*. Tech. rep. KNMI.
- KNMI (1996). *Seismische analyse van de aardbevingen bij Middlestum op 30 Juli 1994, Annen op 16 Augustus, Annen op 31 Januari 1995*. Tech. rep. KNMI.
- van Eck, T., F. Goutbeek, H. Haak, and B. Dost (2004). *Seismic hazard due to small shallow induced earthquakes*. Tech. rep. KNMI.
- Vogel, T.A. (2014). *Visualising KNMI seismologic data using ArcGIS 10.0*. Tech. rep. KNMI.



## D NAM reports on the Groningen gas field consulted during project

Bommer, J.J., B. Dost, B. Edwards, A. Rodriguez-Marek, P.P. Kruiver, P. Meijers, M. Ntinalexis, and P.J. Stafford (2015). *Development of version 2 GMPEs for response spectral accelerations and significant durations from induced earthquakes in the Groningen field*. Tech. rep. Nederlandse Aardolie Maatschappij BV.

DeDontney, N. et al. (2016). *Maximum Magnitude of Induced Earthquakes in the Groningen Gas Field*. Tech. rep. Nederlandse Aardolie Maatschappij BV.



Pickering, M. (2015). *An estimate of the earthquake hypocenter locations in the Groningen Gas Field*. Tech. rep. Nederlandse Aardolie Maatschappij BV.

Romijn, R. (2017). *Groningen velocity model 2017 - Groningen full elastic velocity model September 2017*. Tech. rep. Nederlandse Aardolie Maatschappij BV.

## E Other documents on the Groningen gas field consulted during project

- Arrowsmith, S., C. Young, S. Ballard, M. Slinkard, and K. Pankow (2016). *Pickless seismic event detection using WCEDS*. SAND2016-6887 PE. Sandia National Laboratories.
- Buijze, L., B. Orlic, B.B.T. Wassing, and G.J. Schreppers (2015). "Dynamic rupture modeling of injection-induced seismicity: influence of pressure diffusion below porous aquifers". In: *Proceedings of the 49th US Rock Mechanics/Geomechanics Symposium (ARMA), San Francisco*.
- Chitu, A.G., O. Leeuwenburgh, T.G.G. Candela, S. Osinga, D.A. Kraaijpoel, and BBT Wassing (2017). "Optimizing of operational strategies in producing gas fields mitigating induced seismicity". In: *Schatzalp Workshop on Induced Seismicity in Davos, March 2017*.
- Coppersmith, K., H. Bungum, A. McGarr, I. Wong, J. Ake, T. Dahm, I. Main, and B. Youngs (2016). *Report from the expert panel on maximum magnitude estimates for probabilistic seismic hazard and risk modelling in Groningen gas field*. Mmax Expert Workshop, 8 - 10 March 2016, World Trade Centre, Schiphol Airport, the Netherlands.
- Dost, B. (2016). *Evolution of the Groningen earthquake monitoring network and event catalogue*. Mmax Expert Workshop, 8 - 10 March 2016, World Trade Centre, Schiphol Airport, the Netherlands.
- Dost, B. and J. van Enst (2008). *Proposal for an improved monitoring network for the Groningen field*. Proposal for a joint project KNMI/LOFAR.
- Harris, D.B. (2018). *Detections from the 2015 Zeerijp master event*. PPT sent to KNMI in March 2018.
- Langemeijer, J. (2017). "Estimation of an effective velocity model for the pre-Permian below the North-east Netherlands". MA thesis. Utrecht University, The Netherlands.
- Muntendam-Bos, A.G. and J.A. de Waal (2013). *Reassessment of the probability of higher magnitude earthquakes in the Groningen gas field including a position statement by KNMI*. Tech. rep. State Supervision of Mines.
- Orlic, B. and R. van Eijs (2002). "Modelling of deep subsurface for geohazard risk assessment". In: *Proceedings of the Third DIANA World Conference*.
- Orlic, B., R. van Eijs, and B. Scheffers (2001a). "Geomechanical modelling of the induced seismicity for a gas field". In: *63rd EAGE Conference and Technical Exhibition, Amsterdam*.
- Orlic, B., J.D. van Wees, and R. van Eijs (2001b). "Integrated geomechanical modelling for prediction of subsidence and induced seismicity due to hydrocarbon extraction". In: *Annual Conference of the International Association for Mathematical Geology (IAMG)*.
- Orlic, B., B.B.T. Wassing, J.H. ter Heege, and J. Samuelson (2013). *CATO-2 Deliverable WP3.03-D15: Model/report/papers predicting seal integrity and fault reactivation/seismic risk, including thermo-hydro-chemo-mechanical effects at generic level*. Tech. rep. TNO.
- Paap, B.F., T.P.H. Steeghs, and D. Kraaijpoel (2016). "Detailed seismic modeling of induced seismicity at the Groningen gas field". In: *6th EAGE Workshop on Passive Seismic: From Data to Decision*.
- Paleja, R. and S. Bierman (2016). *Measuring changes in earthquake occurrence rates in Groningen*. Tech. rep.

- Pijpers, F.P. (2016a). *A phenomenological relationship between reservoir pressure and tremor rates in Groningen*. Tech. rep. Statistics Netherlands.
- Pijpers, F.P. (2016b). *Trend changes in tremor rates in Groningen*. Tech. rep. Statistics Netherlands.
- Pijpers, F.P. (2017). *Interim report: correlations between reservoir pressure and earthquake rate*. Tech. rep. Statistics Netherlands.
- Romijn, R. and J. Tomic (2016). *Network status overview*. Groningen Event Location Workshop, 20 October 2016. Presentation by Shell (restricted).
- Ruigrok, E., H. Paulssen, and J. Trampert (2015). *Tremor mapping at the Groningen field*. Poster, Schatzalp meeting on Induced Seismicity 2015 in Davos, Switzerland.
- Smith, J., J. Drew, and R. White (2016). *Coalescence Microseismic Mapping*. University of Cambridge.
- Stafleu, J. and C.W. Dubelaar (2016). *Product specification: subsurface model GeoTOP*. Tech. rep. TNO.
- van Thienen-Visser, K., P. Fokker, M. Nepveu, D. Sijacic, J. Hettelaar, and B. van Kempen (2015). *Recent developments on the seismicity of the Groningen field in 2015*. Tech. rep. TNO.
- van Thienen-Visser, K., M. Nepveu, and J. Hettelaar (2012). *Deterministische hazard analyse voor geïnduceerde seismiciteit in Nederland*. Tech. rep. TNO.
- van Thienen-Visser, K., M. Nepveu, B. van Kempen, M. Kortekaas, J. Hettelaar, L. Peters, S. van Gesel, and J. Breunese (2014). *Recent developments of the Groningen field in 2014 and, specifically, the southwest periphery of the field*. Tech. rep. TNO.
- van Thienen-Visser, K., D. Sijacic, J.D. van Wees, D. Kraaijpoel, and J. Roholl (2016). *Groningen field 2013 to present: gas production and induced seismicity*. Tech. rep. TNO.
- Wassing, B.B.T. (2015). "Modeling of fault reactivation and fault slip in producing gas fields". In: *2nd EAGE Workshop on Geomechanics and Energy: The Ground as Energy Source and Storage*.
- Wassing, B.B.T., L. Buijze, and B. Orlic (2016). "Modelling of fault reactivation and fault slip in producing gas fields using a slip-weakening friction law". In: *Proceedings of the 50th US Rock Mechanics/Geomechanics Symposium (ARMA), Houston*.
- Wassing, B.B.T., P.H. Waarts, W. Roos, M. Nepveu, A.G. Muntendam-Bos, and T. van Eck (2010). "Seismic risk analysis of small earthquakes induced by hydrocarbon production in the Netherlands". In: *72nd European Association of Geoscientists and Engineers Conference and Exhibition 2010 incorporating SPE EUROPEC 2010*.
- Weber, B., D. Rössler, and J. Becker (2015). *Introduction of the key features of SeisComp3*. gempa GmbH, Potsdam, Germany. Oral presentation.

|                          |   |  |                              |
|--------------------------|---|--|------------------------------|
| Report Number:<br>18-004 | Confidential: X<br>Unlimited:   | External: X<br>Internal:   | NORSAR Project No.:<br>10150 |
| Title:                   | Review of the public KNMI induced earthquake catalogue from the Groningen gas field (report project phase 1, WP1: catalogue review) |  |                              |
| Client:                  | Staatstoezicht op de Mijnen, Netherlands  |  |                              |
| Project manager:         | D. Kühn   |  |                              |
| Authors/prepared by:     | B. Dando, B. Goertz-Allmann, D. Kühn, N. Langet, V. Oye, A. Wüstefeld (alphabetical order)  |  |                              |
| Submitted to:            | Staatstoezicht op de Mijnen, Netherlands  |  |                              |
| Contract reference:      |   |  |                              |
| Archive reference:       |   |  |                              |
| Approved by:             | Name:   | Signature:   | Date:                        |
| Department head:         | V. Oye  |  | 18/6-2018                    |
| CEO:                     | A. Strømmen Lycke   |  | 17/6-2018                    |



**NORSAR**

info@norsar.no  
www.norsar.no